博士論文
Ph.D. Dissertation

Successive Search-Based Multi-Objective Optimization and its Application to Multidisciplinary Conceptual Design of Reusable Launch Vehicles

（逐次探索による多目的最適化および 宇宙往還機の複合領域概念設計への応用）

December, 2015

Takahiro Fujikawa
（藤川 貴弘）

Department of Aeronautics and Astronautics
School of Engineering
The University of Tokyo

Dissertation Committee in Charge

Takeshi Tsuchiya（土屋武司）
Supervisor
Professor
Department of Aeronautics and Astronautics, School of Engineering, The University of Tokyo

Shinji Suzuki（鈴木真二）
Professor
Department of Aeronautics and Astronautics, School of Engineering, The University of Tokyo

Kojiro Suzuki（鈴木宏二郎）
Professor
Department of Advanced Energy, Graduate School of Frontier Sciences, The University of Tokyo

Taro Imamura（今村太郎）
Associate Professor
Department of Aeronautics and Astronautics, School of Engineering, The University of Tokyo

Nobuhiro Yokoyama（横山信宏）
Associate Professor
Department of Aerospace Engineering, School of System Engineering, National Defense Academy of Japan

Abstract

Conceptual design studies of reusable launch vehicles (RLVs) for future space transportation are essential for clarifying their technological goals and associated issues. In this dissertation, multi-objective, multidisciplinary design optimization (MDO) of two-stage-to-orbit RLVs with airbreathing engines is conducted in order to obtain promising conceptual design options and to reveal tradeoff relations between mission requirements, technological constraints, and the resulting vehicle scale. To this end, research efforts are devoted to three subjects below.

First, a novel multi-objective optimization method that can well handle optimal control problems is developed. The proposed method is based on the successive search of Pareto optimal solutions using the combination of a gradient-based optimizer, min-max goal programming, and farther-point sampling on Pareto manifolds. The farther point from existing solutions is found via the lower-dimensional mapping of the solutions and a Voronoi-diagram-based search. Then, the goal-programming parameters are determined so that the resulting solution will be located near the acquired farthest point. Numerical experiments for a test optimal control problem demonstrate that the present technique outperforms a multi-objective genetic algorithm in terms of optimality, constraint residual, and diversity of the solutions. Another advantage of the developed method is that it can provide as many solutions as needed independently of the solution quality, which is desirable in practical usages.

Second, so as to incorporate thermal protection system (TPS) analysis into MDO frameworks of RLVs, a transient heat-constrained optimal control method is investigated. PDE-expressed thermal behavior inside a TPS material is spatially discretized and transcribed into a set ODEs, and it is then dealt along with ODEs-expressed vehicle dynamics. This spatial discretization is achieved by a pseudospectral scheme with a procedure that makes boundary conditions satisfied automatically. Superior convergence of the proposed technique to previous methods is shown through solving a test problem.

Finally, multi-objective MDO of two kinds of RLVs with airbreathing engines is performed employing the techniques developed above. Numerical frameworks consisting of vehicle geometry definition, mass property estimation, aerodynamic computation, airframe-propulsion integrated analysis, TPS analysis, and flight trajectory calculation, are constructed. In the TPS analysis, the required thickness of insulation tiles is calculated with the aforementioned method. Then, MDO problems are formulated as forms of augmented multi-objective optimal control problems with the following objectives: maximization of the payload mass to the orbit, minimization of the vehicle gross mass, and minimization of the horizontal takeoff velocity. By solving them using the proposed multi-objective optimizer, Pareto optimal solutions with good spread are successfully obtained, which elucidate the tradeoff sensitivity among objectives. After some inspections are given on selected representative solutions, generic knowledge is extracted from all the obtained solutions via data mining techniques. The results provide insights into the influences of the mission requirement and the technological constraint on the optimal RLV design.

Contents

List of Figures

List of Tables

List of Algorithms

Chapter 1

Introduction

1.1 Research Background: Future Space Transportation Systems

Huge improvement to space transportation systems must be achieved in terms of cost efficiency, reliability, operability, and flexibility in order to attract potential users of outer space and to promote the growth of the space transportation market. For instance, Andrews[1] analyzed data from the Commercial Space Transportation Study (CSTS)[2], and stated that space transportation market is divided into a portion whose demand is almost independent from the transportation cost and another portion that is highly elastic to the cost. Then, he pointed out that a key factor for realizing commercially viable space transportation systems is the elastic part which exists when the transportation cost to orbit is approximately less than $600 per kilogram. Since there is a limit in the improvement of expendable launch vehicles, it is dubious that this critical target cost is achieved by the expendable launch vehicles. To make matters worse, cost reduction efforts above this price can result in the reduction of the total yearly revenue, as the increase of flight rate does not overweigh the reduced revenue per flight. Therefore, reusable launch vehicles (RLVs) or space planes are expected to satisfy the severe requirements for future commercial space transportation systems, and they have been studied for years. Recent research activities on several key technologies required for next-generation RLVs (e.g., reusable propulsion systems, high-temperature materials, and guidance algorithms) in Japan are well summarized in Ref. 3.

An essential effort for realizing RLVs other than the component technology researches is to perform their conceptual design studies early in order to clarify technology goals and to facilitate the development of key technologies accordingly. In fact, basic plan on space policy, established by strategic headquarters for space policy in the government of Japan in 2013[4], has the following statement:

> *Comprehensive discussion centered on our space transportation system, including [...] reusable rocket, etc., should take place immediately from a medium- and long-term viewpoint. Measures should be taken based on the result of the discussion.*

The latest plan released in 2015[5] also mentions that the research and development on RLVs should be promoted in Japan. In response to this plan, the Japan Aerospace Exploration Agency (JAXA) has recently investigated the feasibility of fully-reusable two-stage-to-orbit (TSTO) RLVs as long-term goals

(2030s or later)[3]. The transportation of eight persons or an 800 kg payload into a low Earth orbit is assumed as a tentative mission plan, and conceptual design studies on two types of booster-stage vehicles with different propulsion systems are conducted: one with rocket engines and the other with airbreathing engines. Overview of the research and development activities on the rocket-powered RLVs can be found in Ref. 6.

This dissertation focuses on a horizontal takeoff and landing RLV with airbreathing engines, which is one of the ideal space transportation systems that would achieve aircraft-like reliability and operability. In Japan, mainly two kinds of hypersonic airbreathing engines are currently developed. One of them is a rocket-based combined cycle (RBCC) engine[7,8], which is composed of a dual-mode ramjet/scramjet flow-pass with rocket engines embedded in it, and it attains superior performance to conventional rocket engines. Primary characteristics of the RBCC-powered TSTO system concept considered in JAXA are summarized as follows:

1) Ethanol fuel or hydrocarbon fuel is employed instead of cryogenic liquid hydrogen (LH2), aiming at a compact and easily-handled system that contributes to operating cost reduction.

2) The propulsion system is designed with relatively low combustion pressure so as to realize high reliability and to prolong the operational life of the engine.

3) Deterioration of engine specific impulse due to the use of hydrocarbon fuel and low propulsion-system pressure is compensated by an airbreathing technology (i.e., the utilization of atmospheric oxygen).

4) A horizontal takeoff and landing operation is adopted, leading to improved operability and abort capability compared with a vertical launch option.

Another airbreathing propulsion system is a pre-cooled turbojet (PCTJ) engine[9,10]. The PCTJ engine possesses pre-cooling system using liquid fuel prior to its core engine, and it can be operated up to about Mach 6 with high specific impulse, in contrast that the Mach number limit of convectional turbojet engines is around Mach 3.5. Since the precooling effect can be maximized by using LH2 as coolant, the application of LH2-fueled PCTJ engines to TSTO RLVs is a promising option.

1.2 Previous Works and Research Issues in this Dissertation

1.2.1 Multidisciplinary Design Optimization of RLVs

Conceptual design studies on the TSTO RLVs equipped with ethanol-fueled RBCC engines or with LH2-fueled PCTJ engines are challenging tasks. In the related studies that are currently underway[11,12], a satisfactory design solution that can transport a payload into the orbit is not obtained. General issues in the design studies of RLVs with airbreathing engines are as follows:

1) Difficulty in achieving a feasible design:
RLVs with airbreathing engines can be feasible only by integrating advanced element technologies in each design discipline effectively.

2) Nonlinear engine characteristics:
   Due to the highly nonlinear characteristics of airbreathing engines with respect to operating conditions, a simple vehicle sizing analysis based on the velocity increment is not suitable, in contrast to conventional expendable rockets.

3) Interactions between design disciplines:
   There are several design elements that interact with each other in a complicated manner. First, the most significant interaction is the coupling between vehicle design and flight trajectory design. A notable difference from a conventional aircraft design problem is that launch vehicles do not have a cruising state. Therefore, a steady-state design point for the vehicle and the engine cannot be defined. This makes the design study of such RLVs a challenging task from the viewpoints of solution algorithms and computational cost. Second example of interdisciplinary interdependences is the interaction between aerodynamics and propulsion. Hypersonic airbreathing propulsion systems are typically designed by taking advantage of the interaction with the vehicle airframe. Therefore, the performance of the airbreathing engines cannot be evaluated accurately without considering its interaction with the vehicle aerodynamics (especially ramjet and scramjet). Third, it is also known that thermal state of the vehicle surface and the skin friction coefficient are highly correlated in hypersonic flight[13].

In order to handle these difficulties, the application of multidisciplinary design optimization (MDO) to RLVs or hypersonic vehicles has been studied actively[10,14–25]. MDO is a design optimization framework where numerical optimization techniques are applied to the design problem of systems consisting of multiple interacting disciplines or components[26]. In the case of RLVs, the design disciplines may include vehicle geometry, vehicle main structure, propulsion system, aerodynamics, thermal protection system (TPS), guidance and control, manufacturing and operating cost, and so forth. MDO is a promising methodology for performing conceptual design studies of RLVs while considering interdisciplinary interactions explained above. Previous studies on MDO of RLVs can be primarily distinguished from each other in terms of the employed architecture and the fidelity of the design problem as follows:

- MDO architecture:
  A variety of MDO approaches have been developed as summarized in Ref. 26. Among them, the simplest one is the "all-at-once" (AAO) approach. In the AAO method, system-level variables, system-level objectives, system-level constraints, local-disciplinary variables, local-disciplinary objectives, and local-disciplinary constraints are simultaneously handled by a single optimizer, and hence there is no internal iteration loop. In the other MDO approaches, some formulations such that decompose the original problem into smaller problems are applied, in order to reduce the size of a single problem and to enhance the versatility. Performance comparisons of MDO approaches based on simple test problems[27] and on an RLV design problem[19] have revealed that the AAO formulation has stable and rapid convergence, and it is free from convergence errors caused by coupling variables between disciplines. The application of the AAO approach to MDO of RLVs had successful results in previous researches[14–16,21,25]. As stated in Ref. 14, the MDO

problem of RLVs arising from the AAO formulation can be regarded as an augmented optimal control problem. In short, variables and constraints concerning the vehicle design are appended to an optimal control problem in the forms of static variables and static constraints, and the concurrent optimization of vehicle design and flight trajectory design is achieved. A drawback of the AAO approach is that, it becomes more difficult to implement the MDO framework as the disciplinary design models get more elaborate and more complicated.

- Design fidelity:
  In newer studies on MDO of RLVs, the fidelity of the numerical models is improved, and more detailed design is carried out. For example, high-fidelity CFD analysis[23,25], FEM-based structure analysis[10,22,23], and TPS analysis[20,23] are implemented.

Another concern in investigating conceptual design of RLVs is that there are substantial uncertainties in mission requirements and in future technological developments, when the targeted RLV is a long-term goal[28]. Previous MDO studies on RLVs are, to the best knowledge of the author, devoted to finding an optimal design based on a single design criterion (e.g., payload-mass maximization or vehicle-mass minimization) with predetermined technological constraints. When considering the future uncertainties, on the other hand, it is worth revealing how the change of mission requirements and the relaxation of technological constraints have the influence on the optimal design solution. In other words, in the context of optimization, we want to know 1) tradeoff relations between design objectives, or more generally, tradeoffs between objectives and constraints, and 2) sensitivity between the design preference and the resulting optimal solution.

1.2.2 Synergy of Multi-Objective Optimization and Data Mining

So as to meet the above demand, the present study focuses on the synergy of multi-objective design optimization and data mining. A knowledge-discovery framework combining multi-objective optimization and data mining is sometimes called "multi-objective design exploration"[29,30]. The overview of its procedures is shown in Fig. 1.1. Since a practical design optimization problem has multiple objectives that are competing with other, it is well formulated as a multi-objective optimization problem. The formulated multi-objective optimization problem is solved numerically, and a set of Pareto optimal solutions, which reflect the tradeoff relation between objectives, is obtained. A Pareto optimal solution is defined as a solution whose improvement in an objective can only be achieved by deteriorating at least one other objective. Because the set of Pareto optimal solutions is composed of a large number of solutions, and is difficult to interpret directly, data mining or multi-variate analysis is applied. This procedure yields information such as tradeoff, clusters, sensitivity, and trends, which serve as generic knowledge on the design problem at hand. Previous application fields of multi-objective design exploration include aerodynamic shape[29,31], airbreathing propulsion system[32,33], distributed satellite system[34], supersonic aircraft[35], satellite trajectory[36,37], and flow shop scheduling[38]. It is worth noting now that multi-objective evolutionary algorithms[39,40] are employed as a multi-objective optimizer in these previous researches.

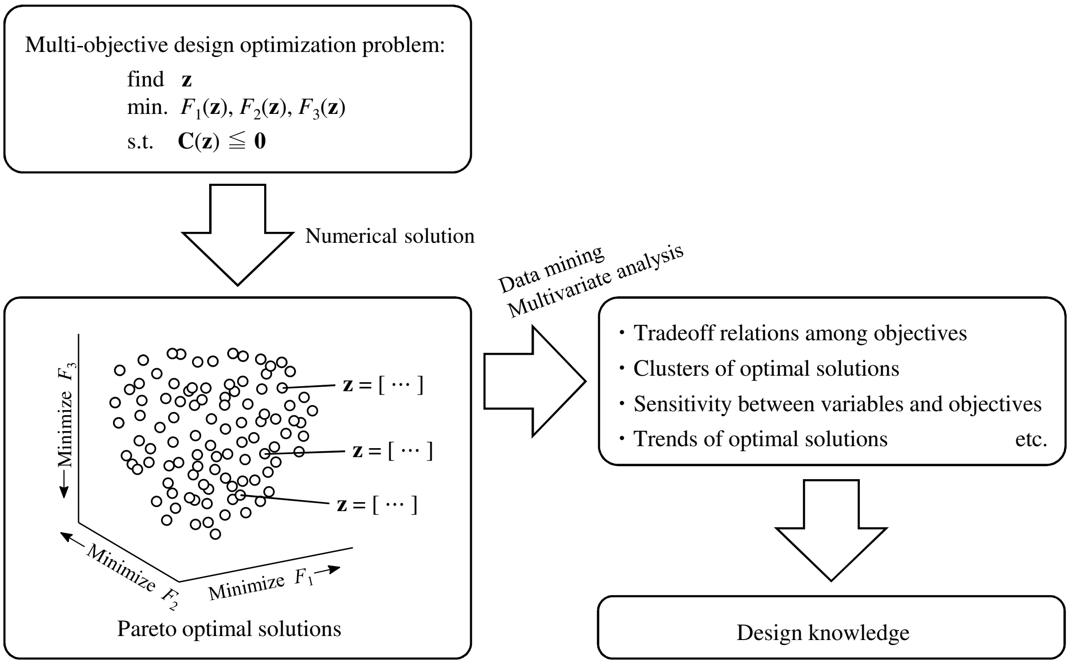

Fig. 1.1 A schematic diagram of the synergy of multi-objective optimization and data mining.

In this dissertation, the multi-objective design exploration is applied to the conceptual design of RLVs, and its multi-objective MDO will be executed. Design objectives are as follows: maximization of the payload transportation capability into a low Earth orbit, minimization of the vehicle gross mass, and minimization of the horizontal takeoff velocity. The takeoff velocity is selected as a design criterion, because it is a major constraint in designing booster vehicles of TSTO RLVs, and the development of landing gear that can withstand high-load and high-speed takeoff would be a challenging technological problem. The derived design knowledge will be helpful not only for establishing design guidelines of this kind of TSTO RLVs but also for conducting future detailed design studies.

1.2.3 Multi-Objective Optimal Control

In order to conduct multi-objective MDO of RLVs efficiently, a methodology for multi-objective optimal control is indispensable. As explained above, the most efficient MDO approach for RLVs is to formulate the MDO problem as an augmented optimal control problem. Distinctive difficulties in solving optimal control problems lie in the fact that they are governed by dynamic variables (i.e., state variables and control variables), ordinary differential equations (ODEs) (i.e., equations of motion), continuous-time constraints (i.e., path constraints), and boundary conditions (i.e., initial and terminal conditions). In this subsection, previous works and issues on numerical methods for multi-objective optimal control are described.

Optimization is a methodology for identifying the best state of a mathematically-expressed system such that minimizes or maximizes a prescribed performance index, or an objective. Among them, methodologies for dealing with dynamic systems governed by differential algebraic equations are called optimal control or trajectory optimization. Thus far, a variety of numerical methods for optimal control have been developed as detailed in Appendix A.1. The most popular family of methods, which are called direct methods, find numerical solutions at discrete times by transcribing the original continuous-time problem into its finite dimensional approximation or a nonlinear programming (NLP) problem[41,42]. The NLP problem is typically solved using a gradient-based optimization method (e.g., sequential quadratic programming[43] or an interior point method[44]). Direct methods are further divided into shooting and collocation methods. In the direct shooting methods, time histories of control variables are parameterized, and the state variables at each time instance are calculated by simulating equations of motion explicitly[45]. In the direct collocation methods, state variables are parameterized as well[46]. Then, differential algebraic equations are implicitly imposed at a finite number of collocation points, and these time-dependent equations are transcribed into static constraints. These previous methods are devoted to solving a single-objective optimal control problem and to obtaining its single solution.

In the field of static optimization, on the other hand, more than one objective is frequently considered, which is termed multi-objective optimization. In the case of multi-objective optimization, the desired output is not a single optimal solution but a collection of Pareto optimal solutions. A goal in numerically solving multi-objective optimization problems is to obtain solutions that are close to the true Pareto front (convergence) and are uniformly distributed (diversity). Mainly employed numerical solution approaches are population-based meta-heuristics, where a large number of candidate solutions stochastically explore the solution space while interacting with each other. Such methodologies are called multi-objective evolutionary algorithms (MOEAs)[39,40], and multi-objective genetic algorithms (MOGAs) are their typical examples.

There are a lot of situations where multiple performance indices should be considered in optimal control problems as well. In recent years, several researches on multi-objective optimal control have been performed. Prats et al.[48] tackled the departure trajectory optimization problem of jet airliners aiming at minimizing fuel consumption, minimizing flight duration, and minimizing noise exposure on the ground. The employed technique is the combination of lexicographic method[39, pp. 72–73] and a gradient-based optimization method. Using the lexicographic method, a multi-objective optimization problem is solved by considering each objective sequentially. Even when the priority order of objectives is altered, optimal solutions that are not located on the boundaries of Pareto front cannot be found. Oyama et al.[37] conducted multi-objective trajectory optimization of a solar observatory satellite using a hybrid approach of an MOGA and a gradient-based optimizer. This consists of an outer loop where the MOGA optimizes significant design variables (e.g., initial azimuth angle) and an inner loop where the gradient-based method optimizes thrust profile of electric propulsion system. Since only a single objective is considered during the inner-loop optimization, the resulting solutions are nothing more than approximate Pareto optimal solutions. Jiao et al.[49] solved multi-objective reentry trajectory optimization of hypersonic vehicles using the goal-attainment method and ant colony optimization. This approach only provides a Pareto optimal solution depending on the relative importance of objectives specified by the user beforehand. Summarizing the above, these existing methods have some limitations.

In addition, it is also questionable that MOEAs are suited to optimal control problems in the sim-

Table 1.1 Characteristics of static optimization problems and optimal control problems.

Problem	Employed parameterization	Typical difficulties
Static optimization problem	–	Expensive functions (e.g., CFD)
Optimal control problem	Direct shooting	Numerical instability[42], Equality boundary conditions
Optimal control problem	Direct collocation	Large number ($> 10^2$) of variables and constraints

ilar way to static optimization problems. In order to discuss this issue, the differences between static optimization problems and optimal control problems are presented below (see also Table 1.1):

- Static optimization problem:
  Static optimization problems often considered in the aerospace field include aerodynamic shape optimization and structure optimization. In these applications, a small number of inequality design constraints are imposed if any. A typical difficulty is that its function evaluation is very expensive when high-fidelity CFD computations or FEM-based structure analyses are conducted.

- Optimal control problem with direct shooting methods:
  The NLP problem arising from an optimal control problem via the direct shooting methods is smaller in size compared to the problem resulting from the direct collocation methods. However, sensitivities between the parameterized control variables and the objective are quite different from each other, and this sometimes leads to numerical instability of gradient-based optimizers[42]. MOEAs cannot necessarily solve this NLP problem efficiently either. Optimal control problems are typically formulated with equality boundary conditions. Since these equality constraints are directly or indirectly dependent on all the parameterized control variables, they must be varied simultaneously in a coordinated manner in order to keep the constraints being satisfied. In the literature, it is reported that MOEAs have some weaknesses in solving such optimization problems[50,51]. As a result, the solutions obtained with MOEAs can suffer from poor convergence, large constraint violation, and unsatisfactory diversity. Although a modified GA for optimal control problems was proposed in Ref. 52, thousands of generations in the GA optimization are still required before the population gets converged. While such a large number of iterations may be acceptable in the case of optimal control problems, it matters in an MDO problem whose function evaluation in each iteration is far more computationally expensive.

- Optimal control problem with direct collocation methods:
  Since the direct collocation methods transcribe an optimal control problem into a large-scale NLP problem (the numbers of variables and constraints are hundreds at least), it becomes intractable for MOEAs. Instead, the NLP problem can be solved efficiently using gradient-based optimization methods by exploiting the sparsity of the problem[42]. A remaining issue is that gradient-based optimization methods cannot deal with multi-objective problems directly.

Considering all the discussions in this subsection, a novel numerical method for obtaining Pareto optimal solutions of multi-objective optimal control problems will be developed in the present study. The applicability of gradient-based optimization methods to multi-objective NLP problems arising from multi-objective optimal control problems via the direct collocation methods will be investigated. Especially, an algorithm for finding a set of Pareto optimal solutions with the uniform distribution will be proposed in order to obtain diverse solutions.

1.2.4 Thermal Protection System Design for RLVs

Another critical subject in the MDO of RLVs is the improvement of the model fidelity of the design problem. Among design disciplines of RLVs, this dissertation focuses on the passive (i.e., nonablative) TPS such as ceramic insulation tiles. In this subsection, previous works and remaining issues on the TPS analysis in the MDO of RLVs are explained.

TPS is one of the significant design disciplines of an RLV, and it has a major impact on the payload-mass fraction, reliability, and operability of the launch system. It is noted that the TPS mass accounts for ten and several percent of the vehicle dry mass in some RLVs[53]. In previous MDO studies on RLVs[15,16,19,25] or on hypersonic aircraft[21,22,24], the TPS mass is estimated by assuming TPS materials and their thickness beforehand based on some historical data[54]. Cowart and Olds[53] called such an approach “offline” or “static”, and they stated the necessity of an “online” or “dynamic” approach where TPS design is performed while considering the actual thermal environment resulting from vehicle shape design and flight trajectory design.

When the trajectory design of expandable reentry vehicles is conducted, it is a common practice to impose a constraint on the stagnation point heat flux[55–58]. This constraint is equivalent to an upper limit on the TPS surface temperature at the stagnation point, when radiative equilibrium is assumed. Given the long flight duration of airbreather-powered RLV booster or hypersonic aircraft, on the other hand, the following design criterion for the passive TPS must be considered as well: TPS backface (an inside surface attached to the vehicle main structures) must not exceed the operating temperature limits of the material used for the main structure throughout the flight[53,59]. This means, instationary or transient thermal states inside TPS materials during the flight have to be considered.

In response to the demand for the conceptual-level analysis and design of TPS for RLVs, several computational tools have been developed[53,59]. In these tools, a heat transfer problem inside TPS materials in the depth direction is numerically solved after the time history of flight conditions and vehicle geometry are supplied. In other words, the one-dimensional heat equation, which is expressed as a second-order partial differential equation (PDE), is solved. Then, the minimum thickness of a TPS layer is determined under the restriction that the backface temperature limit is satisfied.

In some recent MDO studies on RLVs, such TPS sizing tools are incorporated into the MDO architectures in the following way[20,23]: Inner optimization loops for the trajectory design and for the TPS sizing are wrapped with the outer loop where the overall convergence is sought. This MDO formulation with the nested structure, however, is typically known to be computationally less efficient than the AAO approach as explained in Section 1.2.1. When we want to incorporate high-fidelity analysis tools into the AAO-based MDO frameworks, surrogate-modeling techniques can reduce computational burden and relieve difficulty in the implementation, as discussed in Ref. 14. However, the construction of a surrogate model for the TPS analysis is infeasible, because the number of inputs is huge (time history of flight conditions). Instead, an alternative approach will be developed in this dissertation, where the MDO problem is formulated in the form of an augmented PDE-ODE coupled optimal control problem. Here, the PDE stands for the heat equation inside the TPS material, and the ODE means vehicle dynamics. This new type of optimal control problem arising from the presence of the transient heat constraint has been investigated recently [60–62]. In Refs. 61 and 62, the flight trajectory of hypersonic aircraft was optimized considering the TPS backface temperature limit. The formulated PDE-ODE coupled optimal control problem was numerically solved via discretizing the PDE using a finite volume method. In Ref. 60, the instationary heat-constrained optimal control problem of a rocket-powered ground vehicle was introduced, and it was solved using a finite difference scheme. When the large-scale MDO problem of the whole RLV system is considered, the PDE discretization based on these previous methods can easily lead to a huge and numerically intractable optimization problem. In order to overcome this challenge and to incorporate the online TPS analysis into the MDO of RLVs, an efficient method for solving transient heat-constrained optimal control problems will be developed in the present study.

1.3 Research Objectives

Considering the research issues described in Section 1.2, research objectives of the present study are established as follows:

1) Development of a numerical method for solving multi-objective optimal control problems:
   Considering the trajectory-driven nature of the MDO problem of RLVs, a multi-objective optimal control technique is required. The applicability of gradient-based optimization methods to multi-objective NLP problems arising from multi-objective optimal control problems via the direct collocation methods will be investigated. A novel algorithm such that successively searches Pareto optimal solutions so that the diversity of the solutions is enhanced, will be proposed.

2) Development of a transient heat-constrained optimal control method:
   In order to incorporate the TPS analysis into MDO of RLVs in an efficient manner, a numerical method for solving transient heat-constrained optimal control problems will be developed. Since it is formulated as a PDE-ODE coupled optimal control problem, an efficient discretization scheme for transcribing the PDE in a set of ODEs will be examined.

3) Multi-objective design exploration of TSTO RLVs with airbreathing engines:
   Conceptual design studies on a fully-reusable TSTO RLV with LH2-fueled PCTJ engines and that with ethanol-fueled RBCC engines will be performed. Numerical models of the design problems, including TPS analysis, are constructed, and multi-objective MDO problems will be formulated. Multi-objective optimization will be executed using the novel method, and promising conceptual design options will be obtained. Then, the influences of mission requirement and technological

constraint on the optimal RLV design will be revealed via data mining techniques.

1.4 Contests of this Dissertation

This dissertation is organized as follows:

Chapter 1 introduced research background and research issues that have not been addressed sufficiently in previous researches. Then, research objectives of the present study were defined.

A novel numerical technique for multi-objective optimal control is proposed in Chapter 2. After its algorithm is described, performance comparison with an MOGA is performed. Additionally, the applicability of the proposed method to a practical problem is demonstrated.

In Chapter 3, a heat-constrained optimal control method is developed for conducting the instationary TPS analysis in the MDO of RLVs. An efficient numerical scheme is presented, and its validity is illustrated through solving an example problem.

Subsequently, conceptual design studies on TSTO RLVs with airbreathing engines are conducted based on a multi-objective design exploration framework. The multi-objective MDO problems are solved using a novel method developed in Chapter 2. Design knowledge is extracted via applying data mining techniques to the obtained Pareto optimal solutions. A TSTO RLV with PCTJ engines and that with RBCC engines are considered in Chapter 4 and in Chapter 5, respectively.

Finally, results of the present study are summarized, and some recommendations for future work are presented in Chapter 6.

In Appendices A–F, additional explanations are provided on optimization methods and analysis models.

1.5 Mathematical Notations

In this dissertation, vector-valued variables and functions are written with bold upright fonts, and scalar-valued variables and functions are described using italic type, in order to distinguish them. Vector-valued variables and functions are defined as column vectors unless otherwise noted.

Chapter 2

Successive Solution Search Method for Multi-Objective Optimal Control

In this chapter, a novel algorithm for obtaining Pareto optimal solutions to multi-objective optimal control problems is presented. The proposed method is based on the successive search of Pareto optimal solutions using the combination of 1) a gradient-based optimization method, 2) min-max goal programming, and 3) Pareto manifold sampling. The transformation of a multi-objective optimal control problem into its relevant single-objective NLP problem is described in Section 2.1. Section 2.2 details the successive procedures for calculating parameters used in the transformation so that the resulting solution will be located near the farthest point from the existing solutions. Validity and efficiency of the proposed algorithm are shown in Section 2.3 by conducting the performance comparison to an MOGA on a test problem. In Section 2.4, applicability of the proposed algorithm to a practical problem is demonstrated through solving a Space Shuttle reentry problem. Finally, Section 2.5 provides concluding remarks.

2.1 Transformation into Single-Objective NLP Problems

Consider the following generalized continuous-time optimal control problem with M objectives:

$$\text{Problem P}\begin{cases}\text{find} & \mathbf{x}(t),\ \mathbf{u}(t),\ t_0,\ t_\mathrm{f},\ \mathbf{p}\\ \text{min.} & F_1 := \varPhi_1[\mathbf{x}(t_0), t_0, \mathbf{x}(t_\mathrm{f}), t_\mathrm{f}, \mathbf{p}]\\ & \qquad + \displaystyle\int_{t_0}^{t_\mathrm{f}} g_1[\mathbf{x}(t), \mathbf{u}(t), t, \mathbf{p}]\,\mathrm{d}t,\\ & \qquad\qquad \vdots\\ & F_M := \varPhi_M[\mathbf{x}(t_0), t_0, \mathbf{x}(t_\mathrm{f}), t_\mathrm{f}, \mathbf{p}]\\ & \qquad + \displaystyle\int_{t_0}^{t_\mathrm{f}} g_M[\mathbf{x}(t), \mathbf{u}(t), t, \mathbf{p}]\,\mathrm{d}t\\ \text{s.t.} & \dfrac{\mathrm{d}\mathbf{x}}{\mathrm{d}t} = \mathbf{f}[\mathbf{x}(t), \mathbf{u}(t), t, \mathbf{p}],\\ & \mathbf{C}[\mathbf{x}(t), \mathbf{u}(t), t, \mathbf{p}] \le \mathbf{0},\\ & \mathbf{\Psi}[\mathbf{x}(t_0), t_0, \mathbf{x}(t_\mathrm{f}), t_\mathrm{f}, \mathbf{p}] \le \mathbf{0},\end{cases} \tag{2.1}$$

where $t \in [t_0, t_\mathrm{f}]$, $\mathbf{x}(t)\colon [t_0, t_\mathrm{f}] \to \mathbb{R}^{n_x}$, $\mathbf{u}(t)\colon [t_0, t_\mathrm{f}] \to \mathbb{R}^{n_u}$, and $\mathbf{p} \in \mathbb{R}^{n_p}$ are time, state variables, control variables, and static parameters, respectively. The ith objective function, F_i, is composed of the Mayer term, $\varPhi_i$, and the Lagrange term, g_i, (see Appendix A for more details). t_0 and t_f denote the initial time and the terminal time, respectively. All the functions involved (i.e., $\{\varPhi_i\}_{i=1}^{M}$, $\{g_i\}_{i=1}^{M}$, $\mathbf{f}$, $\mathbf{C}$, and $\boldsymbol{\Psi}$) are nonlinear and continuously differentiable. It is noted that any equality constraint can be expressed by simply using two inequality constraints.

Suppose now that we consider the m-element subset out of M objectives, and their indices are denoted by $\mathbb{I}$ $(=: [I_1, \dots, I_m]^\mathrm{T} \in \mathbb{N}^m)$. Here, it is assumed that more than one objective are selected, namely, $m \geq 2$. By applying min-max goal programming[63] to these selected m objectives, the following single-objective problem is obtained:

$$\begin{array}{c}\text{Problem}\\ \tilde{\mathrm{P}}(\mathbb{I}, w_i, F_i^*)\end{array}\left\{\begin{array}{rl}\text{find} & q,\ \mathbf{x}(t),\ \mathbf{u}(t),\ t_0,\ t_\mathrm{f},\ \mathbf{p}\\ \text{min.} & q\\ \text{s.t.} & F_{I_1} - w_1 \cdot q \leq F_1^*,\\ & \qquad\vdots\\ & F_{I_m} - w_m \cdot q \leq F_m^*,\\ & \dfrac{\mathrm{d}\mathbf{x}}{\mathrm{d}t} = \mathbf{f}[\mathbf{x}(t), \mathbf{u}(t), t, \mathbf{p}],\\ & \mathbf{C}[\mathbf{x}(t), \mathbf{u}(t), t, \mathbf{p}] \leq \mathbf{0},\\ & \boldsymbol{\Psi}[\mathbf{x}(t_0), t_0, \mathbf{x}(t_\mathrm{f}), t_\mathrm{f}, \mathbf{p}] \leq \mathbf{0},\end{array}\right. \tag{2.2}$$

where w_i $(\in \mathbb{R}_>)$ is the weight of the I_ith objective, and F_i^* $(\in \mathbb{R})$ is the target value of the I_ith objective. They are independent parameters in the goal-programming method that are specified by the user. When smaller w_i is employed, Problem $\tilde{\mathrm{P}}(\mathbb{I}, w_i, F_i^*)$ gives a solution such that puts larger significance on the I_ith objective. In Eq. (2.2), the minimization of m objectives problem is expressed by the minimization of q $(\in \mathrm{R})$ and newly introduced inequality constraints. Note that optimal q can be written as $q = \max\limits_{i \in \{1,\dots,m\}} \left[\left(F_{I_i} - F_i^*\right)/w_i\right]$, which means that q indicates the maximum weighted deviation of objective values from their corresponding targets. In addition, this is the reason why this procedure for transforming a multi-objective problem into its relevant single-objective problem is called “min-max” goal programming.

Subsequently, Problem $\tilde{\mathrm{P}}(\mathbb{I}, w_i, F_i^*)$ is transcribed into a single-objective NLP problem using any direct collocation method for optimal control (see Appendix A for more details). Throughout this dissertation, a Legendre-Gauss pseudospectral method[64,65] with adaptive mesh refinement[66,67] is employed. This mesh refinement algorithm automatically and iteratively provides discretization meshes which improve computational efficiency and robustness of pseudospectral methods. The resulting NLP problem consists of large numbers of design variables and constraints when it becomes a good approximation to the original continuous-time problem. A set of parameters concerning the discretization mesh used in the direct collocation method is collectively represented by $\mathbf{N}$ for the simplicity of notation. The NLP problem can be briefly written as follows:

$$\text{Problem } \tilde{\mathrm{P}}^{\mathbf{N}}(\mathbb{I}, w_i, F_i^*) \begin{cases} \text{find} & q, \mathbf{z} \\ \text{min.} & q \\ \text{s.t.} & \mathbf{G}^{\mathbf{N}}(q, \mathbf{z}) \leq \mathbf{0}, \end{cases} \tag{2.3}$$

where $\mathbf{z}$ is NLP decision variables that are composed of the parameterized state, the parameterized control, t_0, t_f, and $\mathbf{p}$. $\mathbf{G}^{\mathbf{N}}$ denotes a set of constraint functions derived by applying the direct collocation method to Problem $\tilde{\mathrm{P}}(\mathbb{I}, w_i, F_i^*)$.

Next, let us consider the case where $m = 1$ and only the ith objective, F_i, is extracted. In this instance, Problem P can be directly transcribed into the following single-objective NLP problem without employing goal programming:

$$\text{Problem } \mathrm{P}^{\mathbf{N}}(i) \begin{cases} \text{find} & \mathbf{z} \\ \text{min.} & F_i^{\mathbf{N}}(\mathbf{z}) \\ \text{s.t.} & \mathbf{H}^{\mathbf{N}}(\mathbf{z}) \leq \mathbf{0}, \end{cases} \tag{2.4}$$

where $F_i^{\mathbf{N}}(\mathbf{z})$ and $\mathbf{H}^{\mathbf{N}}(\mathbf{z})$ are the direct collocation transcriptions of the ith objective and constraint functions in Problem P, respectively.

2.2 Successive Search of Optimal Solutions on a Pareto Front Manifold

2.2.1 Preliminaries

In the previous section, a single-objective NLP problem is uniquely obtained in Eq. (2.3) by specifying a set of parameters, $\{\mathbb{I}, w_i, F_i^*, \mathbf{N}\}$. Additionally, the case of $m = 1$ leads to Problem $\mathrm{P}^{\mathbf{N}}(i)$ by determining $\{i, \mathbf{N}\}$. These NLP problems can be efficiently solved using a gradient-based optimizer[43,44], and a solution depending on these independent parameters is obtained. Hereafter, let us call these parameters goal-programming parameters. In min-max goal programming, it is possible to find every Pareto optimal solution by properly changing weight and target[63]. It should be noted that a well-known weighted sum method[39], on the other hand, fails to capture solutions located on the concave region of the Pareto front. Therefore, the remaining problem is how to determine $\{\mathbb{I}, w_i, F_i^*\}$, since $\mathbf{N}$ is a set of parameters automatically provided by the mesh refinement algorithm. In addition to the convergence to the Pareto optimal sets, it is also desired that a multi-objective optimizer finds a set of solutions with a good spread (i.e., obtaining solutions that span the Pareto front entirely and uniformly)[39]. A successive and adaptive algorithm for determining goal-programming parameters such that achieve this goal is developed under the following assumptions on the problem at hand:

Assumption 1 *The Pareto front is compact, that is, bounded and closed.*

Assumption 2 *The Pareto front is not disconnected.*

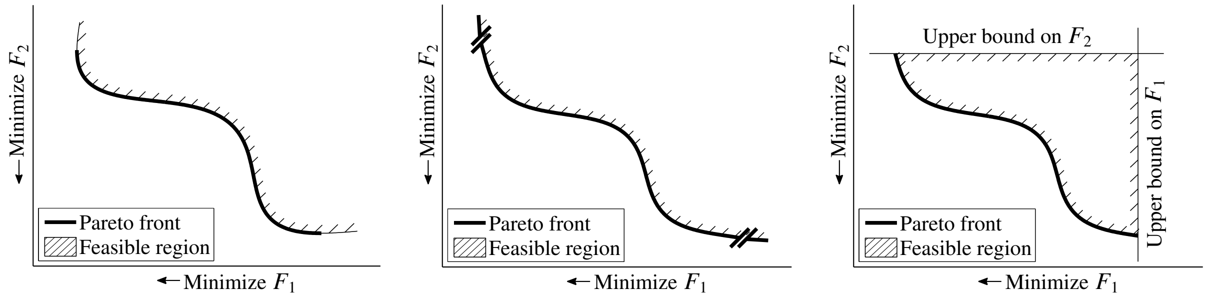

(a) Assumption 1 is satisfied (bounded Pareto front).
(b) Assumption 1 is not satisfied (unbounded Pareto front).
(c) A measure for making Assumption 1 satisfied.

Fig. 2.1 Schematic drawings of Assumption 1.

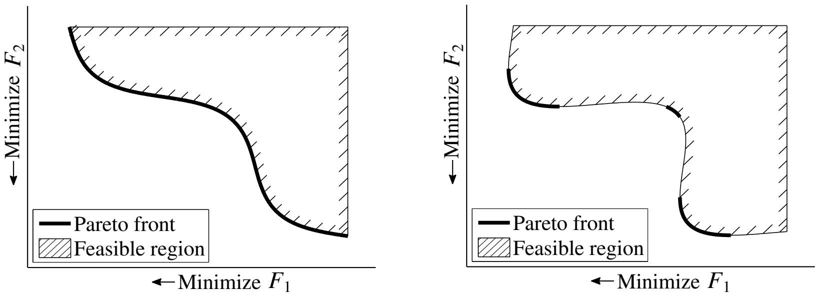

(a) Assumption 2 is satisfied (connected Pareto front).
(b) Assumption 2 is not satisfied (disconnected Pareto front).

Fig. 2.2 Schematic drawings of Assumption 2.

Figures 2.1a and 2.1b present example cases where Assumption 1 is satisfied and is not satisfied, respectively. When the Pareto front of the multi-objective optimization problem at hand is unbounded and does not have a boundary, a possible corrective action is to impose upper bounds on objective functions as shown in Fig. 2.1c. For engineering purposes, it is rational to introduce this kind of upper bounds, because there are usually allowable compromise limits on objectives values. Figure 2.2 presents the schematic drawings of connected and disconnected Pareto fronts.

Next, let us introduce the following general property of Pareto optimal solutions on which the proposed algorithm is based:

Theorem 1 *Under mild regularity conditions, the set of Pareto optimal solutions of an m-objective optimization problem defines a piecewise continuous (m-1)-dimensional manifold.*

Proof. See pp. 163–165 of Ref. 68.

2.2.2 Method Outline

On the basis of the assumptions and the theorem mentioned above, an algorithm is developed as outlined in Algorithm 1. Its basic idea is to successively determine the goal-programming parameters so that the resulting solution will lie at the location where the already obtained solutions are most scarcely located. The first step is to solve NLP problems derived from single-objective problems (i.e., Prob-

Algorithm 1 The outline of the proposed multi-objective optimization algorithm.

```
1.  // Solve single-objective problems ($m = 1$)
2.  for $i = 1, \dots, M$ do
3.      Solve an NLP problem, $\mathrm{P}^{\mathbf{N}}(i)$
4.  end for
5.  // Solve $m$-objective problems ($m = 2, \dots, M$)
6.  for $m = 2, \dots, M$ do
7.      for $j = 1, \dots, \binom{M}{m}$ do
8.          $\mathbb{I} \leftarrow \{$indices of $m$ objectives in the $j$th case out of $\binom{M}{m}$ variations$\}$
9.          repeat
10.             Dimensionality reduction of the solutions obtained so far (Section 2.2.3)
11.             Find the farthest point via a Voronoi diagram (Section 2.2.4)
12.             Calculation of $\{w_i, F_i^*\}$ (Section 2.2.5)
13.             Solve an NLP problem, $\tilde{\mathrm{P}}^{\mathbf{N}}(\mathbb{I}, w_i, F_i^*)$
14.         until Termination condition, Eq. (2.6), is met
15.     end for
16. end for
```

lem $\mathrm{P}^{\mathbf{N}}(i)$, $i = 1, \dots, M$). This corresponds to Lines 2–4 in Algorithm 1. In these procedures, goal programming parameters are not required, and M solutions are produced in the M-dimensional objective space as shown in Fig. 2.3a.

Subsequently, problems with the sequentially increasing number of objective functions are solved. When m-objective problems are considered, there are $\binom{M}{m}$ variations in choosing m elements out of M objectives. Let the geometry constructed by solutions of the problem with the $\mathbb{I}$ ($\in \mathrm{N}^m$)th objectives be denoted by $\mathbb{M}_{\mathbb{I}}$. This represents a locally linear approximation of the true Pareto front (see Fig. 2.3). The boundary of the Pareto front can be built from some Pareto fronts of lower-dimensional problems, that is

$$\partial \mathbb{M}_{\mathbb{I}} = \bigcup_{\mathbb{I}' \subset \mathbb{I}} \mathbb{M}_{\mathbb{I}'}, \tag{2.5}$$

where $\partial \mathbb{M}_{\mathbb{I}}$ means the boundary of the bounded Pareto front $\mathbb{M}_{\mathbb{I}}$. If a termination condition is satisfied at Line 14 for all of the $\binom{M}{m}$ variations, the process goes on to higher-dimensional problems: $m \leftarrow m + 1$. Figure 2.3 illustrates these procedures in the case of $M = 3$. White markers represent the solutions obtained in the present step, and black markers describe the solutions found in previous step(s). The spread of each Pareto front in $m = 2$ is constrained by the solutions in $m = 1$. Likewise, Pareto fronts found in $m = 2$ define the boundary of the Pareto front manifold in $m = 3$. A similar multi-objective optimization procedure, where the number of objective functions is successively increased, can be found in Ref. 69.

In the proposed algorithm, the termination condition at Line 14 is given as follows:

$$d_{\max} := \max_{\mathbf{r} \in \mathbb{M}_{\mathbb{I}}} \left[\min_i \left[d_{\mathrm{geo}}(\mathbf{r},\, \mathbf{s}_i) \right] \right] \leq d_{\mathrm{tol}}. \tag{2.6}$$

$d_{\mathrm{geo}}(\cdot,\, \cdot)\colon \mathbb{R}^M \times \mathbb{R}^M \to \mathbb{R}$ represents a geodesic distance between two points along $\mathbb{M}_{\mathbb{I}}$. $\mathbf{r}$ ($\in \mathbb{R}^M$) indicates

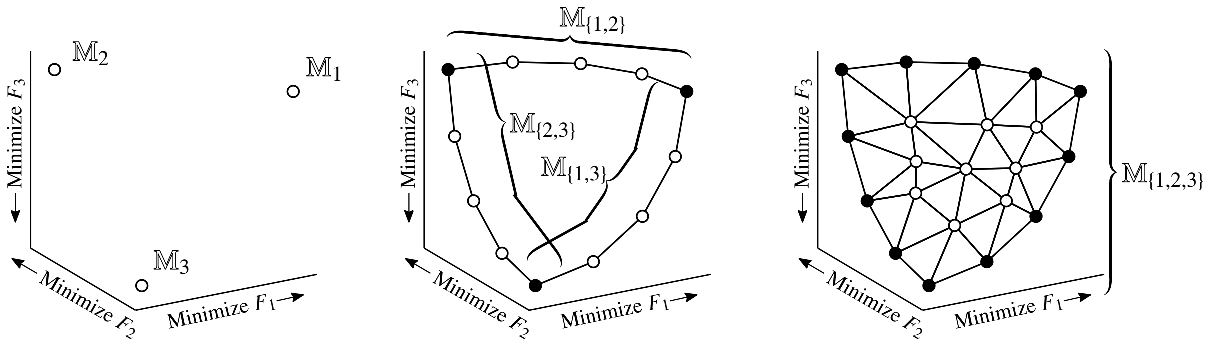

(a) In the step of $m = 1$. (b) In the step of $m = 2$. (c) In the step of $m = 3$.

Fig. 2.3 Procedures for obtaining a set of solutions in the M-dimensional objective space in the case of $M = 3$.

the coordinates of a point in the M-dimensional objective space. $\mathbf{s}_i$ ($\in \mathbb{R}^M$) is the coordinates of the ith solution on $\mathbb{M}_{\mathbb{I}}$ in the objective space, and its elements are denoted by $\mathbf{s}_i =: [s_{1\,i}, \ldots, s_{M\,i}]^{\mathrm{T}}$. Eq. (2.6) means that the geodesic distance to its nearest solution on $\mathbb{M}_{\mathbb{I}}$ must not exceed the user-supplied tolerance, d_{tol} ($\in \mathbb{R}_{>}$), for any point on $\mathbb{M}_{\mathbb{I}}$. Let a point with the maximum geodesic distance to its nearest solution be referred to as the farthest point, and be specially denoted by $\hat{\mathbf{r}} =: [\hat{r}_1, \ldots, \hat{r}_M]^{\mathrm{T}} \in \mathbb{R}^M$. In applying goal programming method at Line 13, the employed goal-programming parameters are determined so that the resulting solution will be located at this farthest point. When Eq. (2.6) is finally satisfied for $m = M$, we have a set of solutions to the original problem, Eq. (2.1). In the subsequent subsections, the procedures for finding the farthest point and those for calculating goal programming parameters are explained.

2.2.3 Dimensionality Reduction Mapping of the Existing Solutions

In seeking the farthest point, the degree of proximity between two points cannot be measured in terms of a Euclidean distance in the M-dimensional objective space. Instead, the appropriate metric is a geodesic distance along the surface on which these points are located. Due to Theorem 1, this constrained surface is equivalent to an $(m-1)$-dimensional manifold, $\mathbb{M}_{\mathbb{I}}$, as depicted in Fig. 2.4a. The $(m-1)$-dimensional manifold is intuitively defined as a geometry that can be locally described by an $(m-1)$-dimensional Euclidean space. Considering this property, Pareto optimal solutions can be mapped into the $(m-1)$-dimensional Euclidean space while substantially preserving local distances using dimensionality reduction techniques as shown in Fig. 2.4b. As a consequence of this dimensionality reduction, the geodesic distance along $\mathbb{M}_{\mathbb{I}}$ can be approximated by a Euclidean distance in this $(m-1)$-dimensional Euclidean space.

Dimensionality reduction methods are classified into two categories: linear techniques and nonlinear techniques. Although nonlinear techniques can handle nonlinear geometries, data points have to be distributed somewhat uniformly in order to unfold a manifold successfully[70]. For this reason, either linear or nonlinear technique is employed depending on the distribution of the solutions obtained so far

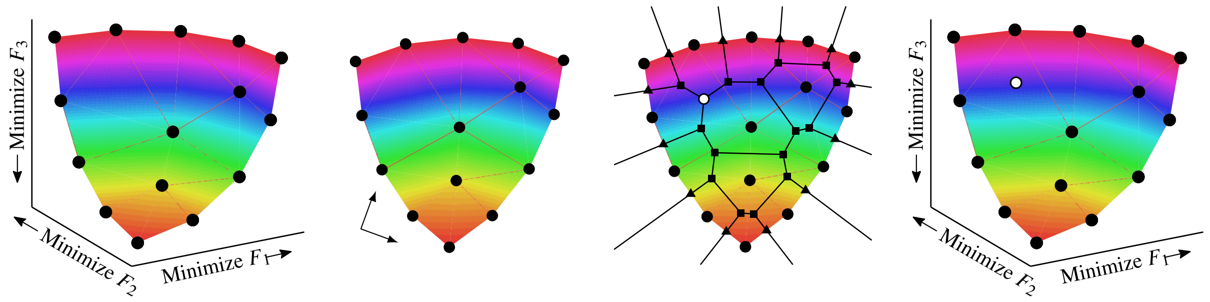

(a) Solutions on $\mathbb{M}_{\mathbb{I}}$ in the M-dimensional objective space.

(b) Mapping in the $(m - 1)$-dimensional space.

(c) A Voronoi diagram and the found farthest point (a white marker).

(d) The farthest point on $\mathbb{M}_{\mathbb{I}}$ in the M-dimensional objective space.

Fig. 2.4 Strategies for finding the farthest point from existing solutions in the case of $[M, m] = [3, 3]$.

as follows:

$$\begin{cases} \text{Isomap}^{[71]} & \text{if } d_{\max} \leq 2d_{\text{tol}}, \\ \text{Linear local tangent space alignment (LLTSA)}^{[72]} & \text{otherwise.} \end{cases} \tag{2.7}$$

It is noted that Pareto fronts do not have drastically nonlinear shapes like a Swiss roll as can be seen in Ref. 71. Therefore, linear techniques do not fail even though the mapping accuracy is deteriorated. Eq. (2.7) means that LLTSA is employed first, and Isomap is used after a sufficient number of solutions are found. Isomap is a nonlinear manifold learning algorithm that is designed to find a lower-dimensional embedding that best preserves interpoint geodesic distances. This property makes Isomap a suitable method to the present purpose. A neighborhood size parameter for Isomap, which is the number of neighbors within which Euclidean distances are regarded as geodesic distances, is set to 12. LLTSA is a linear method, where a lower-dimensional mapping is obtained via aligning local tangent spaces constructed from neighbors of each data point.

When $m = 2$, the corresponding Pareto front is a one-dimensional geometry, that is, a curve. Therefore, the above-mentioned dimensionality reduction procedure is not required. Instead, an angular coordinate, θ, of a polar coordinate system, $[r, \theta]^{\mathrm{T}}$, can be regarded as a local coordinate on this Pareto front manifold based on the following definition:

$$\begin{bmatrix} s_{I_1,i} \\ s_{I_2,i} \end{bmatrix} = \begin{bmatrix} r\cos\theta \\ r\sin\theta \end{bmatrix} + \mathbf{O}, \tag{2.8}$$

where $\mathbf{O} := [O_1, O_2]^{\mathrm{T}}$ is the coordinate of a polar defined as

$$O_k = 1.1 \min_j \left[s_{I_k,j} \right] - 0.1 \max_j \left[s_{I_k,j} \right], \quad k = 1, 2. \tag{2.9}$$

2.2.4 Farthest-Point Finding via a Voronoi Diagram

Once the solutions are mapped into the $(m-1)$-dimensional Euclidean space, the farthest (in terms of a Euclidean distance) point from these embedded solution points can be found using a Voronoi diagram (see Fig. 2.4c). A Voronoi diagram is a way of dividing space into a number of cells so that each cell contains all the spots which are closer to a corresponding point than any other points. In Fig. 2.4c, candidates for the farthest point are 1) Voronoi vertices in an area surrounded by the boundary of the Pareto front (shown by square markers) and 2) intersections of Voronoi edges and the boundary (depicted by triangular markers). The boundary is already constructed in previous steps in Algorithm 1 as explained in Section 2.2.2. Furthermore, solutions are located so densely on this boundary as to satisfy the termination condition, Eq. (2.6). Therefore, the latter candidates for the farthest point can be excluded.

A point in the former candidates such that has the largest Euclidean distance to its nearest solution is defined as the farthest point. Then, the farthest point is mapped back into the original M-dimensional space, and it gives a good approximation to the farthest (in terms of a geodesic distance) point on $\mathbb{M}_\mathbb{I}$ as illustrated in Fig. 2.4d. This inverse mapping is achieved by calculating the circumcenter of a triangle in the M-dimensional objective space constructed by nearby solutions of the farthest point. In Figs. 2.4c and d, white markers represent the farthest point.

When $m = 2$, the Voronoi diagram-based search is unnecessary, since one-dimensional embeddings of the corresponding solutions lie on a straight line. The farthest point can be obtained as the middle point of adjacent two solution points with the largest distance along this line.

2.2.5 Calculation of Goal Programming Parameters

The goal-programming parameters, $\{w_i, F_i^*\}$, are calculated so that the solution of Problem $\tilde{\mathrm{P}}^{\mathbf{N}}(\mathbb{I}, w_i, F_i^*)$ will be located in the vicinity of the acquired farthest point. The target values, $F_i^*,\ i = 1, \ldots, m$, are determined as follows:

$$F_i^* = (1+\alpha)\min_j \left[s_{I_i j}\right] - \alpha \max_j \left[s_{I_i j}\right] \quad \text{for } i = 1, \ldots, m, \tag{2.10}$$

where α represents a margin for placing the target point, and $\alpha = 0.2$ in this dissertation. When $\alpha = 0$, $[F_1^*, \ldots, F_M^*]$ gives the coordinate of the so-called ideal point or utopia point found in the literature on multi-objective optimization.

Subsequently, the weights, $w_i,\ i = 1, \ldots, m$, are calculated in the following manner:

$$w_i = \hat{r}_{I_i} - F_i^* \quad \text{for } i = 1, \ldots, m. \tag{2.11}$$

After the set of weights is obtained, it is normalized so that $\left\| [w_1, \ldots, w_m]^\mathrm{T} \right\|_2 = 1$ in order to enhance the stability of numerical optimization.

Figure 2.5a illustrates these calculation procedures when $[M, m] = [2, 2]$. The target is located at the point where no objectives are attainable with the relative margin of α. The weight vector, $[w_1, w_2]^\mathrm{T}$, is determined so that it points to the farthest point from the target. When Problem $\tilde{\mathrm{P}}^{\mathbf{N}}(\mathbb{I}, w_i, F_i^*)$ is solved

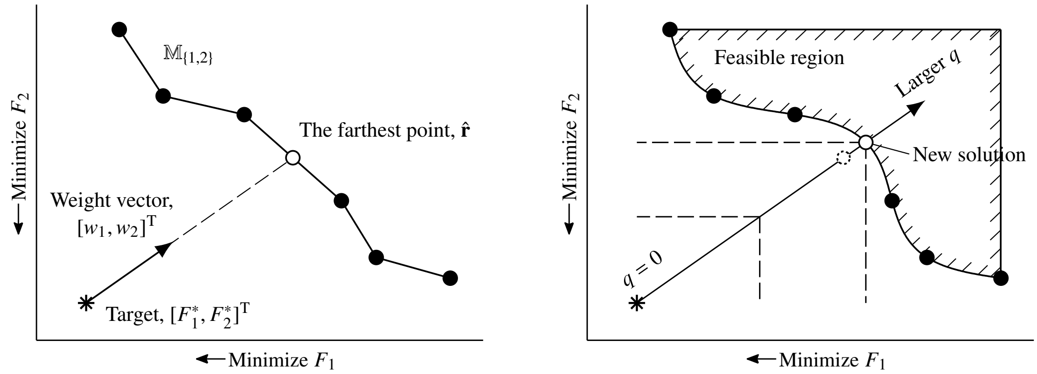

(a) Calculation of goal-programming parameters.

(b) Newly obtained solution when the calculated goal-programming parameters are used.

Fig. 2.5 Procedures for finding a solution close to the farthest point in the case of $[M, m] = [2, 2]$.

with the goal-programming parameters obtained in accordance with the procedures above, the resulting solution is located at the point on the feasible region that minimizes q as shown in Fig. 2.5b. Dashed lines in the figure depict contour lines of q. As $\mathbb{M}_{\mathbb{I}}$ becomes a better approximation to the true Pareto front, the new solution is obtained closer to the intended point (i.e., the farthest point).

2.2.6 Advantages and Limitations

Primary advantages of the proposed approach over multi-objective evolutionary algorithms are given as follows:

1) The search direction of a solution in the objective space can be explicitly specified by the goal-programming parameters, which leads to a uniform distribution of the solutions.
2) An optimization problem with the huge-dimensional decision space and a tiny feasible region can be solved efficiently.
3) It is mathematically guaranteed that all the obtained solutions have local Pareto optimality excluding tiny numerical errors (i.e., a truncation error and a round-off error).
4) The obtained Pareto front manifold and its mapping into the lower-dimensional Euclidean space can be utilized in extracting useful knowledge from the solutions. By using the proposed algorithm, a post-processing procedure for constructing the continuous representation of a Pareto front from the obtained Pareto optimal solutions, such as Ref. 73, is not required.
5) Computational complexity is proportional to the number of Pareto optimal solutions we want to find, and it is not influenced by the number of objectives.

It is also noted that the solution time of Problem $\tilde{\mathrm{P}}^{\mathbf{N}}(\mathbb{I}, w_i, F_i^*)$ can be reduced by determining initial guesses of its decision variables from the previously obtained solution that is closest to the current farthest point.

The proposed method has some limitations. First, the global optimal solution cannot be necessarily found in a multi-modal problem, since the transformed single-objective problem is solved with a gradient-based optimizer. Besides, the multi-modality of objective functions can give rise to holes in the resulting Pareto front, and it makes Assumption 2 on p. 13 violated. Secondly, functions which comprise the problem must be continuously differentiable and must be rather computationally cheap to be evaluated. The second drawback can often be circumvented by replacing undesirable functions by their smooth surrogate models such as polynomial response surfaces, radial basis function network models, and Kriging approximations[74–76].

2.3 Performance Comparison to a Multi-Objective Genetic Algorithm

In this section, a test problem for multi-objective optimal control is described first. Then, the combination of the direct shooting method and a multi-objective genetic algorithm (MOGA) is introduced as a compared method. Finally, computational performance comparisons between the proposed method and the compared method are conducted.

2.3.1 Descriptions of a Test Problem: Rocket Launch Problem

Let us consider the ascent trajectory optimization problem of a rocket launcher[77], which is a well-known nonlinear optimal control problem whose analytic solution is known. This problem is to find optimal thrust angle on the vertical plane from the static condition until the vehicle is inserted into a horizontal trajectory at a targeted altitude. The gravitational force and the decrease of vehicle mass due to fuel consumption are ignored. A schematic drawing of the problem is presented in Fig. 2.6.

The original problem found in Ref. 77 is devoted to maximizing the final velocity under the given final altitude and the predetermined duration. In this disseration, this problem is extended to a three-objective problem, and the targeted attitude and the flight duration are introduced as additional objective functions. The resulting multi-objective problem is formulated as follows:

$$\text{find}\quad [x,\, y,\, u,\, v]^{\mathrm{T}} =: \mathbf{x}(t)\colon [t_0,\, t_\mathrm{f}] \to \mathbb{R}^4, \tag{2.12}$$

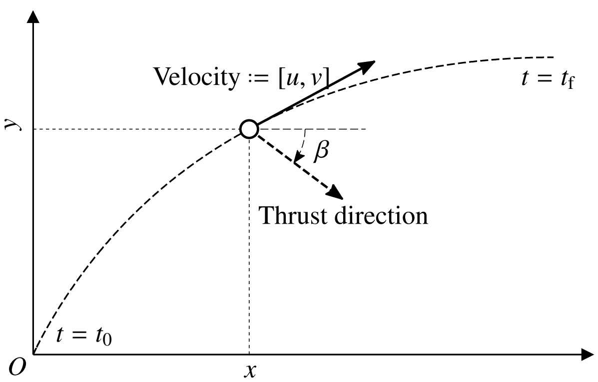

Fig. 2.6 Schematic drawing of the rocket launch problem.

$$\beta =: \mathbf{u}(t)\colon [t_0,\ t_\mathrm{f}] \to [-\pi/2,\ \pi/2], \tag{2.13}$$

$$t_0 \in \mathbb{R}, \tag{2.14}$$

$$t_\mathrm{f} \in \mathbb{R}. \tag{2.15}$$

$$\text{min.}\quad F_1 := -u(t_\mathrm{f}), \tag{2.16}$$

$$F_2 := -y(t_\mathrm{f})/10, \tag{2.17}$$

$$F_3 := 2\,t_\mathrm{f}. \tag{2.18}$$

$$\text{s.t.}\quad \frac{\mathrm{d}x}{\mathrm{d}t} = u, \tag{2.19}$$

$$\frac{\mathrm{d}y}{\mathrm{d}t} = v, \tag{2.20}$$

$$\frac{\mathrm{d}u}{\mathrm{d}t} = \cos\beta, \tag{2.21}$$

$$\frac{\mathrm{d}v}{\mathrm{d}t} = \sin\beta. \tag{2.22}$$

$$\begin{aligned} &x(t_0) = 0, \quad y(t_0) = 0, \quad u(t_0) = 0,\\ &v(t_0) = 0, \qquad t_0 = 0,\\ &v(t_\mathrm{f}) = 0, \qquad t_\mathrm{f} > 0. \end{aligned} \tag{2.23}$$

Since the Pareto front of this problem is unbounded toward the upper side of F_3 in the objective space, the following upper limit on F_3 is introduced in order to make Assumption 1 satisfied:

$$F_3 \le 100. \tag{2.24}$$

In addition, a numerical singularity at $[t_\mathrm{f}, u(t_\mathrm{f})] = (0, 0)$ is eliminated by imposing constraints on the other objective functions as follows:

$$F_1 \le -5, \tag{2.25}$$

$$F_2 \le -5. \tag{2.26}$$

The scaling of objective values in Eqs. (2.16–2.18) stretches the axes of the objective space. With these bounds on objectives, the Pareto front becomes the following two-dimensional compact manifold in the objective space, $[F_1, F_2, F_3]^\mathrm{T}$, as shown in Fig. 2.7:

$$[F_1,\ F_2,\ F_3]^\mathrm{T} = [f(p,q),\ g(p,q),\ 2q]^\mathrm{T}, \tag{2.27}$$

$$f(p,q) := -\log\left(\frac{\sec p + \tan p}{\sec p - \tan p}\right) \Bigg/ \frac{2\tan p}{q}, \tag{2.28}$$

$$g(p,q) := \frac{q^2}{40}\left[\frac{-1}{\sin p} + \log\left(\frac{\sec p + \tan p}{\sec p - \tan p}\right) \Bigg/ (2\tan^2 p)\right], \tag{2.29}$$

where p and q are scalar parameters that satisfy $q \le 50$, $f(p,q) \le -5$, and $g(p,q) \le -5$. It is noted that the Pareto front is described using these two parameters while it is embedded in the three-dimensional

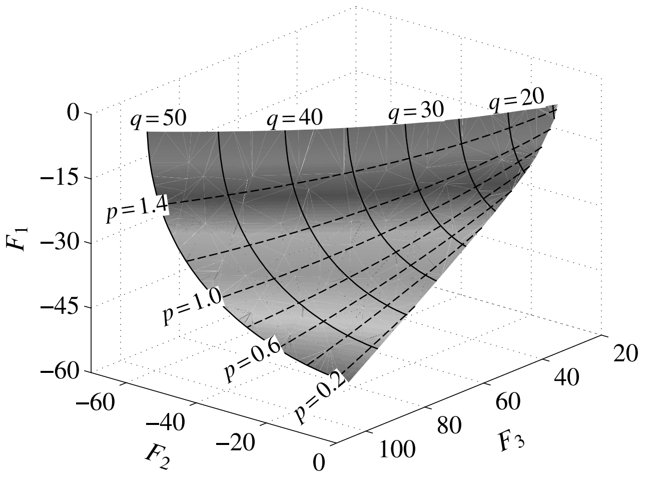

Fig. 2.7 Pareto front of the rocket launch problem.

Euclidean space. As Figure 2.7 illustrates, its shape is nonlinear and non-convex.

2.3.2 Compared Method: Direct Shooting + NSGA-II

Next, the procedure for solving a multi-objective optimal control problem using the combination of a direct shooting method[41,45] and an MOGA is explained so as to conduct the performance comparison in Section 2.3.4. In short, the original multi-objective optimal control problem is transformed into a multi-objective NLP problem by the direct shooting method, and its Pareto optimal solutions are obtained with a population-based search of the MOGA. The direct shooting method parameterizes the control variable, $\mathbf{u}(t)$, at a set of discrete times, and the time histories of the state variables, $\mathbf{x}(t)$, are calculated by solving the initial value problem of state equations explicitly. Numerical instabilities due to this explicit integration[42] make the direct shooting method less popular than direct collocation methods, when they are employed with gradient-based optimization methods. However, an NLP problem arising from the direct shooting transcription is smaller in size and has fewer equality constraints if any, which are desirable properties in applying MOGAs.

The control variable is parameterized by the values at the initial time, $t = 0$, the terminal time, $t = t_\mathrm{f}$, and the equispaced eight points between them. The continuous-time representation of the control is constructed by interpolating these parameters using natural cubic spline. The explicit simulation of state equations is performed using the classic fourth-order Runge-Kutta scheme with 300 uniformly distributed nodes. It is confirmed that absolute and relative errors in the terminal values of the state variables become less than 10^{-5} when 300 nodes is used. As a consequence of the direct shooting parameterization, the original multi-objective optimal control problem in Eqs. (2.12–2.26) is converted into an NLP problem consisting of eleven decision variables (ten parameterized βs and t_f), three objective functions, and four constraints [Eqs. (2.24–2.26) and $v(t_\mathrm{f}) = 0$].

The derived multi-objective NLP problem is solved via NSGA-II[47], a real-coded MOGA. Since NSGA-II is widely applied to practical problems, and many evolutionary algorithms have computational frameworks that are partly similar to NSGA-II[40], NSGA-II is adopted as a reference method in the present study. Genetic algorithms (GAs) are the collection of numerical optimization techniques that mimic the mechanism of natural selection. The search of an optimal solution is achieved by simulating the revolution of a larger number of populations (i.e., candidate solutions) over generations by employing genetic operators. Information of an individual population is coded on chromosome, and GAs are classified into binary-coded GAs or real-coded GAs based on whether the chromosome coding is performed with binary numbers or real numbers. While there are substantial differences among varieties of GAs, in each generation, the following genetic operations are typically applied in this order:

Crossover: New populations (offsprings) are produced via combining the chromosomes of populations survived from the previous generation.

Mutation: Parts of chromosomes of some populations are randomly altered.

Selection: Populations that survive to the next generation are selected according to certain criteria.

MOGAs are the extensions of GAs that enable the solution of multi-objective optimization problems. Primary goals of multi-objective optimization are to make solutions converged to true Pareto optimal sets, and to enhance the diversity among the solutions. In order to achieve these goals, a special sorting operation is implemented in NSGA-Ⅱ, where the populations are sorted depending on their objective function values and dissimilarities from their neighboring populations. After performing this operation called “the nondominate sort”, a population with a higher score is favored in the selection step. For more details on GAs, MOGAs, and NSGA-Ⅱ, see Refs. 39, 40, and 47, for example.

In the present study, simulated binary crossover (SBX)[39] and polynomial mutation[39] are implemented. Chromosomes of the populations in the first generation are generated within the bounds of the decision variables using a uniform pseudorandom number generator. Other parameters for NSGA-Ⅱ are presented in Table 2.1. There are several ways to handle equality/inequality constraints in NSGA-Ⅱ as shown below:

Penalty-function method:

Penalties based on the constraint residuals are appended to objective functions. In the present case, objective values are deteriorated by

$$F_i \leftarrow F_i + \rho \cdot v(t_\mathrm{f})^2, \quad i = 1, 2, 3, \tag{2.30}$$

Table 2.1 Parameter setting of NSGA-Ⅱ.

Parameter	Value
Tournament size	2
Crossover probability	0.9
Mutation probability	0.091
Population size	250, 500, 1000
Number of generations	500, 1000, 2000, 4000
Crossover distribution index, η_c	20
Mutation distribution index, η_m	20

where $\rho \in \mathbb{R}_{>}$ denotes the weight of the penalty term.

Constrained-dominance method[47]:

Magnitudes of constraint violations are considered as a criterion in the nondominate sort of populations. In the present case, a population that does not satisfy $|v(t_{\mathrm{f}})| \leq 0.01$ is determined to be infeasible. Then, the infeasible populations are always scored lower than any feasible solutions in the sorting procedure, so that the infeasible ones are unlikely to survive during the selection step.

Violation-minimization method:

Residuals of constraints are regarded as additional objective functions, and their minimization is carried out along with the original objectives. In the present case, $F_4 := |v(t_{\mathrm{f}})|$.

In this dissertation, the penalty-function method and the constrained-dominance method are adopted, and the comparisons between NSGA-II with these constraint-handling approaches and the proposed method are conducted.

The constraints other than $v(t_{\mathrm{f}}) = 0$ [i.e., Eqs. (2.24–2.26)] are automatically satisfied by repeating the generation of initial populations and offspring populations until all the produced populations meet these constraints.

2.3.3 Quantitative Metrics on the Solution Quality

There are a variety of measures for quantifying the quality of a set of solutions obtained with multi-objective optimization algorithms as well summarized in Ref. 40. Among them, a convergence measure Υ and a diversity measure Δ developed in Ref. 47 are employed with some modifications. The convergence indicates how close the solutions are to the true Pareto front, and the diversity refers to how extensively and uniformly the solutions are distributed on the Pareto front. Each metric gives a non-negative real value, and a smaller value suggests better quality in terms of the corresponding criterion.

Let us suppose that N solutions are obtained in the m-dimensional objective space. Then, Υ is defined as the averaged Euclidean distance in the objective space between the numerical solutions and a known true Pareto front, and it is calculated by

$$\Upsilon := \frac{1}{N} \sum_{i=1}^{N} d_i, \tag{2.31}$$

where d_i is the Euclidean distance between the ith solution and the true Pareto front. In the original work of Ref. 47, Υ is approximately computed by discretizing the Pareto front into a finite number of Pareto optimal solutions and regarding the distance between the ith numerical solution and the nearest Pareto optimal solution as d_i. In order to evaluate the convergence errors of highly accurate solutions obtained using the proposed method more properly, the procedure for computing d_i is improved as follows: The distance between the ith numerical solution and a local plane of the true Pareto front at a point is calculated analytically. The minimum distance between the solution and such planes is searched by varying the point via a gradient-based optimizer, and it gives d_i.

On the other hand, Δ is calculated from 1) the distance between each solution and its nearest neighbor and 2) the distance between the boundary of the true Pareto front and its nearest solution. Since the original definition of Δ in Ref. 47 is applicable only to bi-objective problems, it is modified as follows:

$$\Delta := \frac{\sum_{j \in \mathbb{J}} e_{\mathrm{b}j} + \sum_{i=1}^{N} |e_i - \bar{e}|}{\sum_{j \in \mathbb{J}} e_{\mathrm{b}j} + N\bar{e}}. \tag{2.32}$$

Here, $e_{\mathrm{b}j}$ is the minimum Euclidean distance between the jth solution and the boundary of the Pareto front. $\mathbb{J}$ is the set of indices of the solutions that satisfy the following condition: there exists some part of the Pareto front boundary that is closer to the solution than any other solutions. e_i is the distance between the ith solution and its nearest solution, and $\bar{e}$ is its mean value over $i = 1, \ldots, N$. It is noted that the penalty term in Eq. (2.30) is eliminated when Υ and Δ are evaluated.

2.3.4 Result and Discussion

All the numerical computations in this subsection are executed using a Windows 7™ laptop with an Intel™ Core® i5-3360M 2.80 GHz CPU and 8 GB RAM. Computational procedures are implemented in MATLAB® 2007b, and single-objective NLP problems are solved using SNOPT, an off-the-shelf solver based on a sequential quadratic programing (SQP) algorithm[43,78]. The optimality tolerance and the feasibility tolerance of the solver are 1×10^{-6} and 1×10^{-8}, respectively. The convergence tolerance of the adaptive mesh refinement algorithm[67] for the pseudospectral transcription of continuous-time optimal control problems is 1×10^{-6}.

When NSGA-II is used as an optimizer, all the populations in the last generation do not always satisfy the constraints sufficiently. Therefore, the final populations whose constraint residuals are more than 0.01 are regarded as invalid solutions, and they are removed. In addition, dominated solutions* are omitted as well.

Computational performances of the proposed method and NSGA-II for the rocket launch problem are shown in Table 2.2. As NSGA-II is a probabilistic algorithm, the averaged values of ten runs are presented in the table. As for the proposed method, the value of d_{tol} is varied in each case. The population size, the number of generations, and the constraint-handling method are different from one case to another when NSGA-II is used. Since MATLAB® would not be the best computational platform for executing GAs†, a performance comparison in terms of the CPU time is rather meaningless. Instead, it is noted that the proposed method provides solutions with considerably smaller Υ and Δ in compari-

---

*A solution is called "dominated" when there is another solution that is superior or equal to the considered solution in terms of all the objective values, and is superior in at least one objective.

†Of course, computational procedures of the proposed method and those of the MOGA are implemented in MATLAB® in a better way as possible (e.g., vectorization of loops and memory pre-allocation).

Table 2.2 Computational performance comparison in the rocket launch problem.

(a) The proposed method.

	d_{tol}	NS[*]	CT[†] [s]	Υ[‡]	Δ[§]
Proposed method	9.0	44	65.8	3.83×10^{-7}	0.162
	5.0	131	105.1	6.83×10^{-7}	0.197
	3.0	325	220.2	8.95×10^{-7}	0.197
	2.0	683	592.8	7.83×10^{-7}	0.197
	1.5	1046	1334.0	8.71×10^{-7}	0.191

(b) The direct shooting method with NSGA-II.

	PS[¶]	NG[‖]	NS	CT [s]	Υ	Δ
Shooting + NSGA-II with Penalty const. handling ($\rho = 100$)	250	500	95	34.5	2.72×10^{-0}	0.936
	250	1000	97	68.7	1.82×10^{-0}	0.943
	250	2000	87	136.9	1.02×10^{-0}	0.908
	250	4000	87	273.0	4.46×10^{-1}	0.910
	500	500	204	87.0	2.13×10^{-0}	0.940
	500	1000	198	173.3	1.35×10^{-0}	0.934
	500	2000	189	346.0	7.04×10^{-1}	0.913
	500	4000	189	691.2	2.67×10^{-1}	0.907
	1000	500	434	244.7	1.52×10^{-0}	0.909
	1000	1000	419	488.2	9.10×10^{-1}	0.887
	1000	2000	404	974.6	3.92×10^{-1}	0.874
	1000	4000	401	1947.4	1.71×10^{-1}	0.869

	PS	NG	NS	CT [s]	Υ	Δ
Shooting + NSGA-II with Penalty const. handling ($\rho = 1000$)	250	500	226	37.1	3.70×10^{-0}	0.986
	250	1000	228	73.8	3.08×10^{-0}	0.995
	250	2000	226	147.4	2.27×10^{-0}	1.000
	250	4000	217	294.9	1.44×10^{-0}	0.980
	500	500	465	85.4	2.78×10^{-0}	0.973
	500	1000	468	170.2	2.16×10^{-0}	0.984
	500	2000	458	340.8	1.51×10^{-0}	0.976
	500	4000	448	679.6	1.02×10^{-0}	0.964
	1000	500	933	247.5	3.02×10^{-0}	0.916
	1000	1000	930	493.7	2.25×10^{-0}	0.932
	1000	2000	928	983.9	1.44×10^{-0}	0.940
	1000	4000	923	1962.3	7.09×10^{-1}	0.925

	PS	NG	NS	CT [s]	Υ	Δ
Shooting + NSGA-II with Const.-dominance const. handling	250	500	250	26.9	4.41×10^{-0}	0.988
	250	1000	250	53.7	3.56×10^{-0}	1.003
	250	2000	250	108.1	2.75×10^{-0}	1.001
	250	4000	250	217.1	2.11×10^{-0}	0.970
	500	500	500	60.7	4.45×10^{-0}	0.961
	500	1000	500	122.5	3.48×10^{-0}	0.970
	500	2000	500	245.0	2.49×10^{-0}	0.983
	500	4000	500	493.4	1.61×10^{-0}	0.977
	1000	500	1000	142.8	3.51×10^{-0}	0.942
	1000	1000	1000	287.5	2.55×10^{-0}	0.943
	1000	2000	1000	580.2	1.71×10^{-0}	0.958
	1000	4000	1000	1165.6	9.56×10^{-1}	0.946

Values in Table (b) are averages of ten runs.

[*] Number of nondominated the solutions obtained.

[†] Total computation time.

[‡] Convergence measure of obtained solutions.

[§] Diversity measure of obtained solutions.

[¶] Population size in NSGA-II.

[‖] Number of generations in NSGA-II.

son with the combination of the direct shooting method and NSGA-II. When NSGA-II is used with the penalty-function constraint handling ($\rho = 100$), the number of valid solutions finally obtained is less than half of the population size. Furthermore, the number of the valid solutions decreases as the number of generations is increased. This is attributed to the fact that the improvements in the objective values in Eq. (2.30) can result in the violation of the constraint of $v(t_\mathrm{f}) = 0$. This tradeoff issue between the convergence and the constraint satisfaction is alleviated by increasing the value of ρ. In this case, however, the quality of the obtained solutions is deteriorated from the viewpoints of both Υ and Δ as shown in the table.

Since NSGA-II, or more generally most EAs, is a population-based search strategy, a quit large number of populations are required for finding solutions with sufficient quality. In contrast, the proposed method is based on a successive search, and there is no relation between the number of obtained solutions and their quality. Therefore, the proposed method can provide as many solutions as needed, which is an advantageous property in practical usages.

Distributions of the obtained nondominated solutions in the objective space are shown in Fig. 2.8. By using the proposed method, the distribution density of solutions can be explicitly adjusted via changing d_tol, and a set of solutions with a good spread is found independently of its value (see Figs. 2.8a, 2.8b). On the other hand, sets of the solutions obtained by NSGA-II are less uniformly distributed, and there is some anisotropy in the solution distribution. A reason for this anisotropy can be revealed by inspecting Fig. 2.11. This figure shows an overlay of the solutions obtained using NSGA-II and the true Pareto front. It is noted that the anisotropy of the solution distribution follows the contour lines of a parameter p on the Pareto front. NSGA-II explores solutions through genetic operations (i.e., crossover and mutation) based on pseudorandom numbers. Let us consider a population that satisfies the terminal constraint $v(t_\mathrm{f}) = 0$ sufficiently, and an element of its chromosome that corresponds to the decision variable t_f is altered via the genetic operations. It directly results in the change of q, and the satisfaction of the terminal constraint is maintained. On the other hand, multiple variables must be varied in a coordinated manner for achieving a search in the p direction while meeting the terminal constraint. Summarizing the above, there is some difference in the ease of solution searches between along the p-contour and along the q-contour, and it leads to the anisotropy of the obtained solution distribution. Note that a set of solutions obtained using NSGA-II with the constrained-dominance constraint handling (Fig. 2.8f) is inferior to solution sets obtained by NSGA-II with the penalty-function constraint handling (Figs. 2.8c–2.8e) in terms of the uniformness of the solution distribution. This is because, the constrained-dominance method gives, so to speak, death penalties to populations whose constraint violations exceed the threshold, and it makes the search in the p direction more difficult. A larger penalty weight, ρ, in the penalty-function method brings about a similar effect, and it degrades the diversity of the solutions (compare Fig. 2.8d and Fig. 2.8e).

The weaknesses of MOGAs in handling optimization problems with parameter interactions are stated in the literature[47,50,51]. Numerical experiments in this dissertation revealed that this kind of difficulties can arise in a multi-objective optimal control problem with multi-point boundary conditions as well. Although the following modifications of crossover operations are investigated in some researches so as to overcome this drawback, they are still underway[51]: 1) a crossover operation is modified so that it

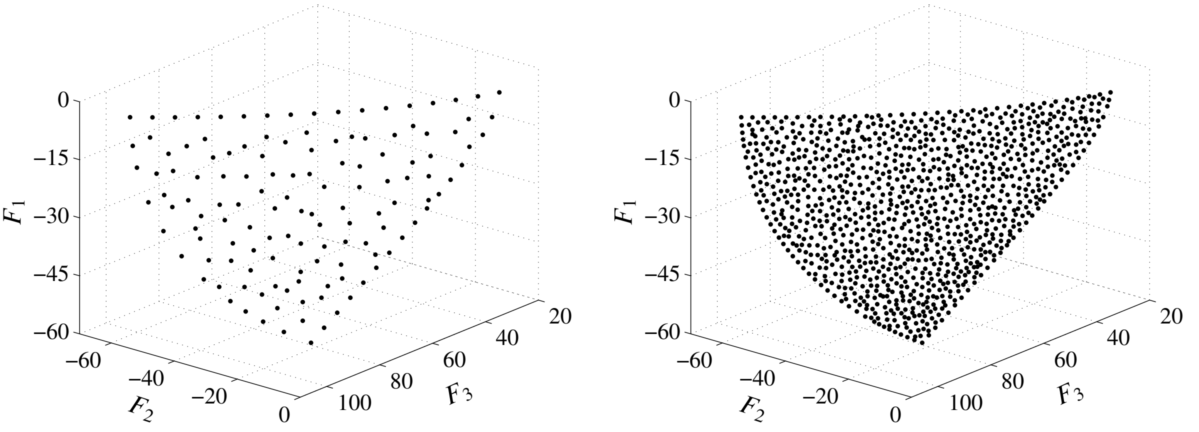

(a) The proposed method with $d_{\text{tol}} = 5$: 131 nondominated solutions, $\Delta = 0.197$.

(b) The proposed method with $d_{\text{tol}} = 1.5$: 1046 nondominated solutions, $\Delta = 0.191$.

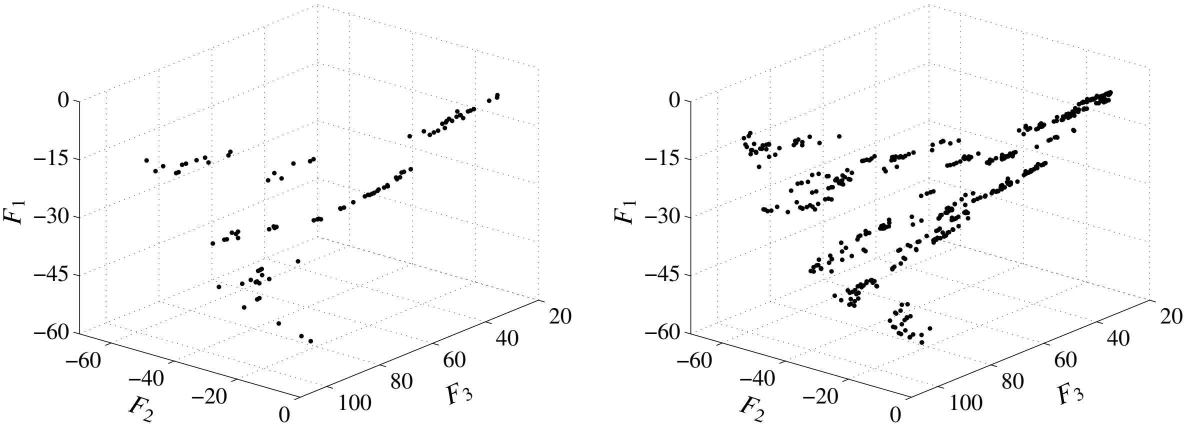

(c) NSGA-II with penalty-function constraint handling ($\rho = 100$), population size 250, and generations 4000: 93 nondominated solutions, $\Delta = 0.935$.

(d) NSGA-II with penalty-function constraint handling ($\rho = 100$), population size 1000, and generations 4000: 436 nondominated solutions, $\Delta = 0.875$.

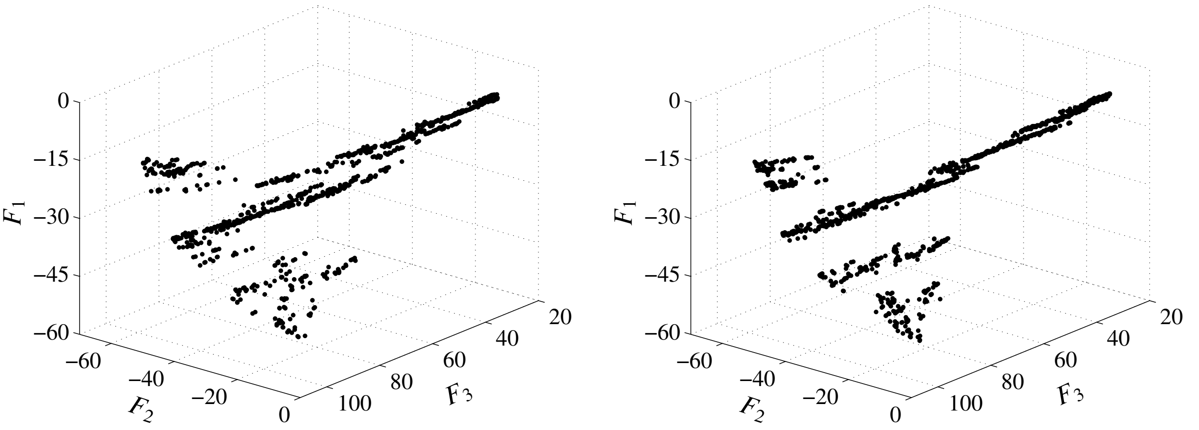

(e) NSGA-II with penalty-function constraint handling ($\rho = 1000$), population size 1000, and generations 4000: 912 nondominated solutions, $\Delta = 0.916$.

(f) NSGA-II with constrained-dominance constraint handling, population size 1000, and generations 4000: 1000 nondominated solutions, $\Delta = 0.948$.

Fig. 2.8 Distribution of nondominated solutions in the objective space.

is applied to multiple decision variables simultaneously instead of to each variable independently; 2) a crossover operator is replaced with a differential evolution algorithm. Many major issues still remain unsolved for the successful application of MOGAs to the numerical solution of multi-objective optimal control problems.

The solution process of the proposed method when $d_{\mathrm{tol}} = 1.5$ is illustrated in Fig. 2.9. Figure 2.9a presents the convergence of $d_{\max}$ defined in Eq. (2.6) as the number of obtained solutions increases. By definition, $d_{\max}$ is responsible for determining the employed dimensionality reduction technique in Section 2.2.3, and for deciding the termination of the overall algorithm in Section 2.2.2. According to the figure, $d_{\max}$ almost monotonically decreases as expected. Figures 2.9b–2.9d show the tentative solutions at representative steps. Along with the solutions in the objective space, their mapping in the lower-dimensional Euclidean space with a Voronoi diagram is presented. It is noted that 105 solutions

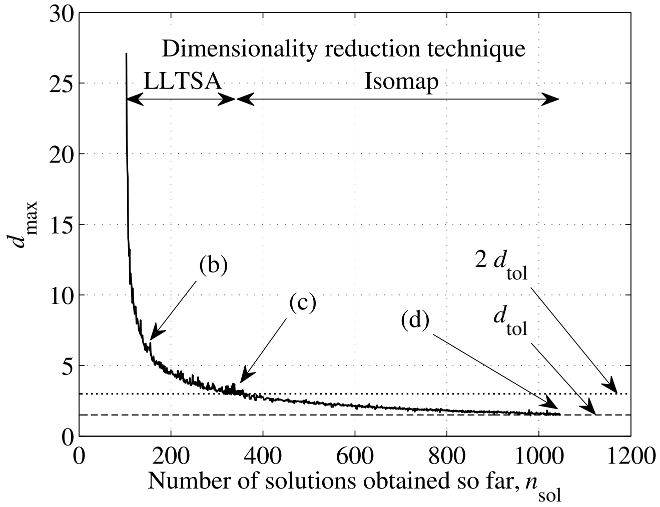

(a) Convergence of $d_{\max}$.

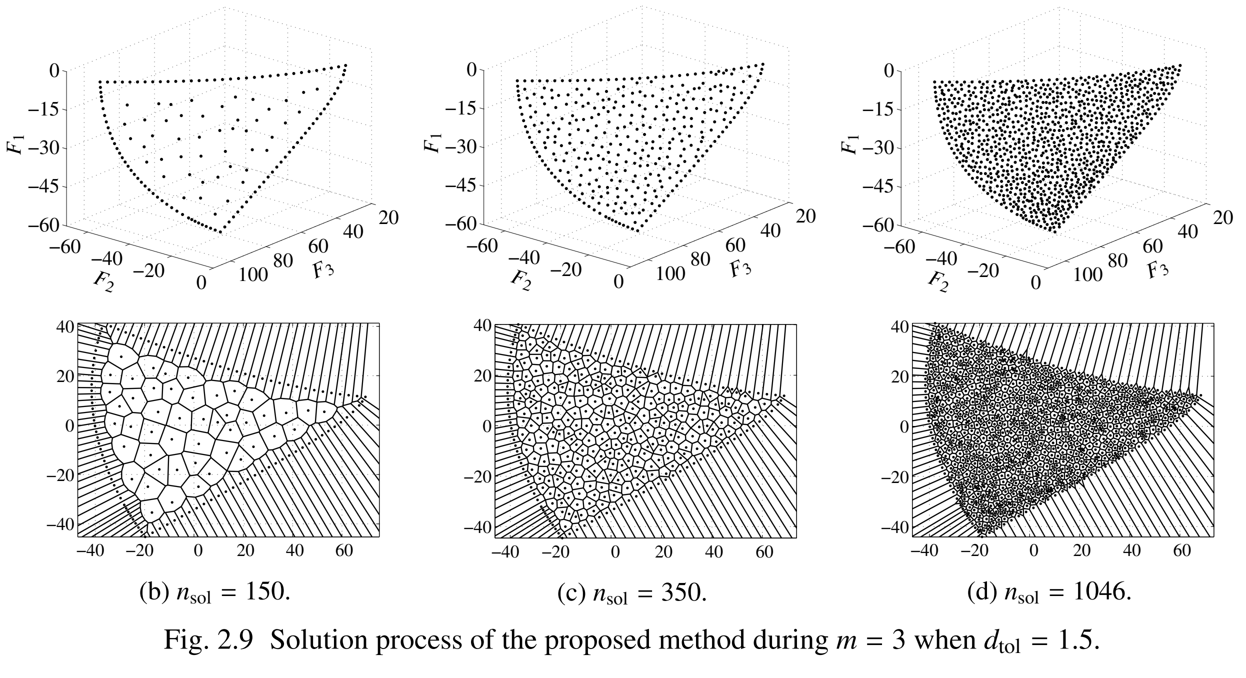

(b) $n_{\mathrm{sol}} = 150$. (c) $n_{\mathrm{sol}} = 350$. (d) $n_{\mathrm{sol}} = 1046$.

Fig. 2.9 Solution process of the proposed method during $m = 3$ when $d_{\mathrm{tol}} = 1.5$.

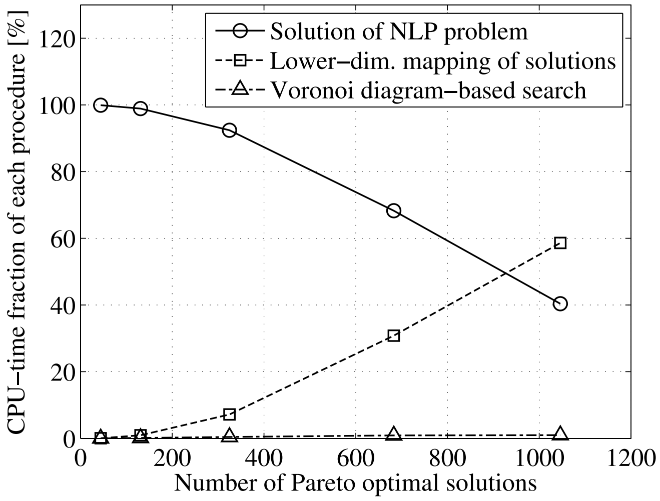

Fig. 2.10 CPU times of procedures in the proposed method in the rocket launch problem.

are already obtained on the boundary of the Pareto front when the step of $m = 3$ begins. As a new solution is properly added in the interior surface of the Pareto front, $d_{\max}$ gets smaller. Slight oscillation of $d_{\max}$ in Fig. 2.9a is owing to that the addition of a new solution can cause the topological change of the Voronoi diagram. This results in the transformation of the structure of $\mathbb{M}_{\{1,2,3\}}$ (see Fig. 2.3c), and hence affects the value of $d_{\max}$.

Computational time of the proposed method is divided into the times needed in the following three procedures, and they are plotted in Fig. 2.10 as the functions of the number of obtained solutions:

1) Solution of NLP problems (Line 3 or 13 in Algorithm 1)

2) Lower-dimensional mapping of solutions (Line 10 in Algorithm 1)

3) Voronoi diagram-based search for the farthest point (Line 11 in Algorithm 1)

As the number of solutions is increased, or equivalently smaller d_{tol} is adopted, computational time accompanied with the lower-dimensional mapping occupies larger fraction in the whole procedures. When the number of solutions is more than one thousand, it accounts for more than half of the total solution time. In practical purposes, however, it is highly probable that such an excessive number of solutions is not required. In addition, it typically takes much more time to solve practical NLP problems in comparison with the present simple test problem. Therefore, the additional computational burden associated with the adaptive determination of goal-programming parameters is relatively low.

Figure 2.12 presents normalized time histories of the control variable β in all the obtained nondominated solutions. The normalized time is obtained by linearly transformating $t \in [t_0(= 0), t_{\mathrm{f}}]$ of each solution into $\tau \in [-1, 1]$. Using τ, the analytic solution of the rocket launch problem is written as[77]

$$\beta(\tau) = \tan^{-1}(-\tau \tan p), \tag{2.33}$$

where p is a parameter of the Pareto front that appeared in Eqs. (2.27–2.29). Figure 2.12 reveals that $\beta(\tau)$

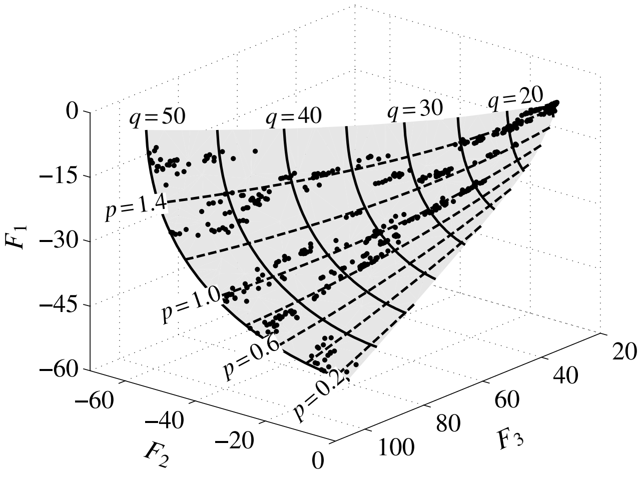

Fig. 2.11 Overlay of numerical solutions via NSGA-Ⅱ and the true Pareto front.

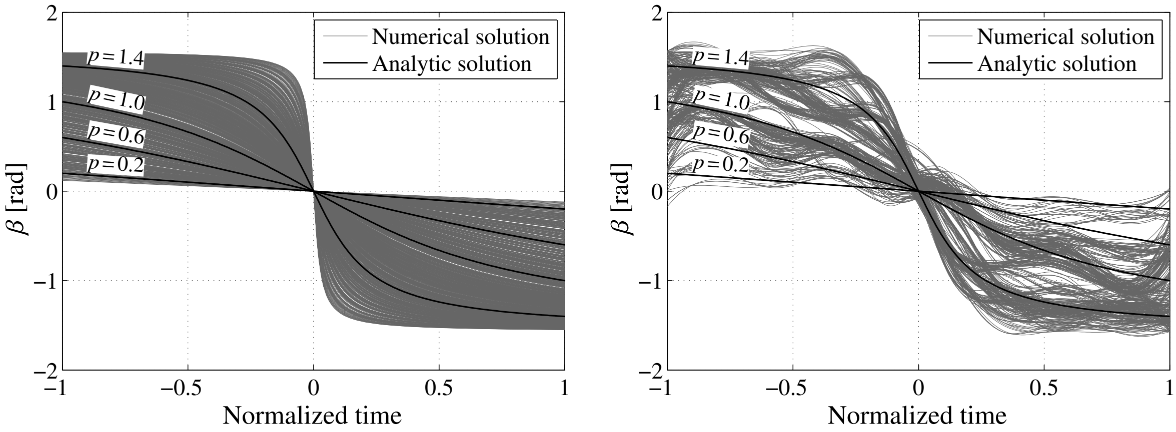

(a) The proposed method with $d_{\text{tol}} = 1.5$: $\Upsilon = 8.71 \times 10^{-7}$.

(b) NSGA-Ⅱ with penalty-function constraint handling ($\rho = 100$), population size 1000, and generations 4000: $\Upsilon = 1.55 \times 10^{-1}$.

Fig. 2.12 Normalized time versus the control variable β (overlay of all the nondominated solutions).

of the nondominated solutions via the proposed method have properly converged to the corresponding exact solutions independently of the value of p. On the other hand, the time histories of the control variable via NSGA-Ⅱ have not adequately converged. This is a reason why numerical solutions obtained using the proposed method have much smaller Υ in Table 2.2 compared with NSGA-Ⅱ.

In the present test problem, optimal time histories of the control variable exhibit rather simple behaviors as described in Eq. (2.33). Therefore, the control variable can be represented using a small number of parameters (ten parameters). When more parameters are required for the sufficient control approximation, the resulting optimization problem has an increased number of decision variables, and it rapidly becomes more difficult to obtain satisfactory solutions using MOGAs[51]. When the proposed technique is employed, a set of solutions with high local optimality and diversity can be found even in such a challenging case.

2.4 Application Example

2.4.1 Multi-Objective Optimization of Space Shuttle Reentry Trajectory

In this section, a multi-objective optimal control problem concerning the reentry of the U. S. Space Shuttle is solved using the proposed technique in order to demonstrate its applicability to a practical problem. Suppose that we wish to design the flight trajectory from the beginning of the reentry to the terminal area energy management (TAEM) interface that 1) maximizes the down-range, 2) maximizes the cross-range, and 3) minimizes the maximum aerodynamic heat flux as illustrated in Fig. 2.13. The motivation of this design problem is to obtain a trajectory in the return flight with a higher range capability and a less thermal load. By increasing the range capability, the flexibility in the selection of the de-orbit conditions is improved, and the diversion capability in the case of emergency is enhanced. It is noted that unpowered flight of a lifting-body orbiter similar to the Space Shuttle orbiter is considered to be a promising methodology for returning to the ground safely in next-generation space transportation systems[3]. On the basis of the variable definitions provided in Table 2.3, the problem is formulated as follows:

find

$$\mathbf{x}(t) := [h,\ \phi,\ \theta,\ v, \gamma,\ \psi]^{\mathrm{T}} : [0,\ t_{\mathrm{f}}] \to \mathbb{R}^6, \tag{2.34}$$

$$\mathbf{u}(t) := [\alpha,\ \sigma]^{\mathrm{T}} : [0,\ t_{\mathrm{f}}] \to \mathbb{R}^2, \tag{2.35}$$

$$t_{\mathrm{f}} \in \mathbb{R}, \tag{2.36}$$

$$\mathbf{p} := Q_{\mathrm{u}} \in \mathbb{R} \tag{2.37}$$

that minimize

$$F_1 := -\phi(t_{\mathrm{f}}), \tag{2.38}$$

$$F_2 := -\theta(t_{\mathrm{f}}), \tag{2.39}$$

$$F_3 := Q_{\mathrm{u}}/1.1356 \tag{2.40}$$

subject to equations of motion of the vehicle,

$$\frac{\mathrm{d}h}{\mathrm{d}t} = v \sin\gamma, \tag{2.41}$$

$$\frac{\mathrm{d}\phi}{\mathrm{d}t} = \frac{v}{r}\cos\gamma\ \sin\psi/\cos\theta, \tag{2.42}$$

$$\frac{\mathrm{d}\theta}{\mathrm{d}t} = \frac{v}{r}\cos\gamma\ \cos\psi, \tag{2.43}$$

$$\frac{\mathrm{d}v}{\mathrm{d}t} = -\frac{D}{m} - \frac{\mu}{r^2}\sin\gamma, \tag{2.44}$$

$$\frac{\mathrm{d}\gamma}{\mathrm{d}t} = \frac{L}{mv}\cos\sigma + \left(\frac{v}{r} - \frac{\mu}{vr^2}\right)\cos\gamma, \tag{2.45}$$

$$\frac{\mathrm{d}\psi}{\mathrm{d}t} = \frac{L}{mv}\sin\sigma/\cos\gamma + \frac{v}{r}\cos\gamma\ \sin\psi\ \tan\theta, \tag{2.46}$$

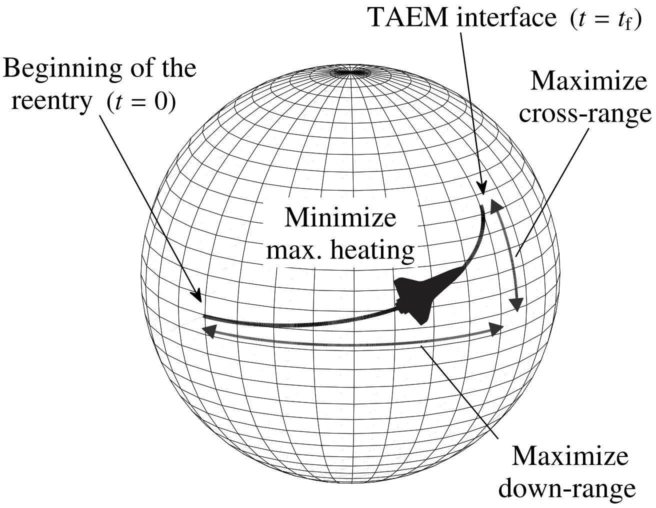

Fig. 2.13 Schematic description of the Space Shuttle reentry problem.

Table 2.3 Variable definitions in the Space Shuttle reentry problem.

Symbol	Description
t	Elapsed time from the beginning of the reentry [s]
h	Altitude [m]
ϕ	Longitude [rad]
θ	Latitude [rad]
v	Velocity [m/s]
γ	Flight path angle [rad]
ψ	Azimuth angle [rad]
α	Angle of attack [rad]
σ	Bank angle [rad]
r	Elevation from the center of the Earth [m]
L	Lift force [N]
D	Drag force [N]
C_L	Lift coefficient
C_D	Drag coefficient
ρ	Atmospheric density [kg/m^3]
Q	Aerodynamic heat flux on the wing leading edge [MW/m^2]
Q_{u}	Maximum value of Q during the reentry [MW/m^2]
m	Constant vehicle mass (= 92,080 kg)
μ	Standard gravitational parameter of the Earth (= 3.986×10^{14} m^3/s^2)
R_{e}	Radius of the Earth (= 6.378×10^6 m)
S	Aerodynamic reference area of the vehicle (= 249.9 m^2)

a limit on the aerodynamic heat flux,

$$Q \leq Q_{\mathrm{u}}, \tag{2.47}$$

and boundary conditions,

$$\begin{aligned} h(0) &= 79.25\ \mathrm{km}, & \phi(0) &= 0\ \mathrm{deg}, \\ \theta(0) &= 0\ \mathrm{deg}, & v(0) &= 7.803\ \mathrm{km/s}, \\ \gamma(0) &= -1\ \mathrm{deg}, & \psi(0) &= 90\ \mathrm{deg}, \\ t_{\mathrm{f}} &> 0\ \mathrm{s}, & h(t_{\mathrm{f}}) &= 24.38\ \mathrm{km}, \\ \phi(t_{\mathrm{f}}) &\geq 135\ \mathrm{deg}, & v(t_{\mathrm{f}}) &= 0.7620\ \mathrm{km/s}, \\ \gamma(t_{\mathrm{f}}) &= -5\ \mathrm{deg}. \end{aligned} \tag{2.48}$$

This formulation is a multi-objective extension of a well-known classical optimal control problem[42], where only the maximization of the cross-range is considered subject to the predetermined upper bound on the heat flux. Down-range maximization and cross-range maximization are equivalently defined as the maximization of the final longitude and that of the final latitude, respectively. Additionally, an upper bound on Q_{u} is imposed in the following manner in order to assume a realistic value of Q_{u}.

$$Q_{\mathrm{u}} \leq 1.1356\ \mathrm{MW/m^2}\ (= 100\ \mathrm{Btu/ft^2 \cdot s}). \tag{2.49}$$

It is noted that $Q_{\mathrm{u}} = \max_{t \in [0,\, t_{\mathrm{f}}]} Q(t)$ because of Eq. (2.47). L and D are defined as the functions of α,

$$L = \frac{1}{2}\rho v^2 C_{\mathrm{L}} S = \frac{1}{2}\rho v^2 \left(a_0 + a_1 \hat{\alpha}\right) S, \tag{2.50}$$

$$D = \frac{1}{2}\rho v^2 C_{\mathrm{D}} S = \frac{1}{2}\rho v^2 \left(b_0 + b_1 \hat{\alpha} + b_2 \hat{\alpha}^2\right) S, \tag{2.51}$$

$$\hat{\alpha} = \frac{180}{\pi}\alpha, \tag{2.52}$$

and Q is empirically expressed by α, v, and ρ as follows:

$$Q = \frac{1}{2} Q_a Q_r, \tag{2.53}$$

$$Q_a = c_0 + c_1 \hat{\alpha} + c_2 \hat{\alpha}^2 + c_3 \hat{\alpha}^3 \tag{2.54}$$

$$Q_r = 17700 \sqrt{\rho} \left(\frac{v}{10000}\right)^{3.07} \tag{2.55}$$

Atmospheric density is modeled by the following exponential function:

$$\rho = \rho_0 \exp(-h/h_{\mathrm{r}}). \tag{2.56}$$

Elevation from the center of the Earth, r, is given by

$$r = h + R_{\mathrm{e}}. \tag{2.57}$$

Parameter values in the above numerical model are as follows:

$$\begin{aligned}
&a_0 = -0.20704, && a_1 = 0.029244, && b_0 = 0.07854 \\
&b_1 = -0.61592 \times 10^{-2}, && b_2 = 0.621408 \times 10^{-3}, && c_0 = 1.0672181 \\
&c_1 = -0.19213774 \times 10^{-1}, && c_2 = 0.21286289 \times 10^{-3}, && c_3 = -0.10117249 \times 10^{-5} \\
&\rho_0 = 1.226\ \mathrm{kg/m^3}, && h_{\mathrm{r}} = 7254\ \mathrm{m}.
\end{aligned} \tag{2.58}$$

This problem is a two-point boundary value problem where altitude, velocity, and flight path angle are specified at the beginning and at the end of the trajectory.

The computational performance of the proposed method for various values of d_{tol} is summarized in Table 2.4. The employed computational environment is almost same as that in Section 2.3.4. The only exception is that the accuracy tolerance in the adaptive mesh refinement process [67] for the pseudospectral transcription of optimal control problems is relaxed to 5×10^{-4}, which is adequate for engineering purposes. The number of solutions and computation time required to satisfy the termination condition, Eq. (2.6), increase in a quadratic way with respect to the inverse of d_{tol}. The NLP problems arising from the transcription of the optimal control problems have huge numbers of variables and constraints when they become good approximations to the original continuous-time problems.

Figure 2.14 shows the obtained solutions for $d_{\mathrm{tol}} = 0.05$ in the objective space. F_1 and F_2 are expressed in terms of distances instead of angles for the ease of comprehension. The result indicates that these three objectives are conflicting with each other. Note also that all the obtained solutions are nondominated, and they successfully spread uniformly on their underlying manifold. Figure 2.15 presents time histories of trajectories in the representative Pareto optimal solutions indicated in Fig. 2.14. There is high diversity in the obtained Pareto optimal trajectories.

Table 2.4 Computational performance of the proposed method in the Space Shuttle reentry problem.

d_{tol}	Number of solutions	CPU time [s]	Number of decision variables*	Number of equality constraints*	Number of inequality constraints*
0.15	41	371	1845	1412	214.4
0.125	51	476	1799	1376	208.8
0.1	73	705	1734	1326	201.5
0.075	110	993	1751	1338	204.1
0.05	232	1990	1668	1275	194.2
0.025	873	8250	1600	1222	186.6

* Averages in the obtained solutions.

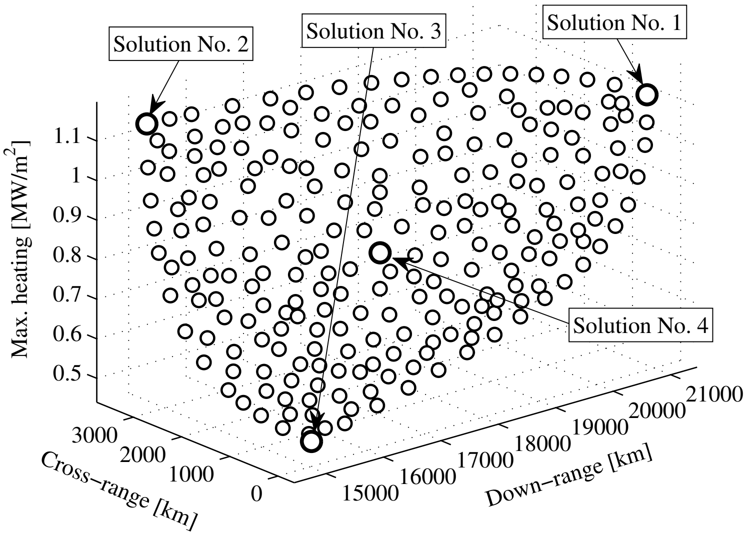

Fig. 2.14 Obtained Pareto optimal solutions in the objective space when $d_{\mathrm{tol}} = 0.05$ for the Space Shuttle reentry problem.

2.4.2 Data Mining from Pareto Optimal Trajectories

In this subsection, some useful and generic knowledge is extracted from the Pareto optimal trajectories by applying proper orthogonal decomposition (POD). Let us analyze control histories (i.e., angle of attack and bank angle) of the obtained 232optimal trajectories when $d_{\mathrm{tol}} = 0.05$. Detailed procedures for performing POD are explained in Appendix F.2. Using POD, a control history of the ith solution, denoted by x_i, is decomposed into that of a representative solution, x_0, and the deviation from it as follows:

$$x_i(\tau) = x_0(\tau) + \sum_{j=1}^{232} a_i^{(j)} \cdot \tilde{x}^{(j)}(\tau), \quad i = 1, \ldots, 232, \tag{2.59}$$

where the deviation is expressed by the linear combination of 232 modes. τ denotes the time that is normalized from $t \in [0,\, t_{\mathrm{f}}]$ to $\tau \in [-1, 1]$. Solution No. 4 is selected as the representative solution. Let us refer to $a_i^{(j)}$ as the coefficient of the jth mode, and $\tilde{x}^{(j)}$ as the basis of the jth mode.

Figure 2.16 shows the result of the POD of angle of attack histories. Mode 1 and mode 2 occupy 90.5% and 6.85% of the whole energy, respectively. As these modes account for almost all the deviation in terms of the energy content, the variety of Pareto optimal trajectories can be extracted through inspecting these dominant modes only. Figure 2.16 suggests the following knowledge:

- In all the optimal solutions, the angle of attack stays on the same value in the last quarter of the trajectory. This angle is equivalent to the angle that maximizes the range, it is maintained after the heating constraint, Eq. (2.47), becomes inactive.
- Angle of attack histories are governed by the value of F_3 (i.e., the maximum heat flux). This is attributed to the fact that α has considerable and direct influence on the value of Q as shown in Eqs. (2.53–2.55). Mode 1 describes that the optimal angle of attack becomes smaller in the

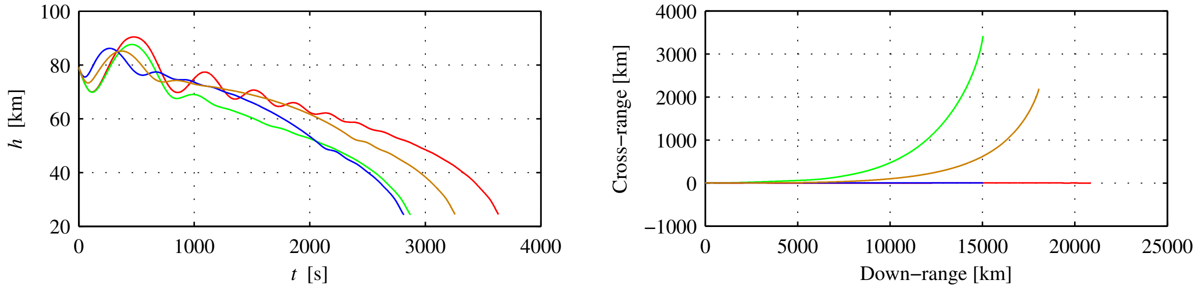

(a) Time histories of altitude. (b) Ground track.

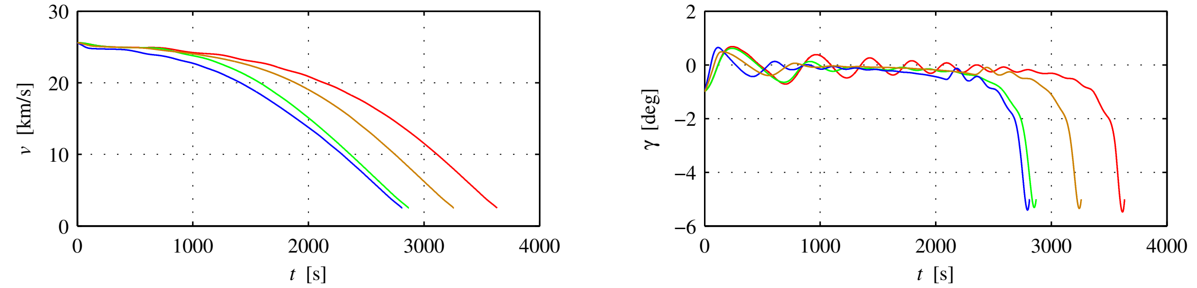

(c) Time histories of velocity. (d) Time history of flight path angle.

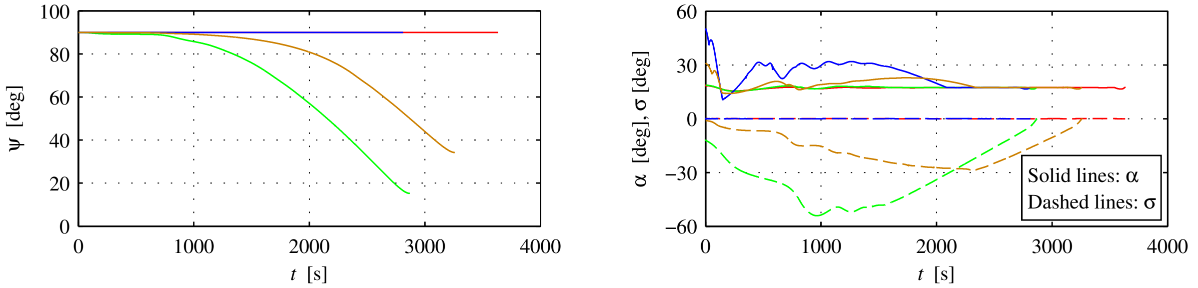

(e) Time histories of azimuth angle. (f) Time history of control variables.

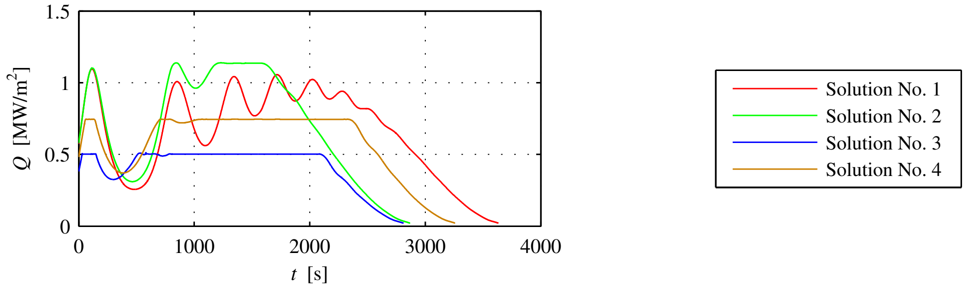

(g) Time histories of aerodynamic heat flux.

Fig. 2.15 Representative optimal solutions for the Space Shuttle reentry problem.

beginning and the middle of the trajectory when F_3 gets larger. The opposite is also true. Mode 2 indicates that there are secondary fluctuations which behave in the same manner between when F_3 is small and when F_3 is sufficiently large.

The result of POD for bank angle histories is presented in Fig. 2.17. In this case, mode 1 and mode 2 occupy 89.8% and 9.12% of the whole energy, respectively. From this figure, the following information is obtained:

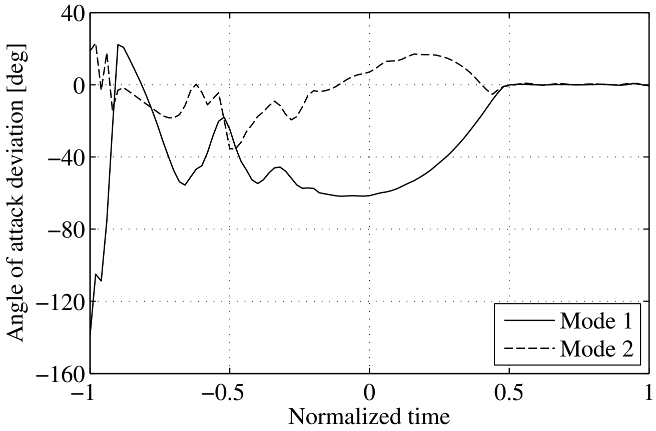

(a) The basis of two dominant modes.

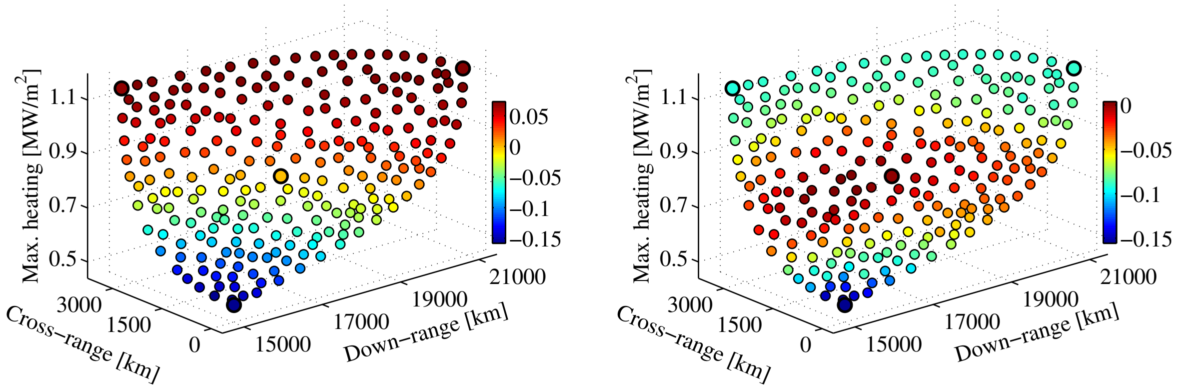

(b) Coefficients of mode 1.

(c) Coefficients of mode 2.

Fig. 2.16 Proper orthogonal decomposition of angle of attack histories.

- Mode 1 explains that the optimal bank angle becomes larger in negative when the relative significance of the maximization of cross-range gets greater, and vice versa. This deviation is large only in the middle of the flight duration, and the angles near the initial and terminal times are almost the same among all the solutions.
- Mode 2 illustrates fluctuations whose coefficients depend on the preference between down-range maximization and cross-range maximization. These fluctuations of optimal bank angles have the opposite sign between in the former half of the flight and in the latter half of the flight.

2.5 Conclusion of this Chapter

In this chapter, a novel numerical approach for efficiently solving multi-objective optimal control problems is presented. In the proposed algorithm, a Pareto optimal solution is successively searched by solving a single-objective NLP problems derived from the original problem via min-max goal programming and a direct collocation method. The farthest point from the existing solutions on the Pareto front in terms of a geodesic distance is determined, and goal-programming parameters are determined so that

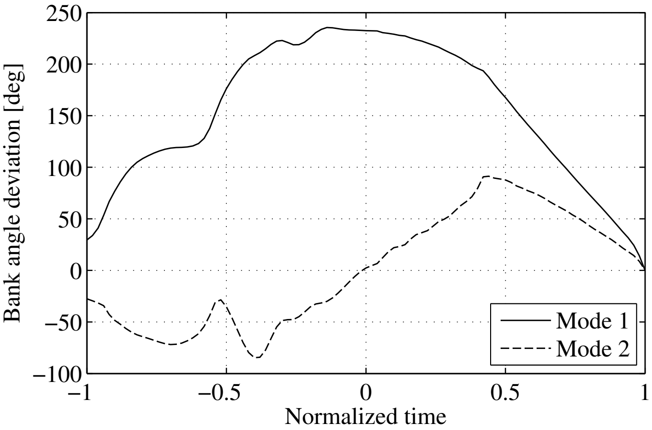

(a) The basis of two dominant modes.

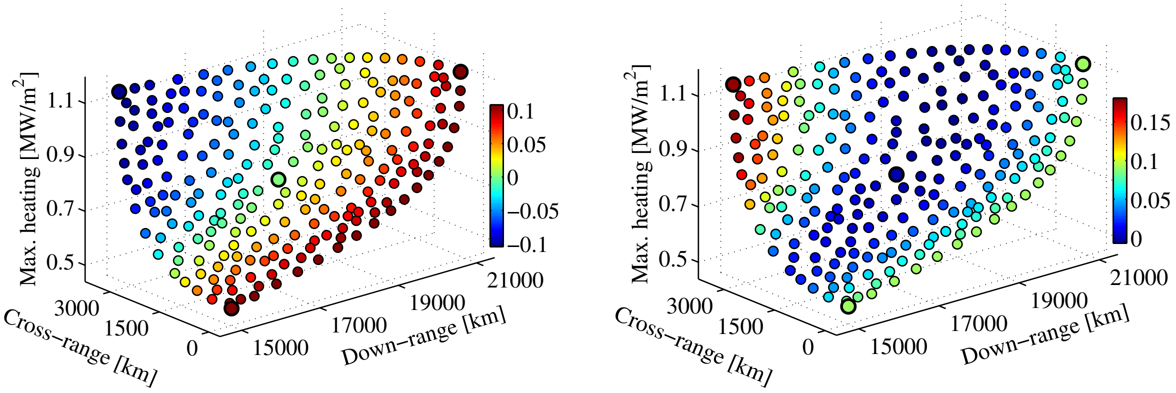

(b) Coefficients of mode 1.

(c) Coefficients of mode 2.

Fig. 2.17 Proper orthogonal decomposition of bank angle histories.

the resulting solution will be located near the farthest point. These successive procedures finally provide a set of solutions with a good convergence and a uniform distribution, which is a desired property for multi-objective optimization algorithms. A numerical experiment using a test problem with multi-point boundary conditions demonstrated that the proposed technique is superior to the combination of an MOGA and a direct shooting method from the viewpoints of optimality, constraint residual, and diversity of the obtained solutions. Additionally, a multi-objective reentry trajectory optimization problem of the Space Shuttle was solved as an application example with practical interests. The proposed technique is particularly advantageous when a moderate number of accurate solutions are desired.

Chapter 3

Transient Heat-Constrained Optimal Control for TPS Design

In this chapter, a novel transient heat-constrained optimal control method for analyzing and designing passive TPS of RLVs is developed. The formulation of an example problem for heat-constrained optimal control is given in Section 3.1. In Section 3.2, previous techniques and the proposed method are explained based on the test problem. The efficiency of the proposed method is demonstrated through conducting numerical experiments in Section 3.3. Finally, Section 3.4 provides concluding remarks of this chapter.

3.1 Formulation of Transient Heat-Constrained Optimal Control

For the sake of simplicity, numerical methods for optimal control of a vehicle with transient heat constraints are explained based on a specific but illustrative example problem. In this dissertation, "the transient heat constraint" means a constraint relating an unsteady thermal state of a vehicle that depends on its flight trajectory not only at present but also in the past. Consider the following test problem formulated as a PDE-ODE coupled optimal control problem whose schematics are shown in Fig. 3.1:

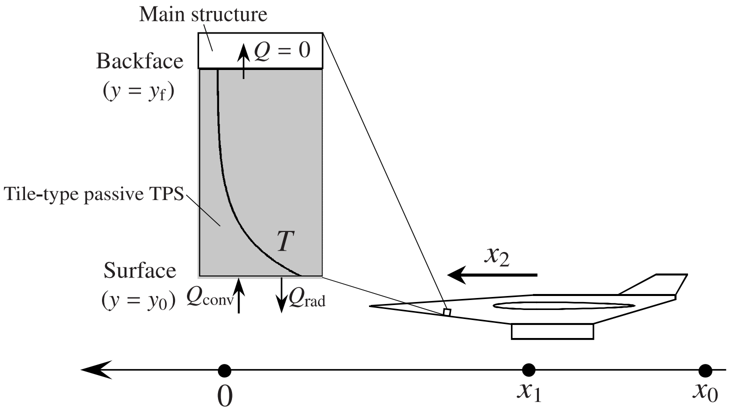

Fig. 3.1 Schematic description of an example problem of transient heat-constrained optimal control.

find

$$x_1(t)\colon [0,\ t_\mathrm{f}] \to \mathbb{R}, \tag{3.1}$$
$$x_2(t)\colon [0,\ t_\mathrm{f}] \to \mathbb{R}, \tag{3.2}$$
$$u(t)\colon [0,\ t_\mathrm{f}] \to \mathbb{R}, \tag{3.3}$$
$$T(y,t)\colon [y_0, y_\mathrm{f}] \times [0,\ t_\mathrm{f}] \to \mathbb{R}, \tag{3.4}$$
$$t_\mathrm{f} \in \mathbb{R} \tag{3.5}$$

with simple bounds

$$x_2(t) \geq 0, \tag{3.6}$$
$$-u_\mathrm{max} \leq u(t) \leq u_\mathrm{max}, \tag{3.7}$$
$$t_\mathrm{f} \geq 0 \tag{3.8}$$

that minimize cost functional

$$J := t_\mathrm{f} + \frac{1}{2}\int_0^{t_\mathrm{f}} \left(\frac{u}{u_\mathrm{max}}\right)^2 \mathrm{d}t \tag{3.9}$$

subject to dynamic constraints based on ODEs,

$$\frac{\mathrm{d}x_1}{\mathrm{d}t} = x_2, \tag{3.10}$$
$$\frac{\mathrm{d}x_2}{\mathrm{d}t} = u, \tag{3.11}$$

a path constraint concerning the temperature limit at the backface of the TPS insulation tile,

$$T(y_\mathrm{f}, t) \leq T_\mathrm{max}, \tag{3.12}$$

and initial and terminal conditions,

$$\begin{aligned} x_1(0) &= x_0, & & x_2(0) = 0, \\ T(y,0) &= T_0, \quad \text{for} \quad y \in [y_0,\ y_\mathrm{f}], & & \\ x_1(t_\mathrm{f}) &= 0, & & x_2(t_\mathrm{f}) = 0. \end{aligned} \tag{3.13}$$

Here, x_1, x_2, and u denote the position, the velocity, and the acceleration of the vehicle, respectively. y is the coordinate inside the tile in the depth direction. $T(y,t)$ indicates the temperature of the tile at position y and time t.

Additionally, the one-dimensional transient heat transfer inside the tile in the depth direction is governed by the following PDE:

$$\frac{\partial T}{\partial t} = \frac{K}{\rho\, C_p} \frac{\partial^2 T}{\partial y^2}, \tag{3.14}$$

with boundary conditions

$$\left.\frac{\partial T}{\partial y}\right|_{y=y_0} = \frac{Q_0}{K} = \frac{1}{K}\left(Q_{\mathrm{rad}} - Q_{\mathrm{conv}}\right), \tag{3.15}$$

$$\left.\frac{\partial T}{\partial y}\right|_{y=y_{\mathrm{f}}} = \frac{Q_{\mathrm{f}}}{K} = 0, \tag{3.16}$$

where K, ρ, and C_p are the thermal conductivity, density, and isobaric heat capacity of the tile. Eq. (3.15) accounts for surface heat flux, Q_0, that consists of a thermal radiation term,

$$Q_{\mathrm{rad}} = \epsilon\, \sigma \left[T(0,t)^4 - {T_0}^4\right] \tag{3.17}$$

and a convective heating term,

$$Q_{\mathrm{conv}} = C_{\mathrm{conv}}\, {x_2}^3. \tag{3.18}$$

Since Eq. (3.18) is a quite simplified model, Q_{conv} has to be evaluated using more appropriate models (e.g., Ref. 79) in real applications. Eq. (3.16) represents an adiabatic backface boundary condition where the backface heat flux, Q_{f}, equals to zero. Imposing the adiabatic condition on the TPS backface is a safe-sided treatment, because it premises that heat does not flow into vehicle main structures behind it. The adiabatic backface condition in the analysis and design of TPS is often used in literature[53,59,80]. In the context of PDEs, Eqs. (3.15, 3.16) are categorized as the Neumann boundary condition, where the derivative of the solution is specified on the boundary of its domain. Another type of boundary condition is the Dirichlet condition, and the value of the solution itself is specified on the boundary. It is noted that, when the Lagrange term in the cost functional and temperature constraint, Eq. (3.12), are removed, The problem reduces to a well-known double integrator problem whose solution is bang-bang control[77].

Values of constants are gathered below:

$$\begin{aligned}
y_0 &= 0, & y_{\mathrm{f}} &= 0.0254, & u_{\max} &= 1.0,\\
T_{\max} &= 450, & x_0 &= -2.5 \times 10^6, & T_0 &= 300,\\
K &= 0.048461, & \rho &= 192.22, & C_p &= 962.95,\\
\epsilon &= 0.97, & \sigma &= 5.6704 \times 10^{-8}, & C_{\mathrm{conv}} &= 7.8498 \times 10^{-6}.
\end{aligned} \tag{3.19}$$

3.2 Discretization of the PDE and Treatment of its Boundary Conditions

It is possible to discretize the PDE, Eq. (3.14), in both y and t using a technique such as the Crank-Nicolson finite difference scheme[81], and to obtain algebraic equations. This is a numerical solution approach used in Ref. 60. In this case, the PDE-ODE coupled optimal control problem are directly transcribed into an NLP problem that can be solved using an off-the-shelf solver (e.g., Refs. 43 and 44). The application of the Crank-Nicolson scheme is equivalent to applying a second order central difference formula and the trapezoidal rule to y and t, respectively. A drawback of this approach is that the transcription of optimal control problems via the trapezoidal rule is known to be inferior in accuracy compared with other methods.

Instead, a more practically convenient and versatile way to handle the PDE-ODE coupled optimal control problem is to discretize the PDE in y only, and to solve the resulting ODE-expressed optimal control problem as usual optimal control problems (see Fig. 3.2). This makes it possible to use more accurate Hermite-Simpson transcription[42] or pseudospectral methods[64,82,83] for optimal control. In the context of the numerical solution of initial-boundary value problems of PDEs, such an approach is called the method of lines[84, p. 55], where the PDEs are discretized in spatial coordinates only, and the discretized system is solved using an existing ODE solver. In previous researches, a finite volume scheme is employed in Ref. 61 and Ref. 62 in order to convert PDE-ODE-coupled optimal control problems into ODE-expressed ones. In this dissertation, more computationally efficient schemes based on a pseudospectral method with some enhancement is proposed. For the sake of completeness, the finite volume scheme and a finite difference scheme are explained below, and subsequently the proposed method is described.

3.2.1 Finite Volume Discretization

Let us divide the y-space into ny grid cells whose size are equally $h\,[= (y_\mathrm{f} - y_0)/ny]$. The time history of the tile temperature on the ith cell is denoted by $T_i(t)$ for $i = 1, \ldots, ny$. A schematic of this procedure is

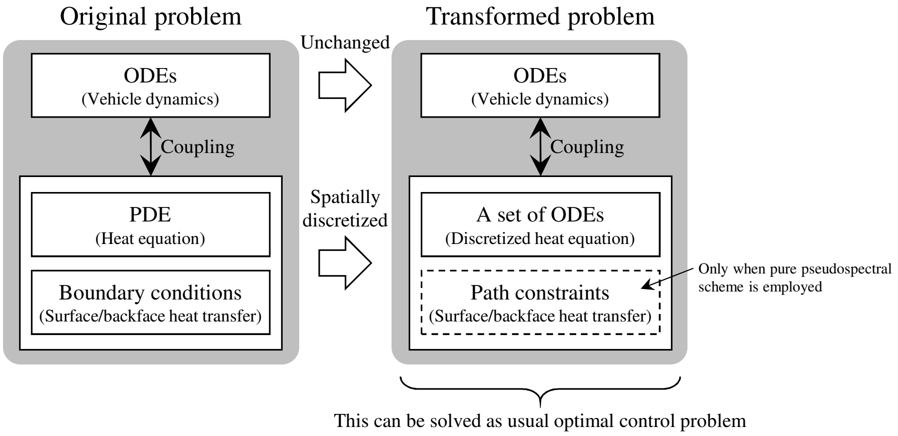

Fig. 3.2 Outline of the solution procedure of a PDE-ODE coupled optimal control problem.

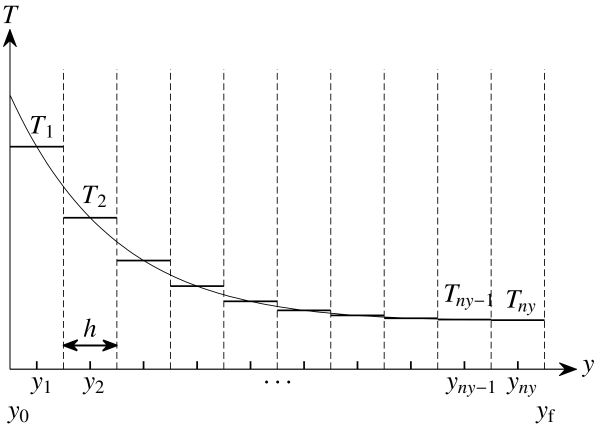

Fig. 3.3 Finite volume discretization.

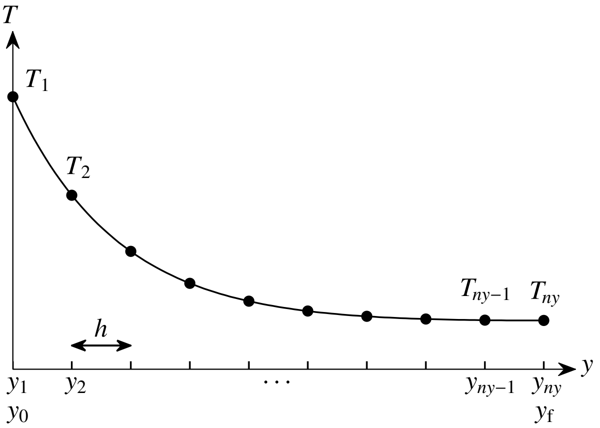

Fig. 3.4 Finite difference discretization.

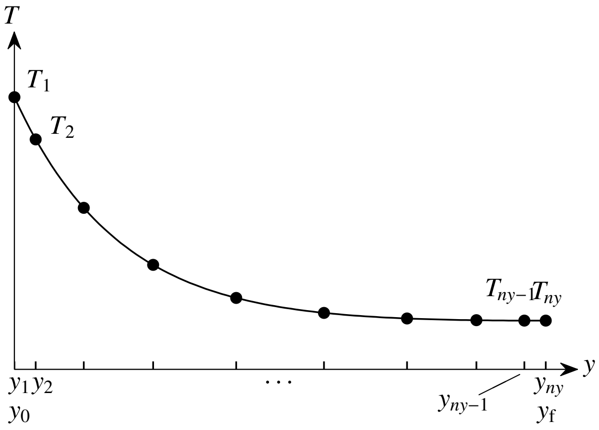

Fig. 3.5 Pseudospectral discretization.

shown in Fig. 3.3.

By employing a second-order midpoint approximation to the heat fluxes between three adjacent interior cells, we have

$$\frac{\mathrm{d}T_i}{\mathrm{d}t} = \frac{K}{\rho C_p}\frac{T_{i+1} - 2T_i + T_{i-1}}{h^2}, \quad i = 2, \dots, ny - 1. \tag{3.20}$$

Next, the same second-order approximation is applied to a boundary cell (i.e., $i = 1$, ny), and the flux outside of the domain is evaluated by the boundary condition. It leads to

$$\frac{\mathrm{d}T_1}{\mathrm{d}t} = \frac{1}{\rho C_p}\frac{(-Q_0/K)\,h + (T_2 - T_1)K}{h^2}, \tag{3.21}$$

$$\frac{\mathrm{d}T_{ny}}{\mathrm{d}t} = \frac{1}{\rho C_p}\frac{(-Q_\mathrm{f}/K)\,h + (T_{ny-1} - T_{ny})K}{h^2}. \tag{3.22}$$

Eqs. (3.20-3.22) define the discretization scheme used in Ref. 62.

As a consequence, we obtain an ODE-expressed optimal control problem whose state variables and control variable are

$$[x_1(t),\ x_2(t),\ T_1(t),\ \ldots,\ T_{ny}(t)]^{\mathrm{T}} =: \mathbf{x}(t) : [0,\ t_{\mathrm{f}}] \to \mathbb{R}^{ny+2}, \tag{3.23}$$

$$[u(t)] =: \mathbf{u}(t) : [0,\ t_{\mathrm{f}}] \to \mathbb{R}. \tag{3.24}$$

Eqs. (3.14–3.16) are replaced with *ny* dynamic constraints of Eqs. (3.20–3.22). In addition, Eq. (3.12) is replaced by

$$T_{ny}(t) \le T_{\max}. \tag{3.25}$$

The initial condition on T in Eq. (3.13) is transformed into

$$T_i(0) = T_0, \quad \text{for } i = 1, \ldots, ny. \tag{3.26}$$

3.2.2 Finite Difference Discretization

Let us distribute *ny* grid nodes uniformly in the y-space. The distances between pairs of adjacent nodes are all $h\,[= (y_{\mathrm{f}} - y_0)/(ny - 1)]$. The time history of the tile temperature at the ith node is denoted by $T_i(t)$ for $i = 1, \ldots, ny$. A schematic of this procedure is presented in Fig. 3.4.

By applying a second-order central difference approximation to $\partial^2 T_i/\partial y^2$ at interior nodes, Eq. (3.14) becomes

$$\frac{\mathrm{d}T_i}{\mathrm{d}t} = \frac{K}{\rho C_p} \frac{T_{i+1} - 2T_i + T_{i-1}}{h^2}, \quad i = 2, \ldots, ny - 1. \tag{3.27}$$

On the other hand, a first-order one-sided difference approximation to $\partial^2 T_i/\partial y^2$ is used at boundary nodes, and the following ODEs are derived:

$$\frac{\mathrm{d}T_1}{\mathrm{d}t} = \frac{2}{\rho C_p} \frac{(-Q_0/K)\,h + (T_2 - T_1)K}{h^2}, \tag{3.28}$$

$$\frac{\mathrm{d}T_{ny}}{\mathrm{d}t} = \frac{2}{\rho C_p} \frac{(-Q_{\mathrm{f}}/K)\,h + (T_{ny-1} - T_{ny})K}{h^2}. \tag{3.29}$$

Finally, we have an ODE-expressed optimal control problem whose state variables and control variable are

$$[x_1(t),\ x_2(t),\ T_1(t),\ \ldots,\ T_{ny}(t)]^{\mathrm{T}} =: \mathbf{x}(t) : [0,\ t_{\mathrm{f}}] \to \mathbb{R}^{ny+2}, \tag{3.30}$$

$$[u(t)] =: \mathbf{u}(t) : [0,\ t_{\mathrm{f}}] \to \mathbb{R}. \tag{3.31}$$

ny dynamic constraints shown in Eqs. (3.27–3.29) are substituted for Eqs. (3.14–3.16). Eq. (3.12) is replaced with

$$T_{ny}(t) \leq T_{\max}. \tag{3.32}$$

Besides, the initial condition on T in Eq. (3.13) becomes

$$T_i(0) = T_0, \quad \text{for} \;\; i = 1, \ldots, ny. \tag{3.33}$$

3.2.3 Pseudospectral Discretization

Let us first transform $y \in [y_0,\ y_\mathrm{f}]$ into $z \in [-1,\ 1]$ using the following affine transformation:

$$y = \frac{y_\mathrm{f} - y_0}{2} z + \frac{y_\mathrm{f} + y_0}{2}. \tag{3.34}$$

Accordingly, $\partial T/\partial y$ and $\partial^2 T/\partial y^2$ are replaced by $[2/(y_\mathrm{f} - y_0)]\,\partial T/\partial z$ and $[2/(y_\mathrm{f} - y_0)]^2\,\partial^2 T/\partial z^2$, respectively. Then, ny Legendre-Gauss-Lobatto (LGL) nodes[85] that all lie on the interval $[-1,\ 1]$ are introduced. The ith LGL node, z_i, is the ith zero of $(1 - z^2)P'_{ny}(z)$, where $P'_{ny}(\cdot)$ denotes the first derivative of the nyth-order Legendre orthogonal polynomial. LGL nodes can be explicitly computed using Golub's algorithm[86], while an iterative procedure is widely used as well[85]. The time history of the tile temperature at z_i is denoted by $T_i(t)$ for $i = 1, \ldots, ny$. A schematic of this procedure is illustrated in Fig. 3.5.

Next, $T(z, t)$ is approximated using an $(ny - 1)$th-order polynomial of z in the following manner:

$$T(z, t) \approx \sum_{i=1}^{ny} T(z_i, t) \cdot \psi_i(z) = \sum_{i=1}^{ny} T_i(t) \cdot \psi_i(z), \tag{3.35}$$

where $\psi_i(z)$ is the Lagrange basis polynomial that is defined as

$$\psi_i(z) := \prod_{\substack{j=1 \\ j \neq i}}^{ny} \frac{z - z_j}{z_i - z_j}. \tag{3.36}$$

The LGL nodes (or more generally, orthogonal nodes) prevents the Runge phenomenon in the polynomial interpolation from occurring. By differentiating Eq. (3.35) with respect to z and evaluating the derivative at z_ℓ, we obtain

$$\begin{aligned} \left.\frac{\partial T(z, t)}{\partial z}\right|_{z=z_\ell} &\approx \sum_{i=1}^{ny} \left.\frac{\partial \psi_i(z)}{\partial z}\right|_{z=z_\ell} \cdot T_i(t) \\ &= \sum_{i=1}^{ny} D_{\ell,i} \cdot T_i(t), \quad \ell = 1, \ldots, ny, \end{aligned} \tag{3.37}$$

where $D_{\ell,i}$ is the $(\ell,\ i)$th element of the differentiation matrix, $\mathbf{D}$. $D_{\ell,i}$ is calculated as follows[85] :

$$D_{\ell,i} = \begin{cases} \dfrac{P_{ny}(z_\ell)}{P_{ny}(z_i)} \dfrac{1}{z_\ell - z_i} & \ell \neq i \\ \dfrac{(ny+1)ny}{4} & \ell = i = 0 \\ -\dfrac{(ny+1)ny}{4} & \ell = i = ny \\ 0 & \text{otherwise.} \end{cases} \tag{3.38}$$

When Eq. (3.37) is collectively written in a matrix form, it becomes

$$\begin{bmatrix} \partial T/\partial z\big|_{z=z_1} \\ \partial T/\partial z\big|_{z=z_2} \\ \vdots \\ \partial T/\partial z\big|_{z=z_{ny-1}} \\ \partial T/\partial z\big|_{z=z_{ny}} \end{bmatrix} = \begin{bmatrix} \\ \\ \mathbf{D} \\ \\ \\ \end{bmatrix} \begin{bmatrix} T_1(t) \\ T_2(t) \\ \vdots \\ T_{ny-1}(t) \\ T_{ny}(t) \end{bmatrix}. \tag{3.39}$$

For the second-order partial derivative, the corresponding differentiation matrix is derived by simply multiplying $\mathbf{D}$ by itself, that is

$$\begin{bmatrix} \partial^2 T/\partial z^2\big|_{z=z_1} \\ \partial^2 T/\partial z^2\big|_{z=z_2} \\ \vdots \\ \partial^2 T/\partial z^2\big|_{z=z_{ny-1}} \\ \partial^2 T/\partial z^2\big|_{z=z_{ny}} \end{bmatrix} = \begin{bmatrix} \\ \\ \mathbf{D}^{(2)} \\ \\ \\ \end{bmatrix} \begin{bmatrix} T_1(t) \\ T_2(t) \\ \vdots \\ T_{ny-1}(t) \\ T_{ny}(t) \end{bmatrix}, \quad \text{where } \mathbf{D}^{(2)} := \mathbf{D}^2. \tag{3.40}$$

It is stated in Ref. 87 that, there are two basic approaches for handling boundary conditions in spectral methods [*]:

Approach 1: to use such an interpolant that satisfies boundary conditions

Approach 2: to impose additional constraints derived from boundary conditions without paying special attention to interpolants.

When Approach 2 is used, differential equations are not enforced at the boundary nodes on which the boundary conditions are imposed instead. It is noted that the larger number of constraints than unknowns results in an ill-conditioned problem. Approach 2 is commonly used in pseudospectral methods due to its flexibility. However, as pointed out in Ref. 88, its drawback is that differential equations are not satisfied at points arbitrarily close to the boundary.

---

[*] A class of spectral methods consists of pseudospectral (or collocation) methods, Galerkin methods, and Tau methods.

To begin with, let us try Approach 2. By collocating the PDE, Eq. (3.14), at interior LGL nodes (i.e., $z_2, \dots, z_{ny-1}$) using Eq. (3.40), it gives

$$\frac{\mathrm{d}}{\mathrm{d}t}\begin{bmatrix} T_2(t) \\ \vdots \\ T_{ny-1}(t) \end{bmatrix} = \frac{K}{\rho C_p}\left(\frac{2}{y_\mathrm{f} - y_0}\right)^2 \begin{bmatrix} D^{(2)}_{2,1} & D^{(2)}_{2,2} & \cdots & D^{(2)}_{2,ny-1} & D^{(2)}_{2,ny} \\ \vdots & \vdots & \ddots & \vdots & \vdots \\ D^{(2)}_{ny-1,1} & D^{(2)}_{ny-1,2} & \cdots & D^{(2)}_{ny-1,ny-1} & D^{(2)}_{ny-1,ny} \end{bmatrix} \begin{bmatrix} T_1(t) \\ T_2(t) \\ \vdots \\ T_{ny-1}(t) \\ T_{ny}(t) \end{bmatrix}. \tag{3.41}$$

Next, algebraic equations arising from boundary conditions are obtained via applying Eq. (3.39) to Eqs. (3.15, 3.16):

$$\frac{2}{y_\mathrm{f} - y_0}\begin{bmatrix} D_{1,1} & D_{1,2} & \cdots & D_{1,ny-1} & D_{1,ny} \\ D_{ny,1} & D_{ny,2} & \cdots & D_{ny,ny-1} & D_{ny,ny} \end{bmatrix} \begin{bmatrix} T_1(t) \\ T_2(t) \\ \vdots \\ T_{ny-1}(t) \\ T_{ny}(t) \end{bmatrix} = \begin{bmatrix} Q_0/K \\ Q_\mathrm{f}/K \end{bmatrix}. \tag{3.42}$$

Finally, we obtain an ODE-expressed optimal control problem whose state variables and control variable are

$$[x_1(t),\, x_2(t),\, T_2(t),\, \dots,\, T_{ny-1}(t)]^\mathrm{T} =: \mathbf{x}(t) : [0,\, t_\mathrm{f}] \to \mathbb{R}^{ny}, \tag{3.43}$$

$$[u(t),\, T_1(t),\, T_{ny}(t)]^\mathrm{T} =: \mathbf{u}(t) : [0,\, t_\mathrm{f}] \to \mathbb{R}^{3}. \tag{3.44}$$

Eq. (3.14) is replaced with $(ny - 2)$ dynamic constraints of Eq. (3.41). Eqs. (3.15, 3.16) are transformed into two path constraints shown in Eq. (3.42). Eq. (3.12) is rewritten as

$$T_{ny}(t) \le T_\mathrm{max}. \tag{3.45}$$

The initial condition on T in Eq. (3.13) is expressed by

$$T_i(0) = T_0, \quad \text{for } \; i = 2, \dots, ny - 1. \tag{3.46}$$

Note that $T_1(t)$ and $T_{ny}(t)$ are included not in state variables but in control variables in contrast to the finite-volume discretization and the finite-difference discretization.

3.2.4 Incorporation of Boundary Conditions

Although Approach 2 for the boundary-condition handling is straightforward to be implemented, it can deteriorate the solution accuracy, because the governing equation of the tile temperature is not satisfied at the locations where boundary conditions accounting for aerodynamic heating are specified. In order to overcome this drawback, Funaro and Gottieb[88] proposed an idea of imposing the combination of boundary conditions and the equation itself at the boundary nodes in the case of hyperbolic PDEs*, and they discussed its advantages. Another attempt is the fictitious point method developed by Fornberg[89], and the method is adopted in this dissertation. The proposed approach is useful when a Neumann boundary condition is imposed as in the case of Eqs. (3.15, 3.16). When a Dirichlet boundary condition is involved, it can be implemented by removing the boundary point from the collocation points and simply substituting the specified boundary value of T.

Let us introduce additional two grid nodes denoted by z_{fp1} and z_{fp2} at any arbitrary locations. These added nodes are called fictitious points, and they can be placed either inside or outside of the domain of z (i.e., $[-1,\ 1]$). The time history of the tile temperature at z_{fp1} and that at z_{fp2} are denoted by $T_{\mathrm{fp1}}(t)$ and $T_{\mathrm{fp2}}(t)$, respectively. Then, the corresponding differentiation matrix for a set of nodes, $\{z_{\mathrm{fp1}}, z_{\mathrm{fp2}}, z_1, \ldots, z_{ny}\}$, is calculated using an algorithm for generating differentiation matrices for arbitrarily distributed nodes[90]. Let the obtained first- and second-order differentiation matrices be denoted by $\hat{\mathbf{D}}$ and $\hat{\mathbf{D}}^{(2)} (= \hat{\mathbf{D}}^2)$, respectively. Elements of these differentiation matrices are defined as follows:

$$\hat{\mathbf{D}} := \begin{bmatrix} \hat{D}_{\mathrm{fp1},\,\mathrm{fp1}} & \hat{D}_{\mathrm{fp1},\,\mathrm{fp2}} & \hat{D}_{\mathrm{fp1},\,1} & \hat{D}_{\mathrm{fp1},\,2} & \cdots & \hat{D}_{\mathrm{fp1},\,ny-1} & \hat{D}_{\mathrm{fp1},\,ny} \\ \hat{D}_{\mathrm{fp2},\,\mathrm{fp1}} & \hat{D}_{\mathrm{fp2},\,\mathrm{fp2}} & \hat{D}_{\mathrm{fp2},\,1} & \hat{D}_{\mathrm{fp2},\,2} & \cdots & \hat{D}_{\mathrm{fp2},\,ny-1} & \hat{D}_{\mathrm{fp2},\,ny} \\ \hat{D}_{1,\,\mathrm{fp1}} & \hat{D}_{1,\,\mathrm{fp2}} & \hat{D}_{1,\,1} & \hat{D}_{1,\,2} & \cdots & \hat{D}_{1,\,ny-1} & \hat{D}_{1,\,ny} \\ \hat{D}_{2,\,\mathrm{fp1}} & \hat{D}_{2,\,\mathrm{fp2}} & \hat{D}_{2,\,1} & \hat{D}_{2,\,2} & \cdots & \hat{D}_{2,\,ny-1} & \hat{D}_{2,\,ny} \\ \vdots & \vdots & \vdots & \vdots & \ddots & \vdots & \vdots \\ \hat{D}_{ny-1,\,\mathrm{fp1}} & \hat{D}_{ny-1,\,\mathrm{fp2}} & \hat{D}_{ny-1,\,1} & \hat{D}_{ny-1,\,2} & \cdots & \hat{D}_{ny-1,\,ny-1} & \hat{D}_{ny-1,\,ny} \\ \hat{D}_{ny,\,\mathrm{fp1}} & \hat{D}_{ny,\,\mathrm{fp2}} & \hat{D}_{ny,\,1} & \hat{D}_{ny,\,2} & \cdots & \hat{D}_{ny,\,ny-1} & \hat{D}_{ny,\,ny} \end{bmatrix}, \tag{3.47}$$

$$\hat{\mathbf{D}}^{(2)} := \begin{bmatrix} \hat{D}^{(2)}_{\mathrm{fp1},\,\mathrm{fp1}} & \hat{D}^{(2)}_{\mathrm{fp1},\,\mathrm{fp2}} & \hat{D}^{(2)}_{\mathrm{fp1},\,1} & \hat{D}^{(2)}_{\mathrm{fp1},\,2} & \cdots & \hat{D}^{(2)}_{\mathrm{fp1},\,ny-1} & \hat{D}^{(2)}_{\mathrm{fp1},\,ny} \\ \hat{D}^{(2)}_{\mathrm{fp2},\,\mathrm{fp1}} & \hat{D}^{(2)}_{\mathrm{fp2},\,\mathrm{fp2}} & \hat{D}^{(2)}_{\mathrm{fp2},\,1} & \hat{D}^{(2)}_{\mathrm{fp2},\,2} & \cdots & \hat{D}^{(2)}_{\mathrm{fp2},\,ny-1} & \hat{D}^{(2)}_{\mathrm{fp2},\,ny} \\ \hat{D}^{(2)}_{1,\,\mathrm{fp1}} & \hat{D}^{(2)}_{1,\,\mathrm{fp2}} & \hat{D}^{(2)}_{1,\,1} & \hat{D}^{(2)}_{1,\,2} & \cdots & \hat{D}^{(2)}_{1,\,ny-1} & \hat{D}^{(2)}_{1,\,ny} \\ \hat{D}^{(2)}_{2,\,\mathrm{fp1}} & \hat{D}^{(2)}_{2,\,\mathrm{fp2}} & \hat{D}^{(2)}_{2,\,1} & \hat{D}^{(2)}_{2,\,2} & \cdots & \hat{D}^{(2)}_{2,\,ny-1} & \hat{D}^{(2)}_{2,\,ny} \\ \vdots & \vdots & \vdots & \vdots & \ddots & \vdots & \vdots \\ \hat{D}^{(2)}_{ny-1,\,\mathrm{fp1}} & \hat{D}^{(2)}_{ny-1,\,\mathrm{fp2}} & \hat{D}^{(2)}_{ny-1,\,1} & \hat{D}^{(2)}_{ny-1,\,2} & \cdots & \hat{D}^{(2)}_{ny-1,\,ny-1} & \hat{D}^{(2)}_{ny-1,\,ny} \\ \hat{D}^{(2)}_{ny,\,\mathrm{fp1}} & \hat{D}^{(2)}_{ny,\,\mathrm{fp2}} & \hat{D}^{(2)}_{ny,\,1} & \hat{D}^{(2)}_{ny,\,2} & \cdots & \hat{D}^{(2)}_{ny,\,ny-1} & \hat{D}^{(2)}_{ny,\,ny} \end{bmatrix}. \tag{3.48}$$

---

[*] Note that the heat equation is a parabolic PDE.

By collocating the PDE, Eq. (3.14), at all the LGL nodes and the fictitious points, we obtain

$$\frac{\mathrm{d}}{\mathrm{d}t}\begin{bmatrix} T_{\mathrm{fp}1}(t) \\ T_{\mathrm{fp}2}(t) \\ T_1(t) \\ T_2(t) \\ \vdots \\ T_{ny-1}(t) \\ T_{ny}(t) \end{bmatrix} = \frac{K}{\rho C_p}\left(\frac{2}{y_{\mathrm{f}}-y_0}\right)^2 \begin{bmatrix} \\ \\ \\ \quad\quad\hat{\mathbf{D}}^{(2)}\quad\quad \\ \\ \\ \\ \end{bmatrix} \begin{bmatrix} T_{\mathrm{fp}1}(t) \\ T_{\mathrm{fp}2}(t) \\ T_1(t) \\ T_2(t) \\ \vdots \\ T_{ny-1}(t) \\ T_{ny}(t) \end{bmatrix}. \tag{3.49}$$

Boundary conditions presented in Eqs. (3.15, 3.16) are transcribed in the following way:

$$\frac{2}{y_{\mathrm{f}}-y_0}\underbrace{\begin{bmatrix} \hat{D}_{1,\mathrm{fp}1} & \hat{D}_{1,\mathrm{fp}2} & \hat{D}_{1,1} & \hat{D}_{1,2} & \cdots & \hat{D}_{1,ny-1} & \hat{D}_{1,ny} \\ \hat{D}_{ny,\mathrm{fp}1} & \hat{D}_{ny,\mathrm{fp}2} & \hat{D}_{ny,1} & \hat{D}_{ny,2} & \cdots & \hat{D}_{ny,ny-1} & \hat{D}_{ny,ny} \end{bmatrix}}_{:=\,\hat{\mathbf{D}}^{(\mathrm{bc})}} \begin{bmatrix} T_{\mathrm{fp}1}(t) \\ T_{\mathrm{fp}2}(t) \\ T_1(t) \\ T_2(t) \\ \vdots \\ T_{ny-1}(t) \\ T_{ny}(t) \end{bmatrix} = \begin{bmatrix} Q_0/K \\ Q_{\mathrm{f}}/K \end{bmatrix}, \tag{3.50}$$

The next and most important step is to eliminate the influences of $T_{\mathrm{fp}1}(t)$ and $T_{\mathrm{fp}2}(t)$ in Eq. (3.49) using Eq. (3.50). This goal is achieved through matrix operations such that make the first and second columns of $\hat{\mathbf{D}}^{(2)}$ zero, and it results in the following relation:

$$\begin{aligned} \frac{\mathrm{d}}{\mathrm{d}t}\begin{bmatrix} T_{\mathrm{fp}1}(t) \\ T_{\mathrm{fp}2}(t) \\ T_1(t) \\ T_2(t) \\ \vdots \\ T_{ny-1}(t) \\ T_{ny}(t) \end{bmatrix} &= \frac{K}{\rho C_p}\left(\frac{2}{y_{\mathrm{f}}-y_0}\right)^2 \left[\begin{array}{cc:c} 0 & 0 & \\ 0 & 0 & \tilde{\mathbf{E}} \\ \hdashline 0 & 0 & \\ 0 & 0 & \\ \vdots & \vdots & \mathbf{E} \\ 0 & 0 & \\ 0 & 0 & \end{array}\right] \begin{bmatrix} T_{\mathrm{fp}1}(t) \\ T_{\mathrm{fp}2}(t) \\ T_1(t) \\ T_2(t) \\ \vdots \\ T_{ny-1}(t) \\ T_{ny}(t) \end{bmatrix} \\ &\quad + \frac{K}{\rho C_p}\frac{2}{y_{\mathrm{f}}-y_0}\left[\begin{array}{c} \tilde{\mathbf{F}} \\ \hdashline \\ \mathbf{F} \\ \\ \end{array}\right]\frac{Q_0}{K} + \frac{K}{\rho C_p}\frac{2}{y_{\mathrm{f}}-y_0}\left[\begin{array}{c} \tilde{\mathbf{G}} \\ \hdashline \\ \mathbf{G} \\ \\ \end{array}\right]\frac{Q_{\mathrm{f}}}{K}, \end{aligned} \tag{3.51}$$

where

$$\left[\begin{array}{cc|c} 0 & 0 & \multirow{2}{*}{$\tilde{\mathbf{E}}$} \\ 0 & 0 & \\ \hline 0 & 0 & \\ \vdots & \vdots & \mathbf{E} \\ 0 & 0 & \end{array}\right] = \hat{\mathbf{D}}^{(2)} - \begin{bmatrix} \hat{D}^{(2)}_{\mathrm{fp1},\,\mathrm{fp1}} & \hat{D}^{(2)}_{\mathrm{fp1},\,\mathrm{fp2}} \\ \hat{D}^{(2)}_{\mathrm{fp2},\,\mathrm{fp1}} & \hat{D}^{(2)}_{\mathrm{fp2},\,\mathrm{fp2}} \\ \hat{D}^{(2)}_{1,\,\mathrm{fp1}} & \hat{D}^{(2)}_{1,\,\mathrm{fp2}} \\ \vdots & \vdots \\ \hat{D}^{(2)}_{ny,\,\mathrm{fp1}} & \hat{D}^{(2)}_{ny,\,\mathrm{fp2}} \end{bmatrix} \begin{bmatrix} \hat{D}_{1,\,\mathrm{fp1}} & \hat{D}_{1,\,\mathrm{fp2}} \\ \hat{D}_{ny,\,\mathrm{fp1}} & \hat{D}_{ny,\,\mathrm{fp2}} \end{bmatrix}^{-1} \hat{\mathbf{D}}^{(\mathrm{bc})}, \tag{3.52}$$

$$\left[\begin{array}{c|c} \tilde{\mathbf{F}} & \tilde{\mathbf{G}} \\ \hline \\ \mathbf{F} & \mathbf{G} \\ \\ \end{array}\right] = \begin{bmatrix} \hat{D}^{(2)}_{\mathrm{fp1},\,\mathrm{fp1}} & \hat{D}^{(2)}_{\mathrm{fp1},\,\mathrm{fp2}} \\ \hat{D}^{(2)}_{\mathrm{fp2},\,\mathrm{fp1}} & \hat{D}^{(2)}_{\mathrm{fp2},\,\mathrm{fp2}} \\ \hat{D}^{(2)}_{1,\,\mathrm{fp1}} & \hat{D}^{(2)}_{1,\,\mathrm{fp2}} \\ \vdots & \vdots \\ \hat{D}^{(2)}_{ny,\,\mathrm{fp1}} & \hat{D}^{(2)}_{ny,\,\mathrm{fp2}} \end{bmatrix} \begin{bmatrix} \hat{D}_{1,\,\mathrm{fp1}} & \hat{D}_{1,\,\mathrm{fp2}} \\ \hat{D}_{ny,\,\mathrm{fp1}} & \hat{D}_{ny,\,\mathrm{fp2}} \end{bmatrix}^{-1}. \tag{3.53}$$

In Eq. (3.51), the influence of the fictitious points on dynamics of $\{T_1, \ldots, T_{ny}\}$ vanishes except round-off errors. Therefore, the first and second rows in Eq. (3.51) can be removed, and we eventually have the following set of ODEs originating from Eqs. (3.14–3.16):

$$\frac{\mathrm{d}}{\mathrm{d}t} \begin{bmatrix} T_1(t) \\ T_2(t) \\ \vdots \\ T_{ny-1}(t) \\ T_{ny}(t) \end{bmatrix} = \frac{K}{\rho C_p} \left(\frac{2}{y_\mathrm{f} - y_0} \right)^2 \begin{bmatrix} \\ \\ & \mathbf{E} & \\ \\ \\ \end{bmatrix} \begin{bmatrix} T_1(t) \\ T_2(t) \\ \vdots \\ T_{ny-1}(t) \\ T_{ny}(t) \end{bmatrix} + \frac{K}{\rho C_p} \frac{2}{y_\mathrm{f} - y_0} \begin{bmatrix} \\ \\ \mathbf{F} \\ \\ \\ \end{bmatrix} \frac{Q_0}{K} + \frac{K}{\rho C_p} \frac{2}{y_\mathrm{f} - y_0} \begin{bmatrix} \\ \\ \mathbf{G} \\ \\ \\ \end{bmatrix} \frac{Q_\mathrm{f}}{K} \tag{3.54}$$

As a consequence, we obtain an ODE-expressed optimal control problem whose state variables and control variable are

$$[x_1(t),\ x_2(t),\ T_1(t),\ \ldots,\ T_{ny}(t)]^\mathrm{T} =: \mathbf{x}(t) : [0,\ t_\mathrm{f}] \to \mathbb{R}^{ny+2}, \tag{3.55}$$

$$[u(t)] =: \mathbf{u}(t) : [0,\ t_\mathrm{f}] \to \mathbb{R}. \tag{3.56}$$

Eqs. (3.14–3.16) are replaced by ny dynamic constraints in Eq. (3.54). In addition, Eq. (3.12) becomes

$$T_{ny}(t) \leq T_\mathrm{max}. \tag{3.57}$$

The initial condition on T in Eq. (3.13) is transcribed into

$$T_i(0) = T_0, \quad \text{for } \ i = 1, \ldots, ny. \tag{3.58}$$

Thermal properties of most TPS materials have considerable dependence on temperature, T, and surrounding static pressure, p. For example, in a TPS material datasheet[98], K is presented as a function of T and p, and C_p is given as a function of T. When such dependence is considered, Eq. (3.54) should be replaced with

$$\frac{\mathrm{d}}{\mathrm{d}t}\begin{bmatrix} T_1(t) \\ T_2(t) \\ \vdots \\ T_{ny-1}(t) \\ T_{ny}(t) \end{bmatrix} = \begin{bmatrix} \\ \\ \quad \mathbf{C} \quad \\ \\ \\ \end{bmatrix} \left\{ \left(\frac{2}{y_\mathrm{f} - y_0} \right)^2 \begin{bmatrix} \\ \\ \quad \mathbf{H} \quad \\ \\ \\ \end{bmatrix} \begin{bmatrix} T_1(t) \\ T_2(t) \\ \vdots \\ T_{ny-1}(t) \\ T_{ny}(t) \end{bmatrix} + \frac{2}{y_\mathrm{f} - y_0} \begin{bmatrix} \\ \\ \mathbf{I} \\ \\ \\ \end{bmatrix} Q_0 + \frac{2}{y_\mathrm{f} - y_0} \begin{bmatrix} \\ \\ \mathbf{J} \\ \\ \\ \end{bmatrix} Q_\mathrm{f} \right\}, \tag{3.59}$$

where $\mathbf{C}$ is given by

$$\mathbf{C} := \mathrm{diag}\left[\frac{1}{\rho\, C_p[T_1(t)]} \; \frac{1}{\rho\, C_p[T_2(t)]} \; \cdots \; \frac{1}{\rho\, C_p[T_{ny-1}(t)]} \; \frac{1}{\rho\, C_p[T_{ny}(t)]} \right]. \tag{3.60}$$

Here, $\mathbf{H}$, $\mathbf{I}$, and $\mathbf{J}$ are equivalent to $\mathbf{E}$, $\mathbf{F}$, and $\mathbf{G}$, respectively, when $\hat{\mathbf{D}}^{(2)}$ in Eqs. (3.52, 3.53) is replaced by

$$\mathrm{diag}(\mathbf{K})\, \hat{\mathbf{D}}^{(2)} + \mathrm{diag}(\hat{\mathbf{D}}\, \mathbf{K}^\mathrm{T})\, \hat{\mathbf{D}}, \tag{3.61}$$

where

$$\mathbf{K} := \Big[K[T_\mathrm{fp1}(t), p] \; K[T_\mathrm{fp2}(t), p] \; K[T_1(t), p] \; \cdots \; K[T_{ny}(t), p] \Big]. \tag{3.62}$$

At each iteration step in the numerical solution of the resulting optimal control problem, $K[T_\mathrm{fp1}(t), p]$ and $K[T_\mathrm{fp2}(t), p]$ are evaluated from $\{K[T_1(t), p], \ldots, K[T_{ny}(t), p]\}$ using Lagrange interpolation. Although $\mathbf{H}$, $\mathbf{I}$, and $\mathbf{J}$ are no longer constant matrices, they are still independent of the choices for the abscissas of fictitious points.

3.3 Numerical Experiment

3.3.1 Experiment Procedure

In this section, the accuracies of discretization schemes presented above are compared through solving the transient heat-constrained optimal control problem in Section 3.1. The PDE and its boundary conditions are transcribed into ODEs using

1) Legendre pseudospectral (PS) method in Section 3.2.3,
2) fictitious-point Legendre PS method in Section 3.2.4,
3) finite volume method in Section 3.2.1, and

4) finite difference method in Section 3.2.2,

with changing the value of ny. The derived ODE-expressed optimal control problems are solved using the Legendre-Gauss pseudospectral method[64,65] as in the case of usual optimal control problems. In all the cases, 100 collocation points are used in the Legendre-Gauss pseudospectral method, that is, the number of temporal discretization nodes is fixed. The resulting NLP problems are solved with SNOPT[43,78], an off-the-shelf solver based on sequential quadratic programming. Because the highly accuracy pseudospectral method for optimal control is used with the sufficiently large number of collocation points, it is assumed that numerical errors in the obtained solutions are all attributed to spatial discretization errors of the PDE into ODEs. A common initial guess for the solution is properly prepared and provided in all the computations.

3.3.2 Result and Discussion

Cost functional values for various choices of discretization schemes and ny are shown in Figs. 3.6 and 3.7. Figure 3.7 is the enlarged view of the gray region in Fig. 3.6. As the value of ny is increased, cost values of solutions with different PDE discretization schemes have converged similar values around 5035.31($=: \tilde{J}^*$) except the finite volume method. Seemingly, the solution via the finite volume method has not fully converged even when $ny = 128$. Since the analytic solution of this example problem is not available*, we postulate that the actual J in the optimal solution of the original continuous-time/space problem is quite close to $\tilde{J}^*$

Poor accuracy of the finite volume scheme would be due to its treatment of boundary conditions. When using the finite volume discretization, $T_{ny}(t)$ refers to the temperature averaged over the boundary cell, while $T_{ny}(t)$ denotes the exactly surface temperature in the other methods (see Figs. 3.3–3.5). This

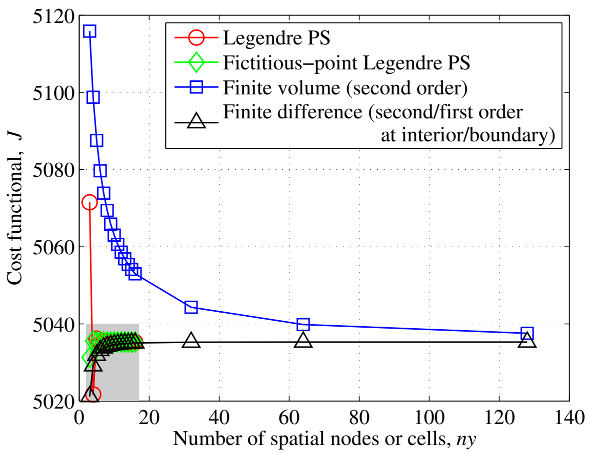

Fig. 3.6 Convergence comparison of PDE discretization schemes in heat-constrained optimal control.

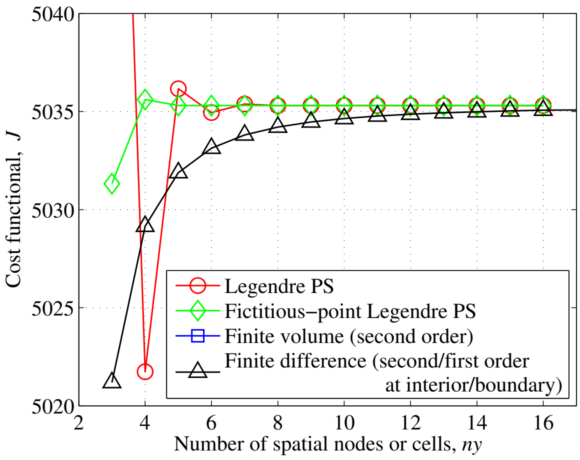

Fig. 3.7 Enlarged view of the gray region in Fig. 3.6.

---

*Only a partially analytic solution has been revealed even in the simplest transient heat-constrained optimal control problem[60].

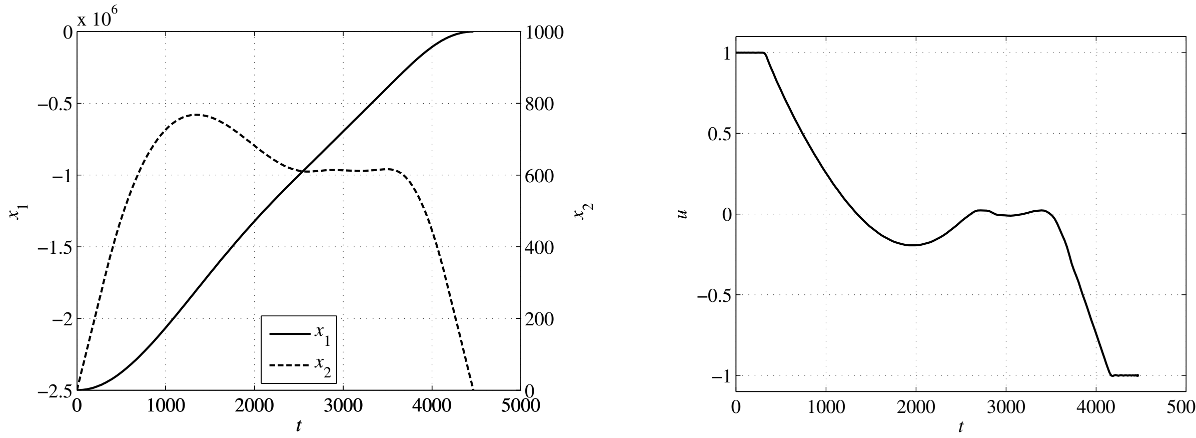

(a) Time history of the state variables.

(b) Time history of the control variable.

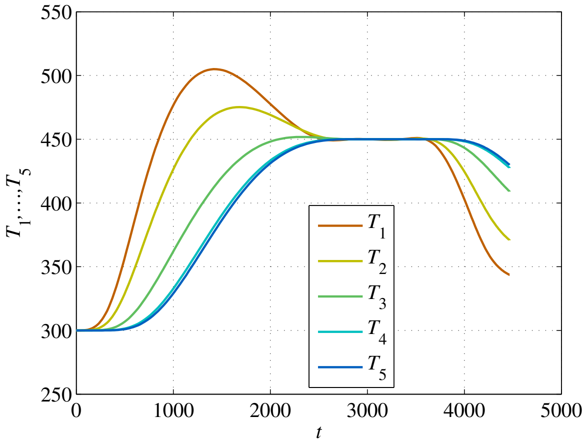

(c) Time history of the tile temperature at several depths.

Fig. 3.8 Obtained solution using the fictitious-point Legendre pseudospectral method with $ny = 5$.

means that the path constraint, $T_{ny}(t) \leq T_{\max}$, becomes an inaccurate approximation of the original backface temperature limit, $T(y_{\mathrm{f}}, t) \leq T_{\max}$, when the finite volume scheme is used with small ny.

While the accuracy of the pure Legendre pseudospectral method is inferior to that of the finite difference scheme when ny is very small*, the solution via the pseudospectral discretization gets converged exponentially as ny is increased. By applying the fictitious point method, the fictitious-point Legendre pseudospectral method achieves superior accuracy over all ranges of ny. The J value with the Legendre PS method and that with the fictitious-point Legendre PS method coincide with each other up to the first ten digits when $ny = 16$.

Although the application of the fictitious point method enables the slight reduction of the acceptable value of ny (e.g., from 7 to 5) only, it leads to considerable reduction of the size of the NLP problem to be solved. It is because that the required number of temporal collocation points is typically dozens or hundreds in order to obtain satisfactory solution in practical problems. Therefore, the numbers of decision variables and constraints in the NLP problem can be reduced by hundreds via reducing ny a

---

*It is noted that the PDE is imposed at one location of y only, when the pure pseudospectral method is used with $ny = 3$.

little.

Figure 3.8 shows the solution obtained using the fictitious-point Legendre pseudospectral method with $ny = 5$. As the velocity, x_2, increases, the temperature on the surface, T_1, rises, which is followed by the increase of the internal temperature. An overshoot of x_2 is observed before it enters into a "cruising" state around $2600 \leq t \leq 3600$. Owing to this overshoot, T_1 once goes above the backface temperature limit, $T_{\max}$. Then, T_1 decreases and follows $T_{\max}$ after $t \approx 2600$. Subsequently, T_1 leaves the limit at $t \approx 3600$, and $T_2, \ldots, T_5$ pursue it. The backface temperature limit, Eq. (3.12), is active approximately in $2600 \leq t \leq 4000$, and the thermal environment inside the tile is stationary only in $2600 \leq t \leq 3600$. At the final time, terminal conditions including $x_2 = 0$ are satisfied. It is noted that $T_1(t_f) \neq T_1(0)$ even though $x_2(t_f) = x_2(0)$. This is a consequence of, so to speak, memory effect[60] because of the heat stored inside the TPS material. Such a behavior of the temperature cannot be determined when only a stationary heat analysis is conducted.

3.4 Conclusion of this Chapter

The thermal behavior of passive TPS for hypersonic vehicles (e.g., insulation tiles) is governed by a PDE-expressed heat equation inside the material. Therefore, when the simultaneous design optimization problem of the flight trajectory and the TPS is formulated, it becomes a PDE-ODE coupled optimal control problem. In order to solve this problem in a numerically efficient manner, a transformation method of the PDE into a set of ODEs is investigated. In this method, a pseudospectral discretization scheme is applied to the spatial coordinate only, and boundary conditions at the TPS surface and backface are handled by the fictitious point method. Then, the resulting ODE-expressed optimal control problem can be solved using a conventional optimal control software. The efficiency of the proposed technique is demonstrated through conducting numerical experiments based on a test problem. The result indicates that the proposed method has a faster convergence rate in comparison with finite volume, finite difference, and pure pseudospectral schemes.

Chapter 4

Multi-Objective, Multidisciplinary Design Optimization of a TSTO RLV with PCTJ Engines

In this chapter, a conceptual design study of a horizontal takeoff TSTO RLV with pre-cooled turbojet (PCTJ) engines is conducted via multi-objective optimization. The PCTJ engine is a sort of hypersonic airbreathing engines, and it can be operated with high specific impulse value up to Mach 6.0 owing to the precooling system located prior to its core engine. Multi-objective MDO is executed on vehicle design and flight trajectory simultaneously with the aim of maximizing the payload mass, minimizing the mated vehicle gross mass, and minimizing the takeoff velocity. After inspecting representative solutions selected from the obtained Pareto optimal solutions, generic knowledge is extracted by applying data mining techniques.

4.1 Overview of Multi-Objective MDO

Figure 4.1 shows the outline of a multi-objective MDO framework for the TSTO RLV with PCTJ engines. This numerical framework consists of the following analysis disciplines: vehicle geometry and mass property, aerodynamics, propulsion, and flight trajectory. The assumed mission is the manned transportation of a payload into a low Earth orbit at 350 km above sea level. Static design variables are gathered in Table 4.1. Besides, state variables, control variables, and phase-switching times for optimal control of the vehicle are included in the design variables of the MDO problem in order to enable concurrent optimization of vehicle design and trajectory design. This point will be detailed later in Section 4.3. For an optimizer, a multi-objective optimization method developed in Chapter 2 is employed. The optimizer varies each of the design variables and passes them to the analysis disciplines. Subsequently, a numerical model in each discipline calculates output values from the design variables and/or input values from other disciplines. As a consequence, objective values and constraint values are computed, and they are fedback to the optimizer. No internal iteration loop exists, and all the objectives and constraints are

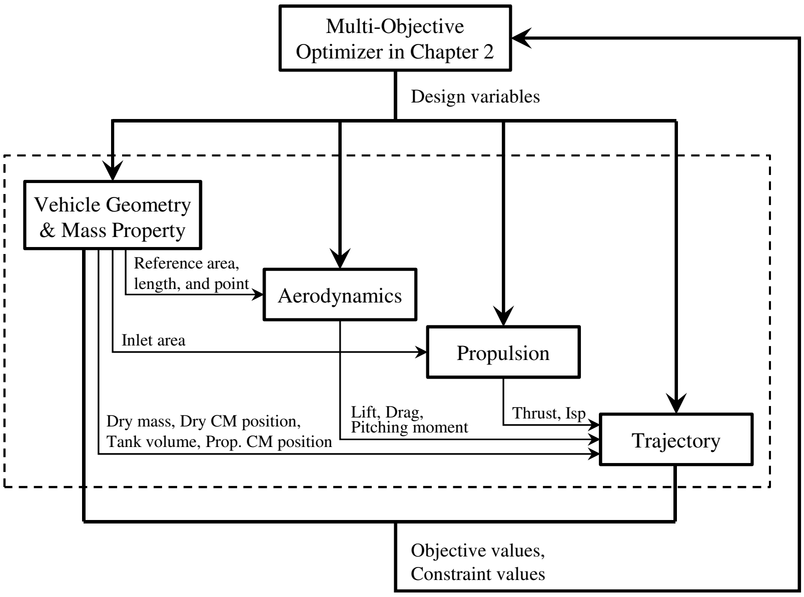

Fig. 4.1 Overview of a multi-objective MDO framework for the TSTO RLV with PCTJ engines.

managed by the single system-level optimizer. Such an MDO approach is called an all-at-once approach as mentioned in Section 1.2.1, which is known to have stable and rapid convergence, and be free from convergence errors between coupling variables in different disciplines[19,27].

Design objectives considered here are 1) maximization of the payload mass, m_{pay}, 2) minimization of the gross mass of the mated vehicle, $m_{\mathrm{gross}}(= m^{(\mathrm{b})}_{\mathrm{gross}} + m^{(\mathrm{o})}_{\mathrm{gross}})$, and 3) minimization of the horizontal takeoff velocity, v_{to}. The takeoff velocity is selected as one of the design criteria, because it is a major technological constraint in designing booster vehicles of TSTO RLVs. It is noted that the takeoff velocity not only determines initial velocity in trajectory computation, but also puts a significant constraint on vehicle design [see Eq. (4.27)]. In order to limit the design search region to an interesting area and to make the resulting Pareto front bounded (see Assumption 1 in p. 13), the following constraints are imposed on the objective values:

$$m_{\mathrm{pay}} \geq 500\ \mathrm{kg}, \tag{4.1}$$

$$m_{\mathrm{gross}} \leq 700\ \mathrm{t}, \tag{4.2}$$

$$v_{\mathrm{to}} \leq 180\ \mathrm{m/s}. \tag{4.3}$$

4.2 Design Assumptions and Numerical Models

In this section, design assumptions are presented, and a numerical model of each analysis discipline is explained.

Table 4.1 Static design variables of the TSTO RLV with PCTJ engines.

		Parameter	Unit	Associated constraints
Vehicle design	Booster	Length of the fuselage, b_l	m	$30 \leq b_\mathrm{l} \leq 80$
		Height of the upper fuselage, b_h	m	$0.01 \leq b_\mathrm{h}/b_\mathrm{l} \leq 0.05$
		Length of the forebody, b_lf	m	$0.3 \leq b_\mathrm{lf}/b_\mathrm{l} \leq 0.6$
		Width of the forebody tip, b_wf	m	$0.5 \leq b_\mathrm{wf}/(6e_\mathrm{h}) \leq 1.0$
		Root chord length of the exposed wing, w_chrd	m	$0.1 \leq w_\mathrm{chrd}/b_\mathrm{l} \leq 0.5$
		Sweepback of the wing leading edge, w_Λ	deg	$45 \leq w_\Lambda \leq 70$
		(Forward, Backward) end of the LOX tank, $(t_\mathrm{lo0}, t_\mathrm{lof})$	m	$5.0 \leq t_\mathrm{lo0} \leq t_\mathrm{lof}$
		(Forward, Backward) end of the LH2 tank, $(t_\mathrm{lh0}, t_\mathrm{lhf})$	m	$t_\mathrm{lof} + 0.5 \leq t_\mathrm{lh0} \leq t_\mathrm{lhf} \leq b_\mathrm{l} - 0.5$
		Height of PCTJ engines, e_h	m	$0.2 \leq (8e_\mathrm{h} + 1)/b_\mathrm{l} \leq 0.5$
		LH2/LOX rocket engine vacuum thrust per unit, $T_\mathrm{rclh,v}$	kN	–
	Orbiter	Length of the fuselage, o_l	m	$10 \leq o_\mathrm{l} \leq 30$
		Backward end of the cabin, cb_f	m	$0.25 \leq cb_\mathrm{f}/o_\mathrm{l} \leq 0.9$
		Ethanol/LOX rocket engine vacuum thrust, $T_\mathrm{rcea,v}$	kN	–
Vehicle performance	Booster	Maximum axial acceleration, $aa^{(\mathrm{b})}_\mathrm{max}$	G	–
		Maximum normal load factor, $lf^{(\mathrm{b})}_\mathrm{max}$	G	–
		Maximum dynamic pressure, $q^{(\mathrm{b})}_\mathrm{max}$	kPa	$q^{(\mathrm{b})}_\mathrm{max} \leq 50$
		Maximum exerted thrust, $T^{(\mathrm{b})}_\mathrm{max}$	kN	–
		Gross mass, $m^{(\mathrm{b})}_\mathrm{gross}$	t	–
	Orbiter	Maximum axial acceleration, $aa^{(\mathrm{o})}_\mathrm{max}$	G	–
		Maximum normal load factor, $lf^{(\mathrm{o})}_\mathrm{max}$	G	$2.5 \leq lf^{(\mathrm{o})}_\mathrm{max}$
		Maximum dynamic pressure, $q^{(\mathrm{o})}_\mathrm{max}$	kPa	$q^{(\mathrm{o})}_\mathrm{max} \leq 50$
		Maximum exerted thrust, $T^{(\mathrm{o})}_\mathrm{max}$	kN	–
		Gross mass, $m^{(\mathrm{o})}_\mathrm{gross}$	t	–

4.2.1 Vehicle Geometry Definition and Mass Property Analysis

In this analysis discipline, geometric design of the booster and the orbiter is defined by some design variables. Then, the dry mass of the vehicles, volume of the tanks, and center of mass of the vehicles and propellants are calculated.

Figure 4.2 presents basic configurations of the vehicles and describes how geometries of the airframe, tanks, and engines are specified by the design variables. In addition to the constraints enumerated in Table 4.1, some inequality constraints are imposed so that the vehicle geometries are determined successfully. The booster has a lifting-body configuration with six PCTJ engines installed on its fuselage undersurface. Airfoils of main wing and tail wings are NACA0005, and the taper ratio of the main wing is fixed at 0.15. 90 % exposed span from the wing tips and 30 % chord from the trailing edge of the main wing are used as elevons. Right and left elevons are deflected in the same direction and angle (positive downward) to serve as elevators. Platforms of the tail wings are scaled so that their total area equals to 10 % of the main wing area. An integral tank of liquid oxygen (LOX) and that of liquid hydrogen (LH2)

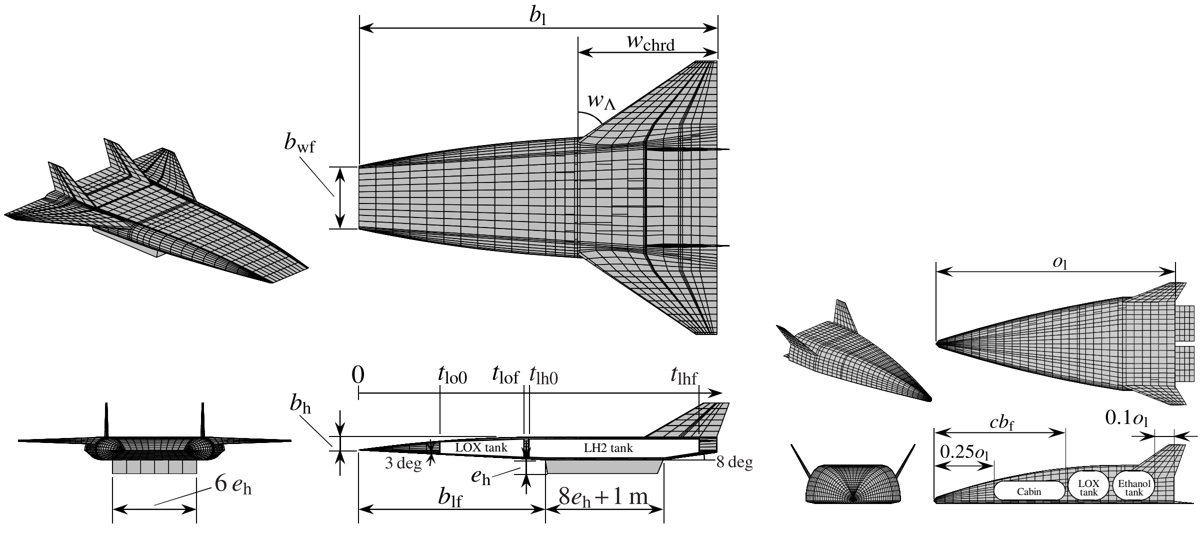

(a) Booster. (b) Orbiter.

Fig. 4.2 Basic configuration and design parameters of vehicles.

are inside the fuselage. The total inlet flow capture area of the PCTJ engines is given by

$$S_{\mathrm{capt}} = 6{e_{\mathrm{h}}}^2. \tag{4.4}$$

As for the orbiter, the vehicle shape is adopted based on Ref. 3 as shown in Fig. 4.2b. Airframe geometry optimization is not conducted, and rather, only scaling is performed. The orbiter is loaded onto the uppersurface of the booster fuselage at such a position that the center of the mass does not move in the axial direction between just before and just after the staging. A constraint on the width of the booster fuselage and that of the orbiter is enforced in order to guarantee the mountability of the orbiter.

Mass property of the vehicles, tank volumes, and accomodated payload mass are computed based on the procedures explained in Appendix E. Inputs to the mass-property model include vehicle geometric parameters such as wetted area, maximum loads such as maximum dynamic pressure during the flight, and gross mass. These input values are present in or calculated from the design variables. The resultant gross mass (i.e., the summation of the calculated dry mass and propellant mass before takeoff) must be consistent with the corresponding gross mass value included in the design variables. This consistency is enforced as one of the constraints in the MDO problem.

4.2.2 Aerodynamic Analysis

In this analysis discipline, aerodynamic characteristics of the booster, the orbiter, and their mated configuration are calculated when a vehicle shape and flight conditions are specified.

Engineering-level CFD methods explained in Appendix C are utilized. In this section, the interaction between airframe and propulsion is ignored, and hence the aerodynamic coeffcients are calculated without considering external nozzle effects. A rationale for neglecting the airframe-propulsion interaction is that, the effects of the forebody pre-compression and the external nozzle are relatively small in the PCTJ engines compared to ramjet or scramjet engines.

Surrogate models for the aerodynamic analysis of the booster are constructed, and they are substituted for the original analysis during optimization computation in order to mitigate the computational burden and to enhance the numerical stability. The surrogate model is also known as a metamodel or a response surface, and it imitates the input-output relation of the original analysis model by means of relatively simple functions. First, let the lift coefficient, $C_{L\mathrm{b}}$, the drag coefficient, $C_{D\mathrm{b}}$, and the pitching moment coefficient around the reference point, $C_{M\mathrm{b}}$, be approximated as second-order polynomials in terms of angle of attack, α, and elevon deflection angle, δ, as follows:

$$C_{L\mathrm{b}} = a_L^{(0,0)} + a_L^{(1,0)}\alpha + a_L^{(2,0)}\alpha^2 + a_L^{(0,1)}\delta + a_L^{(0,2)}\delta^2, \tag{4.5}$$

$$C_{D\mathrm{b}} = a_D^{(0,0)} + a_D^{(1,0)}\alpha + a_D^{(2,0)}\alpha^2 + a_D^{(0,1)}\delta + a_D^{(0,2)}\delta^2, \tag{4.6}$$

$$C_{M\mathrm{b}} = a_M^{(0,0)} + a_M^{(1,0)}\alpha + a_M^{(2,0)}\alpha^2 + a_M^{(0,1)}\delta + a_M^{(0,2)}\delta^2. \tag{4.7}$$

These polynomial response surfaces are constructed using the least squares fit of the responses at the representative combinations of α and δ (5 cases) shown in Table 4.2. Here, the polynomial coefficients, $a_{\{\cdot\}}^{(0,0)}, \ldots, a_{\{\cdot\}}^{(0,2)}$, are the functions of flight Mach number and vehicle design variables concerning aerodynamics. Surrogate models of these coefficients are created using radial basic function (RBF) networks[76] with multiquadric basis for Mach number and with Gaussian basis for the vehicle design variables. In order to train the RBF network surrogate models, 200 sample points are made via a design-of-experiments algorithm developed in Ref. 14. This is a variant of space-filling designs, and it generates sample points that uniformly fill the constrained design space. In addition to these sample points, 200 test points for the cross-validation are prepared using random sampling. Fitting parameters in the surrogate models are optimized based on the input/response relations at the sample and test points using simulated annealing. These procedures yield surrogate models whose coefficients of determination are 0.9918 on average and 0.9481 in the worst case, which is an acceptable prediction error. The coefficient of determination is defined by the mean square error of the surrogate model at test points normalized by the response variance, subtracted from unity or 1.

Table 4.2 Flow conditions in aerodynamic analysis.

Parameter(s)	Sample values	Unit
Mach number	0.2, 0.6, 0.9, 1.2, 3.0, 5.0, 7.0, 10.0, 15.0	–
($\alpha^*, \delta^\dagger$)	(0, 0), (5, 0), (10, 0), (5, -10), (5, 10)	(deg, deg)

* Angle of attack.

† Elevon deflection as an elevator (positive downward).

4.2.3 Propulsion Analysis

In the propulsion analysis, thrust and specific impulse of PCTJ engines and those of rocket engines are calculated when the engine design and flight conditions are provided.

LH2-fueled PCTJ engines, whose images are illustrated in Fig. 4.3, are installed on the booster. The performance of the PCTJ engines is evaluated based on tabular data provided by JAXA[9]. In this tabular data, thrust magnitude per unit inlet area, $C_{T,\mathrm{pctj}}$, and specific impulse, Isp_{pctj}, are defined as the functions of flight altitude and Mach number. On the basis of it, the following polynomial approximation models are constructed:

$$C_{T,\mathrm{pctj}} = \exp\left[c_1(Ma)\cdot h + c_2(Ma)\right], \tag{4.8}$$

$$Isp_{\mathrm{pctj}} = d_1(h)\cdot Ma + d_2(h), \tag{4.9}$$

where h indicates flight altitude, and Ma denotes flight Mach number. $c_1(\cdot)$, $c_2(\cdot)$, $d_1(\cdot)$, and $d_2(\cdot)$ are univariate RBF network models with multiquadric basis, and they are built based on the tabular data. The outputs of these approximation models are presented in Fig. 4.4. The total thrust of the PCTJ engines, T_{pctj}, is given by

$$T_{\mathrm{pctj}} = C_{T,\mathrm{pctj}}\, S_{\mathrm{capt}}. \tag{4.10}$$

It is assumed that the PCTJ engines are operated from the takeoff run, and the operation is stopped before arriving at the Mach number limit of 6.0. Then, six rocket engines with LH2/LOX propellants mounted on the fuselage base of the booster are ignited immediately. Their vacuum specific impulse, $Isp_{\mathrm{rclh,v}}$, and oxidizer-to-fuel mass mixture ratio, $(O/F)_{\mathrm{rclh}}$, are 440 s and 6.03, respectively. Effective thrust, T_{rclh}, and effective specific impulse, Isp_{rclh}, of the rocket engines are computed considering the effect of atmospheric pressure as follows[14, pp. 84, 85]:

$$T_{\mathrm{rclh}} = T_{\mathrm{rclh,v}}\,(1 - 1.9372\times 10^{-6}\, p), \tag{4.11}$$

$$Isp_{\mathrm{rclh}} = Isp_{\mathrm{rclh,v}}\,(1 - 1.9372\times 10^{-6}\, p), \tag{4.12}$$

where p is the atmospheric pressure at the flight altitude in Pa. Optimization of the size of the rocket

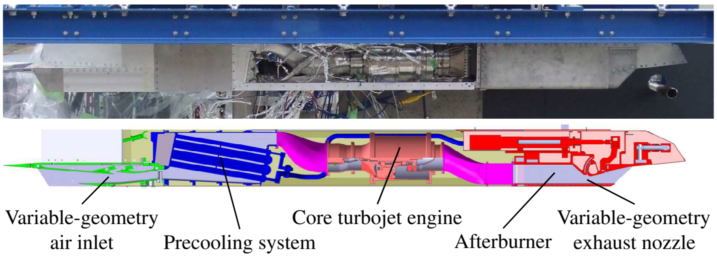

Fig. 4.3 Images of a PCTJ engine (from Ref. 10 with some modifications).

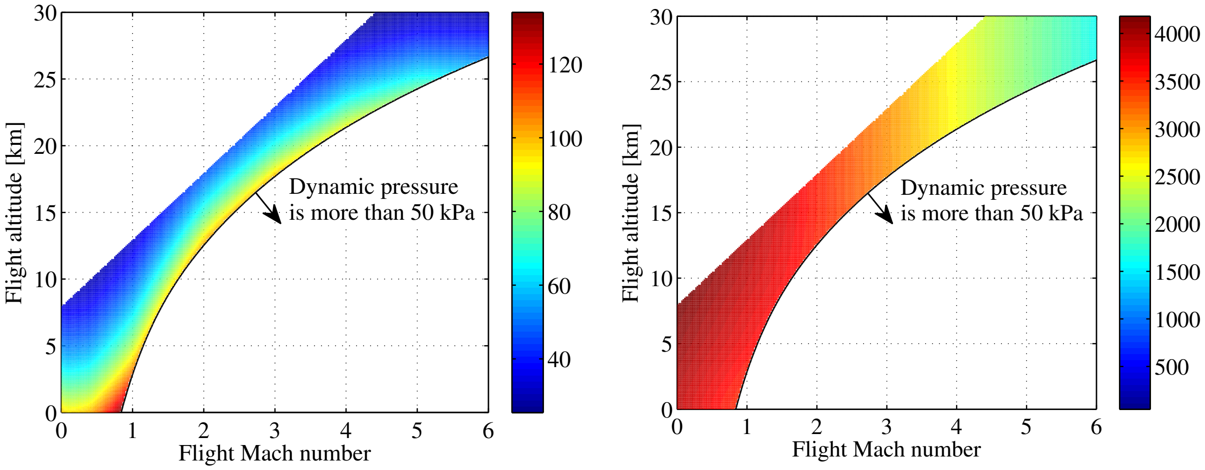

(a) Thrust magnitude per unit inlet area [kN/m^2].

(b) Specific impulse [s].

Fig. 4.4 Performance model of the PCTJ engine.

engines are performed considering their geometric mountability on the fuselage base in the following way[14, p. 85]:

$$\text{(Width of the fuselage base)} \geq D_{\text{rc}}\, N_{\text{rclh}}, \tag{4.13}$$

$$\text{(Height of the fuselage base)} \geq D_{\text{rc}}, \tag{4.14}$$

where N_{rclh} denotes the number of the engine units, and D_{rc} is the diameter of the engine unit given by

$$D_{\text{rc}} = \sqrt{2.771 \times 10^{-3}\, \frac{4}{\pi}\, T_{\text{rclh,v}}\ \text{[kN]}}\ \text{[m]}. \tag{4.15}$$

After the staging, the orbiter is propelled by a rocket engine installed on its fuselage base. Ethanol fuel and LOX are employed, and vacuum specific impulse, $Isp_{\text{rcea,v}}$, and oxidizer-to-fuel mass mixture ratio, $(O/F)_{\text{rcea}}$, are 320 s and 1.6, respectively[3]. Effective thrust and effective specific impulse of the rocket engine (T_{rcea} and Isp_{rcea}) are computed using Eqs. (4.11, 4.12) as well. It is assumed that the thrust of the rocket engines on the booster and the orbiter can be throttled between 50 % and 100 % without affecting their specific impulse values.

4.2.4 Flight Trajectory Analysis

System Dynamics

In the flight trajectory analysis, it is assumed that the trajectory is restricted to a vertical plane, and 2-degree-of-freedom vehicle dynamics is employed. The influence of the rotation of the Earth is not considered for the sake of simplicity. On the basis of the variable definitions provided in Table 4.3, the state equations are described as follows:

For the mated vehicle

$$\dot{v} = \frac{(T_{\mathrm{pctj}} + T_{\mathrm{rclh}} N_{\mathrm{rclh}} \tau \cos \delta_{\mathrm{r}}) \cos \alpha - (D_{\mathrm{m}} + T_{\mathrm{rclh}} N_{\mathrm{rclh}} \tau \sin \delta_{\mathrm{r}} \sin \alpha)}{m} - \frac{\mu}{r^2} \sin \gamma, \tag{4.16}$$

$$\dot{\gamma} = \frac{(L_{\mathrm{m}} + T_{\mathrm{rclh}} N_{\mathrm{rclh}} \tau \sin \delta_{\mathrm{r}} \cos \alpha) + (T_{\mathrm{pctj}} + T_{\mathrm{rclh}} N_{\mathrm{rclh}} \tau \cos \delta_{\mathrm{r}}) \sin \alpha}{mv} + \left(\frac{v}{r} - \frac{\mu}{vr^2} \right) \cos \gamma, \tag{4.17}$$

$$\dot{h} = v \sin \gamma, \tag{4.18}$$

$$\dot{m}_{\mathrm{lh}} = -\frac{T_{\mathrm{pctj}}}{g_0 Isp_{\mathrm{pctj}}} - \frac{T_{\mathrm{rclh}} N_{\mathrm{rclh}} \tau}{g_0 Isp_{\mathrm{rclh}}} \frac{1}{(O/F)_{\mathrm{rclh}} + 1}, \tag{4.19}$$

$$\dot{m}_{\mathrm{lo}} = -\frac{T_{\mathrm{rclh}} N_{\mathrm{rclh}} \tau}{g_0 Isp_{\mathrm{rclh}}} \frac{(O/F)_{\mathrm{rclh}}}{(O/F)_{\mathrm{rclh}} + 1}, \tag{4.20}$$

For the orbiter

$$\dot{v} = \frac{T_{\mathrm{rcea}} \tau \cos \alpha - D_{\mathrm{o}}}{m} - \frac{\mu}{r^2} \sin \gamma, \tag{4.21}$$

$$\dot{\gamma} = \frac{L_{\mathrm{o}} + T_{\mathrm{rcea}} \tau \sin \alpha}{mv} + \left(\frac{v}{r} - \frac{\mu}{vr^2} \right) \cos \gamma, \tag{4.22}$$

$$\dot{h} = v \sin \gamma, \tag{4.23}$$

$$\dot{m}_{\mathrm{ea}} = -\frac{T_{\mathrm{rcea}} \tau}{g_0 Isp_{\mathrm{rcea}}} \frac{1}{(O/F)_{\mathrm{rcea}} + 1}, \tag{4.24}$$

$$\dot{m}_{\mathrm{lo}} = -\frac{T_{\mathrm{rcea}} \tau}{g_0 Isp_{\mathrm{rcea}}} \frac{(O/F)_{\mathrm{rcea}}}{(O/F)_{\mathrm{rcea}} + 1}, \tag{4.25}$$

where

$$r = h + R_{\mathrm{e}}. \tag{4.26}$$

It is noted that subscripts $(\cdot)_{\mathrm{m}}$ and $(\cdot)_{\mathrm{o}}$ indicate that the attached variables are aerodynamic forces of the mated vehicle and those of the orbiter alone, respectively, as explained in Appendix C.2.

Atmosphere Model

A static atmosphere model is built based on U. S. standard atmosphere 1976[91]. A set of relations for calculating various atmospheric quantities is presented for each atmospheric layer in the standard atmosphere model. Since these sets of relations are not necessarily smoothly connected at the interfaces of adjacent layers, smooth models are constructed by interpolating the values at some sampled altitudes using natural cubic spline. The constructed models are shown in Fig. 4.5.

Flight Plan

Flight phases on which the trajectory analysis is conducted are as follows:

1) Horizontal takeoff phase

The mated vehicle takes off horizontally from a runway at sea level. No particular launch site is

Table 4.3 Variables and constants used in the trajectory analysis.

Symbol	Description
h	Altitude
v	Velocity
γ	Flight path angle
m	Vehicle mass
m_{lh}	Mass of remaining liquid hydrogen
m_{lo}	Mass of remaining liquid oxygen
m_{eaf}	Mass of remaining ethanol in the booster fore tank
m_{eaa}	Mass of remaining ethanol in the booster after tank
m_{ea}	Mass of remaining ethanol in the orbiter tank
$\dot{m}_{\mathrm{dump}}$	Mass rate of dumped ethanol
α	Angle of attack
δ_{r}	Thrust deflection angle of the rocket gimbal
τ	Throttling parameter
η	Consumption ratio of the fore ethanol fuel tank
r	Distance from the center of the Earth
R_{e}	Radius of the Earth (= 6.378×10^6 m)
μ	Standard gravitational parameter of the Earth (= 3.986×10^{14} $\mathrm{m}^3/\mathrm{s}^2$)
g_0	Gravitational acceleration at mean sea level (= 9.80665 m/s^2)

assumed in the present study. The takeoff is conducted with full-throttled PCTJ engines and 15 deg angle of attack. The following takeoff analysis[92, 14, pp. 158, 159] is conducted, and takeoff velocity, v_{to}, takeoff distance (ground roll), l_{to}, and the mass of propellants consumed during the takeoff phase, $m_{\mathrm{prop,to}}$, are computed:

$$\dot{\gamma} = \frac{L_{\mathrm{m}} + T \sin(15\pi/180)}{(m_{\mathrm{gross}} - m_{\mathrm{prop,to}})\, v_{\mathrm{to}}} + \left(\frac{v_{\mathrm{to}}}{r} - \frac{g_0}{v_{\mathrm{to}}}\right) \cos\gamma \geq 0, \tag{4.27}$$

$$l_{\mathrm{to}} = -\frac{1}{2k_a} \log\left(1 - \frac{k_a}{k_t} v_{\mathrm{to}}^2\right) + 3v_{\mathrm{to}}, \tag{4.28}$$

$$m_{\mathrm{prop,to}} = \frac{T_{\mathrm{acc}}}{Isp_{\mathrm{acc}}\, g_0} \frac{1}{2\sqrt{k_t\, k_a}} \log\left(\frac{\sqrt{k_t} + \sqrt{k_a} v_{\mathrm{to}}}{\sqrt{k_t} - \sqrt{k_a} v_{\mathrm{to}}}\right), \tag{4.29}$$

where

$$k_t = \frac{T_{\mathrm{acc}}}{m_{\mathrm{gross}}} - 0.03\, g_0, \tag{4.30}$$

$$k_a = \frac{D_{\mathrm{m,acc}}}{m_{\mathrm{gross}}\, v_{\mathrm{acc}}^2}. \tag{4.31}$$

Here, v_{acc} indicates the representative takeoff-roll speed defined as $v_{\mathrm{acc}} = v_{\mathrm{to}}/\sqrt{2}$. T_{acc} and $D_{\mathrm{m,acc}}$

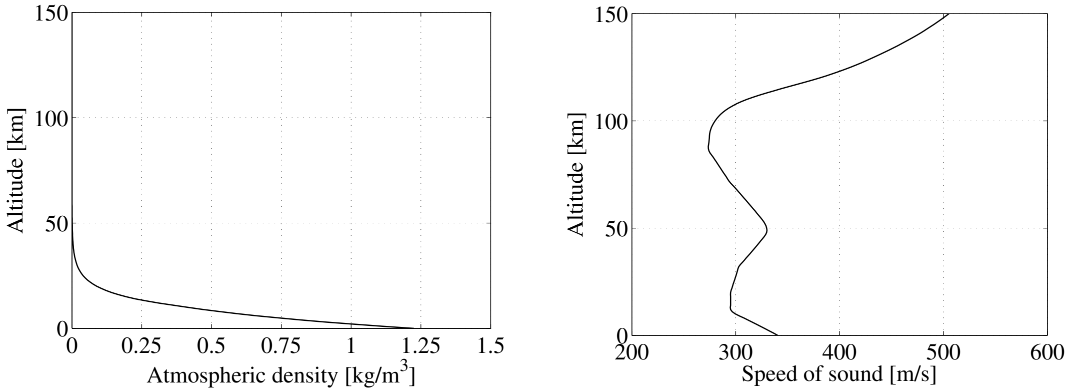

(a) Atmospheric density.

(b) Speed of sound.

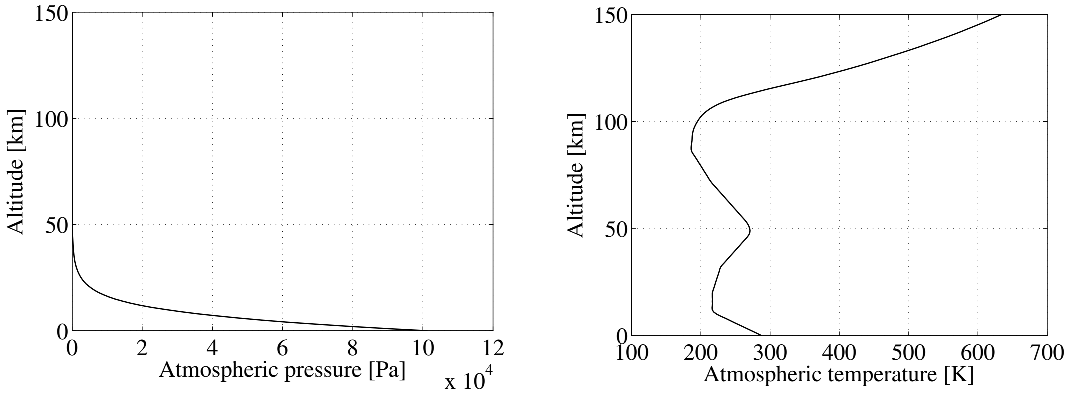

(c) Atmospheric pressure.

(d) Atmospheric temperature.

Fig. 4.5 Static atmosphere model.

refer to thrust and drag force acting on the mated vehicle when $v = v_{\mathrm{acc}}$, respectively.

2) Mated vehicle ascent phase

The mated vehicle is accelerated by PCTJ engines after the takeoff, and they are taken over by LH2/LOX rocket engines on the booster below Mach 6.0. The rocket engine mounted on the orbiter is not used in this phase. Angle of attack, elevon deflection angle, and thrust deflection angle of the rocket engines are bounded as follows:

$$-5 \text{ deg} \leq \alpha \leq 15 \text{ deg}, \tag{4.32}$$

$$-10 \text{ deg} \leq \delta \leq 10 \text{ deg}, \tag{4.33}$$

$$-15 \text{ deg} \leq \delta_{\mathrm{r}} \leq 15 \text{ deg}. \tag{4.34}$$

Elevon deflection angle is limited, because a large deflection can lead to flow separation and reattachment, causing locally high heat flux and elevon effectiveness loss. Axial acceleration, normal load factor, dynamic pressure, and exerted thrust must not exceed the corresponding design limits (see Table 4.1), that is

$$aa(t) \leq aa_{\max}^{(\mathrm{b})} \qquad \text{and} \qquad aa(t) \leq aa_{\max}^{(\mathrm{o})}, \tag{4.35}$$

$$lf(t) \le lf_{\mathrm{max}}^{(\mathrm{b})} \quad \text{and} \quad lf(t) \le lf_{\mathrm{max}}^{(\mathrm{o})}, \tag{4.36}$$

$$\frac{1}{2}\rho v^2 \le q_{\mathrm{max}}^{(\mathrm{b})} \quad \text{and} \quad \frac{1}{2}\rho v^2 \le q_{\mathrm{max}}^{(\mathrm{o})}, \tag{4.37}$$

$$T_{\mathrm{pctj}} + T_{\mathrm{rclh}}\, N_{\mathrm{rclh}} \le T_{\mathrm{max}}^{(\mathrm{b})}, \tag{4.38}$$

where $aa(\cdot)$ and $lf(\cdot)$ denote the axial acceleration and normal load factor, respectively. Since a manned vehicle is assumed, total acceleration $\left[= \sqrt{aa(t)^2 + lf(t)^2}\right]$ is restricted up to 4.0 G maximum. At the terminus of this flight phase, the orbiter is separated from the booster.

3) Orbiter ascent phase

The ethanol/LOX rocket engine on the orbiter is ignited immediately after the staging. Angle of attack is bounded as follows:

$$0 \text{ deg} \le \alpha \le 30 \text{ deg}. \tag{4.39}$$

Axial acceleration, normal load factor, dynamic pressure, and thrust must not exceed their corresponding design limits for the orbiter:

$$aa(t) \le aa_{\mathrm{max}}^{(\mathrm{o})}, \tag{4.40}$$

$$lf(t) \le lf_{\mathrm{max}}^{(\mathrm{o})}, \tag{4.41}$$

$$\frac{1}{2}\rho v^2 \le q_{\mathrm{max}}^{(\mathrm{o})}, \tag{4.42}$$

$$T_{\mathrm{rcea}} \le T_{\mathrm{max}}^{(\mathrm{o})}. \tag{4.43}$$

The total acceleration is limited to no more than 4.0 G.

The trajectory computation based on the equations of motion is not performed after the orbiter reaches an altitude of 100 km or higher and the engine is cut off. The subsequent coasting trajectory is simulated via elliptic orbit equations (refer to, for example, Ref. 93) as follows:

$$r_{\mathrm{apo}} = a\,(1 + e), \tag{4.44}$$

$$v_{\mathrm{apo}} = \sqrt{\mu / r_{\mathrm{apo}}\,(1 - e)}, \tag{4.45}$$

where

$$H = r_{\mathrm{f}}\, v_{\mathrm{f}} \cos \gamma_{\mathrm{f}}, \tag{4.46}$$

$$E = v_{\mathrm{f}}^2/2 - \mu / r_{\mathrm{f}}, \tag{4.47}$$

$$e = \sqrt{2\,E\,H^2/\mu^2 + 1}, \tag{4.48}$$

$$a = -\mu/(2\,E). \tag{4.49}$$

The subscript $(\cdot)_{\mathrm{f}}$ denotes the final value in the trajectory computation based on the equations of

> motion, and r_{apo} and v_{apo} refer to the apogee elevation from the center of the Earth and the velocity at the apogee point, respectively. At the apogee of the coasting trajectory, the orbiter is accelerated again, and it is injected into a circular orbit at 350 km above sea level. The propellant mass needed for this apogee acceleration is calculated by approximating it as an impulsive acceleration whose specific impulse is 320 s. In addition to the propellant consumed during the orbit insertion, some propellant is reserved for an on-orbit operation and a de-orbit operation. The reserved propellant mass is calculated by assuming that the required velocity change in these operations is 250 m/s in total.

The return trajectory of the booster after the staging and that of the orbiter after de-orbit are not considered in this dissertation.

Rigid Body Characteristics of the Vehicle

During the mated vehicle ascent phase, a pitching trim condition and a longitudinal static stability condition are imposed in order to ensure the flyability of the vehicle. The trim condition is expressed as follows:

$$M_{\mathrm{tot}} := M_{\mathrm{arfr}} + M_{\mathrm{pctj}} + M_{\mathrm{rclh}} = 0. \tag{4.50}$$

Here,

$$\begin{aligned}
M_{\mathrm{arfr}} &= M_{\mathrm{m}} + (L_{\mathrm{m}} \cos\alpha + D_{\mathrm{m}} \sin\alpha)\,(x_{\mathrm{cg}} - x_{\mathrm{refb}}) + (L_{\mathrm{m}} \sin\alpha - D_{\mathrm{m}} \cos\alpha)\,(z_{\mathrm{cg}} - z_{\mathrm{refb}}), && (4.51)\\
M_{\mathrm{pctj}} &= T_{\mathrm{pctj}}\,(z_{\mathrm{cg}} - z_{\mathrm{pctj}}), && (4.52)\\
M_{\mathrm{rclh}} &= T_{\mathrm{rclh}} \left[(z_{\mathrm{cg}} - z_{\mathrm{rclh}}) \cos\delta_{\mathrm{r}} + (x_{\mathrm{cg}} - x_{\mathrm{rclh}}) \sin\delta_{\mathrm{r}}\right] && (4.53)
\end{aligned}$$

are the pitching moment produced by the airframe, that by the PCTJ engines, and that by the LH2/LOX rocket engines, respectively. x_{cg} is the axial position of the center of mass, and z_{cg} denotes the height of the center of mass. It should be noted that the pitching moment in the above equations is calculated about the center of mass, which moves during the flight. It is assumed that thrust of the PCTJ engines and that of the rocket engines are exerted at the center of mass of the corresponding engines (see Table E.2 in Appendix E.2). The pitching trim is attained by controlling elevon deflection angle during the PCTJ operation, and by changing thrust deflection angle during the rocket operation. In addition to the trim, the following longitudinal static stability condition is imposed until reaching Mach 8.0:

$$x_{\mathrm{cg}} \leq x_{\mathrm{np}}, \tag{4.54}$$

where x_{np} denotes the axial position of the longitudinal stability neutral point calculated in Appendix C.2.

4.3 Formulation of the Optimization Problem

On the basis of the above numerical models, the multi-objective MDO problem of the TSTO RLV with PCTJ engines is established. As mentioned in Section 1.2.1 and originally stated in Ref. 14, such an MDO architecture as shown in Fig. 4.1 can be formulated as an augmented optimal control problem. In order to describe the flight plan presented in Section 4.2.4, the optimal control problem is divided into five phases shown in Table 4.4. As a consequence, the multi-objective MDO problem is formulated as follows:

$$
\begin{aligned}
\text{find}\quad & \text{state variables, } \mathbf{x}^{(1)},\dots,\mathbf{x}^{(5)}, && (4.55)\\
& \text{control variables, } \mathbf{u}^{(1)},\dots,\mathbf{u}^{(5)}, && (4.56)\\
& \text{initial and terminal times, } t_0^{(1)}, t_\mathrm{f}^{(1)},\dots, t_0^{(5)}, t_\mathrm{f}^{(5)} && (4.57)\\
& \text{static variables shown in Table 4.1, } \mathbf{p} && (4.58)\\
\text{min.}\quad & F_1 := -0.02\, m_\mathrm{pay}\ [\mathrm{kg}] && (4.59)\\
& F_2 := 0.1\, m_\mathrm{gross}\ [\mathrm{t}] && (4.60)\\
& F_3 := 0.25\, v_\mathrm{to}\ [\mathrm{m/s}] && (4.61)\\
\text{s.t.}\quad & \text{simple bounds on objective values, Eqs. (4.1–4.3),} && (4.62)\\
& \text{constraints on static variables presented in Table 4.1,} && (4.63)\\
& \text{consistency condition on the vehicle gross mass explained in Section 4.2.1,} && (4.64)\\
& \text{state equations, Eqs. (4.16–4.20)} \qquad \text{for Phase 1–4,} && (4.65)\\
& \text{state equations, Eqs. (4.21–4.25)} \qquad \text{for Phase 5,} && (4.66)\\
& \text{path constraints presented in Section 4.2.4,} && (4.67)\\
& \text{initial and terminal conditions explained in Section 4.2.4,} && (4.68)\\
& \text{static pitching trim condition, Eq. (4.50)} \qquad \text{for Phase 1–4,} && (4.69)\\
& \text{longitudinal static stability condition, Eq. (4.54)} \qquad \text{for Phase 1–3,} && (4.70)\\
& \text{moutability of rocket engines on the booster base, Eqs. (4.13, 4.14),} && (4.71)\\
& \text{linkage conditions for the continuity of the state variables between adjacent phases.} && (4.72)
\end{aligned}
$$

The formulated multi-objective optimal control problem is solved using a numerical method developed in Chapter 2 with $d_\mathrm{tol} = 2.0$. Numerical models in the MDO problem and the multi-objective optimization methodology are implemented in MATLAB® 2007b with some time-consuming components (e.g., surrogate model evaluation) being coded in C++ MEX. For solving NLP problems, SNOPT[43,78], an off-the-shelf solver based on a sequential quadratic programming algorithm, is employed. The optimality tolerance (the allowed residual of the optimality condition) and the feasibility tolerance (the maximum allowed residual of constraints) are 10^{-6} and 10^{-8}, respectively. Computations are performed on a Windows® 7 machine with an Intel® Core™ i7-4930K CPU and 32 GB RAM.

Table 4.4 Definitions of optimal control phases in the MDO problem of the TSTO RLV with PCTJ engines.

Item	Phase 1	Phase 2
Flight phase	Mated vehicle ascent	Mated vehicle ascent
Propulsion	PCTJ engine	PCTJ engine
Flight Mach number, Ma	$Ma \leq 3.0$	$3.0 \leq Ma \leq 6.0$
Mated vehicle's aero. model	Model 1 (Fig. C.1a)	Model 2 (Fig. C.1b)
State, $\mathbf{x}$	$\mathbf{x}^{(1)} = [h, v, \gamma, m_{\mathrm{lh}}]$	$\mathbf{x}^{(2)} = [h, v, \gamma, m_{\mathrm{lh}}]$
Control, $\mathbf{u}$	$\mathbf{u}^{(1)} = [\alpha, \delta]$	$\mathbf{u}^{(2)} = [\alpha, \delta]$

Item	Phase 3	Phase 4
Flight phase	Mated vehicle ascent	Mated vehicle ascent
Propulsion	LH2/LOX rocket	LH2/LOX rocket
Flight Mach number, Ma	$Ma \leq 8.0$	$8.0 \leq Ma$
Mated vehicle's aero. model	Model 2 (Fig. C.1b)	Model 2 (Fig. C.1b)
State, $\mathbf{x}$	$\mathbf{x}^{(3)} = [h, v, \gamma, m_{\mathrm{lo}}, m_{\mathrm{lh}}]$	$\mathbf{x}^{(4)} = [h, v, \gamma, m_{\mathrm{lo}}, m_{\mathrm{lh}}]$
Control, $\mathbf{u}$	$\mathbf{u}^{(3)} = [\alpha, \delta_{\mathrm{r}}, \tau]$	$\mathbf{u}^{(4)} = [\alpha, \delta_{\mathrm{r}}, \tau]$

Item	Phase 5
Flight phase	Orbiter ascent
Propulsion	Ethanol/LOX rocket
Flight Mach number, Ma	–
Mated vehicle's aero. model	–
State, $\mathbf{x}$	$\mathbf{x}^{(5)} = [h, v, \gamma, m_{\mathrm{lo}}, m_{\mathrm{ea}}]$
Control, $\mathbf{u}$	$\mathbf{u}^{(5)} = [\alpha, \tau]$

4.4 Pareto Optimal Solutions

The specified termination condition of the multi-objective optimizer is satisfied after approximately 12-hour computation, and 260 solutions are obtained. Figures 4.6a and 4.6b depict these solutions in the three-dimensional objective space and their two-dimensional projection, respectively. In these figures, four representative Pareto optimal solutions are shown with emphasis: three extreme solutions and one intermediate solution. The validity of the employed multi-objective optimization technique is demonstrated by the fact that the obtained solutions are uniformly distributed on the bounded Pareto front, and that all the obtained solutions are nondominated. From Fig. 4.6a, it is qualitatively revealed that the three design objectives are conflicting with each other. Figure 4.6b visually explains that vehicle gross mass and payload mass are almost linearly correlated when the takeoff velocity is fixed. The payload mass fraction is increased by relaxing the takeoff-velocity constraint.

Specifications of the representative Pareto optimal solutions are summarized in Table 4.5. When the solution No. 4 is referred, its gross mass before the takeoff run is 412 t, and it is smaller than the maximum takeoff mass of An-225 aircraft* (600 t[94]). It may indicate that there is a realistic possibility in the horizontal takeoff of RLVs of this scale. Compared with historical supersonic aircraft, takeoff mass and takeoff velocity of the solution No. 4 are both larger than those of Concorde (181 t and 111 m/s, respectively[95]). It is also worth mentioning that a fully-reusable TSTO launch vehicle with ethanol-fueled rocket engines is currently investigated in JAXA, and its vertical lift-off mass is 788 t when the mission requirement is the transportation of an 800 kg payload[3]. Therefore, the PCTJ-powered RLV designed in the present study has a smaller gross mass. Of course, a simple comparison is rather meaningless since the underlying design assumptions and numerical models differ substantially.

Among the components of the booster vehicle, the PCTJ engines occupies the largest mass portion, followed by the landing gear and the fuselage. The optimized design limit of maximum dynamic pressure during the flight (i.e., $q_{\mathrm{max}}^{(\mathrm{b})}$ and $q_{\mathrm{max}}^{(\mathrm{o})}$) is 50 kPa, and it is on its allowable upper bound. It is because the improvement of the performance of the PCTJ engines due to higher dynamic pressure overweighs the resulting increase of the airframe mass.

Details of the vehicle design of the representative solutions are presented in Fig. 4.7 and Table 4.6. The solutions No. 1 and No. 2 are mainly distinguished by their payload mass and vehicle gross mass. Major differences in their optimal vehicle shapes are as follows:

1) The size of the orbiter relative to that of the booster is larger in the solution No. 1.
2) Larger PCTJ engines relative to the size of the booster are installed in the solution No. 1. As a consequence, the width-to-length ratio of the booster fuselage is larger in the solution No. 1.

A large main wing and a wide fuselage of the booster in the solution No. 3 enable the lowest takeoff velocity. Solution No. 4 is located somewhat near the center of the solution distribution, and it has

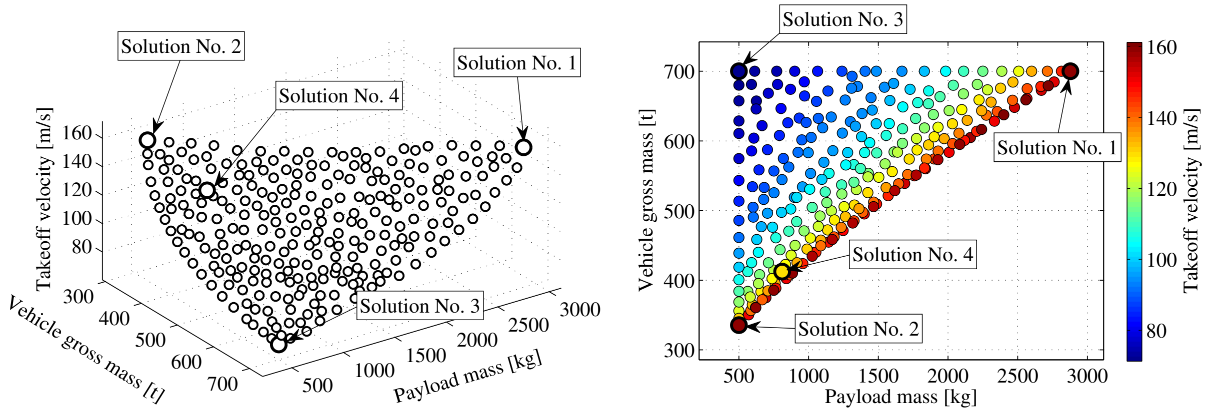

(a) Three-dimensional view. (b) Two-dimensional projection.

Fig. 4.6 Obtained solutions in the objective space.

---

*Antonov An-225 Mriya is the heaviest existing aircraft.

Table 4.5 Specifications of the representative Pareto optimal solutions.

Parameter		Unit	Solution No. 1		Solution No. 2		Solution No. 3		Solution No. 4	
			Booster	Orbiter	Booster	Orbiter	Booster	Orbiter	Booster	Orbiter
Payload mass		kg	2878.0		500.0		500.0		810.2	
Mated vehicle gross mass		t	700.0		335.5		700.0		412.4	
Takeoff velocity		m/s	159.0		159.2		71.3		129.1	
Maximum axial acceleration		G	2.0	2.0	2.2	2.2	2.1	2.1	2.2	2.2
Maximum load factor		G	1.0	2.5	1.0	2.5	1.0	2.5	1.0	2.5
Maximum dynamic pressure		kPa	50.0	50.0	50.0	50.0	50.0	50.0	50.0	50.0
Maximum exerted thrust		kN	6794.8	839.6	3677.5	342.2	8707.0	623.1	4716.8	468.8
Mass	Fuselage	t	30.0	6.0	18.4	2.4	41.2	3.1	19.1	3.1
	Main wing	t	14.9	0.0	7.1	0.0	45.9	0.0	11.3	0.0
	Tail wing	t	2.7	1.3	1.5	0.5	10.7	0.6	2.5	0.6
	Tanks	t	0.0	1.5	0.0	0.5	0.0	0.9	0.0	0.7
	Thermal protection system	t	11.2	4.7	6.7	2.0	24.0	2.5	8.1	2.5
	Landing gear	t	37.5	0.9	16.4	0.3	37.5	0.4	20.7	0.4
	PCTJ engines	t	91.2	0.0	49.9	0.0	106.6	0.0	63.3	0.0
	Rocket engines	t	11.4	1.1	6.1	0.5	14.5	0.8	7.9	0.6
	Thrust structure	t	4.4	2.1	2.4	0.9	5.6	1.6	3.0	1.2
	The others	t	12.1	4.3	7.4	2.3	13.0	3.1	8.4	2.8
	Dry gross	t	215.3	24.7	116.0	9.8	299.0	13.6	144.3	12.9
	LH2	t	156.9	0.0	72.8	0.0	161.9	0.0	85.5	0.0
	Ethanol	t	0.0	31.0	0.0	12.7	0.0	23.2	0.0	17.6
	LOX	t	222.4	49.6	103.9	20.3	165.2	37.0	124.0	28.1
	Gross	t	594.6	105.4	292.7	42.8	626.2	73.8	353.8	58.6

Table 4.6 Vehicle design of the representative Pareto optimal solutions.

Parameter		Unit	Solution No. 1	Solution No. 2	Solution No. 3	Solution No. 4
Booster	Fuselage length	m	65.0	54.9	75.5	51.9
	Fuselage upper height	m	1.6	1.1	2.0	1.4
	Forebody length	m	33.9	30.5	41.0	26.5
	Forebody tip width	m	14.6	9.8	10.8	11.2
	Exposed wing root chord length	m	16.9	13.7	37.7	18.4
	Wing leading edge sweepback	deg	50.9	55.2	45.0	54.7
	LOX tank ends (forward, backward)	m	(5.0, 15.9)	(5.0, 14.2)	(17.1, 21.5)	(5.0, 13.2)
	LH2 tank ends (forward, backward)	m	(16.4, 64.5)	(14.7, 54.4)	(45.4, 75.0)	(13.7, 51.4)
	Height of PCTJ engines	m	2.5	1.8	2.8	2.1
	Total rocket vacuum thrust	kN	6812.0	3686.2	8720.5	4726.9
Orbiter	Fuselage length	m	26.7	17.3	19.7	19.7
	Backward end of the cabin	m	17.7	9.3	9.0	11.0
	Rocket vacuum thrust	kN	839.6	342.2	623.1	468.8

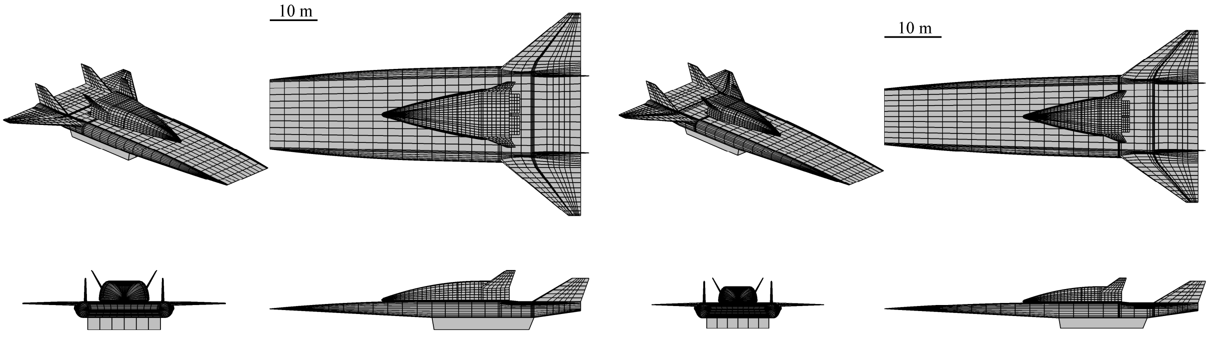

(a) Solution No. 1. (b) Solution No. 2.

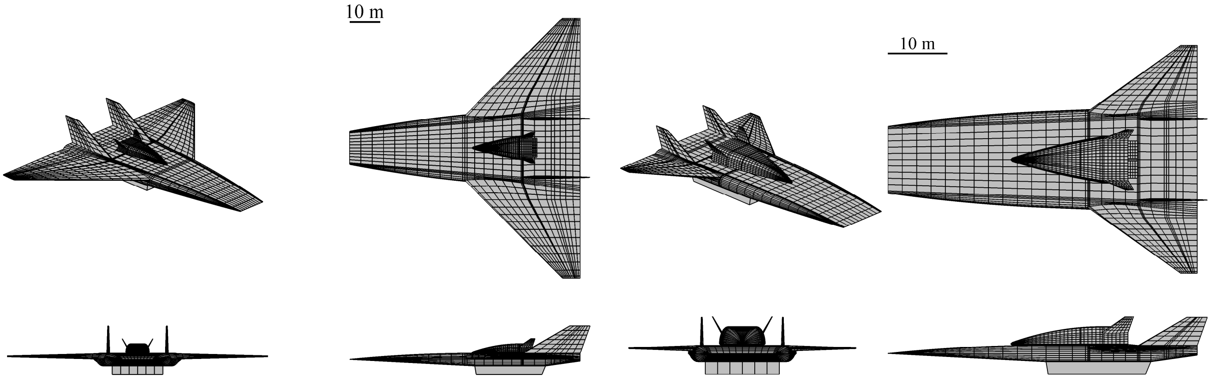

(c) Solution No. 3. (d) Solution No. 4.

Fig. 4.7 Vehicle shape of the representative Pareto optimal solutions.

intermediate characteristics between extreme solutions (i.e., solutions Nos. 1–3).

Time histories of the flight trajectories in the solutions Nos. 1–4 are shown in Figs. 4.8, 4.10, 4.12, and 4.14, respectively. The behavior of the trajectory in the solution No. 4 is explained in detail below. Vehicle thrust-to-mass ratio is 0.64 at the moment of takeoff. Flight path angle increases rapidly due to large angle of attack soon after the takeoff. Subsequently, the angle of attack becomes smaller, and flight path angle is decreased to a negative value. Such a dive maneuver often exits in an optimal flight trajectory of an RLV with airbreathing engines in order to overcome transonic drag rise efficiently, as reported in Ref. 16. After dynamic pressure reaches its upper bound, the angle of attack increases gradually so as to fly along the bound. The operation of the PCTJ engines stops at Mach 6.0, and then the rocket engines on the booster are ignited. During the rocket engine operation, the mated vehicle begins to climb steeply by increasing its angle of attack. When the orbiter is separated from the booster, Mach number and dynamic pressure are 11.7 and 2.5 kPa, respectively. The orbiter alone continues the steep climb and reaches an altitude above 100 km, which is followed by a slight descent. The rocket engines on the booster and on the orbiter are not throttled except a faint throttling around 930 s in order to prevent excessive acceleration. At the terminal time of the trajectory shown in Fig. 4.14, the orbiter is inserted into a coasting trajectory whose apogee altitude is 350 km above sea level. Flight trajectories

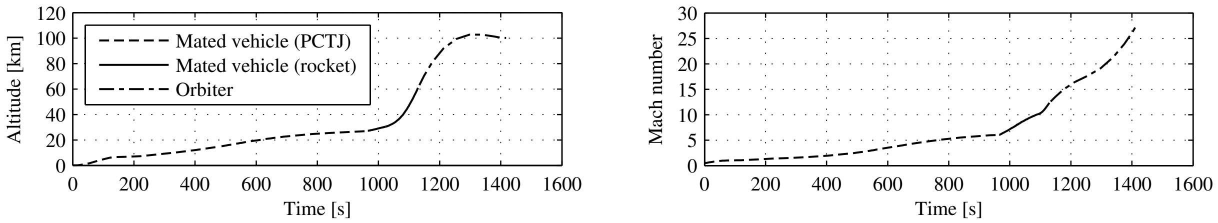

(a) Time history of altitude.

(b) Time history of Mach number.

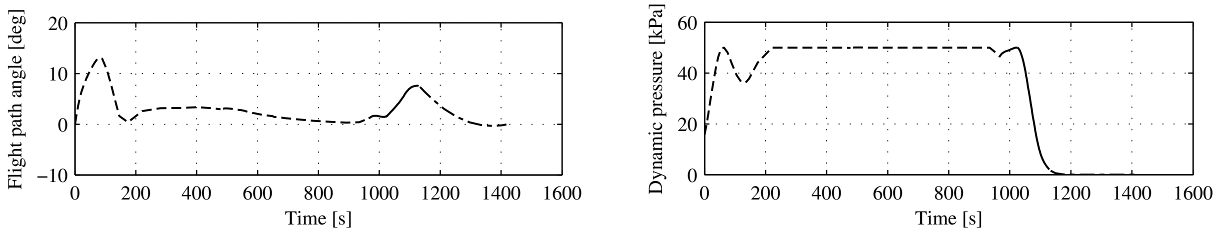

(c) Time history of flight path angle.

(d) Time history of dynamic pressure.

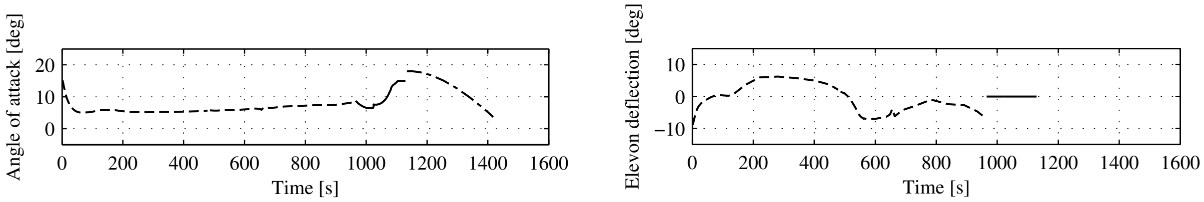

(e) Time history of angle of attack.

(f) Time history of elevon deflection angle.

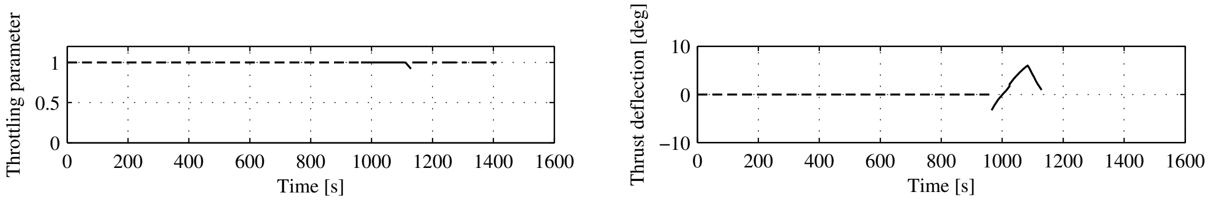

(g) Time history of thrust throttling parameter.

(h) Time history of thrust deflection angle.

Fig. 4.8 Flight trajectory of the solution No. 1.

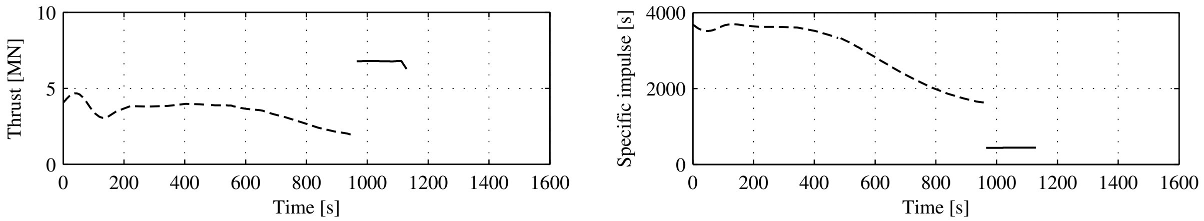

(a) Time history of thrust magnitude.

(b) Time history of specific impulse.

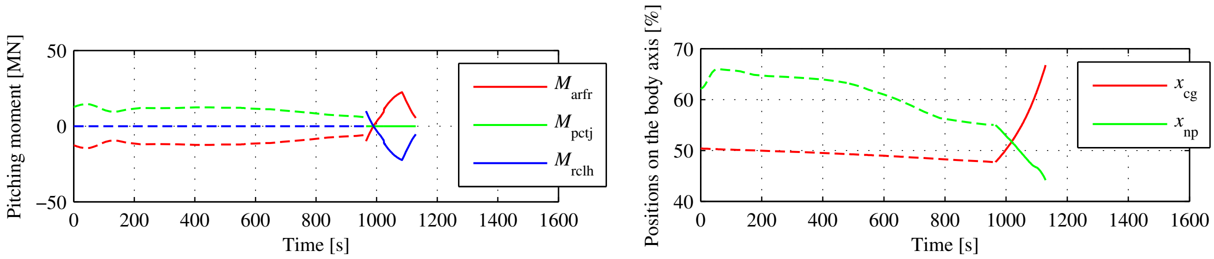

(c) Time history of pitching moment.

(d) Time history of center of mass and neutral point.

Fig. 4.9 Propulsion efficiency and rigid body characteristics of the solution No. 1.

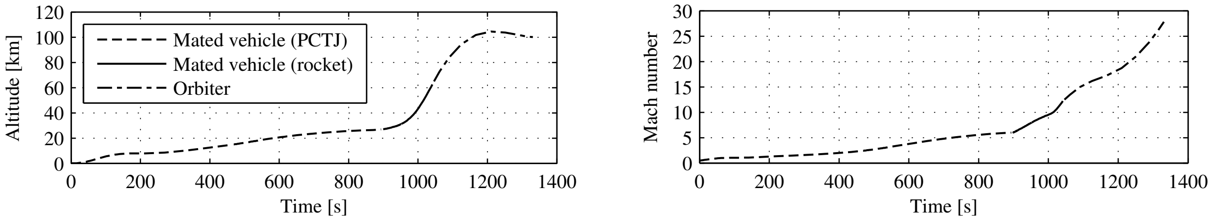

(a) Time history of altitude. (b) Time history of Mach number.

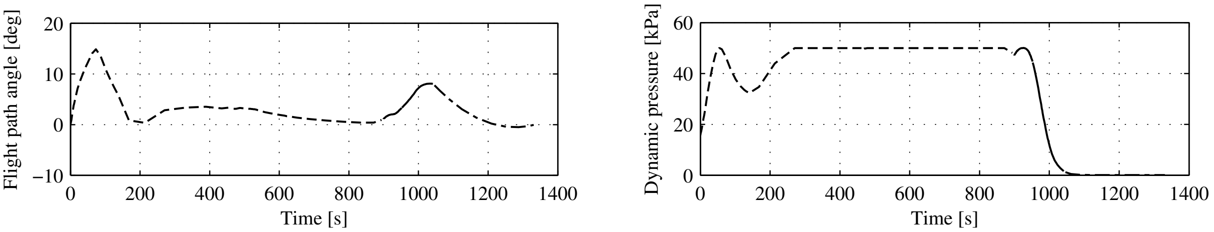

(c) Time history of flight path angle. (d) Time history of dynamic pressure.

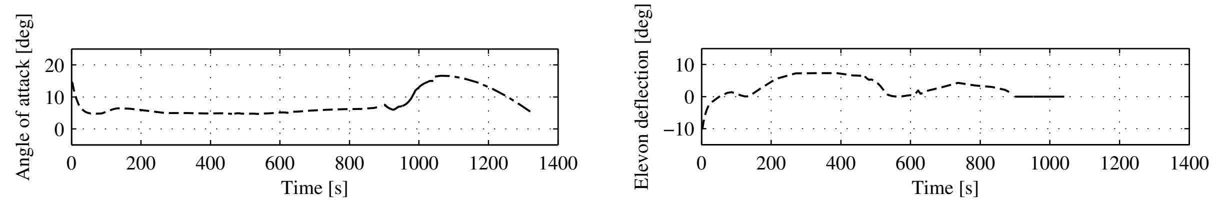

(e) Time history of angle of attack. (f) Time history of elevon deflection angle.

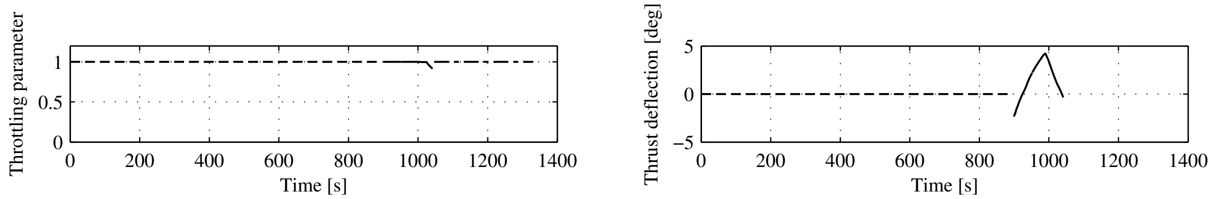

(g) Time history of thrust throttling parameter. (h) Time history of thrust deflection angle.

Fig. 4.10 Flight trajectory of the solution No. 2.

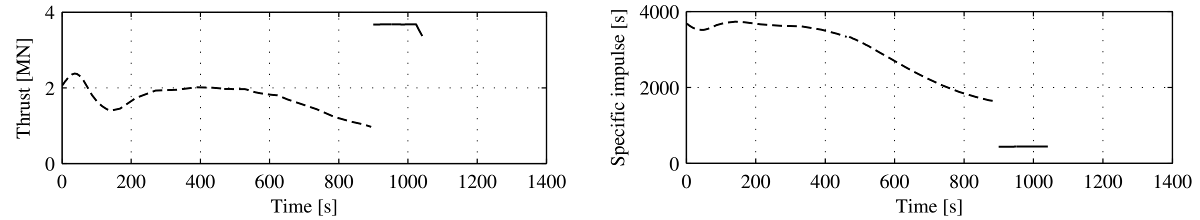

(a) Time history of thrust magnitude. (b) Time history of specific impulse.

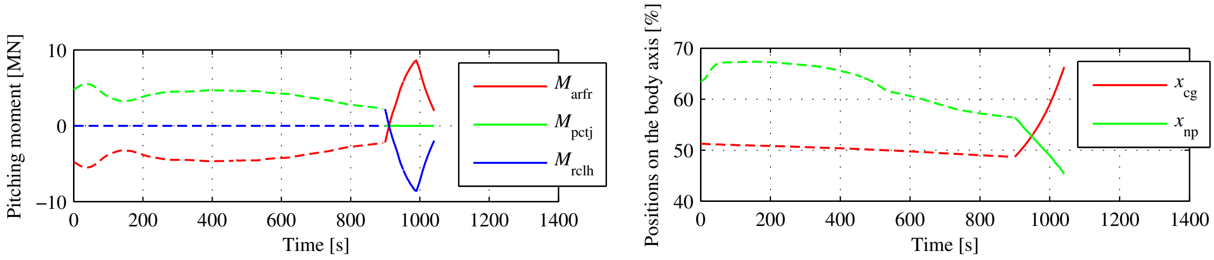

(c) Time history of pitching moment. (d) Time history of center of mass and neutral point.

Fig. 4.11 Propulsion efficiency and rigid body characteristics of the solution No. 2.

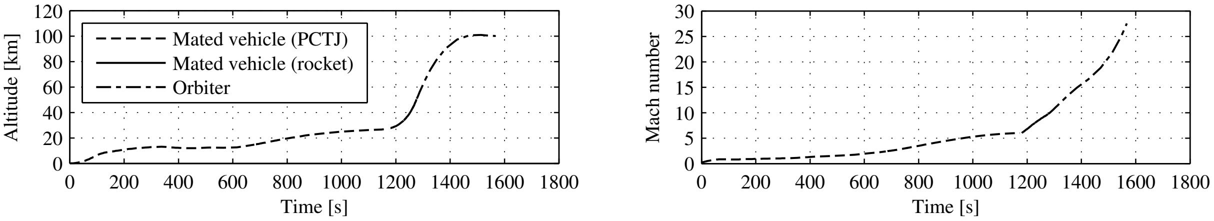

(a) Time history of altitude.

(b) Time history of Mach number.

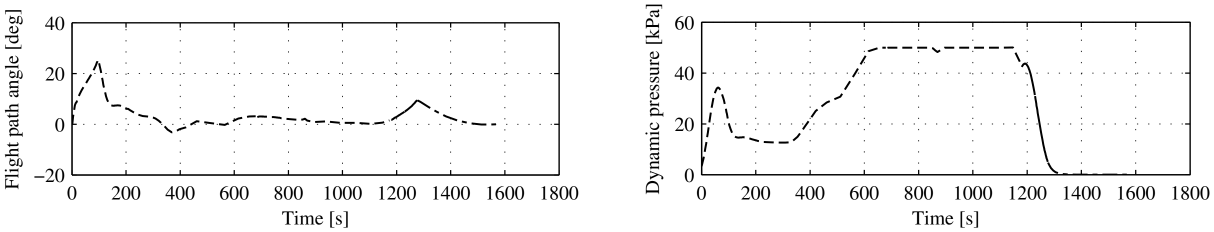

(c) Time history of flight path angle.

(d) Time history of dynamic pressure.

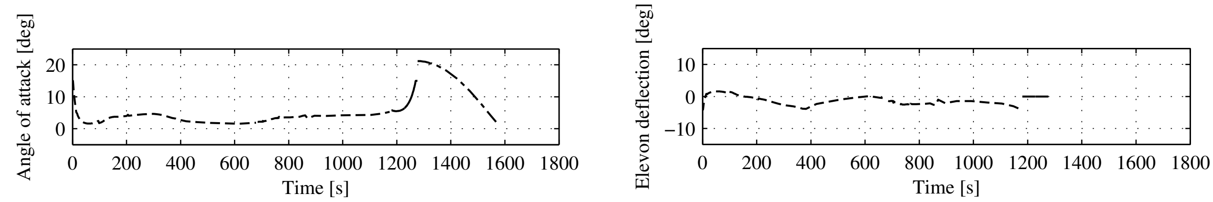

(e) Time history of angle of attack.

(f) Time history of elevon deflection angle.

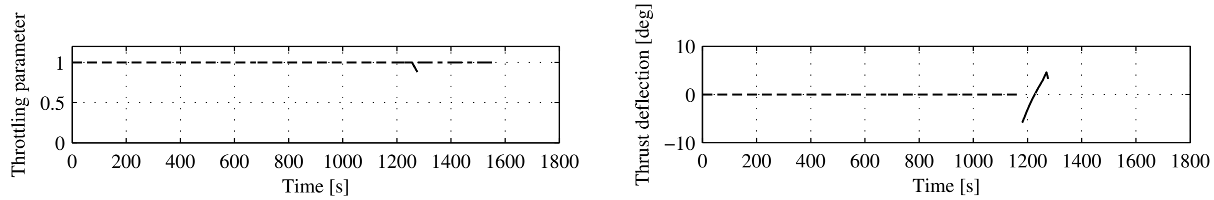

(g) Time history of thrust throttling parameter.

(h) Time history of thrust deflection angle.

Fig. 4.12 Flight trajectory of the solution No. 3.

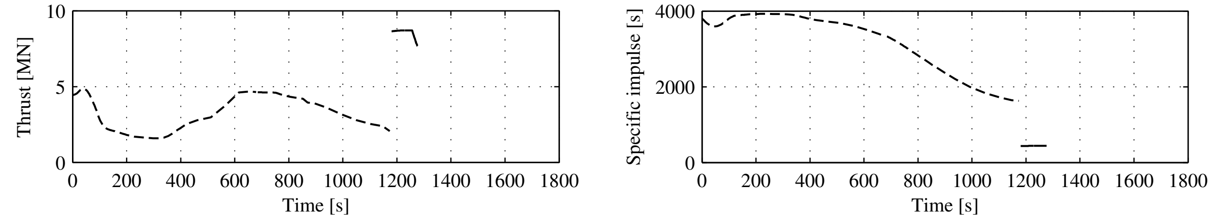

(a) Time history of thrust magnitude.

(b) Time history of specific impulse.

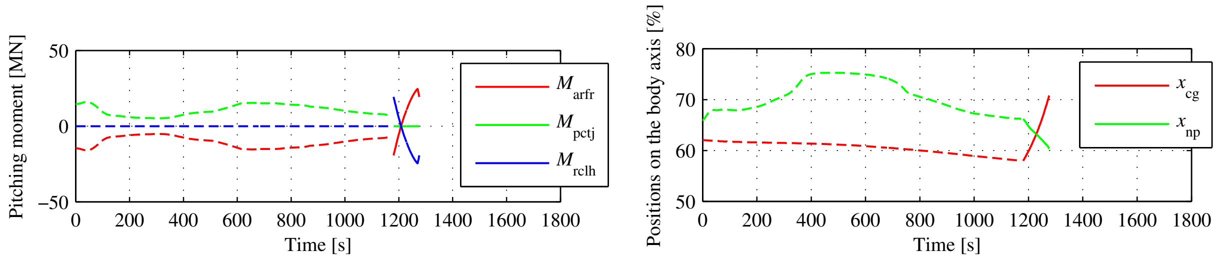

(c) Time history of pitching moment.

(d) Time history of center of mass and neutral point.

Fig. 4.13 Propulsion efficiency and rigid body characteristics of the solution No. 3.

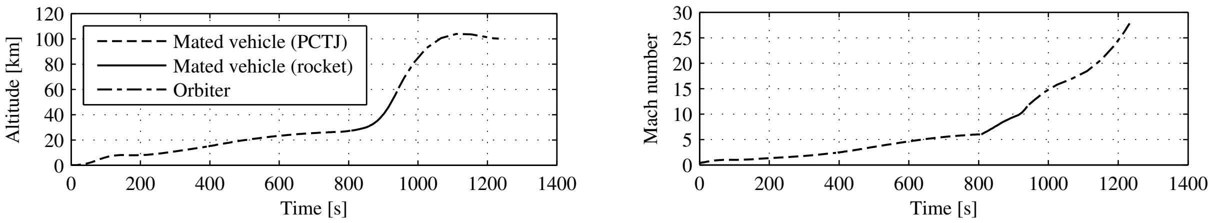

(a) Time history of altitude.

(b) Time history of Mach number.

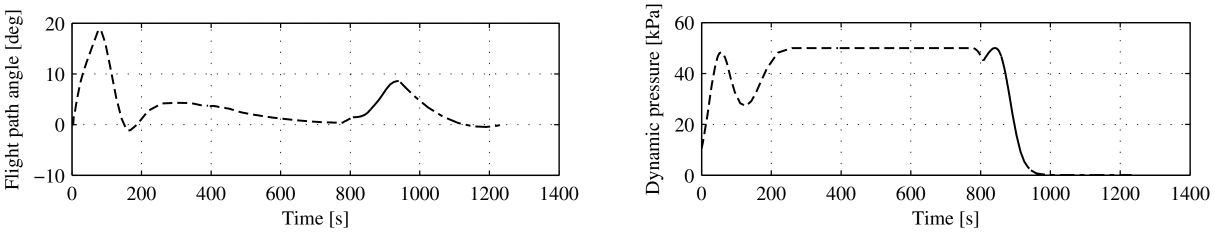

(c) Time history of flight path angle.

(d) Time history of dynamic pressure.

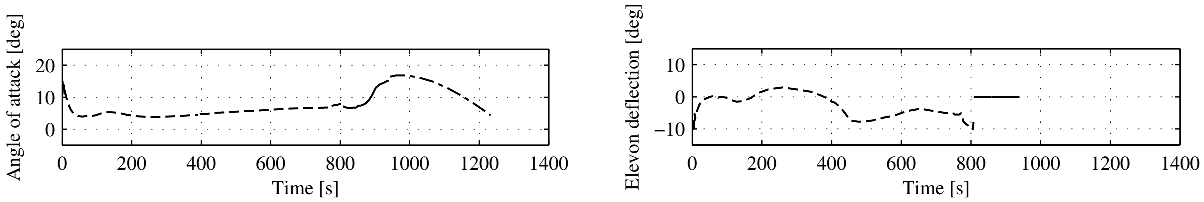

(e) Time history of angle of attack.

(f) Time history of elevon deflection angle.

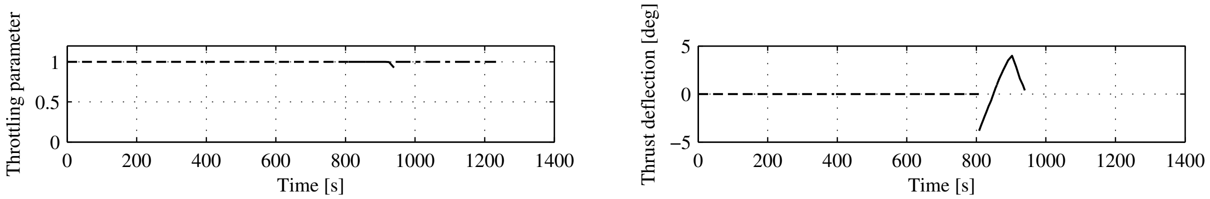

(g) Time history of thrust throttling parameter.

(h) Time history of thrust deflection angle.

Fig. 4.14 Flight trajectory of the solution No. 4.

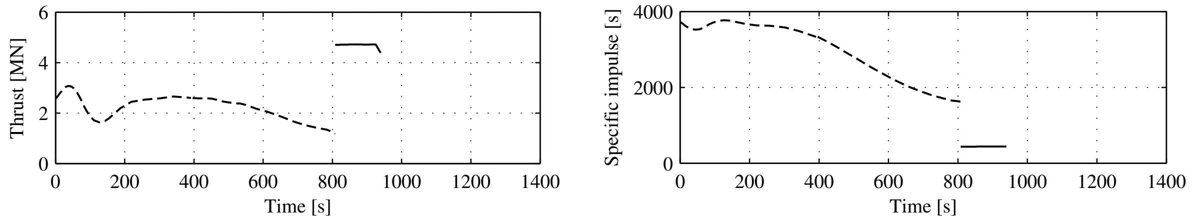

(a) Time history of thrust magnitude.

(b) Time history of specific impulse.

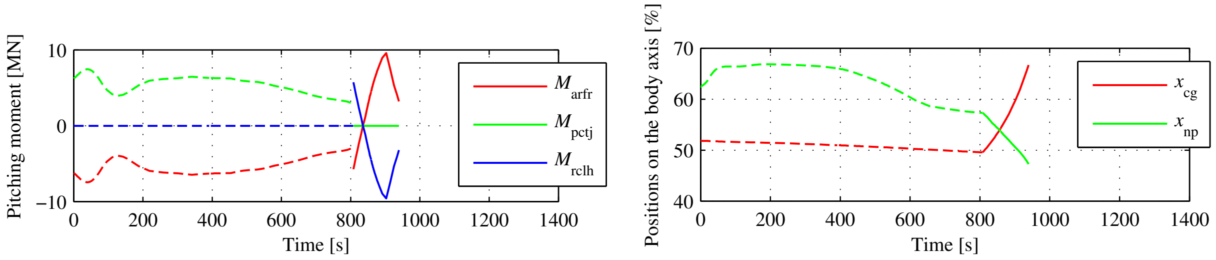

(c) Time history of pitching moment.

(d) Time history of center of mass and neutral point.

Fig. 4.15 Propulsion efficiency and rigid body characteristics of the solution No. 4.

of the other Pareto optimal solutions are qualitatively similar to that of the solution No. 4, while their details are substantially different.

The performance of the propulsion system and the rigid body characteristics of the vehicle during the mated vehicle ascent phase in the solution No. 4 are shown in Fig. 4.15. Total thrust magnitude of the PCTJ engines decreases from 70 s to 200 s after the takeoff due to low dynamic pressure. Even though the thrust and specific impulse of the PCTJ engines are gradually deteriorated in higher Mach number, the optimal switchover Mach number to the rocket operation is 6.0, and it is the operating limit of the PCTJ engines. In Fig. 4.14c, pitching moment around the center of mass produced by the airframe, that by the PCTJ engines, and that by the rocket engines are shown, and it can be seen that the summation of them equals to zero. As for the longitudinal static stability, the center of mass is not located backward of the stability neutral point before 870 s or below Mach 8.0, and this means that the stability is ensured. The results in the solutions Nos. 1–3 are presented in Figs. 4.9, 4.11, and 4.13, respectively, and they have similar characteristics to that of the solution No. 4. In all the Pareto optimal solutions, optimal Mach number where the operation of the PCTJ engines stops is 6.0, which means that the PCTJ engines should be operated as long as possible.

4.5 Knowledge Discovery in Pareto Optimal Solutions Using Data Mining Techniques

In the preceding section, only four representative solutions are selected from the obtained Pareto optimal solutions, and observations are made on them. In this section, generic and comprehensible knowledge is extracted from all the solutions by applying data mining techniques. The results provide insights into how the variations of the payload requirement and the takeoff constraint have the influence on the resulting optimal design of the TSTO RLV with PCTJ engines.

4.5.1 Data Mining from Optimal Vehicle Designs

Figure 4.16 is the scatter plot matrix of objective values and notable vehicle design parameters. Details on scatter plot matrices are described in Appendix F.1. The following information is extracted from Fig. 4.16:

1) Optimal solutions can be classified into the following two groups with different characteristics: solutions whose takeoff velocity is more than 80 m/s, and those whose takeoff velocity is no more than 80 m/s. Since such low takeoff velocity is not indispensable for RLVs, the former group includes suitable design solutions.

2) Since the mated vehicle horizontally takes off a runway, the takeoff velocity and the wing loading at the moment of takeoff are highly associated. Because lower takeoff velocity inevitably leads to a larger and heavier booster, less velocity increment should be assigned to the booster.

3) In the Pareto optimal booster designs, the decrease of the wing loading is primarily achieved by

enlarging the exposed wing and by increasing fuselage width-to-length ratio. Optimal fuselage length is not highly related to the wing loading when the takeoff velocity is higher than 80 m/s, and it has a considerable relation with the vehicle gross mass instead.

4) Optimal design of the propulsion system of the booster (i.e., the total inlet area of the PCTJ engines and the total vacuum thrust of the LH2/LOX rocket engines) is primarily determined by the gross mass of the mated vehicle. In addition, these propulsion design parameters are almost linearly correlated.

5) Optimal orbiter size relative to the booster length and vacuum thrust of the orbiter rocket are heavily associated with the payload mass. The orbiter design does not have a significant influence on the takeoff velocity.

6) Optimal dynamic pressure at the moment of staging is distributed in $[1.7, 5.1]$ kPa, and it is significantly related to the takeoff-velocity requirement.

7) Optimal vehicle thrust-to-mass ratio at the takeoff falls within a narrow range $[0.56, 0.67]$, and the ratio has some correlation with the payload mass.

4.5.2 Data Mining from Optimal Flight Trajectories

Proper orthogonal decomposition (POD), whose procedure is presented in Appendix F.2, is applied to angle-of-attack history during the mated vehicle ascent phase. It is because the mated vehicle ascent phase is the most distinctive flight phase of the TSTO RLV with PCTJ engines, and angle of attack is a primary control variable in this phase. Since a flight trajectory in each solution has different duration, it is rather meaningless to compare time histories of angle of attack directly. Instead, optimal angle of attack as a function of flight Mach number, $\alpha(Ma)$, is computed beforehand, and the comparison is made on the angle of attack at each Mach number. Using POD, the angle-of-attack history of the ith Pareto optimal solution, $\alpha_i(Ma)$, is expressed by the summation of that of a nominal solution, $\alpha_0(Ma)$, and the deviation from it in the following manner:

$$\alpha_i(Ma) = \alpha_0(Ma) + c_i^{(1)} \cdot \tilde{\alpha}^{(1)}(Ma) + c_i^{(2)} \cdot \tilde{\alpha}^{(2)}(Ma) + \cdots + c_i^{(260)} \cdot \tilde{\alpha}^{(260)}(Ma), \quad i = 1, \ldots, 260, \tag{4.73}$$

where the deviation is further decomposed into a series of POD modes. The coefficient and the basis of the jth mode are denoted by $c_i^{(j)}$ and $\tilde{\alpha}^{(j)}(\cdot)$, respectively. The solution No. 4 is adopted as the nominal solution, and therefore $\alpha_0(Ma)$ is calculated from Figs. 4.14b and 4.14e.

In the present case, 72.1 % of the whole energy content is occupied by the first POD mode, and its coefficient and basis are shown in Fig. 4.17. The following observations are obtained:

1) The coefficient depends mainly on the takeoff velocity. This indicates that optimal angle of attack at each Mach number is primarily associated with the takeoff velocity, or equivalently wing loading of the vehicle. The coefficient has minor dependence on the payload mass as well.

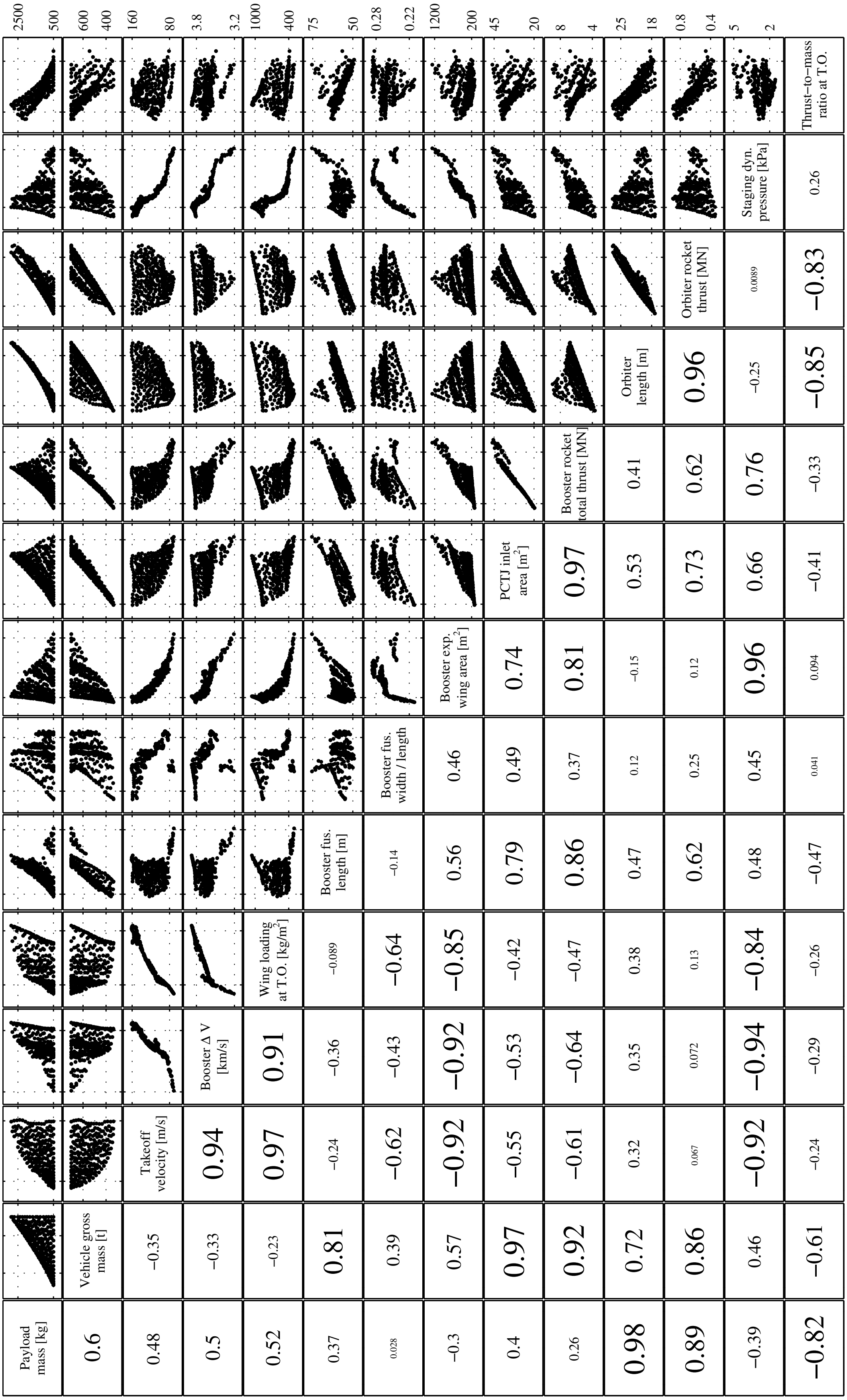

Fig. 4.16 Scatter plot matrix of the Pareto optimal solutions to multi-objective MDO of the TSTO RLV with PCTJ engines.

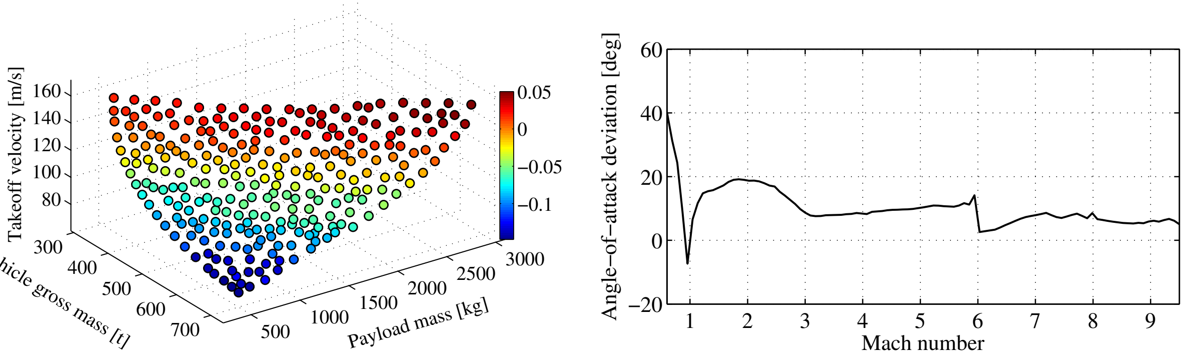

(a) Coefficient of the first POD mode, $c_i^{(1)}$.

(b) Basis of the first POD mode, $\tilde{\alpha}^{(1)}(Ma)$.

Fig. 4.17 Proper orthogonal decomposition (POD) of angle-of-attack histories of the Pareto optimal solutions.

2) The basis describes how the optimal angle of attack during the flight is deviated when the takeoff-velocity requirement is varied. As the takeoff velocity becomes higher, larger angle of attack is required in the subsonic region in order to achieve initial climb (see, for example, before 90 s in Fig. 4.14c) properly. On the other hand, optimal angle of attack is decreased more drastically during the dive maneuver around Mach 1.0 in solutions with higher takeoff velocity. During the flight when Mach number is within $[1, 6]$, optimal angle of attack takes on a positive correlation with the takeoff velocity again. When Mach number goes above 6, and the vehicle is propelled by the LH2/LOX rocket engines, the positive sensitivity between optimal angle of attack and the takeoff velocity becomes low.

Chapter 5

Multi-Objective, Multidisciplinary Design Optimization of a TSTO RLV with RBCC Engines

In this chapter, a multidisciplinary conceptual design study is performed on a horizontal takeoff TSTO RLV with rocket-based combined-cycle (RBCC) engines. The RBCC engine is composed of a dual-mode ramjet/scramjet flow-pass and rocket engines embedded in it, and it attains superior performance to conventional rocket engines. In comparison with the design study of a PCTJ-powered RLV in Chapter 4, airframe-propulsion integration and TPS analysis are newly considered. Multi-objective MDO is conducted aiming to maximize the payload mass, minimize the mated vehicle gross mass, and minimize the takeoff velocity using the numerical method developed in Chapter 2. After some inspections are made on representative Pareto optimal solutions, data mining techniques are employed in order to extract more generic and insightful knowledge from all the obtained solutions. Since some descriptions that overlap with the contents of Chapter 4 are removed in the present chapter, refer to the previous chapter for the duplicate part.

5.1 Overview of Multi-Objective MDO

Figure 5.1 gives the outline of a multi-objective MDO framework for the TSTO RLV propelled by RBCC engines. This numerical framework consists of analysis disciplines of vehicle geometry and mass property, aerodynamics, propulsion, flight trajectory, and TPS. Among design variables in the MDO framework, static variables are presented in Table 5.1. State variables, control variables, and phase-switching times are also included in the design variables, as will be detailed in Section 5.3. Design objectives considered here are 1) maximization of the payload mass, m_{pay}, 2) minimization of the gross mass of the mated vehicle (booster and orbiter), $m_{\mathrm{gross}}(= m_{\mathrm{gross}}^{(\mathrm{b})} + m_{\mathrm{gross}}^{(\mathrm{o})})$, and 3) minimization of horizontal takeoff velocity, v_{to}. The following bounds are introduced in order to confine the search region of the design

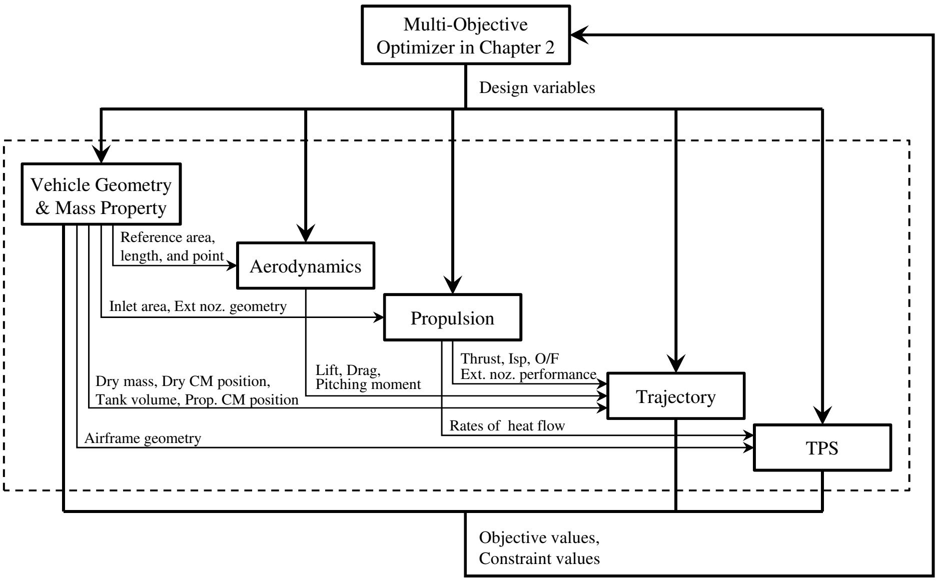

Fig. 5.1 Overview of a multi-objective MDO framework for the TSTO RLV with RBCC engines.

space to an interesting area and to make the resulting Pareto front bounded (see Assumption 1 in p. 13):

$$m_{\mathrm{pay}} \geq 200 \text{ kg} \tag{5.1}$$

$$m_{\mathrm{gross}} \leq 800 \text{ t} \tag{5.2}$$

$$v_{\mathrm{to}} \leq 200 \text{ m/s}. \tag{5.3}$$

5.2 Design Assumptions and Numerical Models

5.2.1 Vehicle Geometry Definition and Mass Property Analysis

The basic configuration of the booster is depicted in Fig. 5.2a. Design variables determine geometries of the airframe, tanks, and engines. In addition to the constraints presented in Table 5.1, some inequality constraints are imposed in order to ensure that the vehicle geometries are determined by the design variables successfully. Five RBCC engines are installed on the undersurface of the fuselage. The total inlet flow capture area of the RBCC engines is given by

$$S_{\mathrm{capt}} = \frac{5}{1.81} e_{\mathrm{h}}^2. \tag{5.4}$$

The flat undersurface of the forebody is employed to supply the uniformly pre-compressed airflow into the engines, and that of the afterbody acts as an external nozzle. The external nozzle considered in the present study is also called a single expansion ramp nozzle, and it is frequently used in hypersonic airbreathing propulsion systems (e.g., NASA X43 experimental vehicle[96]). The airfoils of the main wing and the vertical tail wings are NACA0005, and the taper ratio of the main wing is fixed at 0.15. 90 % exposed span from the wing tips and 30 % chord from the trailing edge of the main wing are used

Table 5.1 Static design variables of the TSTO RLV with RBCC engines.

		Parameter	Unit	Associated constraints
Vehicle design	Booster	Length of the fuselage, b_l	m	$30 \leq b_\mathrm{l} \leq 60$
		Height of the upper fuselage, b_h	m	$0.01 \leq b_\mathrm{h}/b_\mathrm{l} \leq 0.05$
		Inclination of the forebody undersurface, b_wed	deg	$3.0 \leq b_\mathrm{wed} \leq 8.0$
		Angle of the external nozzle, b_ext	deg	$3.0 \leq b_\mathrm{ext} \leq 20.0$
		Length of the forebody, b_lf	m	$0.3 \leq b_\mathrm{lf}/b_\mathrm{l} \leq 0.6$
		Width of the forebody tip, b_wf	m	$0.5 \leq b_\mathrm{wf}/[(5/1.81)e_\mathrm{h}] \leq 0.8$
		Leading edge position of the exposed wing, w_0	m	$0.25 \leq w_0/b_\mathrm{l} \leq 0.75$
		Root chord length of the exposed wing, w_chrd	m	$0.25 \leq w_\mathrm{chrd}/b_\mathrm{l} \leq 0.75$
		Sweepback of the wing leading edge, w_Λ	deg	$45 \leq w_\Lambda \leq 70$
		(Forward, Backward) end of the fore ethanol tank, $(t_\mathrm{eaf0}, t_\mathrm{eaff})$	m	$5.0 \leq t_\mathrm{eaf0} \leq t_\mathrm{eaff}$
		(Forward, Backward) end of the LOX tank, $(t_\mathrm{lo0}, t_\mathrm{lof})$	m	$t_\mathrm{eaff} + 0.5 \leq t_\mathrm{lo0} \leq t_\mathrm{lof}$
		(Forward, Backward) end of the aft ethanol tank, $(t_\mathrm{eaa0}, t_\mathrm{eaaf})$	m	$t_\mathrm{lof} + 0.5 \leq t_\mathrm{eaa0} \leq t_\mathrm{eaaf} \leq b_\mathrm{l} - 0.5$
		Thickness of the ceramic tile TPS on the undersurface, h_tps	m	–
		Height of RBCC engines, e_h	m	$0.2 \leq 5.96e_\mathrm{h}/b_\mathrm{l} \leq 0.5$
		Maximum thrust of RBCC embedded rocket engines, $T_\mathrm{R,max}$	kN	$100 \leq T_\mathrm{R,max}/S_\mathrm{capt}$ [kN/m^2] ≤ 400
	Orbiter	Length of the fuselage, o_l	m	$10 \leq o_\mathrm{l} \leq 30$
		Backward end of the cabin, cb_f	m	$0.25 \leq cb_\mathrm{f}/o_\mathrm{l} \leq 0.9$
		Ethanol/LOX rocket engine vacuum thrust, $T_\mathrm{rcea,v}$	kN	–
Vehicle performance	Booster	Maximum axial acceleration, $aa^{(b)}_\mathrm{max}$	G	–
		Maximum normal load factor, $lf^{(b)}_\mathrm{max}$	G	–
		Maximum dynamic pressure, $q^{(b)}_\mathrm{max}$	kPa	$q^{(b)}_\mathrm{max} \leq 50$
		Maximum exerted thrust, $T^{(b)}_\mathrm{max}$	kN	–
		Gross mass, $m^{(b)}_\mathrm{gross}$	t	–
	Orbiter	Maximum axial acceleration, $aa^{(o)}_\mathrm{max}$	G	–
		Maximum normal load factor, $lf^{(o)}_\mathrm{max}$	G	$2.5 \leq lf^{(o)}_\mathrm{max}$
		Maximum dynamic pressure, $q^{(o)}_\mathrm{max}$	kPa	$q^{(o)}_\mathrm{max} \leq 50$
		Maximum exerted thrust, $T^{(o)}_\mathrm{max}$	kN	–
		Gross mass, $m^{(o)}_\mathrm{gross}$	t	–

as elevons. The tail wings are scaled so that their total area equals 10 % of the main wing area. Two integral tanks of ethanol fuel (fore and aft) and cylindrical tanks of LOX are located inside the fuselage. Some control over the position of the center of mass is possible during the flight by adjusting the ratio of consumption of ethanol fuel between the fore and aft tanks.

As for the orbiter, a lifting body configuration shown in Fig. 5.2b is adopted based on Ref. 3, and its scaling is conducted. Since the orbiter is loaded onto the uppersurface of the booster, the orbiter width must not be larger than the distance between tail wings of the booster.

Mass property of the vehicles, tank volumes, and accommodated payload mass are computed based on the procedures explained in Appendix E. The consistency condition on the vehicle gross mass is introduced in the identical way to Section 4.2.1.

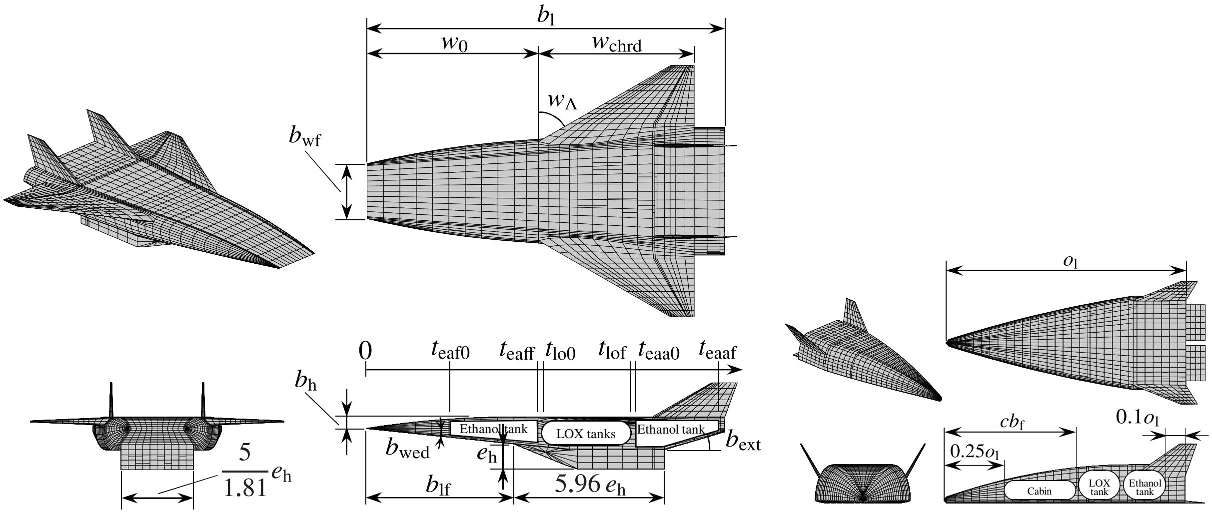

(a) Booster. (b) Orbiter.

Fig. 5.2 Basic configuration and design parameters of vehicles.

5.2.2 Aerodynamic Analysis

The aerodynamic analysis models are described in Appendix C. The external nozzle ramp is excluded when computing aerodynamic coefficients of the booster, because the forces acting on the ramp are considered in the airframe-propulsion integrated analysis in Section 5.2.3 instead.

During the optimization computation, these aerodynamic analyses are replaced by their surrogate models. The procedures for constructing the surrogate models are same as those in Section 4.2.2. As a result, adequate surrogate models, whose coefficient of determination is 0.9883 on average and 0.9682 in the worst case, are obtained.

5.2.3 Airframe-Propulsion Integrated Analysis

In this analysis discipline, thrust, specific impulse, oxidizer-to-fuel mass mixture ratio, and external nozzle performance are calculated when the engine design, the booster airframe, and flight conditions are provided.

Ethanol-fueled RBCC engines, whose conceptual image is illustrated in Fig. 5.3, are installed on the booster. RBCC engines are capable of being operated in ejector-jet (i.e., ducted rocket), ramjet, and scramjet modes, successively in that order. Ejector-jet and scramjet modes are operated by keeping the output of embedded rockets high (rocket chamber pressure is 6 MPa). In ramjet mode, on the other hand,

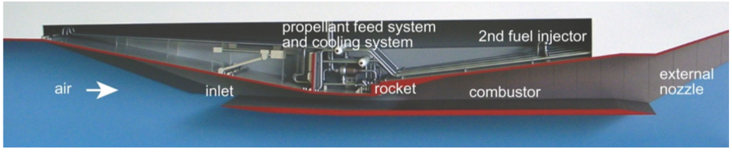

Fig. 5.3 A conceptual image of an RBCC engine[11].

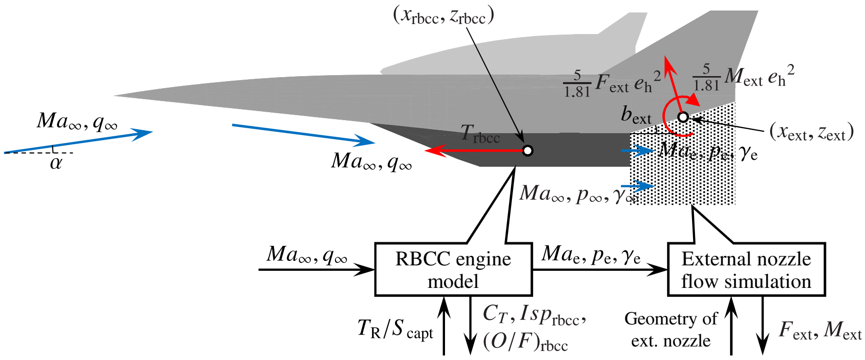

(a) During the operation in ejector-jet mode.

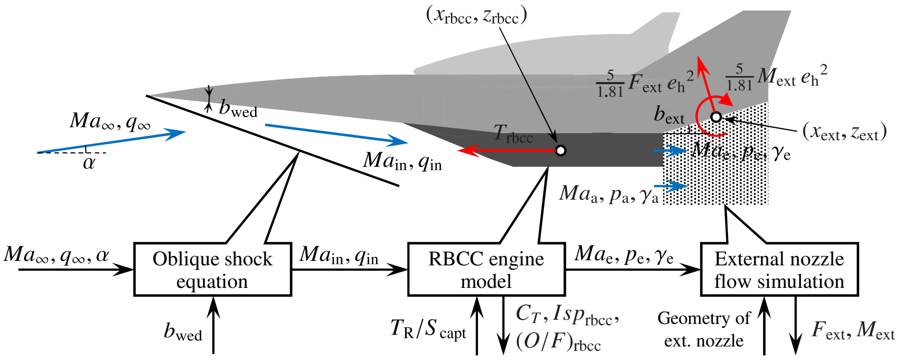

(b) During the operation in ramjet mode or scramjet mode.

Fig. 5.4 Overview of airframe-propulsion integrated analysis for the RBCC propulsion system.

the rocket chamber pressure is reduced to 0.6 MPa in order to attain higher specific impulse owing to airbreathing effects. The best acceleration performance is achieved by properly switching these operating modes depending on flight conditions.

The detailed geometry of the engine flow-pass is fixed (the overall length-to-height and height-to-width ratios of an engine unit are 5.96 and 1.81, respectively, and a throat-to-inlet area ratio is 0.2[97]), and the flow-pass is scaled based on a design variable, $e_{\rm h}$. In addition, the maximum thrust of the embedded rockets, $T_{\rm R,max}$, is also variable. An airframe-propulsion integrated analysis, whose overview is shown in Fig. 5.4, is conducted to evaluate the performance of the RBCC engine considering interactions between airframe and propulsion. For simplicity, influence of engine operation on the flow field around the airframe during the subsonic ejector-jet mode is neglected. The analysis is composed of three calculation steps: pre-compression calculation, RBCC engine model evaluation, and external nozzle simulation. Procedures in these steps are explained below.

1) Pre-compression analysis

A shock wave generated from the booster nose prior to the undersurface is equivalent to an oblique shock wave past a two-dimensional wedge whose angle is $(\alpha + b_{\rm wed})$. Approximating polynomials for the oblique shock equations shown in Eqs. (C.30–C.34) are employed, and inlet inflow conditions to RBCC engines (i.e., Mach number, $Ma_{\rm in}$, and dynamic pressure, $q_{\rm in}$) are obtained. In ejector-jet mode, the pre-compression analysis is not conducted, and the inlet inflow conditions

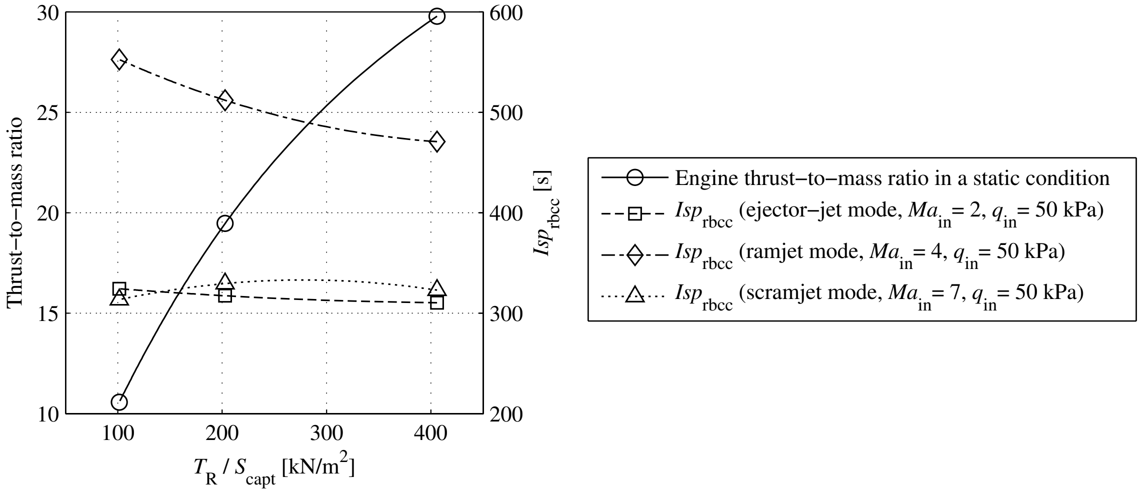

Fig. 5.5 Effects of $T_\mathrm{R}/S_\mathrm{capt}$ on the RBCC engine performance.

are approximated to be identical to the free-stream flow conditions.

2) RBCC engine analysis

The performance dataset of the RBCC engine at a set of representative inflow conditions (Ma_in and q_in) and $T_\mathrm{R}/S_\mathrm{capt}$ is prepared using a quasi-one-dimensional analytical engine model[97] in advance. Here, T_R denotes the total thrust magnitude produced by the rocket engines embedded in the RBCC engines. The outputs of the engine analysis include ram thrust coefficient, $C_{T,\mathrm{rbcc}}$, specific impulse, Isp_rbcc, oxidizer-to-fuel mass mixture ratio, $(O/F)_\mathrm{rbcc}$, and engine exhaust flow conditions, $\{Ma_\mathrm{e}, p_\mathrm{e}, \gamma_\mathrm{e}\}$. Constraints on the inlet inflow conditions are as follows:

$$0.0 \le Ma_\mathrm{in} \le 3.5 \quad \text{and} \quad 1\ \text{kPa} \le q_\mathrm{in} \le 100\ \text{kPa} \quad \text{for ejector-jet mode,} \tag{5.5}$$

$$3.0 \le Ma_\mathrm{in} \le 6.0 \quad \text{and} \quad 30\ \text{kPa} \le q_\mathrm{in} \le 100\ \text{kPa} \quad \text{for ramjet mode,} \tag{5.6}$$

$$3.5 \le Ma_\mathrm{in} \quad \text{and} \quad 1\ \text{kPa} \le q_\mathrm{in} \le 100\ \text{kPa} \quad \text{for scramjet mode.} \tag{5.7}$$

It is noted that ramjet mode is available when the engine inflow Mach number is 3.0 (the designed start Mach number of the inlet) or higher. In order to examine the effects of $T_\mathrm{R}/S_\mathrm{capt}$ on the RBCC engine performance, the engine thrust-to-mass ratio in a static condition and Isp_rbcc in some operating conditions are presented as functions of $T_\mathrm{R}/S_\mathrm{capt}$ in Fig. 5.5. This figure illustrates that a larger embedded rocket relative to the engine flow-pass gives a higher thrust-to-mass ratio of the engine, while it leads to decrease of Isp_rbcc except in scramjet mode.

Surrogate models of the engine-model responses [i.e., $C_{T,\mathrm{rbcc}}$, Isp_rbcc, $(O/F)_\mathrm{rbcc}$, Ma_e, p_e, and γ_e] for each engine mode are constructed using the combination of polynomial fitting and RBF networks as follows:

$$\begin{aligned} C_{T,\mathrm{rbcc}} = {} & d^{(0,0)}(Ma_\mathrm{in}) + d^{(1,0)}(Ma_\mathrm{in})\, q_\mathrm{in} + d^{(0,1)}(Ma_\mathrm{in})\, T_\mathrm{R}/S_\mathrm{capt} \\ & + d^{(2,0)}(Ma_\mathrm{in})\, {q_\mathrm{in}}^2 + d^{(0,2)}(Ma_\mathrm{in}) \left(T_\mathrm{R}/S_\mathrm{capt}\right)^2 + d^{(1,1)}(Ma_\mathrm{in})\, q_\mathrm{in}\, T_\mathrm{R}/S_\mathrm{capt}, \end{aligned} \tag{5.8}$$

$$\begin{aligned} Isp_{\mathrm{rbcc}} = {} & e^{(0,0)}(Ma_{\mathrm{in}}) + e^{(1,0)}(Ma_{\mathrm{in}})\, q_{\mathrm{in}} + e^{(0,1)}(Ma_{\mathrm{in}})\, T_{\mathrm{R}}/S_{\mathrm{capt}} \\ & + e^{(2,0)}(Ma_{\mathrm{in}})\, {q_{\mathrm{in}}}^2 + e^{(0,2)}(Ma_{\mathrm{in}}) \left(T_{\mathrm{R}}/S_{\mathrm{capt}}\right)^2 + e^{(1,1)}(Ma_{\mathrm{in}})\, q_{\mathrm{in}}\, T_{\mathrm{R}}/S_{\mathrm{capt}}, \end{aligned} \tag{5.9}$$

$$\begin{aligned} (O/F)_{\mathrm{rbcc}} = {} & f^{(0,0)}(Ma_{\mathrm{in}}) + f^{(1,0)}(Ma_{\mathrm{in}})\, q_{\mathrm{in}} + f^{(0,1)}(Ma_{\mathrm{in}})\, T_{\mathrm{R}}/S_{\mathrm{capt}} \\ & + f^{(2,0)}(Ma_{\mathrm{in}})\, {q_{\mathrm{in}}}^2 + f^{(0,2)}(Ma_{\mathrm{in}}) \left(T_{\mathrm{R}}/S_{\mathrm{capt}}\right)^2 + f^{(1,1)}(Ma_{\mathrm{in}})\, q_{\mathrm{in}}\, T_{\mathrm{R}}/S_{\mathrm{capt}}, \end{aligned} \tag{5.10}$$

$$\begin{aligned} Ma_{\mathrm{e}} = {} & g^{(0,0)}(Ma_{\mathrm{in}}) + g^{(1,0)}(Ma_{\mathrm{in}})\, q_{\mathrm{in}} + g^{(0,1)}(Ma_{\mathrm{in}})\, T_{\mathrm{R}}/S_{\mathrm{capt}} \\ & + g^{(2,0)}(Ma_{\mathrm{in}})\, {q_{\mathrm{in}}}^2 + g^{(0,2)}(Ma_{\mathrm{in}}) \left(T_{\mathrm{R}}/S_{\mathrm{capt}}\right)^2 + g^{(1,1)}(Ma_{\mathrm{in}})\, q_{\mathrm{in}}\, T_{\mathrm{R}}/S_{\mathrm{capt}}, \end{aligned} \tag{5.11}$$

$$\begin{aligned} p_{\mathrm{e}} = {} & h^{(0,0)}(Ma_{\mathrm{in}}) + h^{(1,0)}(Ma_{\mathrm{in}})\, q_{\mathrm{in}} + h^{(0,1)}(Ma_{\mathrm{in}})\, T_{\mathrm{R}}/S_{\mathrm{capt}} \\ & + h^{(2,0)}(Ma_{\mathrm{in}})\, {q_{\mathrm{in}}}^2 + h^{(0,2)}(Ma_{\mathrm{in}}) \left(T_{\mathrm{R}}/S_{\mathrm{capt}}\right)^2 + h^{(1,1)}(Ma_{\mathrm{in}})\, q_{\mathrm{in}}\, T_{\mathrm{R}}/S_{\mathrm{capt}}, \end{aligned} \tag{5.12}$$

$$\begin{aligned} \gamma_{\mathrm{e}} = {} & i^{(0,0)}(Ma_{\mathrm{in}}) + i^{(1,0)}(Ma_{\mathrm{in}})\, q_{\mathrm{in}} + i^{(0,1)}(Ma_{\mathrm{in}})\, T_{\mathrm{R}}/S_{\mathrm{capt}} \\ & + i^{(2,0)}(Ma_{\mathrm{in}})\, {q_{\mathrm{in}}}^2 + i^{(0,2)}(Ma_{\mathrm{in}}) \left(T_{\mathrm{R}}/S_{\mathrm{capt}}\right)^2 + i^{(1,1)}(Ma_{\mathrm{in}})\, q_{\mathrm{in}}\, T_{\mathrm{R}}/S_{\mathrm{capt}}, \end{aligned} \tag{5.13}$$

where $d^{(\cdot,\cdot)}(\cdot)$, $e^{(\cdot,\cdot)}(\cdot)$, $f^{(\cdot,\cdot)}(\cdot)$, $g^{(\cdot,\cdot)}(\cdot)$, $h^{(\cdot,\cdot)}(\cdot)$, and $i^{(\cdot,\cdot)}(\cdot)$ are the RBF networks with multiquadric basis[76].

In ejector-jet and scramjet modes, thrust of the RBCC engines alone (i.e., without external nozzle effects), denoted by T_{rbcc}, is calculated in the following manner:

$$T_{\mathrm{rbcc}} = C_{T,\mathrm{rbcc}}\, S_{\mathrm{capt}} + T_{\mathrm{R}}, \tag{5.14}$$

where

$$T_{\mathrm{R}} = T_{\mathrm{R,max}}\, \tau. \tag{5.15}$$

Throttling parameter, τ, is allowed to vary within the range $[0.5, 1]$ in scramjet mode, and $\tau = 1$ otherwise. In ramjet mode, thrust is given by

$$T_{\mathrm{rbcc}} = C_{T,\mathrm{rbcc}}\, S_{\mathrm{capt}}. \tag{5.16}$$

The responses of the constructed performance models of the engine alone at a typical engine design point are shown in Fig. 5.6. Figures 5.6a and 5.6b show thrust magnitude and specific impulse, respectively, provided that total embedded rocket thrust is 4482.7 kN and the total inlet flow capture area is 22.2 m^2. These figures correspond to the case where the engine is switched to ramjet mode and scramjet mode when $M_{\mathrm{in}} = 3.0$ and $M_{\mathrm{in}} = 5.5$, respectively.

3) External nozzle analysis

The external nozzle performance is computed based on a two-dimensional external nozzle flow model developed in Appendix B. Engine exhaust conditions required in the nozzle flow model are evaluated using Eqs. (5.11–5.13). The outputs of the model are F_{ext} and M_{ext}, which denote the

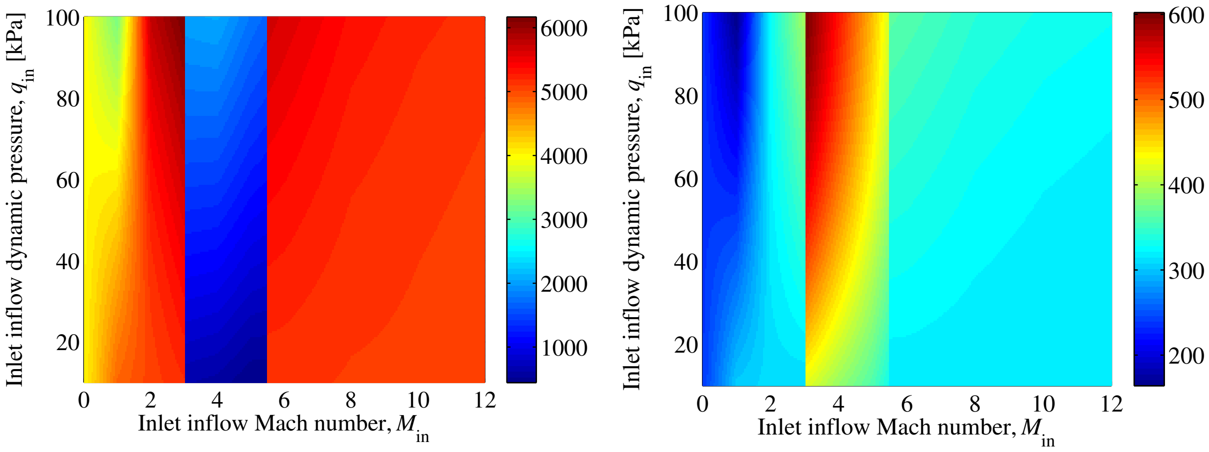

(a) Thrust magnitude of engine alone, T_{rbcc}, [kN].

(b) Specific impulse of engine alone, Isp_{rbcc}, [s].

Fig. 5.6 The performance of RBCC engines when T_{R} = 4482.7 kN and S_{capt} = 22.2 m^2.

force and the pitching moment acting on the external nozzle ramp per unit ramp width times unit engine height, respectively. It is noted that surrogate models of F_{ext} and M_{ext} built in Appendix B.3 are employed during optimization computation instead of the original external nozzle flow model. Since the ramp width is $(5/1.81)e_{\mathrm{h}}$, and the engine height is e_{h}, the actually exerted force and moment are given by $(5/1.81)F_{\mathrm{ext}}\,e_{\mathrm{h}}{}^2$ and $(5/1.81)M_{\mathrm{ext}}\,e_{\mathrm{h}}{}^2$, respectively.

The orbiter is propelled by an ethanol/LOX rocket engine mounted on its fuselage base. Refer to Section 4.2.3 for its specifications.

5.2.4 TPS Analysis

In the TPS analysis, thermal balance of the active cooling system is evaluated, and the required thickness of passive TPS is calculated. It is noted that the TPS analysis is performed only on the booster vehicle.

Thermal Protection System Concept of the Booster Vehicle

A thermal protection strategy for the booster vehicle is as follows:

- Embedded rockets and flow-passes of RBCC engines
  Regenerative cooling using ethanol fuel is applied to embedded rockets, inlet, and combustor of the RBCC engines. The usage of LOX as coolant is not considered due to safety issues of the manned vehicle in the present study.

- Leading edges of nose, main wing, and engine cowls
  Optimal staging Mach number of TSTO RLVs with RBCC engines is generally between 10 and 12, and then the radiative equilibrium temperature on leading edges with 0.1 m radii typically reaches above 3000 K. Therefore, active cooling using ethanol fuel is employed as a thermal protection strategy.

- Vehicle undersurface
  Ceramic insulation tiles are installed on the undersurface in order to prevent the aerodynamic heating at the surface from reaching the main metal structures whose operating temperature limit is low.

Stationary Thermal Balance Analysis of Active Cooling System

To the actively cooled parts of the booster vehicle (i.e., RBCC engines and leading edges of nose, main wing, and engine cowls), a stationary thermal analysis is performed as explained in Appendices D.1 and D.2. When the mass flow rate of the ethanol fuel consumed in the RBCC combustor is not less than that of the ethanol employed as coolant, total thermal balance is achieved. When the cooling requirement is excessive, on the other hand, some ethanol is dumped into the atmosphere without consumed in the engines after it flows in cooling pipes. The dumped ethanol mass rate, $\dot{m}_{\text{dump}}$, is calculated by

$$\dot{m}_{\text{dump}} = \max[(\dot{m}_{\text{cool,eng}} + \dot{m}_{\text{cool,le}} - \dot{m}_{\text{fuel}}),\ 0], \tag{5.17}$$

where $\dot{m}_{\text{cool,eng}}$ and $\dot{m}_{\text{cool,le}}$ are the required mass rates of the ethanol coolant for RBCC engines and leading edges, respectively. They are obtained via the aerodynamic heating models explained in Appendices D.1 and D.2. $\dot{m}_{\text{fuel}}$ indicates the consumption mass rate of the ethanol fuel in the RBCC combustors, which is given by

$$\dot{m}_{\text{fuel}} = \frac{T_{\text{rbcc}}}{g_0 Isp_{\text{rbcc}}} \frac{1}{(O/F)_{\text{rbcc}} + 1}. \tag{5.18}$$

The dumping of ethanol fuel can be apparently regarded as the decrease of specific impulse of the engines. Since the $\max(\cdot,\cdot)$ function cannot be handled by gradient-based optimization methods due to its lack of smoothness, Eq. (5.17) is transformed into the following alternative form:

$$\dot{m}_{\text{dump}} \geq \dot{m}_{\text{cool,eng}} + \dot{m}_{\text{cool,le}} - \dot{m}_{\text{fuel}}, \tag{5.19}$$

$$\dot{m}_{\text{dump}} \geq 0. \tag{5.20}$$

It is noted that either Eq. (5.19) or Eq. (5.20) becomes active after optimization is properly performed.

Instationary Thermal Analysis of Ceramic Tiles on the Booster Undersurface

For the undersurface of the booster vehicle, aerodynamic heat flux is computed from flight conditions and vehicle geometry using the procedures in Appendix D.3. Then, the convective heat flux at the surface, Q_{conv}, and thermal radiation flux at the surface, Q_{rad}, at each time are obtained. HTP-12[98] ceramic tile is adopted as the passive TPS material on the booster undersurface. This choice is due to the fact that ceramic TPS with a similar material (composition of SiO_2 and Al_2O_3) was developed in Japan[99], and physical and thermal properties of HTP-12 are available in open literature[98]. Since the thermal characteristics are dependent on temperature and ambient pressure, they are approximated with

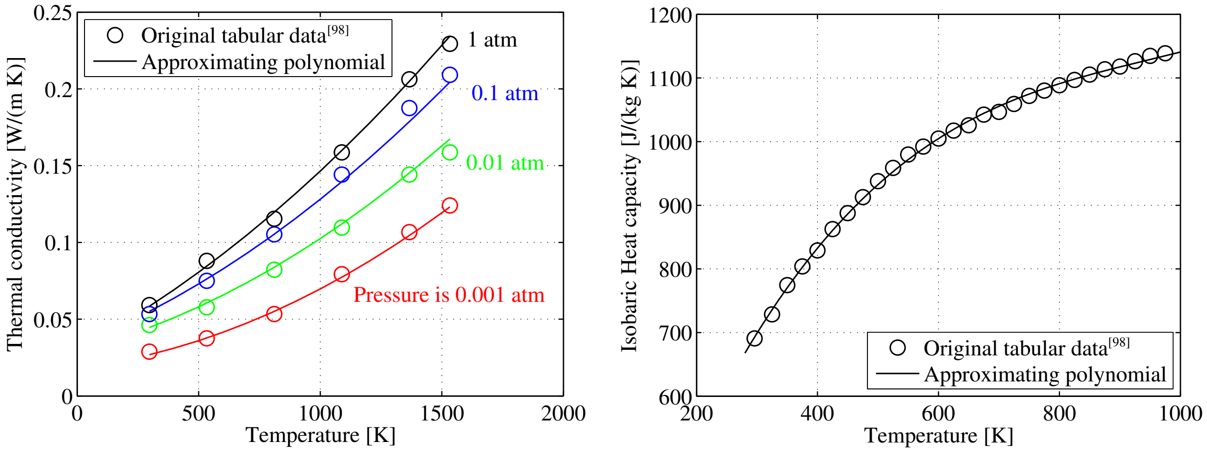

(a) Thermal conductivity, $K(T, p)$.

(b) Isobaric heat capacity, $C_p(T)$.

Fig. 5.7 Thermal properties of HTP-12 ceramic tile.

polynomials as follows:

$$K(T, p) = -0.02615 - 2.355 \times 10^{-5} T + 3.187 \times 10^{-8} T^2 + 0.02937 \log_{10} p - 3.603 \times 10^{-3} (\log_{10} p)^2 + 2.149 \times 10^{-5} T \log_{10} p, \quad (5.21)$$

$$C_p(T) = 33.76 + 3.001 T - 2.921 \times 10^{-3} T^2 + 1.027 \times 10^{-6} T^3, \quad (5.22)$$

where K is the thermal conductivity [W/(m K)], C_p is the isobaric heat capacity [J/(kg K)], T is the temperature [K], and p is the surrounding static pressure [Pa]. The constructed polynomial models are shown in Fig. 5.7.

One-dimensional thermal analysis inside the ceramic tile in the depth direction is conducted based on the procedures explained in Chapter 3. The governing equations are described by the following second-order PDE with boundary conditions:

$$\frac{\partial T(y, t)}{\partial t} = \frac{K(T, p_e)}{\rho C_p(T)} \frac{\partial^2 T(y, t)}{\partial y^2}, \quad (5.23)$$

$$\left. \frac{\partial T(y, t)}{\partial y} \right|_{y=0} = \frac{1}{K(T, p_e)} (Q_{\text{rad}} - Q_{\text{conv}}), \quad (5.24)$$

$$\left. \frac{\partial T(y, t)}{\partial y} \right|_{y=h_{\text{tps}}} = 0, \quad (5.25)$$

where $T(y, t)$: $[0, h_{\text{tps}}] \times [0, t_{\text{f}}] \to \mathbb{R}$ is the temperature of the ceramic tile at the distance of y from the surface and time t. p_{e} indicates the static pressure of the airflow at the outer edge of the boundary layer around the vehicle undersurface, and it is calculated in Appendix D.3. ρ denotes the density of HTP-12 ($= 192.22$ kg/m^3). The criterion of the TPS design is to ensure that the backface temperature, $T(h_{\text{tps}}, t)$, does not exceed the operating limit of the material used in the vehicle main structure, T_{max}, during the flight. In this dissertation, it is assumed that the main structure is made from an aluminum alloy, and $T_{\text{max}} = 450$ K. Before the takeoff run, the tile temperature is identical to the atmospheric temperature at sea level.

Eqs. (5.23–5.25) are transformed into the following set of ODEs using the fictitious-point Legendre pseudospectral method[89]:

$$\frac{\mathrm{d}}{\mathrm{d}t}\begin{bmatrix} T_1(t) \\ T_2(t) \\ T_3(t) \\ T_4(t) \\ T_5(t) \end{bmatrix} = \begin{bmatrix} & & \\ & \mathbf{C} & \\ & & \end{bmatrix} \left\{ \left(\frac{2}{h_{\mathrm{tps}}}\right)^2 \begin{bmatrix} & & \\ & \mathbf{H} & \\ & & \end{bmatrix} \begin{bmatrix} T_1(t) \\ T_2(t) \\ T_3(t) \\ T_4(t) \\ T_5(t) \end{bmatrix} + \frac{2}{h_{\mathrm{tps}}} \begin{bmatrix} \\ \mathbf{I} \\ \\ \end{bmatrix} (Q_{\mathrm{conv}} - Q_{\mathrm{rad}}) \right\}, \tag{5.26}$$

where **C**, **H**, and **I** are computed based on the procedures in Section 3.2.4. Here, the number of spatial discretization nodes is 5, and $T_1, \ldots, T_5$ denote the tile temperatures at these discrete depths. T_1 refers to the temperature on the surface, and T_5 indicates that on the backface bonded to the vehicle main structure. The constraint on the backface temperature limit can be written as*

$$T_5(t) \leq 450 \text{ K}. \tag{5.27}$$

Initial conditions on the tile temperature are as follows:

$$T_1(0) = T_2(0) = T_3(0) = T_4(0) = T_5(0) = 290 \text{ K}. \tag{5.28}$$

5.2.5 Flight Trajectory Analysis

System Dynamics

In the flight trajectory analysis, the following 2-degree-of-freedom vehicle dynamics on a vertical plane is employed:

For the mated vehicle

$$\dot{v} = \frac{T_{\mathrm{rbcc}} \cos\alpha - [D_{\mathrm{m}} - \frac{5}{1.81} F_{\mathrm{ext}}\, e_{\mathrm{h}}{}^2 \sin(b_{\mathrm{ext}} - \alpha)]}{m} - \frac{\mu}{r^2} \sin\gamma, \tag{5.29}$$

$$\dot{\gamma} = \frac{[L_{\mathrm{m}} + \frac{5}{1.81} F_{\mathrm{ext}}\, e_{\mathrm{h}}{}^2 \cos(b_{\mathrm{ext}} - \alpha)] + T_{\mathrm{rbcc}} \sin\alpha}{mv} + \left(\frac{v}{r} - \frac{\mu}{vr^2}\right)\cos\gamma, \tag{5.30}$$

$$\dot{h} = v \sin\gamma, \tag{5.31}$$

$$\dot{m}_{\mathrm{eaf}} = -\frac{T_{\mathrm{rbcc}}}{g_0 Isp_{\mathrm{rbcc}}} \frac{\eta}{(O/F)_{\mathrm{rbcc}} + 1} - \dot{m}_{\mathrm{dump}}\eta, \tag{5.32}$$

$$\dot{m}_{\mathrm{eaa}} = -\frac{T_{\mathrm{rbcc}}}{g_0 Isp_{\mathrm{rbcc}}} \frac{1-\eta}{(O/F)_{\mathrm{rbcc}} + 1} - \dot{m}_{\mathrm{dump}}(1-\eta), \tag{5.33}$$

$$\dot{m}_{\mathrm{lo}} = -\frac{T_{\mathrm{rbcc}}}{g_0 Isp_{\mathrm{rbcc}}} \frac{(O/F)_{\mathrm{rbcc}}}{(O/F)_{\mathrm{rbcc}} + 1}, \tag{5.34}$$

For the orbiter

---

*450 K is a typical operating temperature limit of aluminium alloys.

$$\dot{v} = \frac{T_{\mathrm{rcea}}\tau \cos\alpha - D_{\mathrm{o}}}{m} - \frac{\mu}{r^2}\sin\gamma, \tag{5.35}$$

$$\dot{\gamma} = \frac{L_{\mathrm{o}} + T_{\mathrm{rcea}}\tau \sin\alpha}{mv} + \left(\frac{v}{r} - \frac{\mu}{vr^2}\right)\cos\gamma, \tag{5.36}$$

$$\dot{h} = v\sin\gamma, \tag{5.37}$$

$$\dot{m}_{\mathrm{ea}} = -\frac{T_{\mathrm{rcea}}\tau}{g_0 Isp_{\mathrm{rcea}}}\frac{1}{(O/F)_{\mathrm{rcea}} + 1}, \tag{5.38}$$

$$\dot{m}_{\mathrm{lo}} = -\frac{T_{\mathrm{rcea}}\tau}{g_0 Isp_{\mathrm{rcea}}}\frac{(O/F)_{\mathrm{rcea}}}{(O/F)_{\mathrm{rcea}} + 1}, \tag{5.39}$$

where

$$r = h + R_{\mathrm{e}}. \tag{5.40}$$

Variable definitions are presented in Table 4.3. The static atmosphere model developed in Section 4.2.4 is employed.

Flight Plan

A flight plan considered in the present study is described by the following three phases:

1) Takeoff phase

   The mated vehicle takes off horizontally from a runway at sea level. The maximum RBCC engine thrust is exerted, and angle of attack for liftoff is 15 deg. A horizontal takeoff analysis identical to that in Section 4.2.4 is conducted, and takeoff velocity, v_{to}, takeoff distance (ground roll), l_{to}, and propellant consumption during the takeoff phase, $m_{\mathrm{prop,to}}$, are evaluated.

2) Mated vehicle ascent phase

   The mated vehicle is accelerated by the RBCC engines. The rocket engine mounted on the orbiter is not used. Angle of attack and elevon deflection angle are bounded as follows:

$$-5 \text{ deg} \le \alpha \le 15 \text{ deg}, \tag{5.41}$$

$$-10 \text{ deg} \le \delta \le 10 \text{ deg}. \tag{5.42}$$

   Constraints on axial acceleration, normal load factor, dynamic pressure, exerted thrust, and total acceleration are imposed in the same way as Section 4.2.4. At the terminus of this phase, the orbiter is separated from the booster.

   This flight phase is further divided into three sub-phases where the RBCC engines are operated in different modes (ejector-jet, ramjet, and scramjet modes in this order). Switchover times between engine operating modes are included in the design variables of the MDO problem, and they are optimized to achieve the best acceleration performance.

3) Orbiter ascent phase

The orbiter is accelerated by the ethanol/LOX rocket engine ignited immediately after the staging. Angle of attack is bounded as follows:

$$0\ \text{deg} \le \alpha \le 30\ \text{deg}. \tag{5.43}$$

Flight conditions are constrained in the identical manner to Section 4.2.4.

After the orbiter reaches an altitude of 100 km or higher, and the rocket engine is cut off, the trajectory computation is performed based on elliptic orbit equations instead of equations of motion. At the apogee of this coasting trajectory, the orbiter is accelerated again, and it is injected into a circular orbit that is 350 km above sea level. Propellants required for the apogee acceleration, an on-orbit operation, and de-orbit are calculated and reserved at the moment of the engine cut-off, as detailed in Section 4.2.4.

Return trajectories of the booster and the orbiter to landing sites are not considered.

Rigid Body Characteristics of the Vehicle

During the mated vehicle ascent phase, a static pitching trim condition is enforced as follows:

$$M_{\text{tot}} := M_{\text{arfr}} + M_{\text{rbcc}} + M_{\text{extn}} = 0. \tag{5.44}$$

Here,

$$M_{\text{arfr}} = M_{\text{m}} + (L_{\text{m}} \cos\alpha + D_{\text{m}} \sin\alpha)(x_{\text{cg}} - x_{\text{refb}}) + (L_{\text{m}} \sin\alpha - D_{\text{m}} \cos\alpha)(z_{\text{cg}} - z_{\text{refb}}), \tag{5.45}$$

$$M_{\text{rbcc}} = T_{\text{rbcc}}(z_{\text{cg}} - z_{\text{rbcc}}), \tag{5.46}$$

$$M_{\text{extn}} = \frac{5}{1.81} M_{\text{ext}}\, {e_{\text{h}}}^2 + \frac{5}{1.81} F_{\text{ext}}\, {e_{\text{h}}}^2 \left[(z_{\text{cg}} - z_{\text{ext}}) \sin b_{\text{ext}} + (x_{\text{cg}} - x_{\text{ext}}) \cos b_{\text{ext}}\right] \tag{5.47}$$

are the pitching moment generated by the airframe, that by the RBCC engines, and that by the external nozzle, respectively. Additionally, the following equation describes non-negative longitudinal static stability:

$$\frac{\partial M_{\text{tot}}}{\partial \alpha} = \frac{\partial M_{\text{arfr}}}{\partial \alpha} + \frac{\partial M_{\text{rbcc}}}{\partial \alpha} + \frac{\partial M_{\text{extn}}}{\partial \alpha} \le 0. \tag{5.48}$$

In order to calculate the value of $\partial M_{\text{tot}}/\partial \alpha$ accurately, the following procedures are employed:

1) The relation between α and M_{tot} is described by 1) the pre-compression equations, 2) the RBCC engine model, 3) the external nozzle model, 4) the aerodynamic model, and 5) Eqs. (5.44–5.47).

2) $\partial M_{\text{tot}}/\partial \alpha$ is decomposed into the partial derivatives of these component functions (e.g., $\partial F_{\text{ext}}/\partial p_{\text{e}}$) using the chain rule in calculus.

3) Exact partial derivatives of the component functions are available by using an analytical relation for RBF network surrogate models shown in Eq. (B.27), or by using an automatic differentiation algorithm[100].

5.3 Formulation of the Optimization Problem

On the basis of the above numerical models, the multi-objective MDO problem of the TSTO RLV with RBCC engines is established. The MDO architecture illustrated in Fig. 5.1 is formulated as an augmented optimal control problem. In order to express the flight plan in Section 5.2.5, the optimal control problem is composed of six phases described in Table 5.2. As a consequence, the multi-objective MDO problem is written as follows:

find state variables, $\mathbf{x}^{(1)}, \ldots, \mathbf{x}^{(6)}$, (5.49)
control variables, $\mathbf{u}^{(1)}, \ldots, \mathbf{u}^{(6)}$, (5.50)
initial and terminal times, $t_0^{(1)}, t_\mathrm{f}^{(1)}, \ldots, t_0^{(6)}, t_\mathrm{f}^{(6)}$ (5.51)
static variables shown in Table 5.1, $\mathbf{p}$ (5.52)
min. $F_1 := -0.04\, m_\mathrm{pay}$ [kg] (5.53)
$F_2 := 0.1\, m_\mathrm{gross}$ [t] (5.54)
$F_3 := 0.25\, v_\mathrm{to}$ [m/s] (5.55)
s.t. simple bounds on objective values, Eqs. (5.1–5.3), (5.56)
constraints on static variables presented in Table 5.1, (5.57)
consistency condition on the vehicle gross mass explained in Section 5.2.1, (5.58)
constraints on the inflow conditions to RBCC engines, Eqs. (5.5–5.7), (5.59)
thermal balance conditions for active cooling system, Eqs. (5.19, 5.20) for Phase 1–5, (5.60)
discretized thermal eq. and associated constraints, Eqs. (5.26–5.28) for Phase 1–5, (5.61)
state equations, Eqs. (5.29–5.34) for Phase 1–5, (5.62)
state equations, Eqs. (5.35–5.39) for Phase 6, (5.63)
path constraints presented in Section 5.2.5, (5.64)
initial and terminal conditions explained in Section 5.2.5, (5.65)
static pitching trim condition, Eq. (5.44) for Phase 1–5, (5.66)
longitudinal static stability condition, Eq. (5.48) for Phase 1–5, (5.67)
linkage conditions for the continuity of the state variables between adjacent phases. (5.68)

The formulated multi-objective optimal control problem is solved using a numerical method proposed in Chapter 2 with $d_\mathrm{tol} = 3.0$. Computational environments are same as the descriptions in Section 4.3.

Table 5.2 Definitions of optimal control phases in the MDO problem of the TSTO RLV with RBCC engines.

Item	Phase 1	Phase 2
Flight phase	Mated vehicle ascent	Mated vehicle ascent
Propulsion	RBCC engine (ejector-jet)	RBCC engine (ejector-jet)
Flight Mach number, Ma	$Ma \leq 1.8$	$Ma \leq 1.8$
Mated vehicle's aero. model	Model 1 (Fig. C.1a)	Model 1 (Fig. C.1a)
External nozzle conditions	Type 1 [Eq. (B.14)]	Type 2 [Eq. (B.15)]
State, $\mathbf{x}$	$\mathbf{x}^{(1)} = [h, v, \gamma, m_{\text{lo}}, m_{\text{eaf}}, m_{\text{eaa}},$ $T_1, T_2, T_3, T_4, T_5]$	$\mathbf{x}^{(2)} = [h, v, \gamma, m_{\text{lo}}, m_{\text{eaf}}, m_{\text{eaa}},$ $T_1, T_2, T_3, T_4, T_5]$
Control, $\mathbf{u}$	$\mathbf{u}^{(1)} = [\alpha, \delta, \eta, \dot{m}_{\text{dump}}]$	$\mathbf{u}^{(2)} = [\alpha, \delta, \eta, \dot{m}_{\text{dump}}]$

Item	Phase 3	Phase 4
Flight phase	Mated vehicle ascent	Mated vehicle ascent
Propulsion	RBCC engine (ejector-jet)	RBCC engine (ramjet)
Flight Mach number, Ma	$1.8 \leq Ma$	–
Mated vehicle's aero. model	Model 1 (Fig. C.1a)	Model 2 (Fig. C.1b)
External nozzle conditions	Type 3 [Eq. (B.16)]	Type 4 [Eq. (B.17)]
State, $\mathbf{x}$	$\mathbf{x}^{(3)} = [h, v, \gamma, m_{\text{lo}}, m_{\text{eaf}}, m_{\text{eaa}},$ $T_1, T_2, T_3, T_4, T_5]$	$\mathbf{x}^{(4)} = [h, v, \gamma, m_{\text{lo}}, m_{\text{eaf}}, m_{\text{eaa}},$ $T_1, T_2, T_3, T_4, T_5]$
Control, $\mathbf{u}$	$\mathbf{u}^{(3)} = [\alpha, \delta, \eta, \dot{m}_{\text{dump}}]$	$\mathbf{u}^{(4)} = [\alpha, \delta, \eta, \dot{m}_{\text{dump}}]$

Item	Phase 5	Phase 6
Flight phase	Mated vehicle ascent	Orbiter ascent
Propulsion	RBCC engine (scramjet)	Ethanol/LOX rocket
Flight Mach number, Ma	–	–
Mated vehicle's aero. model	Model 2 (Fig. C.1b)	–
External nozzle conditions	Type 3 [Eq. (B.16)]	–
State, $\mathbf{x}$	$\mathbf{x}^{(5)} = [h, v, \gamma, m_{\text{lo}}, m_{\text{eaf}}, m_{\text{eaa}},$ $T_1, T_2, T_3, T_4, T_5]$	$\mathbf{x}^{(6)} = [h, v, \gamma, m_{\text{lo}}, m_{\text{ea}}]$
Control, $\mathbf{u}$	$\mathbf{u}^{(5)} = [\alpha, \delta, \tau, \eta, \dot{m}_{\text{dump}}]$	$\mathbf{u}^{(6)} = [\alpha, \tau]$

5.4 Pareto Optimal Solutions

A set of 168 solutions is found through the optimization computation in about 36 hours. The obtained solutions are displayed in the objective space in Fig. 5.8. The distribution of the solutions indicates that the three objectives are conflicting with each other. Figure 5.8b suggests that the mated gross mass changes almost linearly with respect to the payload mass when the takeoff velocity is fixed. The payload mass fraction becomes smaller when lower takeoff velocity is required.

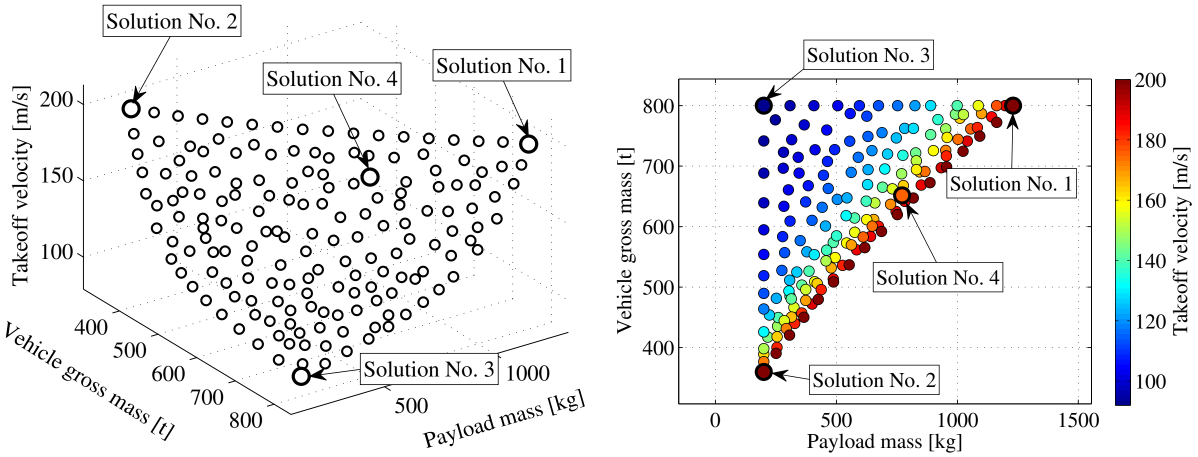

(a) Three-dimensional view.

(b) Two-dimensional projection.

Fig. 5.8 Obtained solutions in the objective space.

Table 5.3 presents specifications of four representative solutions indicated in Fig. 5.8. When the solution No. 4 of the RBCC-powered system is compared with the solution No. 4 of the PCTJ-powered system presented in Section 4.4, The RBCC-powered system is inferior in term of the objective values. Of course, a simple comparison is rather meaningless since the underlying design assumptions, especially the employed kinds of fuel, are different. A distinctive difference between the PCTJ-powered system and the RBCC-powered system is that it is more difficult to realize low takeoff velocity in the RBCC-powered system. This is because ethanol whose density is much higher than liquid hydrogen is applied to the propellant of RBCC engines aiming to reduce the vehicle size. However, the small but heavy vehicle suffers from higher takeoff velocity unless the vehicle has larger wings. The gross mass of the solution No. 4 of the RBCC-powered system is larger than the maximum takeoff mass of An-225 aircraft (600 t[94]), and further design improvements are required. Among the components of the booster vehicle, the mass of the landing gear occupies the largest portion, followed by that of the RBCC engines.

Details of the vehicle design in the representative optimal solutions are shown in Table 5.4 and Fig. 5.9. The booster fuselage has the minimum width required to load the orbiter on its uppersurface. The fuselage base of the booster is fully used as the external nozzle in solutions No. 1 and No. 2. Optimal inclination angle of the forebody undersurface is large, and this means that the improvement of the propulsive efficiency due to stronger pre-compression outweighs the increase in the drag of the airframe. The main wing is located at the rear end of the fuselage. This moves the neutral point for longitudinal static stability of the airframe rearward, and it is advantageous from the stability point of view. As for the RBCC engine design, $T_{\mathrm{R,max}}/S_{\mathrm{capt}}$ of the solution No. 4 is 290.9 kN/m^2. Solution No. 1 and solution No. 2 differ in their payload mass and vehicle gross mass with regard to objective values. The consequent differences in vehicle design mainly exist in the fuselage width of the booster, sweepback angle of the main wing, relative size of RBCC engines, and relative size of the orbiter. Solution No. 3 achieves the lowest takeoff velocity, but it inevitably results in large wings and heavier RBCC engines. Solution No. 4 has intermediate characteristics between the extreme solutions.

Table 5.3 Specifications of the representative Pareto optimal solutions.

Parameter		Unit	Solution No. 1		Solution No. 2		Solution No. 3		Solution No. 4	
			Booster	Orbiter	Booster	Orbiter	Booster	Orbiter	Booster	Orbiter
Payload mass		kg	1230.1		200.0		200.0		771.8	
Mated vehicle gross mass		t	800.0		359.8		800.0		651.6	
Takeoff velocity		m/s	200.0		200.0		92.0		175.4	
Maximum axial acceleration		G	3.1	3.1	3.6	3.6	3.8	3.8	3.2	3.2
Maximum load factor		G	1.2	2.5	1.3	2.5	1.3	2.5	1.2	2.5
Maximum dynamic pressure		kPa	43.2	43.2	42.2	42.2	33.1	33.1	41.9	41.9
Maximum exerted thrust		kN	6030.0	515.8	2925.7	187.3	9564.8	445.9	4908.4	368.1
Mass	Fuselage	t	11.0	3.7	6.6	1.5	16.7	2.2	9.1	2.8
	Main wing	t	9.4	0.0	4.0	0.0	24.3	0.0	8.1	0.0
	Tail wing	t	2.1	0.8	1.1	0.3	5.9	0.5	1.9	0.6
	Tanks	t	3.2	0.9	1.4	0.3	3.5	0.6	2.6	0.6
	Thermal protection system	t	2.7	3.0	1.5	1.3	4.2	1.9	2.4	2.3
	Landing gear	t	43.6	0.5	17.8	0.2	43.6	0.3	34.6	0.4
	RBCC engines	t	19.1	0.0	8.8	0.0	33.6	0.0	15.8	0.0
	Rocket engines	t	0.0	0.7	0.0	0.3	0.0	0.6	0.0	0.5
	Thrust structure	t	3.9	1.3	1.9	0.5	6.1	1.1	3.2	0.9
	The others	t	13.6	3.1	7.8	1.7	14.0	2.6	11.7	2.6
	Dry gross	t	108.6	15.2	50.8	6.2	152.0	10.1	89.6	11.5
	Ethanol	t	271.2	20.1	124.0	7.4	248.7	17.7	223.6	14.4
	LOX	t	352.7	32.2	159.5	11.9	343.3	28.3	289.6	23.1
	Gross	t	732.4	67.6	334.3	25.5	743.9	56.1	602.7	48.9

Table 5.4 Vehicle design of the representative Pareto optimal solutions.

Parameter		Unit	Solution No. 1	Solution No. 2	Solution No. 3	Solution No. 4
Booster	Fuselage length	m	41.1	34.3	50.2	37.6
	Fuselage upper height	m	1.1	0.9	1.7	1.0
	Forebody undersurface inclination	deg	8.0	8.0	6.9	8.0
	External nozzle angle	deg	15.1	13.7	11.1	15.0
	Forebody length	m	15.0	13.3	21.0	14.7
	Forebody tip width	m	4.2	3.0	8.1	3.9
	Exposed wing leading edge position	m	21.5	18.9	18.6	18.8
	Exposed wing root chord length	m	19.6	15.4	31.5	18.7
	Wing leading edge sweepback	deg	53.0	58.7	47.4	51.1
	Fore ethanol tank ends (forward, backward)	m	(5.0, 17.2)	(5.0, 16.0)	(5.0, 12.3)	(5.0, 15.4)
	LOX tank ends (forward, backward)	m	(17.7, 32.4)	(16.5, 29.0)	(21.0, 29.4)	(15.9, 29.9)
	Aft ethanol tank ends (forward, backward)	m	(32.9, 40.6)	(29.5, 33.8)	(45.4, 49.7)	(30.4, 37.1)
	Ceramic tile thickness on undersurface	mm	20.4	20.4	15.0	21.0
	Height of RBCC engines	m	2.4	1.7	3.2	2.3
	RBCC embedded rocket thrust	kN	5024.5	2390.9	8048.2	4068.3
Orbiter	Fuselage length	m	21.5	13.9	17.2	18.9
	Backward end of the cabin	m	12.9	6.7	6.6	11.0
	Rocket thrust	kN	515.8	187.3	445.9	368.1

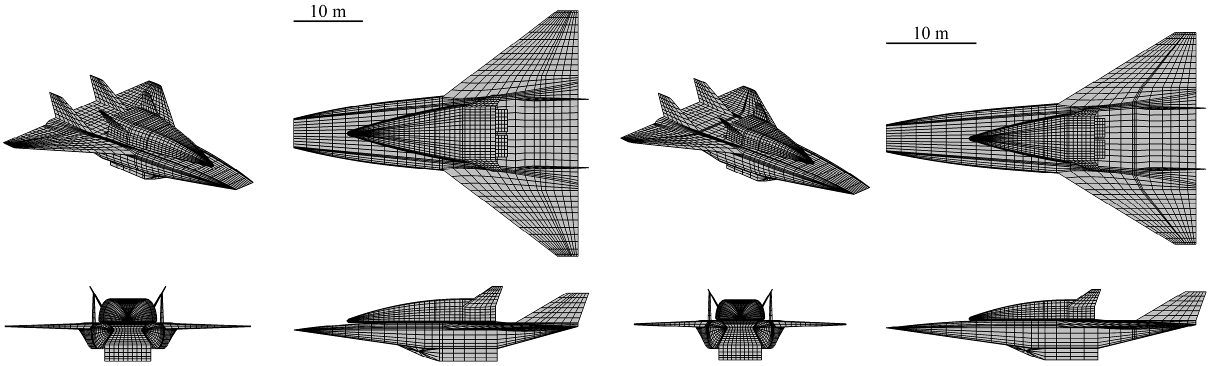

(a) Solution No. 1.

(b) Solution No. 2.

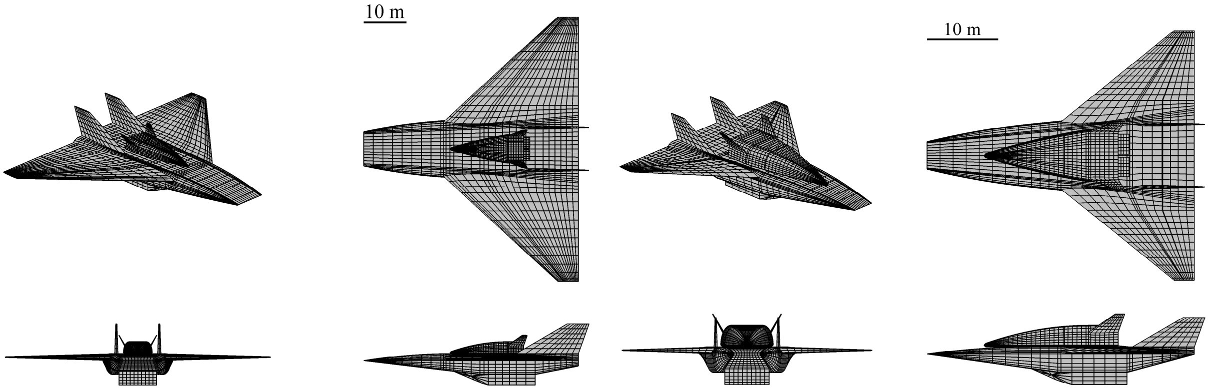

(c) Solution No. 3.

(d) Solution No. 4.

Fig. 5.9 Vehicle shape of the representative Pareto optimal solutions.

The flight trajectories of the solutions Nos. 1–4 are shown in Figs. 5.10, 5.14, 5.18, and 5.22, respectively. The behavior of the trajectory in the solution No. 4 is detailed below. After the horizontal takeoff, the mated vehicle accelerates and climbs with a large angle of attack. Since the vehicle thrust-to-weight ratio at takeoff is 0.638, which is less than 1, the lift force must play a major role in the takeoff. During ejector-jet mode operation, flight dynamic pressure increases, decreases, and increases again. Instead of flying with the maximum dynamic pressure, this maneuver is intended to increase the altitude rapidly and to enhance the performance of the external nozzle. Figure 5.22c indicates that the optimal flight trajectory does not have a dive phase in the transonic region, in contrast to the TSTO RLV with the PCTJ engines studied in Chapter 4, This dissimilarity can be attributed to the fact that the thrust-to-mass ratio of the RBCC engine is higher than that of the hypersonic turbojet engine. Therefore, the optimal RBCC-powered vehicle has enough thrust performance to pass the transonic drag rise without a dive maneuver. The engine operating mode is switched over to ramjet mode at a flight Mach number of 3.8. This corresponds to the condition where the engine inflow Mach number, Ma_{in}, reaches 3.0 and therefore ramjet mode becomes available. Ramjet mode is operated at the maximum dynamic pressure prior to 370 s, at which point the dynamic pressure begins decreasing. Subsequently, the RBCC engines are switched to scramjet mode when the vehicle reaches Mach 5.9. During the acceleration in the scramjet mode, the engines are gradually throttled down. Finally, the vehicle begins a steep climb by raising its angle of attack.

When the propellant in the booster is used up, the orbiter is separated from the booster. At that moment, Mach number and dynamic pressure are 11.9 and 4.8 kPa, respectively. The rocket engine on the orbiter is ignited and operated at full throttle. The orbiter ascends quickly to an altitude of 100 km and then continues to accelerate while descending slightly. At the terminal time, the orbiter is on an elliptic orbit with an apogee of 350 km above sea level.

Figure 5.22f indicates that the thermal balance of the active cooling system is achieved without dumping the ethanol. It is also noted that most of the ethanol coolant is used for cooling the RBCC engines. Since the path constraint in Eq. (5.19) becomes active around 450 s, the thermal-balance requirements actually have influences on the system design. Until 90 s after the takeoff, ethanol fuel is mainly consumed from the aft tank, followed by the consumption only from the fore tank until 360 s. After there is an oscillating behavior between 360 s and 450 s, the fuel is expended only from the aft tank again. This switching strategy in the fuel consumption maximizes the effectiveness of the elevons while attaining non-negative static stability.

Time histories of the performance of the RBCC engines and the rigid body characteristics of the vehicle in solution No. 4 are given in Fig. 5.24. Note that the performance of the total RBCC propulsion system including the external nozzle is defined as follows:

$$T_{\mathrm{tot}} = T_{\mathrm{rbcc}} + \frac{5}{1.81} F_{\mathrm{ext}}\, e_{\mathrm{h}}{}^{2} \sin b_{\mathrm{ext}}, \tag{5.69}$$

$$Isp_{\mathrm{tot}} = Isp_{\mathrm{rbcc}} \left(1 + \frac{5}{1.81} \frac{F_{\mathrm{ext}}\, e_{\mathrm{h}}{}^{2} \sin b_{\mathrm{ext}}}{T_{\mathrm{rbcc}}} \right), \tag{5.70}$$

where the subscript $(\cdot)_{\mathrm{tot}}$ indicates that the attached variable indicates the quantity of the total RBCC propulsion system. In the early part of the flight (prior to 140 s), the external nozzle generates negative thrust, namely, drag. This is due to the fact that the nozzle is in an over-expansion condition or in a slight under-expansion condition, and the mean ramp pressure becomes lower than the ambient-flow pressure. It is noted that the external nozzle also decreases lift force when it is in such a condition. After the nozzle expansion condition becomes an under expansion (i.e., $p_{\mathrm{e}} > p_{\mathrm{a}}$ in Fig. 5.4b), thrust and specific impulse are augmented. Flow fields in the external nozzle at some representative times are presented in Fig. 5.24. At 65 s, the external nozzle is in an optimum-expansion condition (i.e., $p_{\mathrm{e}} = p_{\mathrm{a}}$), and the thrust augmentation by the nozzle becomes largest in negative. Around 35 s, the magnitude of thrust augmentation is almost zero, even though the nozzle is in a strong over-expansion condition. This is because, in an excessively over-expanded nozzle, the pressure of exhaust flow increases as it interacts with the ambient flow (see Fig. B.5a). In Fig. 5.24b and Fig. 5.24c, the ramp pressure monotonically decreases as it goes downstream. This rate of decrease becomes higher after expansion waves generated at the cowl lip arrive on the ramp wall. A triangular high-pressure area located soon after the combustor exit is called the potential core of the exhaust. During ramjet mode, the exhaust Mach number becomes lower, since the chamber pressure of the embedded rockets is reduced. This results in shorter potential

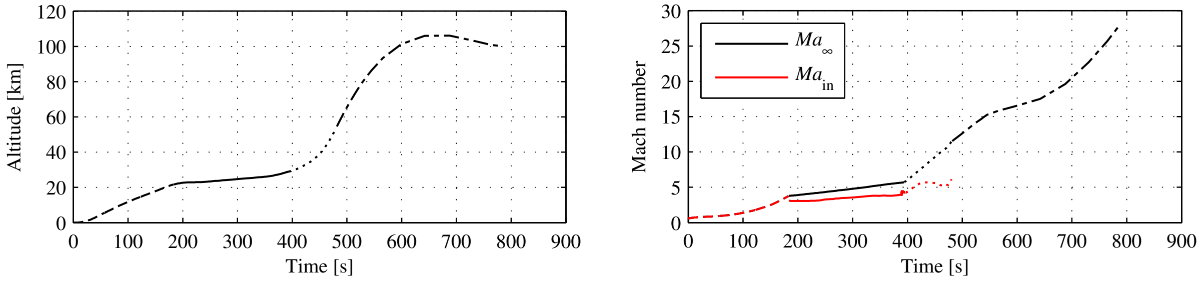

(a) Time history of altitude. (b) Time history of Mach number.

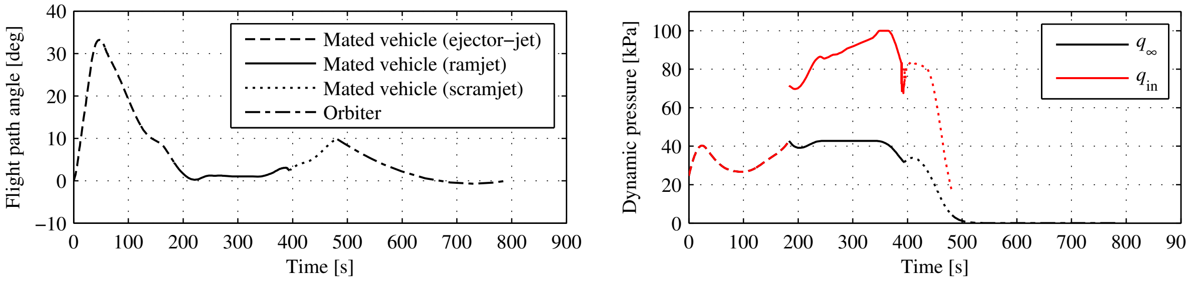

(c) Time history of flight path angle. (d) Time history of dynamic pressure.

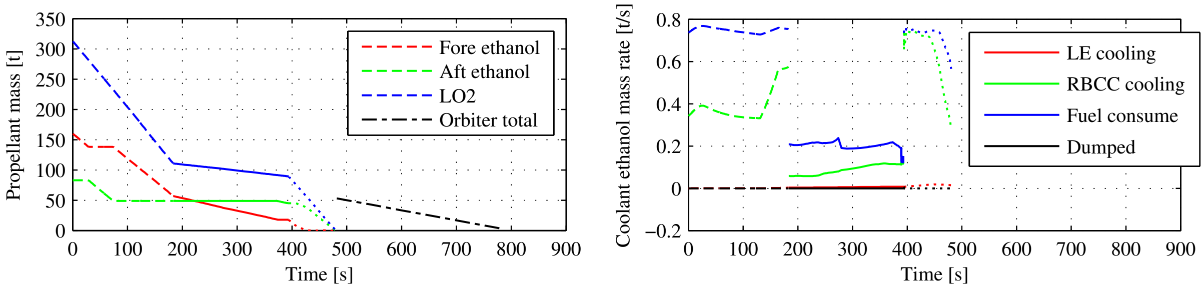

(e) Time history of remaining propellant mass. (f) Time history of thermal balance in active cooling.

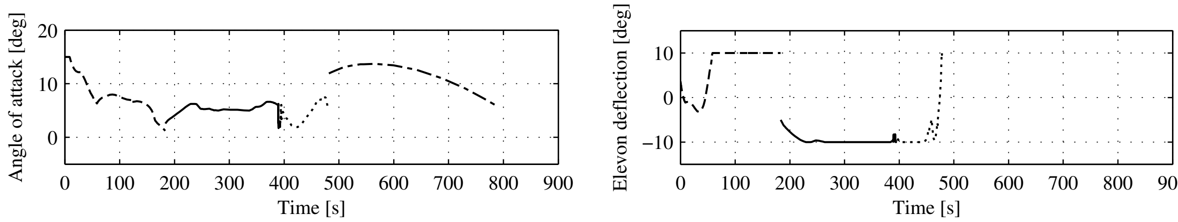

(g) Time history of angle of attack. (h) Time history of elevon deflection angle.

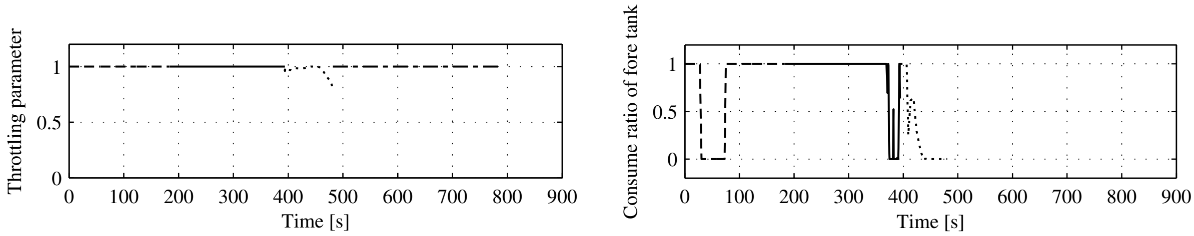

(i) Time history of thrust throttling parameter. (j) Time history of the usage ratio of the fore ethanol tank.

Fig. 5.10 Flight trajectory of the solution No. 1.

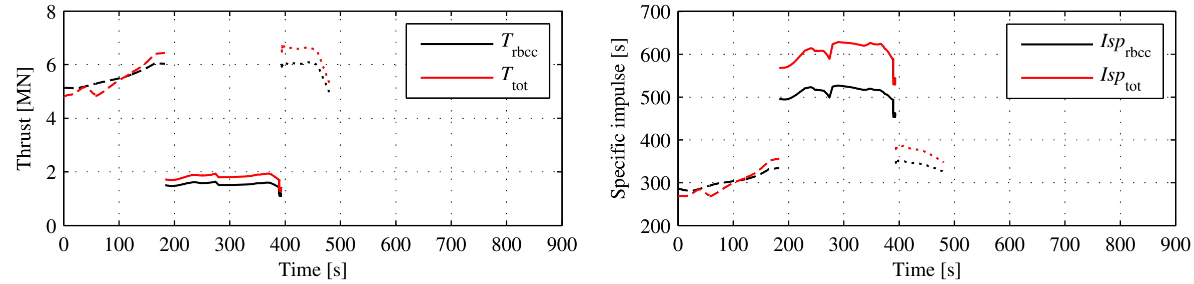

(a) Time history of thrust magnitude.

(b) Time history of specific impulse.

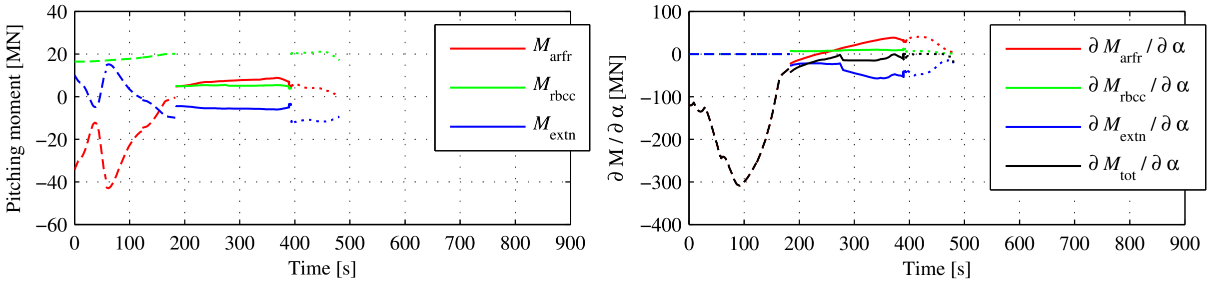

(c) Time history of pitching moment.

(d) Time history of longitudinal stability derivative.

Fig. 5.11 Propulsion efficiency and rigid body characteristics of the solution No. 1.

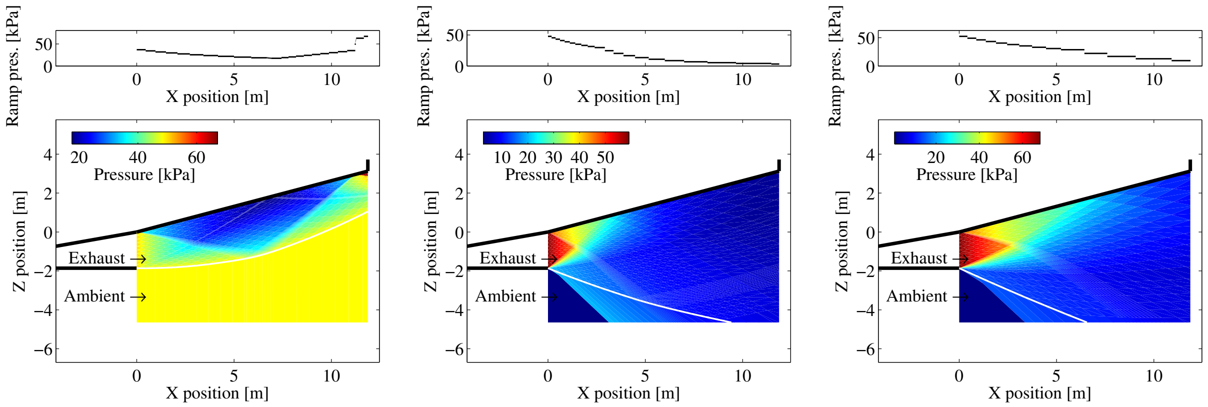

(a) 59 s.

(b) 289 s.

(c) 423 s.

Fig. 5.12 External nozzle flow of the RBCC engines in the solution No. 1.

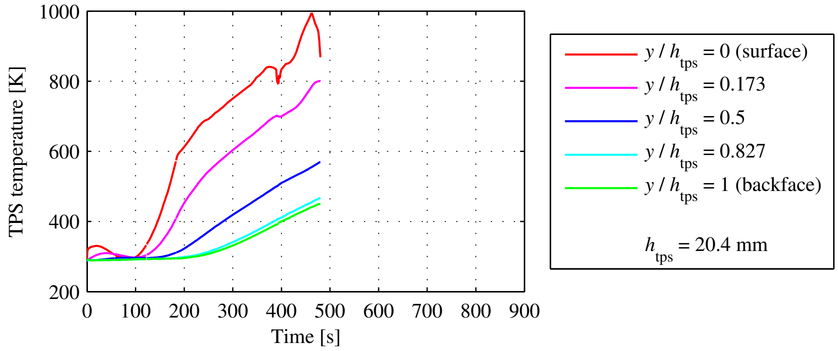

Fig. 5.13 Time history of ceramic tile temperature on the booster undersurface in the solution No. 1.

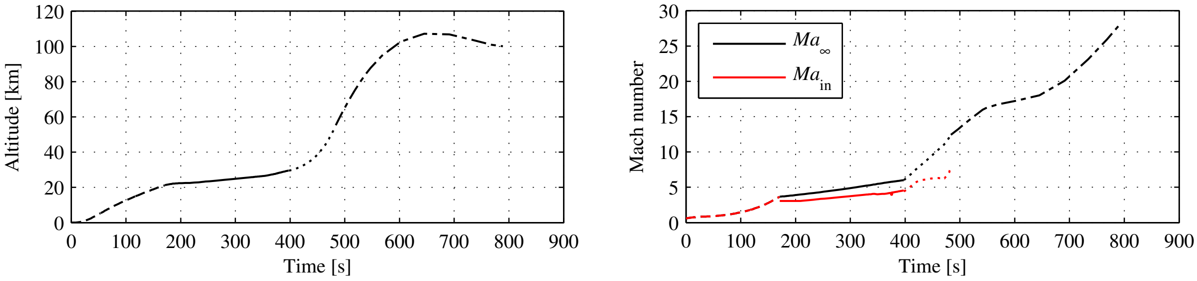

(a) Time history of altitude.

(b) Time history of Mach number.

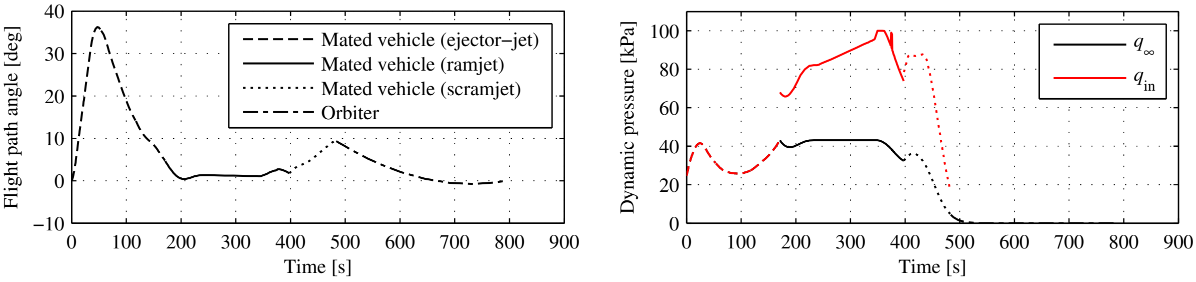

(c) Time history of flight path angle.

(d) Time history of dynamic pressure.

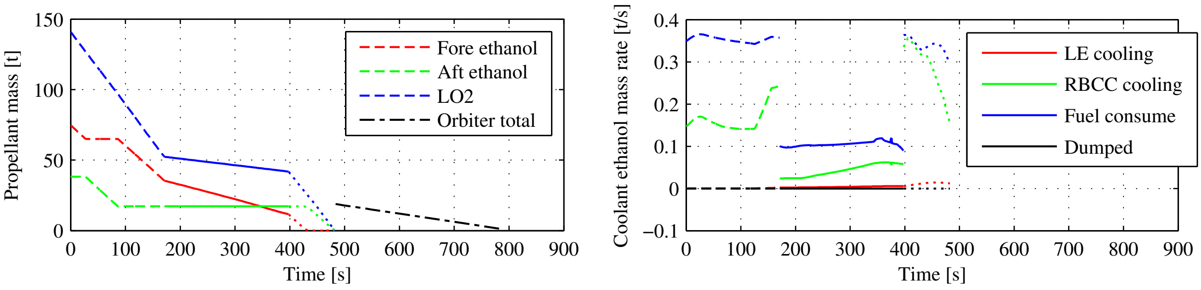

(e) Time history of remaining propellant mass.

(f) Time history of thermal balance in active cooling.

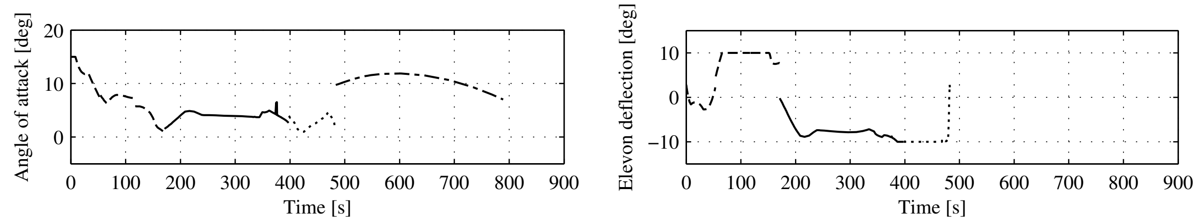

(g) Time history of angle of attack.

(h) Time history of elevon deflection angle.

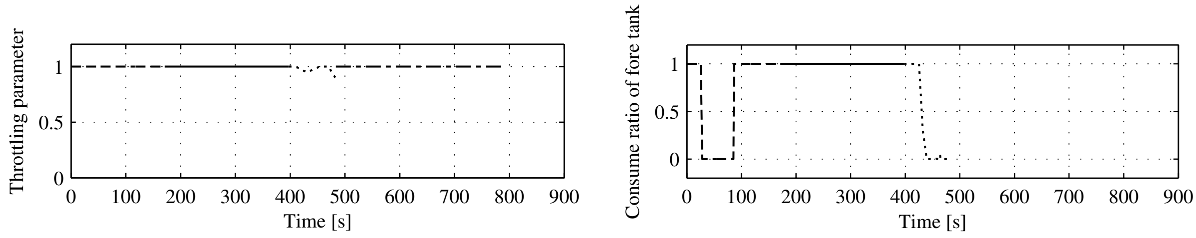

(i) Time history of thrust throttling parameter.

(j) Time history of the usage ratio of the fore ethanol tank.

Fig. 5.14 Flight trajectory of the solution No. 2.

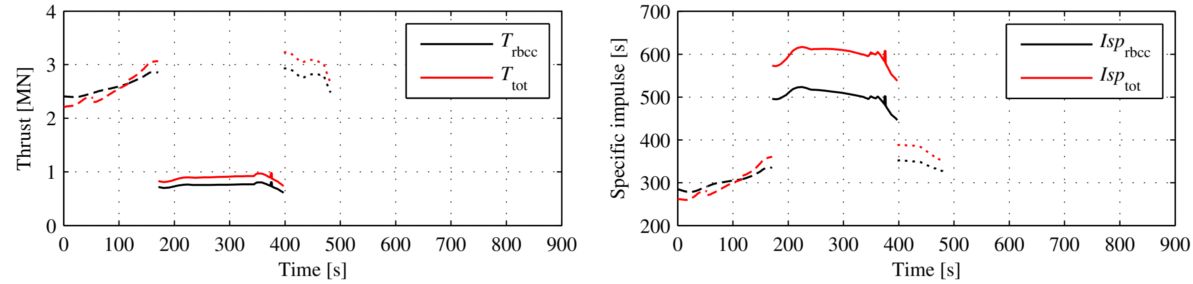

(a) Time history of thrust magnitude.

(b) Time history of specific impulse.

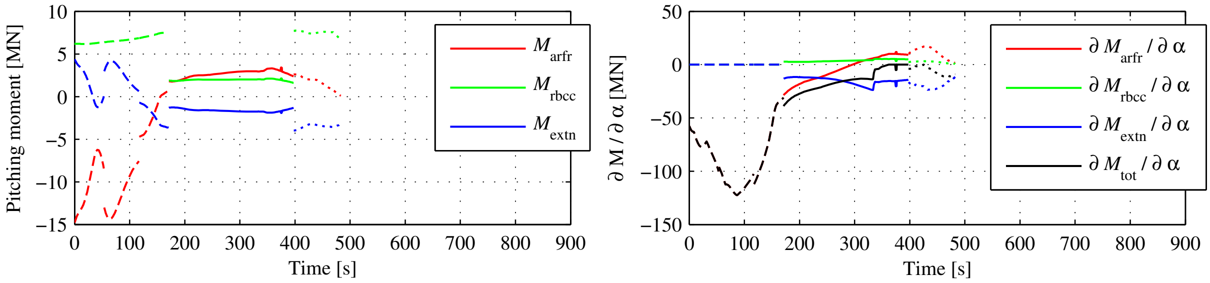

(c) Time history of pitching moment.

(d) Time history of longitudinal stability derivative.

Fig. 5.15 Propulsion efficiency and rigid body characteristics of the solution No. 2.

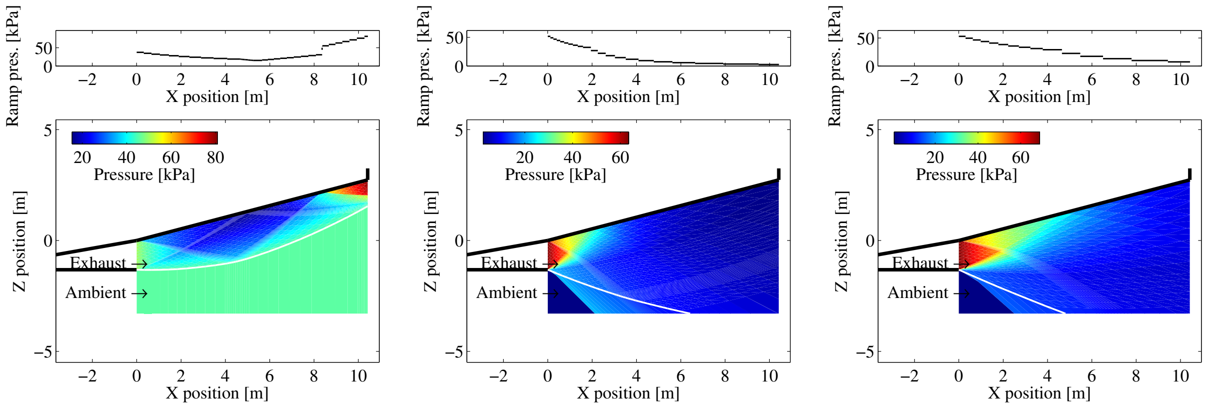

(a) 59 s.

(b) 284 s.

(c) 426 s.

Fig. 5.16 External nozzle flow of the RBCC engines in the solution No. 2.

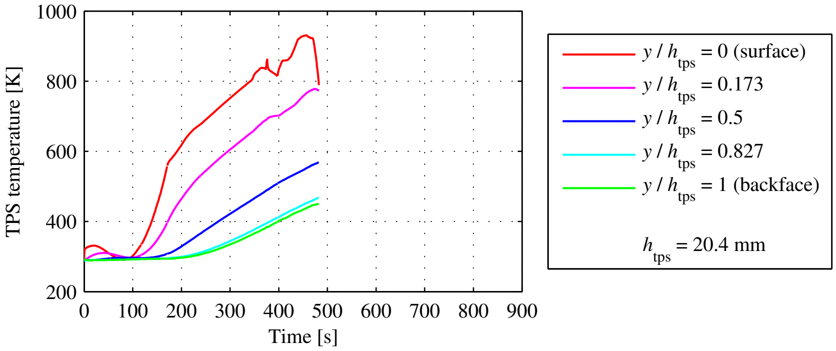

Fig. 5.17 Time history of ceramic tile temperature on the booster undersurface in the solution No. 2.

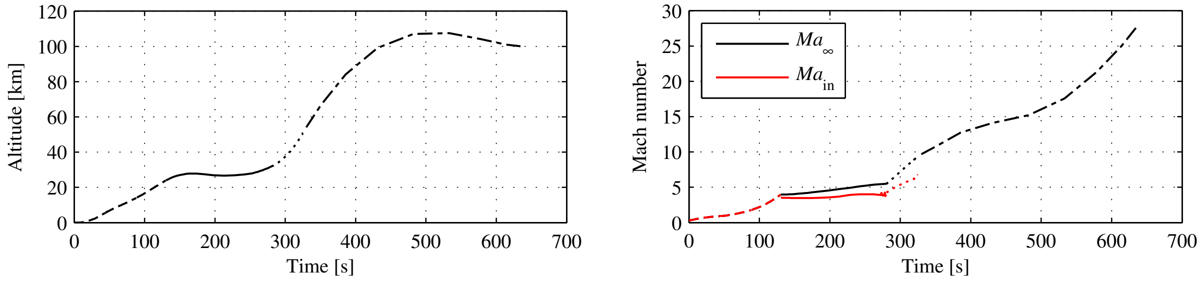

(a) Time history of altitude.

(b) Time history of Mach number.

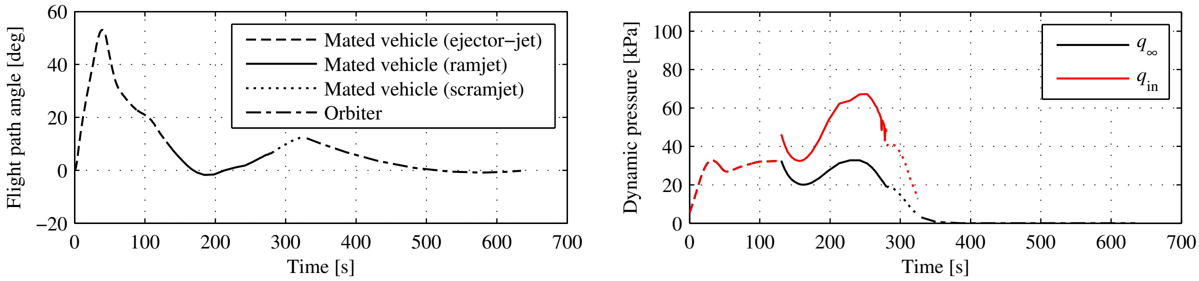

(c) Time history of flight path angle.

(d) Time history of dynamic pressure.

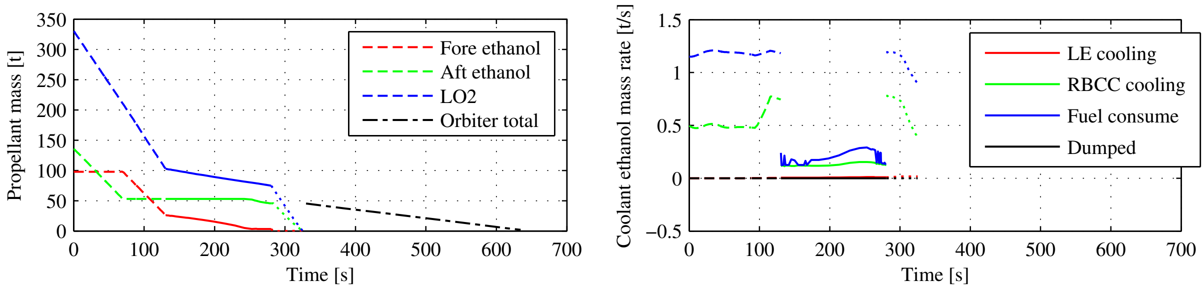

(e) Time history of remaining propellant mass.

(f) Time history of thermal balance in active cooling.

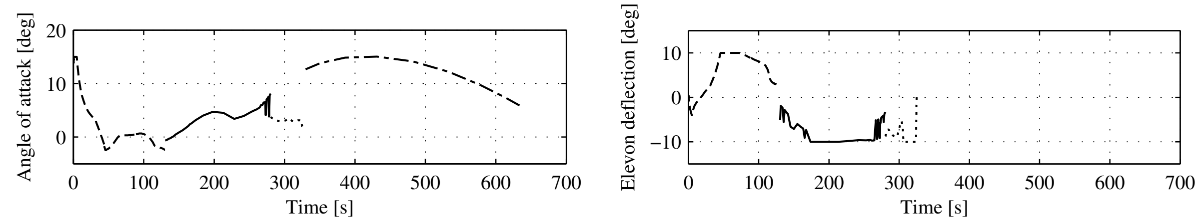

(g) Time history of angle of attack.

(h) Time history of elevon deflection angle.

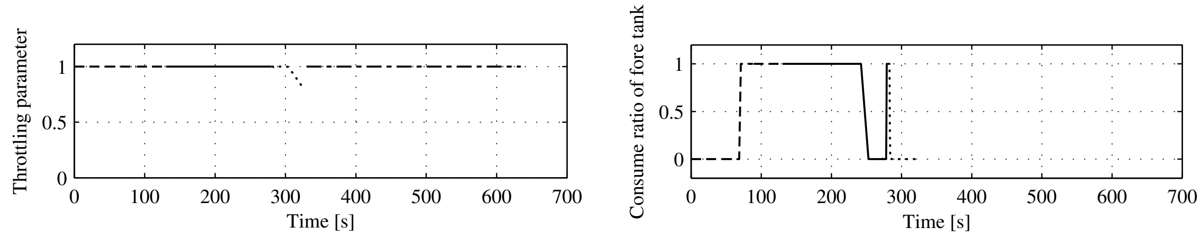

(i) Time history of thrust throttling parameter.

(j) Time history of the usage ratio of the fore ethanol tank.

Fig. 5.18 Flight trajectory of the solution No. 3.

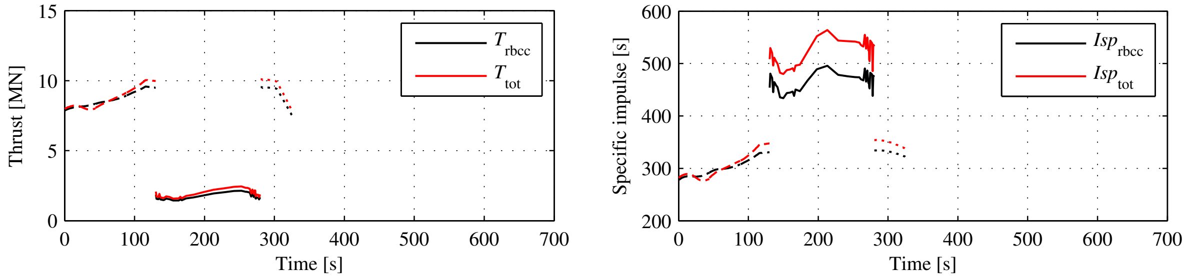

(a) Time history of thrust magnitude.

(b) Time history of specific impulse.

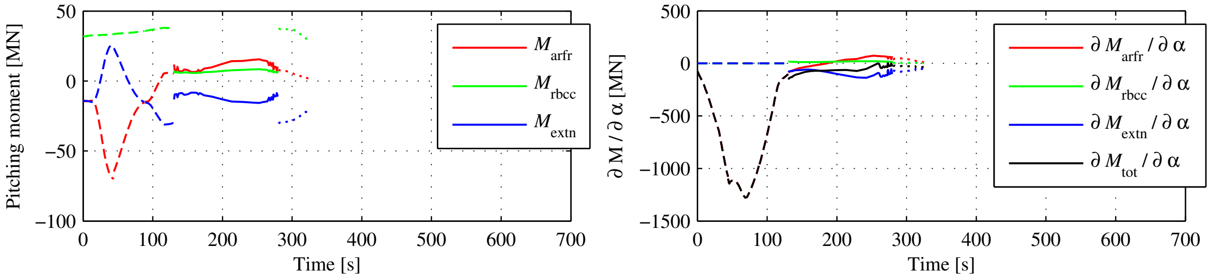

(c) Time history of pitching moment.

(d) Time history of longitudinal stability derivative.

Fig. 5.19 Propulsion efficiency and rigid body characteristics of the solution No. 3.

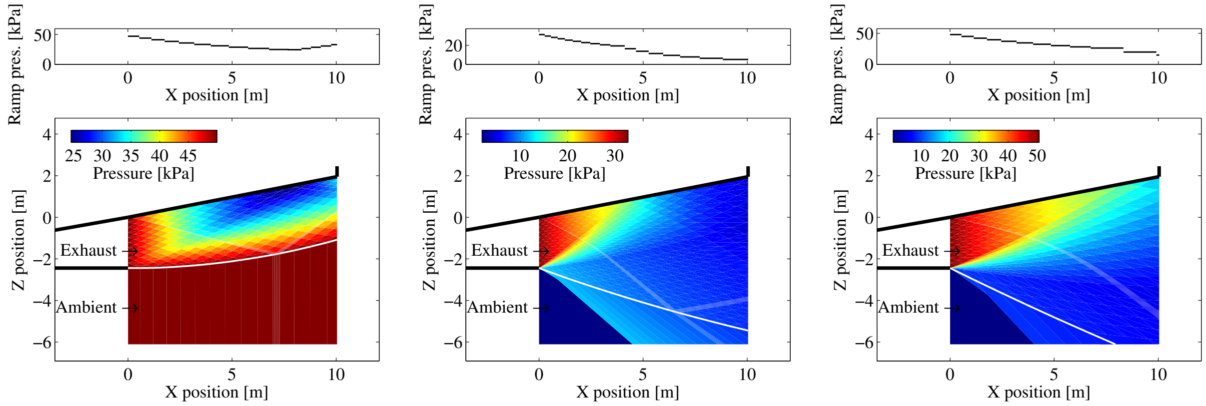

(a) 44 s.

(b) 205 s.

(c) 295 s.

Fig. 5.20 External nozzle flow of the RBCC engines in the solution No. 3.

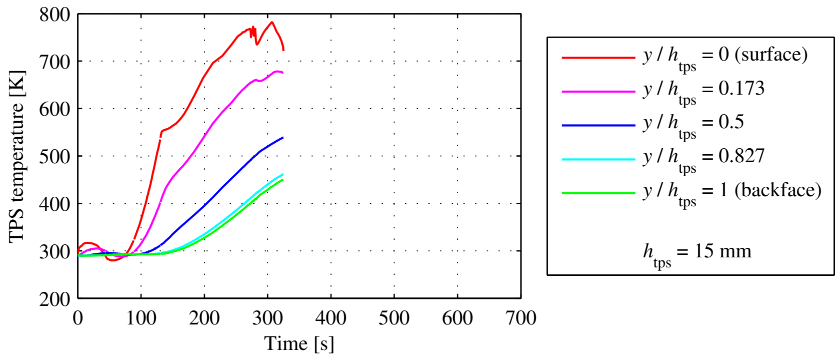

Fig. 5.21 Time history of ceramic tile temperature on the booster undersurface in the solution No. 3.

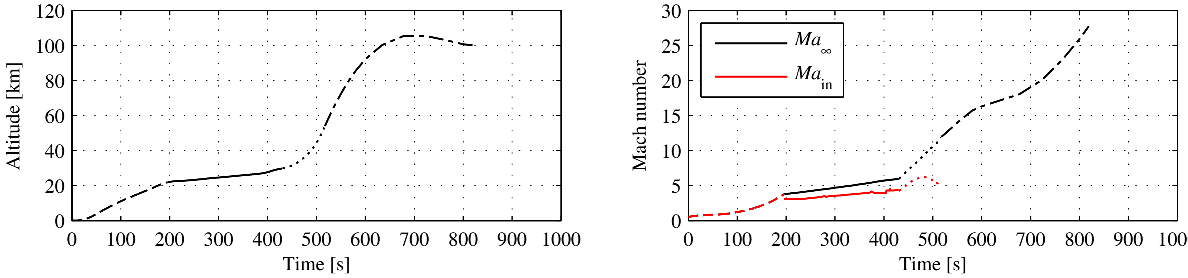

(a) Time history of altitude.

(b) Time history of Mach number.

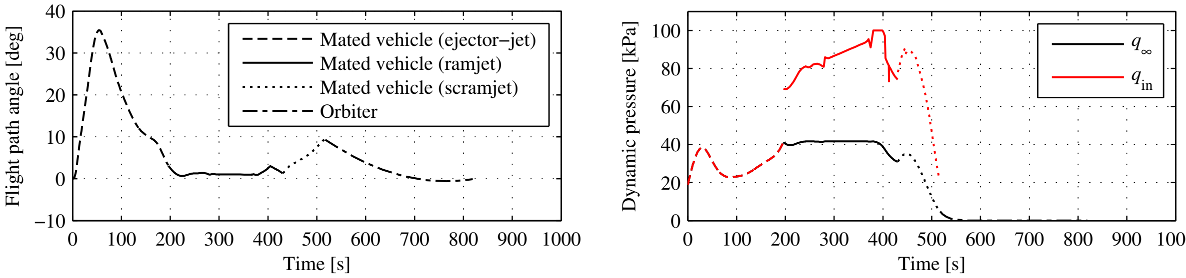

(c) Time history of flight path angle.

(d) Time history of dynamic pressure.

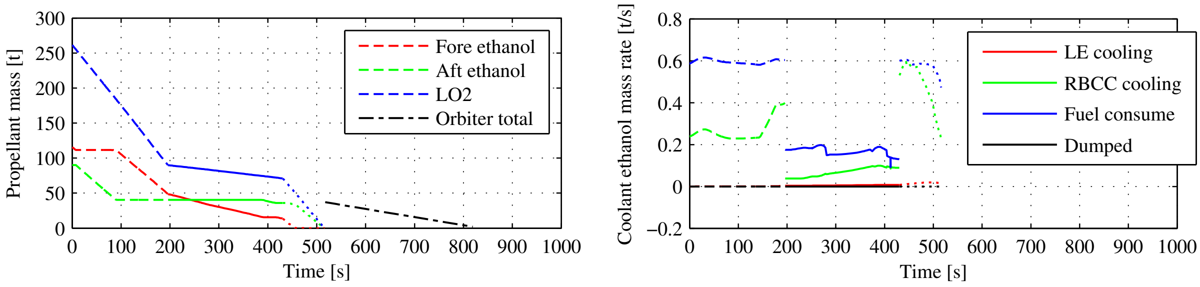

(e) Time history of remaining propellant mass.

(f) Time history of thermal balance in active cooling.

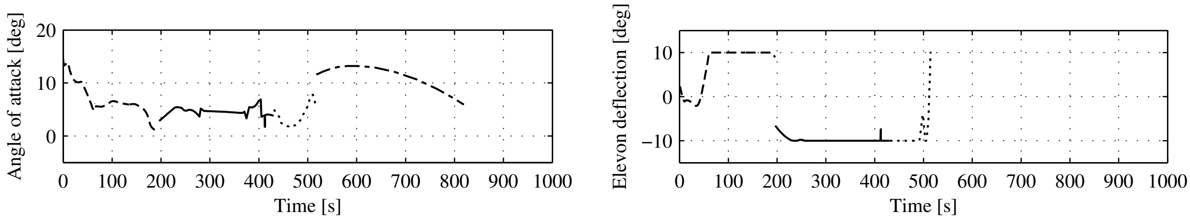

(g) Time history of angle of attack.

(h) Time history of elevon deflection angle.

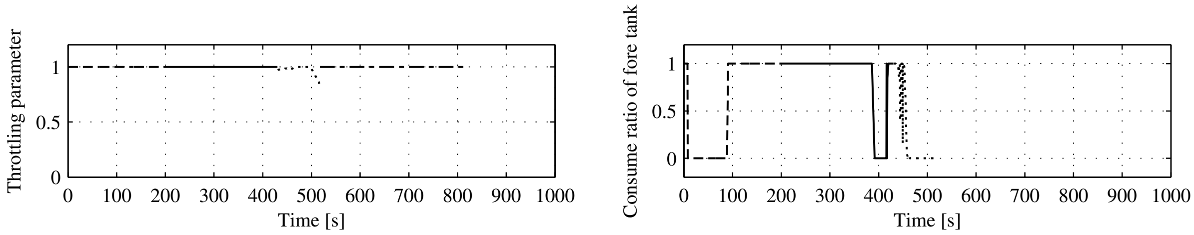

(i) Time history of thrust throttling parameter.

(j) Time history of the usage ratio of the fore ethanol tank.

Fig. 5.22 Flight trajectory of the solution No. 4.

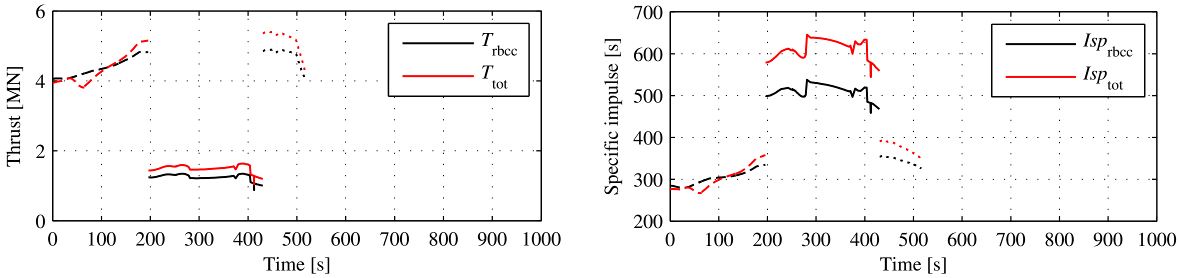

(a) Time history of thrust magnitude. (b) Time history of specific impulse.

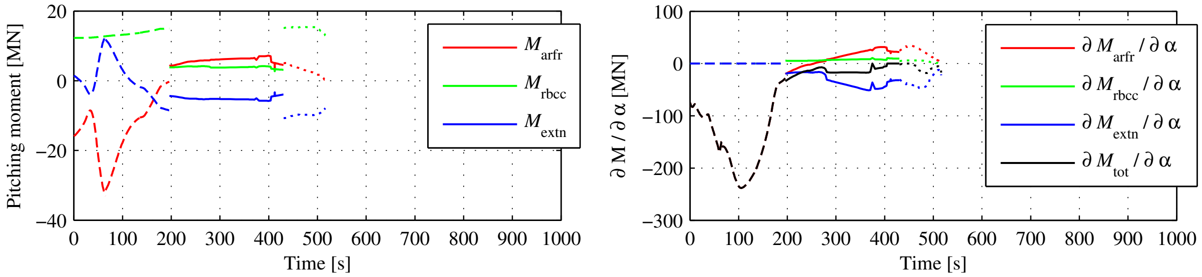

(c) Time history of pitching moment. (d) Time history of longitudinal stability derivative.

Fig. 5.23 Propulsion efficiency and rigid body characteristics of the solution No. 4.

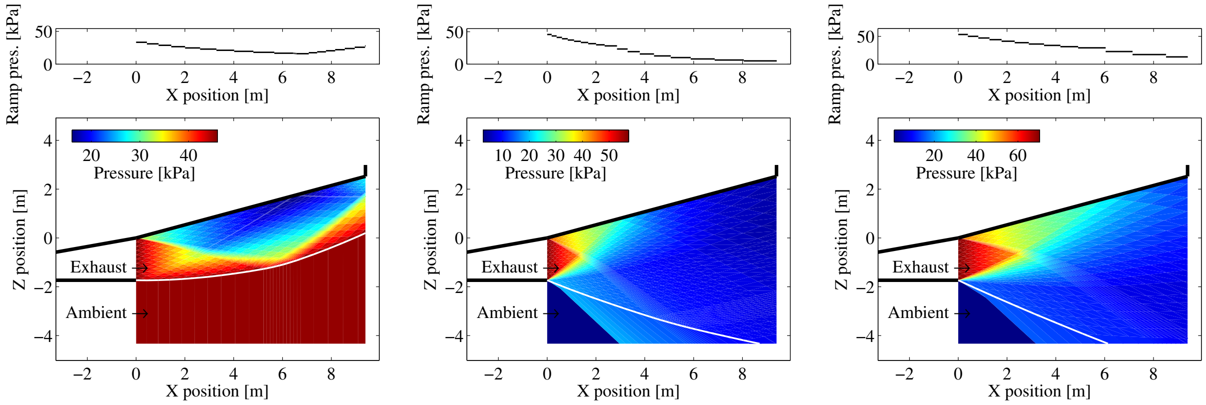

(a) 66 s. (b) 313 s. (c) 459 s.

Fig. 5.24 External nozzle flow of the RBCC engines in the solution No. 4.

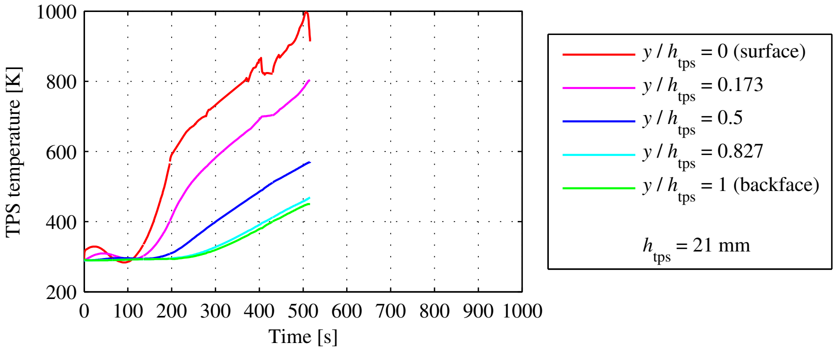

Fig. 5.25 Time history of ceramic tile temperature on the booster undersurface in the solution No. 4.

core in ramjet mode compared with that in scramjet mode. As a consequence of slower exhaust flow in ramjet mode, expansion waves generated at the cowl lip reach the ramp wall at more upstream locations, and the wall pressure decreases more sharply.

Figure 5.23c shows that there are large differences of pitching moments generated by RBCC engines and the external nozzle between different engine operating modes. The requirement of maintaining pitching trim throughout multiple engine modes results in the saturation of the elevon deflection angle even though the vehicle has large elevons. If the propulsion system has a gimbal or a thrust vectoring mechanism as in the case of Ref. 15, this problem would be solved. As for the longitudinal static stability, the stability of the airframe alone is lost ($\partial M_{\mathrm{arfr}}/\partial\alpha > 0$) after 255 s or above Mach 4.3. In addition, since $\partial M_{\mathrm{rbcc}}/\partial\alpha > 0$, the moment produced by the RBCC engines slightly deteriorates the stability. It is because, a larger angle of attack makes the pre-compression prior to the inlet stronger, and it leads to larger thrust and a larger positive pitching moment produced by the RBCC engines. These instabilities are compensated by the moment induced by the external nozzle. A larger angle of attack increases pressure on the external nozzle ramp, and this results in a larger negative pitching moment (i.e., $\partial M_{\mathrm{extn}}/\partial\alpha < 0$). In total, non-negative stability is attained throughout the ascent flight.

As a consequence of TPS design, the required thickness of the ceramic tile TPS installed on the booster undersurface, h_{tps}, in solution No. 4 is 21.0 mm. Figure 5.25 shows the time history of the tile temperature. It is noted that the temperature on the backface that is bonded to the vehicle main structure does not exceed the upper bound, 450 K, during the ascent flight. In calculating aerodynamic heat flux on the vehicle surface, a shock wave or an expansion fan generated at the booster nose is taken into account. Therefore, the temperature at the surface changes rapidly in response to abrupt changes of angle of attack around 400 s. In actual flight, the tile temperature on the backface continues to increase in the return flight. Therefore, the truly needed tile thickness would be larger than 21.0 mm.

Optimal flight trajectories of the other solutions have basic features similar to that of solution No. 4, while their details are substantially different among solutions.

5.5 Knowledge Discovery in Pareto Optimal Solutions Using Data Mining Techniques

It is troublesome or impossible to examine all the obtained solutions one by one. In order to extract comprehensive knowledge from the solutions, data mining techniques are employed in this section.

5.5.1 Data Mining from Optimal Vehicle Designs

The scatter plot matrix of objective values and some notable parameters is given in Fig. 5.26. See Appendix F.1 for details on scatter plot matrices. The following observations can be made:

1) Optimal velocity increment allocation to the booster is distributed between 3.1 km/s to 4.0 km/s, or from Mach 9.5 to Mach 12.4, and it is highly associated with the takeoff-velocity requirement.

When lower takeoff velocity is enforced, the increase of the booster dry mass is inevitable, and hence less velocity increment should be assigned to the booster.

2) In Pareto optimal booster designs, the decrease of the takeoff velocity is primarily achieved by enlarging the exposed wing and by increasing fuselage width-to-length ratio. Optimal fuselage length is related to the takeoff velocity only when it is lower than 130 m/s.

3) Optimal external nozzle ramp angle of the RBCC engines has a strong relation with the takeoff-velocity requirement. Smaller ramp angle alleviates the over-expansion of the external nozzle in low altitude, and it is favorable in terms of takeoff performance. Since hypersonic acceleration performance is deteriorated by reducing the ramp angle, this tradeoff relation must be considered in designing the external nozzle.

4) The embedded rocket thrust and the total inlet area of RBCC engines are in a strong linear relation. It is also noted that these design parameters of RBCC engines and the vehicle gross mass are correlated.

5) The payload mass and length of the orbiter are highly associated, implying that a larger orbiter vehicle is required for transporting more payload. Optimal vacuum thrust of the orbiter rocket engine is determined by the orbiter size. Not surprisingly, optimal orbiter design does not depend on the takeoff-velocity requirement.

6) Optimal flight Mach numbers at which ramjet mode is started can be clustered into two groups: ramjet mode is employed as soon as possible when it becomes available ($M_{\text{in}} = 0$), or not. In the former group, ramjet start Mach number is around 3.7. When the external nozzle angle is reduced considering the takeoff performance, ramjet mode is not operated in low Mach number where it suffers from low thrust (see Fig. 5.6a).

7) Flight dynamic pressure at the moment of staging differs among solutions within the range of $[4.4, 6.6]$ kPa, and it has no significant correlation with the other parameters. Compared to the TSTO RLV with PCTJ engines, the optimal staging dynamic pressure in the present case is higher.

8) The optimal thrust-to-mass ratio at takeoff is within $[0.62, 1.1]$, and it has a significant correlation with the takeoff velocity. This suggests that the design of the TSTO RLV with RBCC engines is strongly constrained by the takeoff-performance requirement. Realizing a low takeoff velocity around 100 m/s is not realistic, since the thrust-to-mass ratio becomes more than one. It is noted that the optimal thrust-to-mass ratio of the PCTJ-powered vehicle is around 0.6, and the ratio is almost independently from the takeoff velocity (see Section 4.5.1).

5.5.2 Data Mining from Optimal Flight Trajectories

Proper orthogonal decomposition (POD) is employed in the same way as Section 4.5.2. The flight trajectory of solution No. 4 is selected as a nominal trajectory. In the present case, the first POD mode

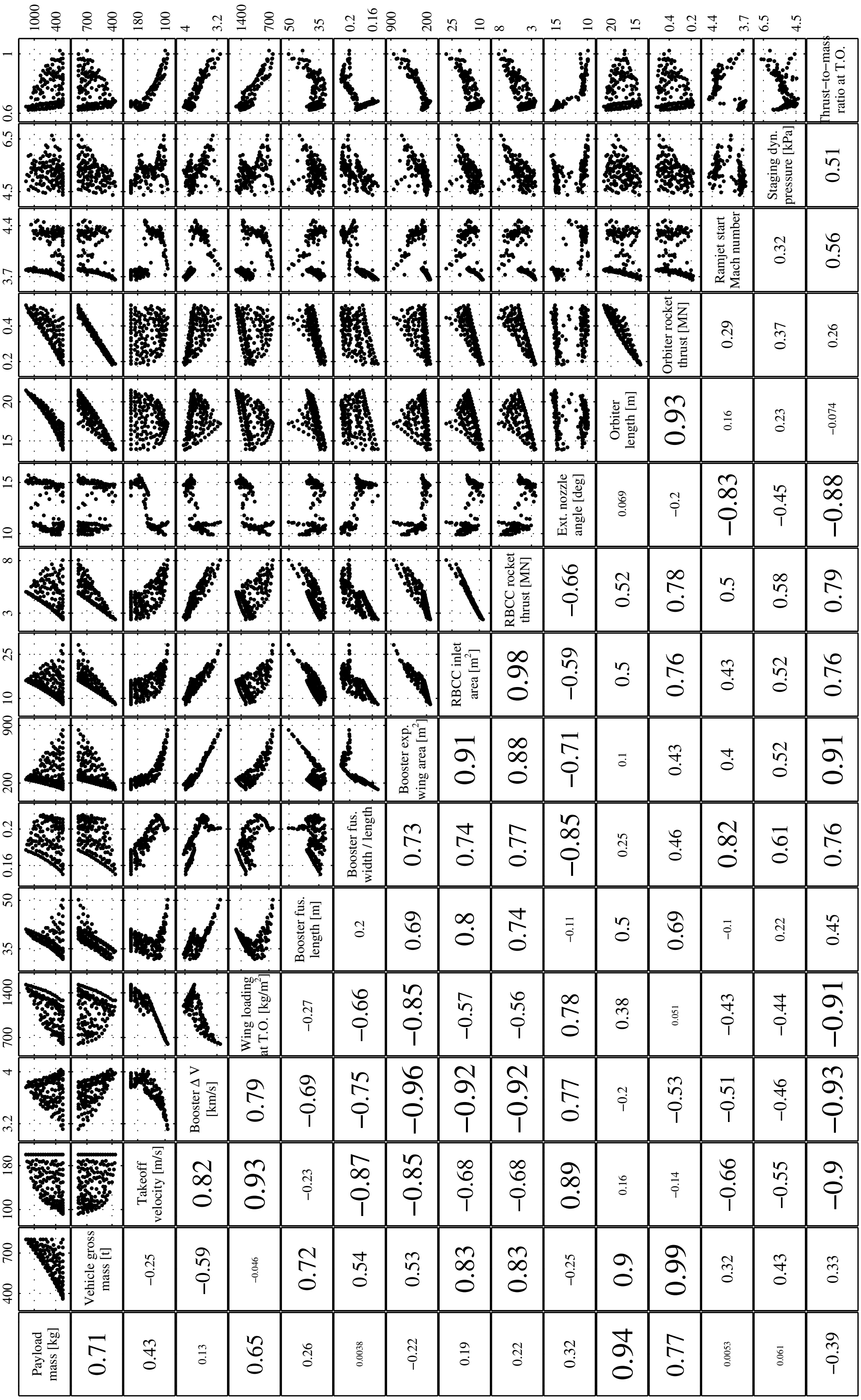

Fig. 5.26 Scatter plot matrix of the Pareto optimal solutions to multi-objective MDO of the TSTO RLV with RBCC engines.

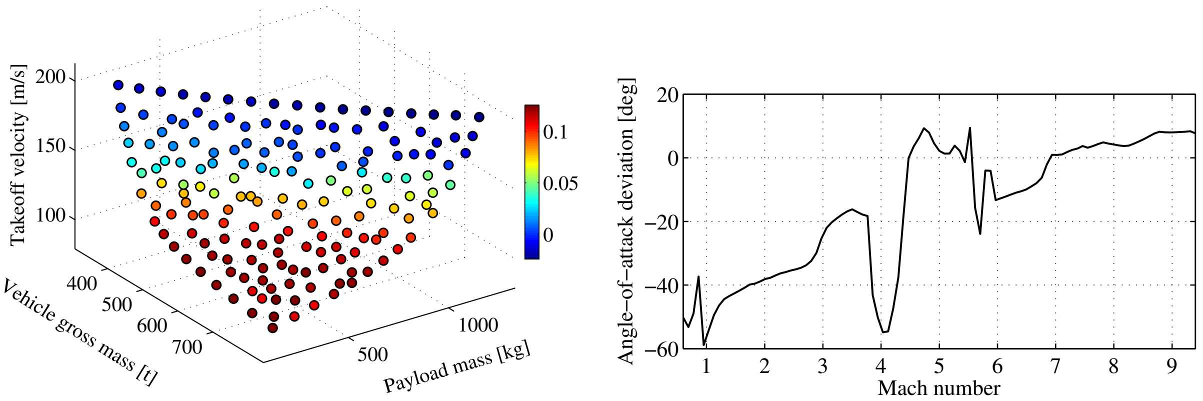

(a) Coefficient of the first POD mode.

(b) Basis of the first POD mode.

Fig. 5.27 Proper orthogonal decomposition (POD) of angle-of-attack histories of the Pareto optimal solutions.

accounts for 87.8 % of the whole deviations from the nominal trajectory in terms of the energy content. Figures 5.27a and 5.27b show the coefficient and basis of the first mode, respectively. The following knowledge is acquired:

1) Figure 5.27a indicates that the coefficient depends mainly on the takeoff velocity. This means that optimal angle of attack at each Mach number is principally associated with the takeoff velocity, or equivalently, wing loading.

2) The deviation of optimal angle of attack resulting from the variation of the takeoff velocity can be described using the basis shown in Fig. 5.27b. As the takeoff velocity becomes higher, optimal angle of attack gets larger when Mach number is less than 3.5. The sensitivity between the optimal angle of attack and the takeoff velocity becomes lower as the Mach number increases. Rapid change of the basis value around Mach 4 is due to the fact that ramjet mode is started at a different Mach number around 4 in each Pareto optimal trajectory. During the ramjet mode operation, angle of attack is less sensitive to the takeoff velocity. The positive basis value above Mach 7 indicates the tendency that the beginning of the steep climb before the staging is delayed as the takeoff velocity is higher. This observation is consistent with the positive correlation between the optimal staging velocity and takeoff velocity revealed in the scatter plot matrix.

Chapter 6

Summary

6.1 Conclusion

In order to promote the commercial usage of outer space, there is an increasing need for reusable launch vehicles (RLVs). In particular, RLVs with airbreathing engines are expected to reduce the transportation cost into the orbit by more than an order of magnitude and to have aircraft-like operability and reliability. An essential effort for realizing such RLVs is to conduct their conceptual design studies early so as to clarify technology goals and to facilitate the development of key technologies accordingly. A major concern in designing RLVs with airbreathing engines is the existence of complex interactions between design disciplines. A notable difference from design problems of aircraft is that RLVs do not have a cruising state, and the interaction between vehicle design and flight trajectory design must be considered. Therefore, multidisciplinary design optimization (MDO), where design optimization and optimal control of the vehicle are coupled, is indispensable for carrying out RLV design effectively. Another issue is that, it is preferable to perform the conceptual design studies while considering uncertainties in mission requirements and future technological developments, since the targeted RLVs are long-term goals. In order to handle these difficulties and demands, the present study focused on a knowledge-discovery framework based on the synergy of multi-objective optimization and data mining. Proposals were mainly given regarding the following two challenging subjects for performing multi-objective MDO of RLVs efficiently: a multi-objective optimization method suited to optimal control problems, and a numerical technique for integrating thermal protection system (TPS) into the MDO of RLVs.

First, a novel optimization method for efficiently obtaining Pareto optimal solutions to multi-objective optimal control problems was developed in Chapter 2. On the basis of the insight that multi-objective evolutionary algorithms have some weaknesses in handling parameter interactions and equality constraints that are inherent in optimal control problems, the proposed method successively searches a Pareto optimal solution using a gradient-based optimizer. Since gradient-based optimization methods cannot solve a multi-objective problem directly, the original problem is transformed into a relevant single-objective one by means of min-max goal programming. Parameters used in the min-max goal programming are specified adaptively so that the resulting solution will be located near the farthest point from the solutions obtained so far in the objective space. The farthest point is determined by exploiting the property that the Pareto front of a multi-objective optimization problem defines a manifold whose dimension is lower than the number of objectives by one. Existing solutions on the Pareto-front manifold are mapped into a lower dimensional Euclidean space using linear or nonlinear dimensionality reduction technique depending on the uniformness of the solution distribution. Then, the farthest point in this Euclidean space is searched via a Voronoi diagram. Next, the found point is mapped back to the original objective space, and it gives the farthest point from the existing solutions in terms of the geodesic distance along the Pareto front. By successively employing gradient-based optimization, min-max goal programming, and the Pareto manifold sampling, a set of Pareto optimal solutions with a good spread is finally obtained. Performances of the present method and a multi-objective genetic algorithm (MOGA) were compared by conducting numerical experiments using a test problem with a terminal equality constraint. The result revealed that the proposed technique outperforms the MOGA in terms of optimality, constraint residual, and diversity of the obtained solutions. In addition, the applicability of the developed method to a more complex and practical problem was demonstrated through solving a space-shuttle reentry problem.

Second, a numerical method for conducting the passive TPS design in the MDO of RLVs was developed in Chapter 3. While the TPS is a significant design discipline in RLVs, it has been seldom considered in previous studies on the MDO of RLVs. A primary design criterion of passive TPS is to ensure that the temperature of its backface bonded to the vehicle's main structure does not exceeds the specified limit throughout the flight. The simultaneous design optimization problem of flight trajectory and TPS is formulated as a transient heat-constrained optimal control problem, where ODE-expressed vehicle dynamics and PDE-expressed thermal behavior are coupled. So as to solve the formulated problem efficiently, the discretization of the PDE in the spatial coordinate using a Legendre pseudospectral method with the special treatment of boundary conditions was proposed. The boundary condition at the TPS surface is described by aerodynamic heating and thermal radiation, and that at the TPS backface is defined as the adiabatic condition. Using the developed method, pseudospectral discretization that automatically satisfies these boundary conditions is obtained. The discretized PDE gives a set of ODEs, and they are solved using a conventional optimal control software along with the vehicle dynamics. As a result, the flight trajectory is optimized while satisfying the backface temperature limit of TPS. Numerical experiments showed that the proposed technique has a faster convergence rate compared to previous approaches.

In Chapter 4, multi-objective MDO of a two-stage-to-orbit (TSTO) RLV with pre-cooled turbojet (PCTJ) engines was conducted using the multi-objective optimization method developed above. A fully reusable system with a horizontal takeoff and landing capability was considered. The booster vehicle is propelled by LH2-fueled PCTJ engines and LH2/LOX rocket engines, and the orbiter vehicle is accelerated by an ethanol/LOX rocket engine. The transportation of a payload into a circular low Earth orbit whose altitude is 350 km above sea level was defined as a mission. An MDO framework consisting of vehicle geometry definition, mass property estimation, aerodynamic computation, propulsion analysis, and trajectory calculation was constructed. The estimation of the vehicle's mass property was based on a statistical relation. For the aerodynamic analysis, engineering-level CFD methods were employed.

Propulsion performance was evaluated using tabular data derived from analytical models. In the flight trajectory computation, pitching trim and longitudinal static stability were taken into account in addition to the point-mass dynamics. Surrogate modeling techniques were applied to the aerodynamic computation and the propulsion analysis in order to mitigate their computational burden and to enhance the numerical stability of gradient-based optimization. Design objectives considered were 1) maximization of the payload mass, 2) minimization of the gross mass of the mated vehicle, and 3) minimization of the horizontal takeoff velocity. The takeoff velocity was selected as a design criterion, because it is a major constraint in designing booster vehicles of TSTO RLVs. The multi-objective MDO problem was formulated as a multi-objective optimal control problem whose static parameters contain vehicle design variables. While the formulated problem was composed of thousands of variables and constraints after dynamic variables in optimal control are parameterized, it was successfully solved using the developed multi-objective optimization method.

As a result, uniformly distributed Pareto optimal solutions were obtained. The Pareto optimal solutions include a solution which weights 412 t, transports an 810 kg payload, and has 129-m/s takeoff velocity, for instance. First, tradeoff relations among design objectives were qualitatively shown. Vehicle gross mass and payload mass are almost linearly correlated when the takeoff velocity is fixed. The payload mass fraction is increased by relaxing the takeoff-velocity constraint. Next, some inspections were made on the vehicle design and flight trajectory of four representative solutions. In all the obtained Pareto optimal solutions, the mated vehicle is accelerated by the PCTJ engines up to the operating limit, Mach 6.0. Then, data mining techniques were employed in order to extract more generic and insightful knowledge from the solutions. A scatter plot matrix was used to visualize the correlations of the pairs of design objective values and notable vehicle design parameters. Proper orthogonal decomposition (POD) was applied to the angle-of-attack history of Pareto optimal trajectories. This revealed that the optimal angle of attack during the ascent flight is primarily associated with the designed takeoff velocity, or equivalently wing loading of the vehicle.

In Chapter 5, multi-objective MDO of a TSTO RLV with rocket-based combined cycle (RBCC) engines was performed. The booster vehicle is propelled by ethanol/LOX RBCC engines, and the orbiter vehicle is accelerated by an ethanol/LOX rocket engine. In addition to the MDO framework built in Chapter 4, airframe-propulsion integrated analysis and thermal analysis were implemented as well. In the airframe-propulsion integrated analysis, inlet inflow conditions during ramjet mode and scramjet mode are given by a pre-compression calculation. The flow field in an external nozzle behind the combustor exist is simulated using a two-dimensional enhanced method of characteristics for supersonic flow. Thermal analysis was performed on 1) active cooling system for the RBCC engines and vehicle leading edges, and 2) ceramic tile TPS on the booster under-surface. In the passive TPS analysis, a numerical technique developed in Chapter 3 was employed, and the required thickness of the tile was determined in the MDO. Design objectives identical to those in Chapter 4 were considered. Although the formulated multi-objective MDO problem is larger and more complex than the problem derived in Chapter 4, it was satisfactorily solved using the proposed multi-objective optimization method.

A set of Pareto optimal solutions with a good diversity in the objective space was obtained. The tradeoff relation among design objectives was qualitatively same as the relation in the TSTO RLV with PCTJ engines. A distinctive difference between the PCTJ-powered system and the RBCC-powered system is that it is more difficult to realize low takeoff velocity in the RBCC-powered system. This is because ethanol whose density is higher than liquid hydrogen is applied to the propellant of RBCC engines aiming to reduce the vehicle size. However, a small but heavy vehicle suffers from higher takeoff velocity unless the vehicle has larger wings. Specifications of a representative Pareto optimal solution are as follows: gross mass is 652 t, payload mass is 772 kg, and takeoff velocity is 175 m/s. The PCTJ-powered system is superior to the RBCC-powered system in term of the objective values, while simple comparison is rather meaningless since the underlying design assumptions are somewhat different. A notable knowledge indicated in a scatter plot matrix is that the optimal external nozzle angle is highly related to the takeoff-velocity requirement. Smaller nozzle angle makes the expansion of engine exhaust weaker, and it is favorable for performing takeoff. This can be regarded as an outcome of tradeoff relations between takeoff performance and hypersonic acceleration performance. According to the knowledge extraction using POD, the optimal ascent trajectory of the TSTO RLV with RBCC engines is determined by the designed takeoff velocity, which is similar to the PCTJ-powered vehicle.

By performing multi-objective MDO of RLVs, this dissertation provided some insight into the coupling structure between the preference in design objectives and the resulting optimal design of the RLVs. The discovered knowledge will serve as a guideline for conducting more detailed design studies or for creating novel RLV concepts.

6.2 Novelties of the Present Research

For the sake of clarity, major novelties in the present research (i.e., the attempts that cannot be found in previous researches) are enumerated below:

1) An algorithm for successively determining goal-programming parameters was developed in order to find uniformly spread Pareto optimal solutions to multi-objective optimization problems.

2) The validity and efficiency of the fictitious-point pseudospectral method in PDE-ODE coupled optimal control were investigated.

3) The MDO problem of an RLV with TPS analysis was formulated as an augmented PDE-ODE coupled optimal control problem.

4) Multi-objective MDO of RLVs were conducted.

5) As the outputs of multi-objective optimization of RLVs, tradeoff relations among payload capability, vehicle gross mass, and takeoff-velocity requirement were obtained. In addition, the influence of a preference in the tradeoff relationship on the optimal RLV design (i.e., optimal values for design variables) were revealed.

6) Proper orthogonal decomposition was applied to time-history data in Pareto optimal solutions.

6.3 Recommendations for Future Work

In future studies, the work carried out in this dissertation would be improved or utilized in terms of the following aspects:

1) Application of the developed multi-objective optimizer to trajectory-driven design problems
   An advantage of the multi-objective optimization method proposed in Chapter 2 is that highly accurate and uniformly distributed solutions are obtained as many as needed. This property is desirable in practical usages, and the method is well applicable to varieties of trajectory-driven design optimization problems (e.g., trajectory planning of airliners and trajectory design of spacecraft).

2) Integrated design of flight trajectory and TPS in hypersonic experimental vehicles
   An efficient technique for the simultaneous optimization of flight trajectory and passive TPS investigated in Chapter 3 can become a useful tool for designing hypersonic experimental vehicles. Since trajectory design and TPS design are usually conducted independently now, the integration of these design efforts can accelerate the design process and can enhance the vehicle performance. Note that hypersonic flight experiment projects are currently active around the world[101–104].

3) Improvements in numerical models of RLV design problems
   Improvements in the fidelity of numerical models are indispensable for obtaining more reliable design solutions and for acquiring more insightful design knowledge. Particularly, attention should be paid to the following topics with high priority because of the current low fidelity and a large impact on the system performance:

   - Implementation of FEM-based mass property estimation of the vehicle
   - Investigation of the fly-forward/back trajectory of the booster after staging

4) Parallelization of the proposed multi-objective optimization algorithm
   The multi-objective optimization technique developed in Chapter 2 is a successive search algorithm, where goal-programming parameters are determined based on all the Pareto optimal solutions found so far. In other words, a new solution obtained at an iteration step depends on the solutions in previous steps. Such a situation is called “loop-carried dependence”, and it hinders the solution procedure from being parallelized. This can be a drawback considering the recent progress of parallel computing capabilities such as multi-processor machines and multi-core CPUs.

   Fortunately, however, this issue can be solved by the following simple but ingenious modifications of the algorithm. Its outline is illustrated in Fig. 6.1. Suppose that the parallel computing architecture is composed of multiple processes (or multiple threads) and data shared by them. The shared data contains all the solutions obtained so far and all the current farthest points in the objective space, and it is accessed by a single process at a time. In the figure, the existing solutions and farthest points are depicted with black dots and white triangles, respectively. When a single-objective problem arising from the goal-programming transformation is solved in a process, the corresponding farthest point point in the shared data is removed, and the newly obtained solution is stored

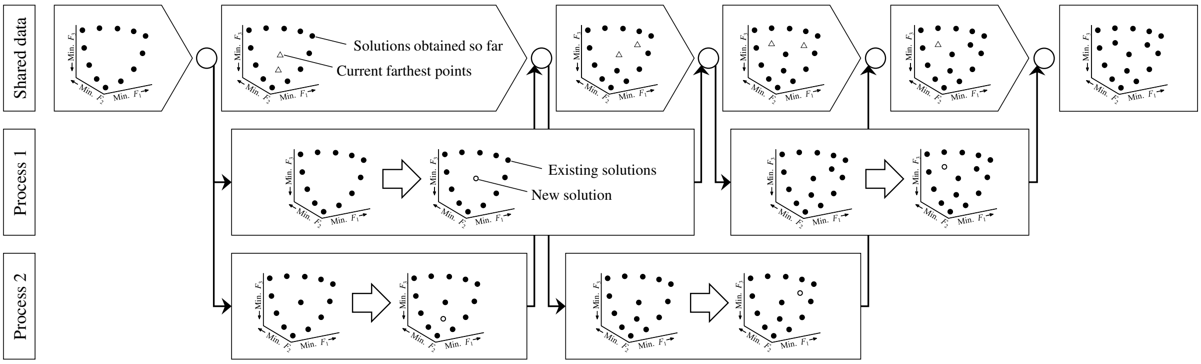

Fig. 6.1 Schematic drawing of the parallel-computing strategy for the multi-objective optimization algorithm in Chapter 2.

instead. Then the next farthest point and resulting goal-programming parameters are determined using the algorithm in Section 2.2. During this step, farthest points in other processes stored in the shared data are treated as if they are already-obtained solutions. As a consequence, the optimization computations in different processes can be performed asynchronously. The rationale of this approach is that the positions of a farthest point (denoted by $\triangle$ in the figure) and the resulting new solution (by $\circ$) are not so different in the objective space. The above parallel-computing strategy is superior in terms of the following viewpoints:

- Granularity
  The granularity in parallel computing is defined as the amount of computation relative to that of communication. When the granularity is small, the overhead associated with the communication deteriorates the overall computational performance. In the present method, all the data required to be communicated is the objective values of existing solutions and the coordinates of farthest points. Computation performed per each communication is equivalent to the solution of an optimization problem, and it takes more than one minute in practical problems. Therefore, its granularity is very large.
- Load balance
  If the computational load is not equally allocated to each process, it leads to some dead time of computational resources. Such a load imbalance is caused by a situation where the data synchronization between processes is needed. When the optimization computation is involved, the concern for the load imbalance becomes critical, because the required solution times in similar optimization problems can be very different due to its iterative nature. The present parallelization algorithm is, on the other hand, based on the asynchronous communication between a process and the shared data, and it is free from the load imbalance.

Implementation of the above parallel-computing strategy and the verification of its efficiency are interesting research topics.

Appendix A

Pseudospectral Methods for Nonlinear Optimal Control

In this appendix chapter, existing numerical methods for nonlinear optimal control problems, especially a family of pseudospectral methods, are described briefly first. Then, the formulation of the Legendre-Gauss pseudospectral method with segment decomposition is shown, which is employed throughout the present study.

A.1 Numerical Methods for Nonlinear Optimal Control

Missions in the aerospace field typically involve severe requirements or constraints on time, energy consumption, the operational performance, and so on. This has motivated the development of optimal control theories since 1950s. Since it is usually difficult to analytically find the solution to a general nonlinear optimal control problem, a variety of numerical solution techniques have been developed. Numerical methods for nonlinear optimal control are broken up into two primary categories: direct methods and indirect methods[41], as shown in Fig. A.1. Figure A.1 is drawn so that the descriptions around Legendre pseudospectral methods are particularly detailed.

When the indirect methods are employed, calculus of variations is first applied to the time-continuous optimal control problem, and the first-order necessary condition for optimality is derived. The optimality condition is expressed as a form of multi-point boundary value problem of Hamiltonian, and it is numerically solved after performing discretization. Therefore, the indirect methods are sometimes called a “first optimize then discretize” approach. Although indirect methods have the advantage of high accuracy in their solution, they suffer from small radii of convergence and the necessity of 1) analytical derivation of the optimality criteria, 2) nonintuitive initial guesses for the costate, and 3) the prior establishment of the constrained and unconstrained arcs of inequality path constraints.

When the direct methods are used, on the other hand, the original problem is first transcribed into its finite-dimensional approximation or a nonlinear programming (NLP) problem. Then, the solution such that satisfies its first-order necessary conditions for optimality, which is known as Karush-Kuhn-Tucker

- indirect methods[77]
    - indirect shooting
    - indirect collocation
- direct methods
    - direct shooting[42,45]
    - direct collocation
        - fixed-degree Runge-Kutta[42,46,105]
        - pseudospectral methods
            - Jacobi
            - Chebyshev[106,107]
            - Legendre[65]
                - Legendre-Gauss-Lobatto[82]
                - Legendre-Gauss[64]
                - Legendre-Gauss-Radau[83]

Fig. A.1 Classification of numerical methods for nonlinear optimal control.

(KKT) conditions, is obtained using NLP algorithms. Therefore, the direct methods are sometimes called a “first discretize then optimize” approach. Direct methods are free from aforementioned drawbacks of the indirect methods, and they have gained popularity. Direct methods are further divided into the shooting method and the collocation methods. The direct shooting method parameterizes control variables at a set of discrete times, and the state variables are then obtained by solving the initial value problem of ordinary differential equations explicitly. Numerical instabilities due to this explicit integration[42] make the direct shooting method less popular than the direct collocation methods. The direct collocation method parameterizes both state variables and the control variables, and differential-algebraic equations are imposed at finite number of nodes (collocation points). The direct collocation methods are probably most widely used today for their computational stability and versatility. In traditional direct collocation parameterization, the problem domain is divided into a large number of subintervals, and differential equations are implicitly enforced using a fixed low-order Runge-Kutta scheme (e.g, the trapezoidal rule or the Hermite-Simpson rule) in each interval. As the number of subintervals is increased, the accuracy of the resulting solution is improved.

A.2 Pseudospectral Methods

Meanwhile, the application of pseudospectral methods to the direct collocation approach for optimal control has been actively studied in recent years[64,82,83,106]. The pseudospectral method is originally used in the numerical solution of partial differential equations[84,87]. In the pseudospectral method, sophisticatedly distributed Gaussian quadrature nodes[108] are employed as the colocation points without dividing the whole domain into subintervals, and the derivatives of the state variables at the collocation points are approximated with the derivatives of the interpolants. When the order of the approximating polynomial is raised, the numerical solution gradually converges to the solution of the original continuous-time optimal control problem. In other words, the pseudospectral methods adopt a variable high-order global polynomial as a basis function (Fig. A.2b) in contrast to a fixed low-order piecewise polynomial used

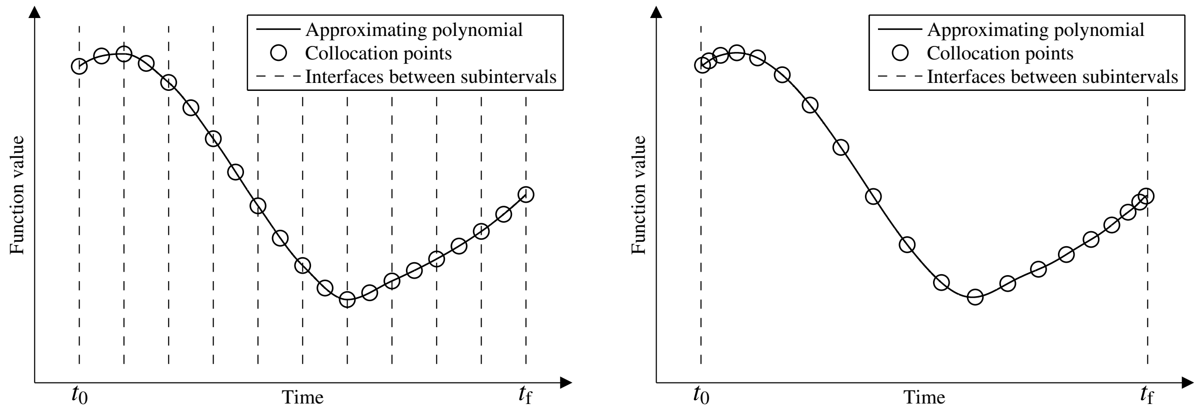

(a) Fixed-order Runge-Kutta method.
(b) Pseudospectral method.

Fig. A.2 Examples of discretization mesh used in direct collocation methods.

in the conventional direct collocation methods (Fig. A.2a). The Runge phenomenon[*] is prevented by employing the Gaussian quadrature nodes as data points for interpolation. Primary advantages of the pseudospectral method over the traditional direct collocation methods based on fixed-order Runge-Kutta schemes are as follows:

1) Exponential convergence rate of the obtained solution[65,109]
   The error between the numerical solution and the continuous-time solution decreases exponentially with respect to the increase in the number of collocation points. This rate is much faster than the polynomial-order convergence achieved by Runge-Kutta schemes. This results in considerable reductions of the CPU time and memory resources required to obtain the solution with the desired accuracy level.

2) Highly accurate mapping between the KKT multiplier and costate variables[64,65]
   Costate variables of the optimal control problem can be accurately computed from the KKT multipliers. It is noted that the KKT multipliers are provided by NLP solvers after the optimization computation is finished. The calculated costate values enables the optimality validation of the obtained numerical solution on the basis of the Pontryagin's maximum (or minimum) principle.

There are a variety of Gaussian quadrature nodes, and they directly leads to various types of pseudospectral methods. Performance comparisons between different pseudospectral methods can be found in literature[83,109]. While Ref. 109 states that the Legendre-Gauss (LG) pseudospectral method[64] fails to work properly in some cases, its convergence rate is generally superior to that of the other Legendre pseudospectral methods[83]. Therefore, the LG pseudospectral method and the Legendre-Gauss-Lobatto (LGL) pseudospectral method[82] are both implemented in the present study. Then, the LGL pseudospectral method is employed only when the LG pseudospectral method does not work well.

Major limitations of the pseudospectral methods are

---

[*] A fictitious oscillation of an interpolant observed in high-order polynomial approximation.

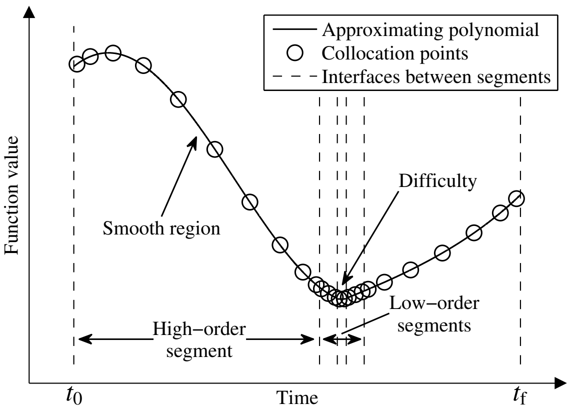

Fig. A.3 Schematic of the discretization mesh generated by an adaptive mesh refinement algorithm for the pseudospectral methods[67].

1) Deterioration of the convergence rate when the solution is not sufficiently smooth
   When a nonsmooth function is approximated using a global polynomial interpolation, the resulting interpolant suffers from oscillating behaviors known as the Gibbs phenomenon. In addition to this spurious oscillation, the convergence rate of the numerical solution to the continuous-time solution is substantially degraded.

2) Significant increase of the computational burden when increasing the approximation order
   Since the pseudospectral methods use a single approximating polynomial in the whole problem domain, the NLP problem to be solved has a denser constraint Jacobian matrix in comparison with conventional direct collocation methods. Given that the number of collocation points is denoted by N, the number of nonzero elements in the Jacobian arising from the pseudospectral methods is the order of $\mathcal{O}(N^2)$, while that resulting from the trapezoidal rule is the order of $\mathcal{O}(N)$. This means that the pseudospectral methods incur higher computation cost when the same number of collocation points are used, while the exponential convergence rate of the pseudospectral methods usually overweighs this problem. This drawback becomes apparent when a problem with a highly nonlinear or nonsmooth solution must be solved with high accuracy, because an intractable NLP problem is produced when the required number of collocation points is used.

In order to overcome these drawbacks, the segment decomposition approach[110] is employed in the present study, and the time domain is divided into a small number of segments where different approximating polynomials are used. Since the appropriate segmentation cannot be known a prior, an adaptive mesh refinement algorithm[66,67] is used to automatically determine the number of segments, locations of the segments, and the number of collocation points in each segment. This mesh refinement algorithm conducts segmentations only around the difficulties in the polynomial approximation (e.g., smoothness irregularities and high nonlinearities of the solution) as shown in Fig. A.3. This enables the enhanced approximation accuracy and the relief of computational cost.

A.3 The Legendre-Gauss Pseudospectral Method with Segment Decomposition

In this section, the transcription of a nonlinear optimal control problem into a nonlinear programming problem using the Legendre-Gauss pseudospectral method with segment decomposition is explained. While some part of the contents can be found in Section 2 of Ref. 66, it is reviewed for the completeness of this dissertation. It should be noted that the descriptions in this section can be extended to other pseudospectral methods by introducing some slight modifications. Let us consider the following generalized continuous-time nonlinear optimal control problem with cost functional in a Bolza form:

$$\begin{aligned}
\text{find}\quad & \mathbf{x}(t) : [t_0, t_\mathrm{f}] \to \mathbb{R}^{n_x},\ \mathbf{u}(t) : [t_0, t_\mathrm{f}] \to \mathbb{R}^{n_u},\ t_0 \in \mathbb{R},\ t_\mathrm{f} \in \mathbb{R},\ \mathbf{p} \in \mathbb{R}^{n_p}, && && \text{(A.1)}\\
\text{min.}\quad & J := \Phi[\mathbf{x}(t_0), t_0, \mathbf{x}(t_\mathrm{f}), t_\mathrm{f}, \mathbf{p}] + \int_{t_0}^{t_\mathrm{f}} g[\mathbf{x}(t), \mathbf{u}(t), t, \mathbf{p}]\,\mathrm{d}t \ \in \mathbb{R} && \text{(Cost functional)}, && \text{(A.2)}\\
\text{s.t.}\quad & \frac{\mathrm{d}\mathbf{x}}{\mathrm{d}t} = \mathbf{f}[\mathbf{x}(t), \mathbf{u}(t), t, \mathbf{p}] \ \in \mathbb{R}^{n_x} && \text{(Dynamic constraints)}, && \text{(A.3)}\\
& \mathbf{C}[\mathbf{x}(t), \mathbf{u}(t), t, \mathbf{p}] \le \mathbf{0} \ \in \mathbb{R}^{n_c} && \text{(Path constraints)}, && \text{(A.4)}\\
& \boldsymbol{\Psi}[\mathbf{x}(t_0), t_0, \mathbf{x}(t_\mathrm{f}), t_\mathrm{f}, \mathbf{p}] \le \mathbf{0} \ \in \mathbb{R}^{n_\psi} && \text{(Boundary conditions}^*\text{)}, && \text{(A.5)}
\end{aligned}$$

where $\mathbf{x}(t)$, $\mathbf{u}(t)$, t_0, t_f, and $\mathbf{p}$ are typically called state variables, control variables, initial time, terminal time, and static variables. t is a independent variable, and it denoted time in the most cases. When a cost functional is defied by the summation of a term relating initial/terminal states, Φ, and a term about a running cost, $\int_{t_0}^{t_\mathrm{f}} g\,\mathrm{d}t$, it is in a Bolza form. The others are a Mayer form with Φ only and a Lagrange form with $\int_{t_0}^{t_\mathrm{f}} g\,\mathrm{d}t$ only.

A pair, $\{\mathbf{x}(t), \mathbf{u}(t), t_0, t_\mathrm{f}, \mathbf{p}\}$, that satisfies at least the constraints [Eq. (A.3–A.5)] is called a feasible solution. Among a set of feasible solutions, a solution with the minimum cost is called the (globally) optimal solution. It is known that the globally optimal solution is very difficult to find, and therefore solutions that are locally optimal in the corresponding neighborhoods are sometimes searched instead. While general nonlinear functions can be handled in the nonlinear optimal control problem, it is preferable to formulate the problem so that all the included functions are continuously differentiable. This regularity condition is required for treating the problem analytically and for applying gradient-based optimization methods. In order to satisfy this qualification, a multi-phase formulation is often used in practical and complex optimal control problems as follows: the problems domain is divided into several phases, and different functions are used to express the problem in each phase. Then, the constraints concerning the relations among phases, called linkage conditions, are imposed. In this section, a single-phase problem is considered for the briefness of the description.

Let us divide the domain $[t_0, t_\mathrm{f}]$ into N_s segments whose ith interval is distributed in $[t_0^{(i)}, t_\mathrm{f}^{(i)}]$. Superscripts in parentheses indicate the index of the segment to which the variable or function belongs.

---

[*] The boundary conditions include constraints on static variables, $\mathbf{p}$, in addition to the constraints on the initial and terminal state of the dynamic system.

Segments are aligned consecutively, that is

$$t_0 = t_0^{(1)} < t_f^{(1)} = t_0^{(2)} < \cdots < t_f^{(N_s-1)} = t_0^{(N_s)} < t_f^{(N_s)} = t_f, \tag{A.6}$$

and state variables must be C^0 continuous at the interfaces of the adjacent segments. Then, the independent variable in the ith segment is converted from $t \in [t_0^{(i)}, t_f^{(i)}]$ to $\tau \in [-1, 1]$ using the following affine transformation:

$$t^{(i)}(\tau) := \frac{t_f^{(i)} - t_0^{(i)}}{2}\tau + \frac{t_f^{(i)} + t_0^{(i)}}{2}. \tag{A.7}$$

This transformation is required because the Gaussian quadrature nodes, on which the Legendre-Gauss pseudospectral methods are based, are located in $[-1, 1]$.

As a result of this segment decomposition and interval normalization, the original problem in Eq. (A.1–A.5) is rewritten as follows:

$$\begin{aligned}
\text{find}\quad & \{\mathbf{x}^{(i)}(t)\}_{i=1}^{N_s},\ \{\mathbf{u}^{(i)}(t)\}_{i=1}^{N_s},\ t_0,\ t_f,\ \mathbf{p}, && && \text{(A.8)}\\
\text{min.}\quad & J := \Phi[\mathbf{x}^{(1)}(-1), t_0, \mathbf{x}^{(N_s)}(+1), t_f, \mathbf{p}] && && \\
& \qquad + \sum_{i=1}^{N_s} \frac{t_f^{(i)} - t_0^{(i)}}{2} \int_{-1}^{+1} g[\mathbf{x}^{(i)}(\tau), \mathbf{u}^{(i)}(\tau), t^{(i)}(\tau), \mathbf{p}]\, \mathrm{d}\tau, && && \text{(A.9)}\\
\text{s.t.}\quad & \frac{\mathrm{d}\mathbf{x}^{(i)}}{\mathrm{d}\tau} = \frac{t_f^{(i)} - t_0^{(i)}}{2} \mathbf{f}[\mathbf{x}^{(i)}(\tau), \mathbf{u}^{(i)}(\tau), t^{(i)}(\tau), \mathbf{p}], && \text{for}\ \ i = 1, \ldots, N_s && \text{(A.10)}\\
& \mathbf{C}[\mathbf{x}^{(i)}(\tau), \mathbf{u}^{(i)}(\tau), t^{(i)}(\tau), \mathbf{p}] \le \mathbf{0}, && \text{for}\ \ i = 1 \ldots, N_s && \text{(A.11)}\\
& \boldsymbol{\Psi}[\mathbf{x}^{(1)}(-1), t_0, \mathbf{x}^{(N_s)}(+1), t_f, \mathbf{p}] \le \mathbf{0} && && \text{(A.12)}\\
& \mathbf{x}^{(i)}(+1) = \mathbf{x}^{(i+1)}(-1), && \text{for}\ \ i = 1 \ldots, N_s - 1. && \text{(A.13)}
\end{aligned}$$

Here, $\mathbf{x}^{(i)}(\tau)$ and $\mathbf{u}^{(i)}(\tau)$ are the shorthand of $\mathbf{x}^{(i)}\left[t^{(i)}(\tau)\right]$ and that of $\mathbf{u}^{(i)}\left[t^{(i)}(\tau)\right]$, respectively.

Using pseudospectral methods, continuous-time constraints are collocated at the corresponding quadrature nodes [e.g, the Legendre-Gauss (LG) nodes for the LG pseudospectral method]. Suppose that $N^{(i)}$ LG nodes are used in the ith segment, and their abscissas are denoted by $\tau_1^{(i)}, \ldots, \tau_{N^{(i)}}^{(i)}$. Here, $\tau_l^{(i)}$ is defined as the lth root of the $N^{(i)}$th-order Legendre orthogonal polynomial[108], and all the nodes are located onto the open interval $(-1, +1)$. The computation of the LG nodes can be performed using the Golub-Welsh algorithm[111] instead of finding the roots directly. The total number of collocation points, N, is given by

$$N := \sum_{i=1}^{N_s} N^{(i)}. \tag{A.14}$$

It is noted that the initial point, $\tau_0^{(i)} := -1$, and the terminal point, $\tau_{N^{(i)}+1}^{(i)} := +1$, in each segment do not belong to collocation points of the LG pseudospectral method. Instead, these end points are introduced as additional discretization points for state variables.

The relative locations of the segment interfaces can be either fixed or moveable in the interval of $[t_0, t_\mathrm{f}]$. In the present study, let us suppose that the ith segment occupies the predetermined fixed fraction, $t^{(i)}_\mathrm{frac}[:= (t^{(i)}_\mathrm{f} - t^{(i)}_0)/(t_\mathrm{f} - t_0)]$, based on the discussion in Section 2.3 of Ref. 66. Therefore, the following relations hold:

$$t^{(i)}_0 = t_0 + (t_\mathrm{f} - t_0) \sum_{l=1}^{i-1} t^{(l)}_\mathrm{frac}, \tag{A.15}$$

$$t^{(i)}_\mathrm{f} = t_0 + (t_\mathrm{f} - t_0) \sum_{l=1}^{i} t^{(l)}_\mathrm{frac}, \tag{A.16}$$

$$t^{(i)}_k = \frac{t_\mathrm{f} - t_0}{2} t^{(i)}_\mathrm{frac} \left(\tau^{(i)}_k + 1\right) + t_0 + (t_\mathrm{f} - t_0) \sum_{l=1}^{i-1} t^{(l)}_\mathrm{frac}, \tag{A.17}$$

$$\frac{t^{(i)}_\mathrm{f} - t^{(i)}_0}{2} = \frac{t_\mathrm{f} - t_0}{2} t^{(i)}_\mathrm{frac}. \tag{A.18}$$

As a consequence, the discretization mesh for the Legendre-Gauss pseudospectral method with segment decomposition can be specified by the following set of parameters:

1) The number of segments, N_s
2) The fraction of each segment in the problem domain, $\left\{t^{(i)}_\mathrm{frac}\right\}_{i=1}^{N_\mathrm{s}}$
3) The number of LG nodes in each segment, $\left\{N^{(i)}\right\}_{i=1}^{N_\mathrm{s}}$

These parameters are automatically determined by the mesh refinement algorithm[67], and they are collectively denoted by **N** in Section 2.1.

Next, state variables expressed as continuous-time functions, $\mathbf{x}^{(i)}(\tau)$, are replaced with their $N^{(i)}$th-order approximating polynomials, $\tilde{\mathbf{x}}^{(i)}(\tau)$, as follows:

$$\mathbf{x}^{(i)}(\tau) \approx \tilde{\mathbf{x}}^{(i)}(\tau) = \sum_{l=0}^{N^{(i)}} \tilde{\mathbf{x}}^{(i)}(\tau^{(i)}_l) \cdot L^{(i)}_l(\tau), \tag{A.19}$$

where $\{L^{(i)}_l(\tau)\}_{i=1}^{N^{(i)}}$ is a set of Lagrange basis functions defined by

$$L^{(i)}_l(\tau) := \prod_{\substack{m=0 \\ m \neq l}}^{N^{(i)}} \frac{\tau - \tau^{(i)}_m}{\tau^{(i)}_l - \tau^{(i)}_m}, \quad \text{for } i = 1, \ldots, N^{(i)}. \tag{A.20}$$

The Lagrange basis polynomials satisfy the following relation:

$$L^{(i)}_l(\tau^{(i)}_k) = \delta_{lk}, \quad \text{for } k = 0, \ldots, N^{(i)}, \tag{A.21}$$

where δ_{lk} refers the Kronecker delta. This means that the resulting approximating polynomial can be parameterized by their values at the discrete points $\tau^{(i)}_0, \ldots, \tau^{(i)}_{N^{(i)}}$. Similarly, let the approximating function of the control variables in the ith segment be denoted by $\tilde{\mathbf{u}}^{(i)}(\tau)$. The state variables at the terminal point of each segment can be derived as follows:

$$\tilde{\mathbf{x}}^{(i)}(+1) = \tilde{\mathbf{x}}^{(i)}(-1) + \int_{-1}^{+1} \frac{\mathrm{d}\tilde{\mathbf{x}}^{(i)}}{\mathrm{d}\tau}\,\mathrm{d}\tau. \tag{A.22}$$

By differentiating Eq. (A.19) with respect to τ and evaluating the first derivative at LG nodes, gradient of the approximating polynomial of the state variable is obtained as follows:

$$\begin{aligned} \left.\frac{\mathrm{d}\tilde{\mathbf{x}}^{(i)}}{\mathrm{d}\tau}\right|_{\tau_k^{(i)}} &= \sum_{l=0}^{N^{(i)}} \tilde{\mathbf{x}}^{(i)}(\tau_l^{(i)}) \cdot \left.\frac{\mathrm{d}L_l^{(i)}(\tau)}{\mathrm{d}\tau}\right|_{\tau_k^{(i)}} \\ &=: \sum_{l=0}^{N^{(i)}} D_{k,\,l+1}^{(i)} \cdot \tilde{\mathbf{x}}^{(i)}(\tau_l^{(i)}). \end{aligned} \tag{A.23}$$

$D_{k,\,l+1}^{(i)}$ is the $(k,\ l+1)$th element of the pseudospectral differentiation matrix[85] in the ith segment, $\mathbf{D}^{(i)} \in \mathbb{R}^{N^{(i)}\times(N^{(i)}+1)}$. The differentiation matrix for the Legendre-Gauss pseudospectral method is computed by[64,65]

$$\begin{aligned} D_{k,\,l+1}^{(i)} &:= \left.\frac{\mathrm{d}L_l^{(i)}(\tau)}{\mathrm{d}\tau}\right|_{\tau_k^{(i)}} \\ &= \begin{cases} \displaystyle\sum_{\substack{m=0\\ m\neq k}}^{N^{(i)}} \frac{1}{\tau_k^{(i)} - \tau_m^{(i)}}, & \text{if } k = l \\ \displaystyle\frac{1}{\tau_l^{(i)} - \tau_k^{(i)}} \prod_{\substack{m=0\\ m\neq l,k}}^{N^{(i)}} \frac{\tau_k^{(i)} - \tau_m^{(i)}}{\tau_l^{(i)} - \tau_m^{(i)}}, & \text{if } k \neq l. \end{cases} \end{aligned} \tag{A.24}$$

Definite integrals in the cost functional, Eq. (A.9), and the terminal-state constraint, Eq. (A.22), are replaced by their Legendre-Gauss quadrature approximations[108,111], and they become

$$\begin{aligned} \int_{-1}^{+1} g[\mathbf{x}^{(i)}(\tau), \mathbf{u}^{(i)}(\tau), t^{(i)}(\tau), \mathbf{p}]\,\mathrm{d}\tau &\approx \int_{-1}^{+1} g[\tilde{\mathbf{x}}^{(i)}(\tau), \tilde{\mathbf{u}}^{(i)}(\tau), t^{(i)}(\tau), \mathbf{p}]\,\mathrm{d}\tau \\ &= \sum_{k=1}^{N^{(i)}} w_k^{(i)} \cdot g[\tilde{\mathbf{x}}^{(i)}(\tau_k^{(i)}), \tilde{\mathbf{u}}^{(i)}(\tau_k^{(i)}), t^{(i)}(\tau_k^{(i)}), \mathbf{p}], \end{aligned} \tag{A.25}$$

$$\int_{-1}^{+1} \frac{\mathrm{d}\tilde{\mathbf{x}}^{(i)}}{\mathrm{d}\tau}\,\mathrm{d}\tau = \sum_{k=1}^{N^{(i)}} w_k^{(i)} \cdot \left.\frac{\mathrm{d}\tilde{\mathbf{x}}^{(i)}}{\mathrm{d}\tau}\right|_{\tau_k^{(i)}}, \tag{A.26}$$

where $w_1^{(i)}, \ldots, w_{N^{(i)}}^{(i)}$ are the weights of the Legendre-Gauss quadrature computed using the Golub-Welsh algorithm[111]. As a result, Eq. (A.22) is transformed by employing Eq. (A.26) and Eq. (A.23) as follows:

$$\begin{aligned}\mathbf{x}^{(i)}(1) \approx \tilde{\mathbf{x}}^{(i)}(1) &= \tilde{\mathbf{x}}^{(i)}(-1) + \sum_{k=1}^{N^{(i)}} w_k^{(i)} \cdot \left[\sum_{l=0}^{N^{(i)}} D_{k\,l+1}^{(i)} \cdot \tilde{\mathbf{x}}^{(i)}(\tau_l^{(i)})\right] \\ &= \tilde{\mathbf{x}}^{(i)}(-1) + \sum_{l=0}^{N^{(i)}} \tilde{\mathbf{x}}^{(i)}(\tau_l^{(i)}) \cdot \left[\sum_{k=1}^{N^{(i)}} w_k^{(i)} \cdot D_{k\,l+1}^{(i)}\right]. \end{aligned} \tag{A.27}$$

Next, new variables are introduced with the following definitions:

$$\mathbf{X}_k^{(i)} := \tilde{\mathbf{x}}^{(i)}(\tau_k^{(i)}) \in \mathbb{R}^{n_x} \quad \text{for } \ i = 1, \ldots, N_\mathrm{s}, \ \ k = 0, \ldots, N^{(i)} + 1, \tag{A.28}$$

$$\mathbf{U}_k^{(i)} := \tilde{\mathbf{u}}^{(i)}(\tau_k^{(i)}) \in \mathbb{R}^{n_u} \quad \text{for } \ i = 1, \ldots, N_\mathrm{s}, \ \ k = 1, \ldots, N^{(i)}. \tag{A.29}$$

Let us impose the differential-algebraic equations [Eqs. (A.10, A.11)] at the LG nodes using Eq. (A.23), and then, Eqs. (A.8–A.13, A.27) are transcribed as follows:

$$\begin{aligned}
\text{find} \quad & \{\mathbf{X}_k^{(i)}\}_{i\in\{1,\ldots,N_\mathrm{s}\},\, k\in\{0,\ldots,N^{(i)}+1\}} && \text{(Parameterized state variables)} && \text{(A.30)} \\
& \{\mathbf{U}_k^{(i)}\}_{i\in\{1,\ldots,N_\mathrm{s}\},\, k\in\{1,\ldots,N^{(i)}\}} && \text{(Parameterized control variables)} \\
& t_0 && \text{(Initial time)} \\
& t_\mathrm{f} && \text{(Terminal time)} \\
& \mathbf{p} && \text{(Static variables)}
\end{aligned}$$

$$\begin{aligned}\text{min.} \quad J := \mathit{\Phi}[\mathbf{X}_0^{(1)}, t_0, \mathbf{X}_{N^{(N_\mathrm{s})}+1}^{(N_\mathrm{s})}, t_\mathrm{f}, \mathbf{p}] \\ + \sum_{i=1}^{N_\mathrm{s}} \frac{t_\mathrm{f} - t_0}{2} t_\mathrm{frac}^{(i)} \sum_{k=1}^{N^{(i)}} w_k^{(i)} \cdot g[\mathbf{X}_k^{(i)}, \mathbf{U}_k^{(i)}, t^{(i)}(\tau_k^{(i)}), \mathbf{p}]\end{aligned} \tag{A.31}$$

$$\text{s.t.} \quad \sum_{l=0}^{N^{(i)}} D_{k,\,l+1}^{(i)} \cdot \mathbf{X}_l^{(i)} - \frac{t_\mathrm{f} - t_0}{2} t_\mathrm{frac}^{(i)} \mathbf{f}[\mathbf{X}_k^{(i)}, \mathbf{U}_k^{(i)}, t^{(i)}(\tau_k^{(i)}), \mathbf{p}] = \mathbf{0},$$

$$\text{for } \ k = 1, \ldots, N^{(i)}, \ \ i = 1, \ldots, N_\mathrm{s} \tag{A.32}$$

$$\mathbf{C}[\mathbf{X}_k^{(i)}, \mathbf{U}_k^{(i)}, t^{(i)}(\tau_k^{(i)}), \mathbf{p}] \leq \mathbf{0}, \qquad \text{for } \ k = 1, \ldots, N^{(i)}, \ \ i = 1, \ldots, N_\mathrm{s} \tag{A.33}$$

$$\mathbf{\Psi}[\mathbf{X}_0^{(1)}, t_0, \mathbf{X}_{N^{(N_\mathrm{s})}+1}^{(N_\mathrm{s})}, t_\mathrm{f}, \mathbf{p}] \leq \mathbf{0} \tag{A.34}$$

$$\mathbf{X}_{N^{(i)}+1}^{(i)} - \mathbf{X}_0^{(i+1)} = \mathbf{0}, \qquad \text{for } \ i = 1, \ldots, N_\mathrm{s} - 1, \tag{A.35}$$

$$\mathbf{X}_{N^{(i)}+1}^{(i)} - \mathbf{X}_0^{(i)} - \sum_{l=0}^{N^{(i)}} \mathbf{X}_l^{(i)} \cdot \left[\sum_{k=1}^{N^{(i)}} w_k^{(i)} \cdot D_{k,\,l+1}^{(i)}\right] = \mathbf{0}, \qquad \text{for } \ i = 1, \ldots, N_\mathrm{s} - 1. \tag{A.36}$$

It is noted that, $\{\tau_k^{(i)}\}_{i=1,\ldots,N_\mathrm{s},\, k=1,\ldots,N^{(i)}}$ is completely determined from t_0 and t_f using Eq. (A.18). Since the interfaces between adjacent segments, initial time, and terminal time are not collocation points, dynamic constraints and path constraints are not imposed on them. By assigning the same variable both to $\mathbf{X}_{N^{(i)}+1}^{(i)}$ and to $\mathbf{X}_0^{(i+1)}$ in the computational implementation, Eq. (A.35) can be removed. Eqs. (A.30–A.36) constitute an NLP problem that can be regarded as a discretization or a finite-dimensional approximation of the original continuous-time optimal control problem, Eqs. (A.1–A.5). When gradient-based optimization methods are applied to the derived NLP problem, sparsity of the problem can be exploited in computing its gradient information. For more details on the gradient calculation, see Appendix A.3 in Ref. 66 or Ref. 112.

Appendix B

External Nozzle Model for RBCC Engines

This appendix chapter discusses how to implement the influence of an external nozzle in evaluating the performance of RBCC engines in an MDO framework. A numerical model of the external nozzle flow is presented, and procedures for constructing its surrogate model are developed.

B.1 Quasi-One-Dimensional Model

In some previous researches on the conceptual design of TSTO RLVs with RBCC engines[97], a quasi-one-dimensional model of the external nozzle flow is used. The pressure on the nozzle ramp surface is estimated based on the following assumptions:

- In proper/under expansion condition (Fig. B.1a):
  The exhaust gas of the engine is expanded quasi-one-dimensionally along a flow-pass surrounded by the nozzle ramp and an extended line from the engine cowl (the dashed line shown in the figure) in an isentropic manner.

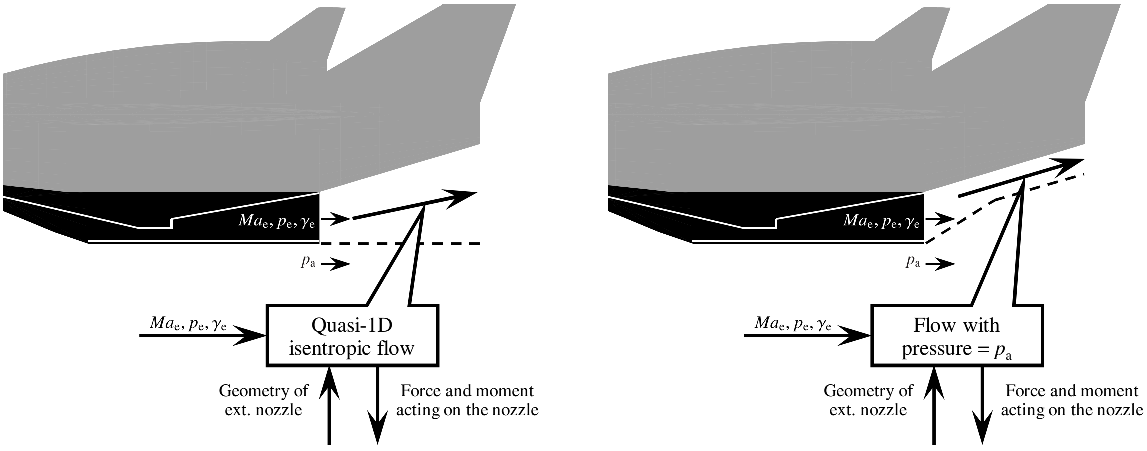

(a) In proper/under expansion condition ($p_e \geq p_a$). (b) In over expansion condition ($p_e < p_a$).

Fig. B.1 Overview of a quasi-one-dimensional model for the external nozzle flow.

- In over-expansion condition (Fig. B.1b):
  The exhaust flow goes along the nozzle ramp with static pressure identical to the free-stream pressure.

The force and pitching moment acting on the external nozzle are obtained by integrating the calculated flow pressure over the entire ramp surface after the free-stream pressure is subtracted. While this model is simple and easy to use, the thrust augmentation by the external nozzle tends to be overestimated[113]. It is noted that this numerical model of the external nozzle always produces non-negative thrust. In reality, however, the nozzle can produce negative thrust in an over-expansion condition as experimentally shown in Ref. 113. It is due to the fact that flight conditions, or ambient flow conditions, are not properly considered, and generation and interaction of pressure waves (shock wave, compression wave, expansion wave) are neglected in this model.

B.2 Two-Dimensional Model

In this section, a two-dimensional model based on an enhanced method of characteristics[*] is presented. This model is adopted from Ref. 115 with some modifications.

B.2.1 Model Description

A numerical model that overcomes defects of the quasi-one-dimensional model, produces more accurate results, and still has reasonably low computational cost is required. While the method of characteristics[114] is a powerful tool for such purposes, it is applicable to isentropic flows only, since it takes advantage of the Riemann invariants of hyperbolic PDEs for supersonic fluid. In order to extend the applicability of the method to the flow with shock waves, a computational algorithm was developed in Ref. 115. However, Ref. 115 focuses on the experimental system where the RBCC combustor is replaced with a supersonic bell nozzle, meaning that the top-surface inclination of the combustor (see Fig. 5.3) is ignored. In addition, an isentropic expansion fan is represented by a single wave, and this can lead to large errors in under-expanded nozzle conditions. Therefore, in this dissertation, the algorithm in Ref. 115 is modified so that it considers top-surface inclination of the combustor and approximates the expansion fan by more than one wave. These procedures are described in the remainder of this subsection.

Initial Conditions

As a perturbation in a supersonic flow field propagates unidirectionally from upstream to downstream, the flow computation is also performed alike. Initial conditions of this flow propagation are specified as shown in Fig. B.3a. This figure illustrates the side view of the booster rearbody. Ma, p, γ, and θ denote Mach number, static pressure, heat capacity ratio, and flow angle, respectively. Hereafter, quantities with the subscript $(\cdot)_\mathrm{a}$ indicate ambient or environment flow conditions, and those with the subscript $(\cdot)_\mathrm{e}$

---

[*] Strictly speaking, the present method is classified into a method of waves instead of a method of characteristics[114], while these terminologies are often used without being distinguished.

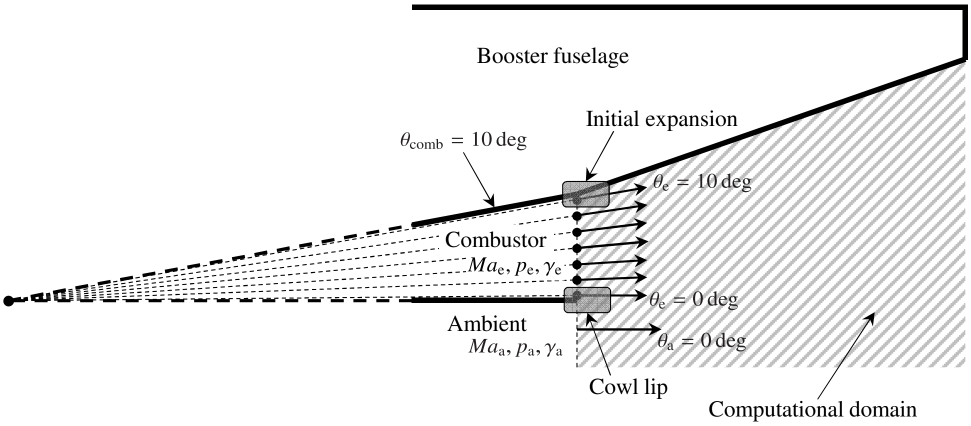

Fig. B.2 Initial conditions of the flow computation using the two-dimensional method of characteristics.

represent engine-exhaust conditions. It should be noted that the top-surface inclination of the combustor of the RBCC engines considered in the present study is 10 deg. Therefore, the exhaust flow field at the combustor exit is discretized into small cells, and an appropriate flow angle is assigned to each cell.

Initial Expansion

The exhaust gass goes through an initial expansion via an infinite number of Mach waves generated at the beginning point of the external nozzle ramp. The infinite number of Mach waves are replaced with a finite number of pressure waves, and the directions of these pressure waves are arranged equiangularly. Flow conditions after a single pressure wave are calculated using the following isentropic equations when the deflection angle, θ_δ, is specified:

$$Ma_2 = \{Ma \mid \nu(Ma, \gamma) - \nu(Ma_1, \gamma) - \theta_\delta = 0\}, \tag{B.1}$$

$$p_2 = p_1 \left(\frac{1 + \frac{\gamma-1}{2} {Ma_2}^2}{1 + \frac{\gamma-1}{2} {Ma_1}^2} \right)^{\frac{-\gamma}{\gamma-1}}, \tag{B.2}$$

$$\theta_2 = \theta_1 + \theta_\delta, \tag{B.3}$$

where

$$\nu(Ma, \gamma) = \sqrt{\frac{\gamma+1}{\gamma-1}} \arctan \sqrt{\frac{\gamma-1}{\gamma+1}(Ma^2 - 1)} - \arctan \sqrt{Ma^2 - 1} \tag{B.4}$$

is a Prandtl-Meyer function. Here, $(\cdot)_1$ and $(\cdot)_2$ indicate flow conditions before the wave and after the wave, respectively. θ_δ is predetermined so that the flow after the initial expansion goes along the nozzle ramp, Eq. (B.1) is solved using `fsolve`, a nonlinear equation solver in MATLAB®.

Wave Generation at the Cowl Lip

At the cowl lip, different types of pressure waves are generated based on a nozzle expansion condition. Figure B.3 shows the four cases distinguished by ambient flow Mach number and the expansion condition. A superscript with a parenthesis indicates a serial number assigned to each flow-field cell. $\{Ma_\mathrm{e}^{(1)}, p_\mathrm{e}^{(1)}, \theta_\mathrm{e}^{(1)}\}$ and $\{Ma_\mathrm{a}^{(1)}, p_\mathrm{a}^{(1)}, \theta_\mathrm{a}^{(1)}\}$ are already known as explained in Fig. B.2. In all the cases shown in Fig. B.2, static pressure and flow angle must be identical across a slip line (supersonic) or across a free boundary (subsonic or transonic). The iterative algorithm developed in Ref. 115 is employed in order to find downstream flow conditions that satisfy this constraint. Its procedure is explained below using the case of Fig. B.3a as an example. Hereafter, γ_e denotes the heat capacity ratio of the engine exhaust, and γ_a indicates that of the ambient flow.

1) The value of $p_\mathrm{e}^{(4)} = p_\mathrm{a}^{(2)}$ is assumed.

2) $Ma_\mathrm{e}^{(4)}$ and $\theta_\mathrm{e}^{(4)}$ are computed using the following isentropic flow equations:

$$Ma_\mathrm{e}^{(4)} = \sqrt{\frac{\left(p_\mathrm{e}^{(4)}/p_\mathrm{e}^{(1)}\right)^{\frac{\gamma_\mathrm{e}-1}{-\gamma_\mathrm{e}}} \cdot \left(1 + \frac{\gamma_\mathrm{e}-1}{2} Ma_\mathrm{e}^{(1)^2}\right) - 1}{(\gamma_\mathrm{e} - 1)/2}}, \tag{B.5}$$

$$\theta_\mathrm{e}^{(4)} = \theta_\mathrm{e}^{(1)} - \left[\nu(Ma_\mathrm{e}^{(4)}, \gamma_\mathrm{e}) - \nu(Ma_\mathrm{e}^{(1)}, \gamma_\mathrm{e})\right]. \tag{B.6}$$

3) $Ma_\mathrm{a}^{(2)}$ and $\theta_\mathrm{a}^{(2)}$ are calculated based on the following two-dimensional oblique shock equations:

$$\theta_\mathrm{s} = \arcsin\sqrt{\frac{p_\mathrm{a}^{(2)}/p_\mathrm{a}^{(1)}(\gamma_\mathrm{a}+1) + (\gamma_\mathrm{a}-1)}{2\gamma_\mathrm{a}\, Ma_\mathrm{a}^{(1)^2}}}, \tag{B.7}$$

$$\theta_\delta = \operatorname{arccot}\left[\left(\frac{(\gamma_\mathrm{a}+1) Ma_\mathrm{a}^{(1)^2}}{2\left(Ma_\mathrm{a}^{(1)^2}\sin^2\theta_\mathrm{s} - 1\right)} - 1\right)\tan\theta_\mathrm{s}\right], \tag{B.8}$$

$$Ma_\mathrm{a}^{(2)} = \sqrt{\frac{(\gamma_\mathrm{a}-1)\, Ma_\mathrm{a}^{(1)^2}\sin^2\theta_\mathrm{s} + 2}{\left[2\gamma_\mathrm{a} Ma_\mathrm{a}^{(1)^2}\sin^2\theta_\mathrm{s} - (\gamma_\mathrm{a}-1)\right]\sin^2(\theta_\mathrm{s} - \theta_\delta)}}, \tag{B.9}$$

$$\theta_\mathrm{a}^{(2)} = \theta_\mathrm{a}^{(1)} - \theta_\delta. \tag{B.10}$$

4) $\theta_\mathrm{e}^{(4)} = \theta_\mathrm{a}^{(2)}$ must be satisfied. The value of $p_\mathrm{e}^{(4)} = p_\mathrm{a}^{(2)}$ such that meets this condition is searched using `fzero`, a nonlinear root finding algorithm in MATLAB®, which is based on a bisection method. When oblique shocks are involved, it is recommended to use `fzero` instead of `fsolve`. It is noted that a nonlinear oblique shock equation has two solutions, one of which represents a physically appropriate weak shock. The desired solution can always be obtained when a bisection method is employed with a properly chosen initial interval.

5) When $\theta_\mathrm{e}^{(4)} = \theta_\mathrm{a}^{(2)}$ is satisfied, we finally have downstream flow conditions (i.e., $\{Ma_\mathrm{e}^{(4)}, p_\mathrm{e}^{(4)}, \theta_\mathrm{e}^{(4)}\}$ and $\{Ma_\mathrm{a}^{(2)}, p_\mathrm{a}^{(2)}, \theta_\mathrm{a}^{(2)}\}$).

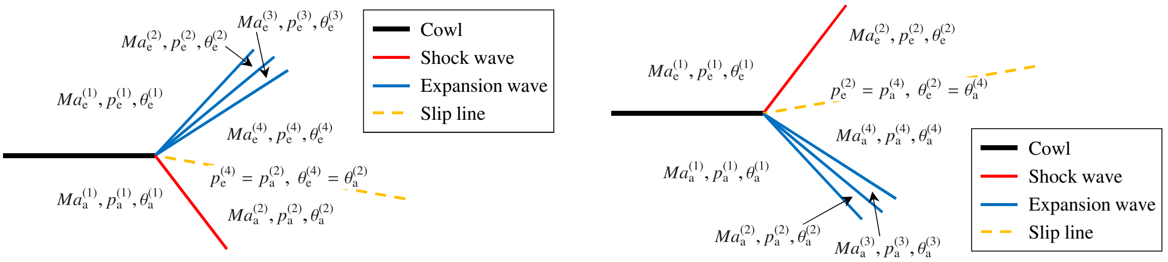

(a) When $Ma_a^{(1)} \geq 1.8$ and $p_e^{(1)} \geq p_a^{(1)}$ (proper/under

(b) When $Ma_a^{(1)} \geq 1.8$ and $p_e^{(1)} < p_a^{(1)}$ (over expansion).

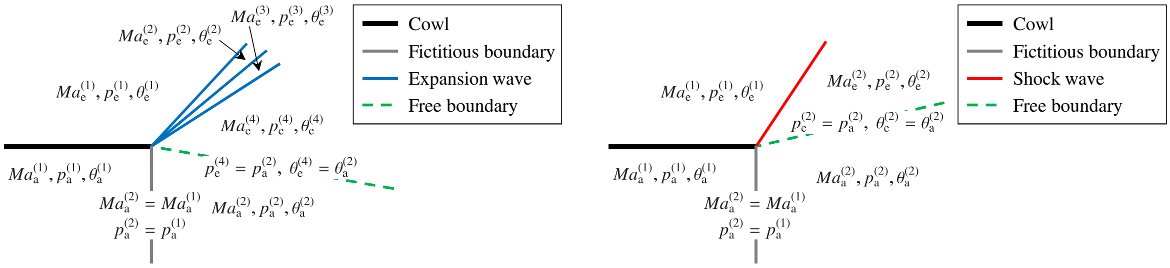

(c) When $Ma_a^{(1)} < 1.8$ and $p_e^{(1)} \geq p_a^{(1)}$ (proper/under expansion).

(d) When $Ma_a^{(1)} < 1.8$ and $p_e^{(1)} < p_a^{(1)}$ (over expansion).

Fig. B.3 Schematic descriptions of the wave generation at the cowl lip.

When ambient flow is subsonic or transonic (see Figs. B.3c and B.3d), the ambient flow is approximated to be static, and it is assumed that the following relations hold:

$$Ma_a^{(1)} = Ma_a^{(2)} = 0, \tag{B.11}$$

$$p_a^{(1)} = p_a^{(2)}. \tag{B.12}$$

Wave Interaction

After the initial expansion and the wave generation at the cowl lip are simulated, the computation step successively proceeds from upstream to downstream by 1) detecting the intersection of pressure waves and then 2) computing flow conditions behind the wave intersection. Figure B.4 shows a schematic description for the calculation of the wave interaction. After detecting the intersection of two waves, the types of new waves shaped from the intersection point can be identified from the intersected wave types. Wave types include shock wave, expansion wave, compression wave, slip line, and free boundary. For example, when the wave 1 and wave 2 are an expansion wave and a shock wave, respectively, the wave 3 is a shock wave, and wave 4 is an expansion wave. Subsequently, the value of $p_{\{e,a\}}^{(i+1)} = p_{\{e,a\}}^{(j+1)}$ such that leads to $\theta_{\{e,a\}}^{(i+1)} = \theta_{\{e,a\}}^{(j+1)}$ is iteratively found using the above-mentioned algorithm. As a result, downstream flow conditions (i.e., $\{Ma_{\{e,a\}}^{(i+1)}, p_{\{e,a\}}^{(i+1)}, \theta_{\{e,a\}}^{(i+1)}\}$ and $\{Ma_{\{e,a\}}^{(j+1)}, p_{\{e,a\}}^{(j+1)}, \theta_{\{e,a\}}^{(j+1)}\}$) and directions of newly-generated waves are obtained.

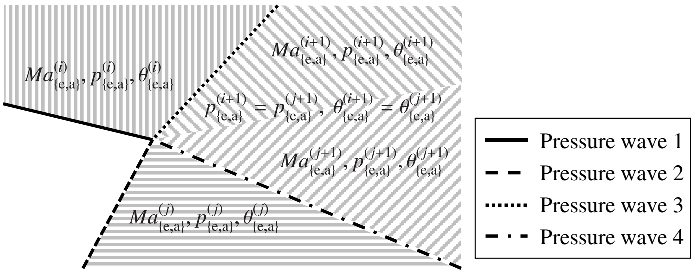

Fig. B.4 Schematic description of the wave interaction.

Wave Reflection on the Nozzle Ramp

When a pressure wave meets the external nozzle ramp surface, the wave is reflected. Flow conditions behind the reflection are calculated with the regular-reflection relations.

Termination of the Computation

Computational domain needed for calculating the pressure distribution on the entire nozzle ramp is shown in Fig. B.2. The force and pitching moment acting on the external nozzle are computed by integrating the pressure distribution over the entire ramp surface after the free-stream pressure is subtracted. The pitching moment is calculated around the center of the nozzle ramp. The force and moment per “unit ramp width times unit engine height” are denoted by F_{ext} and M_{ext}, respectively.

B.2.2 Model Validation

The accuracy of the two-dimensional external nozzle model built in Section B.2.1 is verified by comparing its results with CFD simulations. As test cases, the nozzle geometry and flow conditions are selected as presented in Table B.1 and Table B.2, respectively. CFD setups are shown in Table B.3.

The forces acting on the external nozzle ramp per unit width are calculated via two-dimensional models (the present enhanced model and the model in Ref. 115) and the CFD simulations, and the results are summarized in Table B.4. The results of CFD computations are provided by Mr. Mikoshiba and Prof. Matsuo at Department of Mechanical Engineering, Keio University. Differences between the model outputs and the CFD results are presented by normalizing them by the CFD results. Due to the time constraints, the CFD simulations in Case 1 and Case 2 are not performed yet. When ambient flow is

Table B.1 Nozzle geometry for the validation of the two-dimensional external nozzle flow model.

Parameter	Value
Combustor exit height [m]	2.005
Combustor ramp inclination angle [deg]	10.00
External nozzle ramp inclination angle [deg]	15.20
External nozzle expansion ratio	2.436

Table B.2 Flow conditions for the validation of the two-dimensional external nozzle flow model.

Parameter		Case 1	Case 2	Case 3	Case 4	Case 5	Case 6
Combustor exhaust	Mach number	2.347	2.553	2.725	2.377	1.464	2.526
	Static pressure [Pa]	58291	49838	43118	56153	74779	69959
	Heat capacity ratio	1.233	1.237	1.240	1.161	1.247	1.151
	Gas constant [J/(K kg)]	342.28	349.86	353.98	328.51	299.81	303.99
	Temperature [K]	1938.0	1827.9	1725.3	2336.5	2130.1	2336.8
	Molar fraction of N_2	0.2022	0.1615	0.1359	0.2108	0.6393	0.3587
	O_2	0.0210	0.0230	0.0271	0.0000	0.0075	0.0172
	H_2O	0.3632	0.3730	0.3780	0.4116	0.1908	0.3513
	CO_2	0.1329	0.1297	0.1269	0.1850	0.1129	0.1973
	CO	0.1642	0.1826	0.1935	0.1275	0.0214	0.0480
	H_2	0.0591	0.0700	0.0750	0.0491	0.0058	0.0120
Ambient flow	Mach number	0.802	0.915	1.240	2.874	4.991	8.268
	Static pressure [Pa]	84716	48913	23734	6862	2684	740
	Heat capacity ratio	1.402	1.402	1.402	1.402	1.402	1.402
	Gas constant [J/(K kg)]	288.68	288.68	288.68	288.68	288.68	288.68
	Temperature [K]	276.9	249.4	218.7	215.3	219.9	230.1
Description		Subsonic Ejector-jet Over-exp.	Subsonic Ejector-jet Over-exp.	Transonic Ejector-jet Under-exp.	Supersonic Ejector-jet Under-exp.	Supersonic Ramjet Under-exp.	Supersonic Scramjet Under-exp.

Table B.3 Governing equations and computational schemes in CFD computations.

Item	Description
Governing equations	Two-dim. compressive Navier-Stokes equations The ideal gas law Conservation law of chemical species
Chemical species	N_2, O_2, H_2O, CO_2, CO, H_2
Discretization of convection term	Yee's non-MUSCL type 2nd-order TVD
Discretization of viscos term	2nd-order central difference
Time integration method	Implicit LU-ADI
Turbulence model	RANS (k-ω model)
The number of grid points	500,000 (in Case 3), 300,000 (in Cases 4–6)
Minimum grid size	10×10^{-6} m
Boundary condition on the ramp wall	No slip condition
Outflow boundary condition	Zeroth-order extrapolation

Table B.4 The force acting on the external nozzle per unit width calculated by two-dimensional models and the CFD simulations

Test case	2D model [kN/m]		CFD [kN/m]	Deviation from CFD [%]	
	Enhanced	Ref. 115		Enhanced	Ref. 115
Case 1	244.44	209.15	–	–	–
Case 2	71.09	52.50	–	–	–
Case 3	53.71	43.42	54.39	1.250	20.169
Case 4	70.23	67.93	69.15	1.562	1.764
Case 5	65.42	77.00	65.70	0.426	17.199
Case 6	90.03	81.82	87.91	2.412	6.928

supersonic or hypersonic, the results obtained using the enhanced two-dimensional model coincide with the CFD results well, and it is superior to the accuracy of the model in Ref. 115.

Flow fields and ramp-pressure distributions obtained by the enhanced two-dimensional model and those provided by CFD simulations are shown in Fig. B.5 and Fig. B.6, respectively. Because the no-slip condition is imposed on the nozzle ramp in the CFD simulations, the ramp pressure somewhat increases around the beginning of the nozzle ramp. Except Case 3, the flow fields from the model and those from the CFD simulation are in good agreement. As for the Case 3, ambient flow is approximated to be static in the two-dimensional model, and this results in the dissimilarity of the ambient flow fields. However, since the subsonic ambient flow has no influence on the ramp pressure when the external nozzle is an under-expanded condition, the ramp pressure distributions in the model and in CFD are almost the same. In over-expanded nozzles, on the other hand, there are strong interactions between the exhaust flow and the ambient flow. According to the two-dimensional model, a diamond shock pattern is generated in Case 1 as a result of the flow interaction. In Case 2, the ramp pressure increases from upstream to downstream after compression waves reflected from the jet free boundary reach the nozzle ramp. The accuracy validation of the two-dimensional model in Case 1 and 2 should be conducted in the future work.

It is noted that the effective force produced by the external nozzle is computed by subtracting the ambient pressure force from the values shown in Table B.4. Actually, negative force is acting on the external nozzle in over-expansion cases (i.e., Case 1 and 2), and it is equivalent to the decreases of thrust and lift.

B.3 Surrogate Modeling of 2D External Nozzle Model

In order to avoid iterative and costly evaluations of the two-dimensional external nozzle model during the optimization computation, surrogate models for F_{ext} and M_{ext} are constructed beforehand. Procedures for constructing a surrogate model consists of three steps: conducting design of experiments, training the surrogate model, and validating the obtained surrogate model. Input variables to the two-dimensional

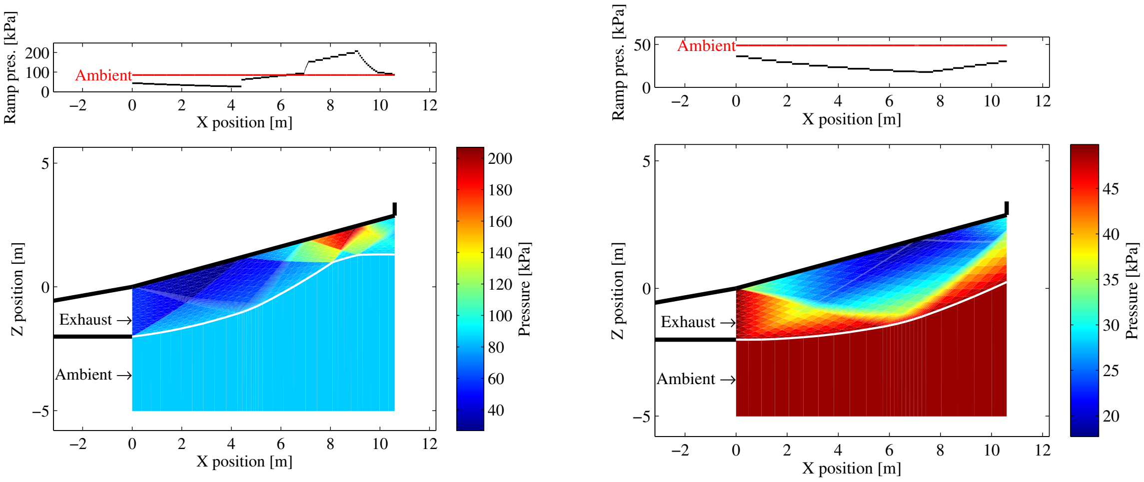

(a) Case 1.

(b) Case 2.

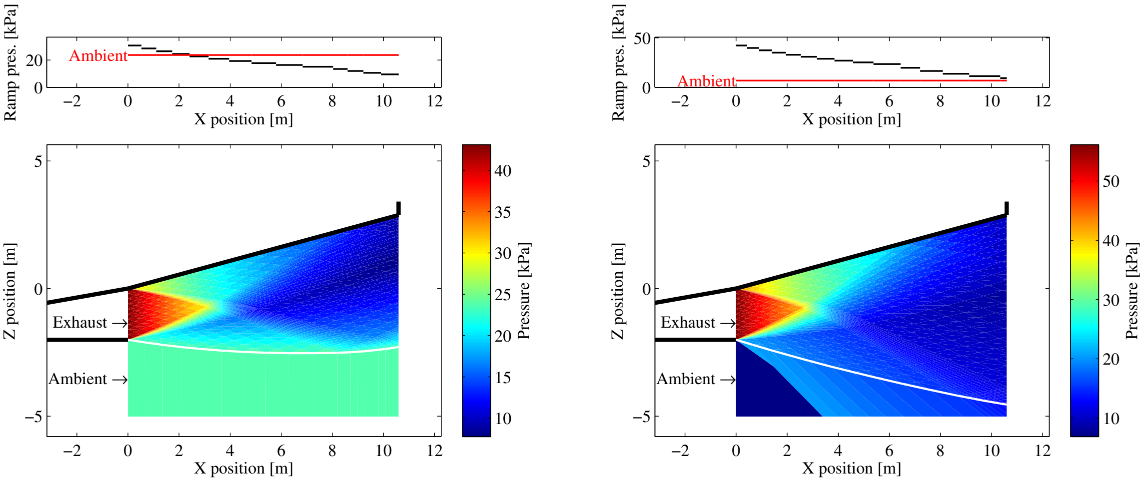

(c) Case 3.

(d) Case 4.

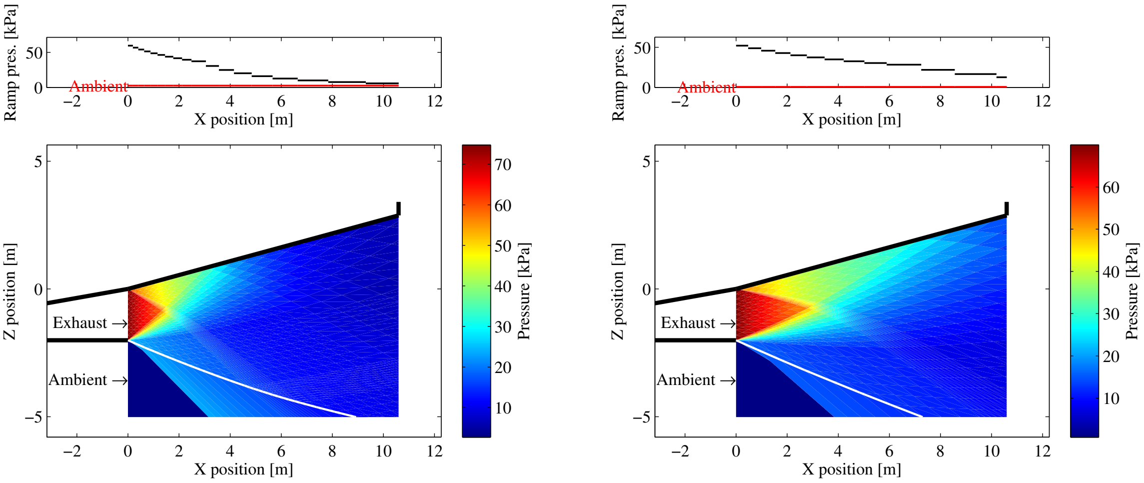

(e) Case 5.

(f) Case 6.

Fig. B.5 Outputs of the two-dimensional external nozzle flow model.

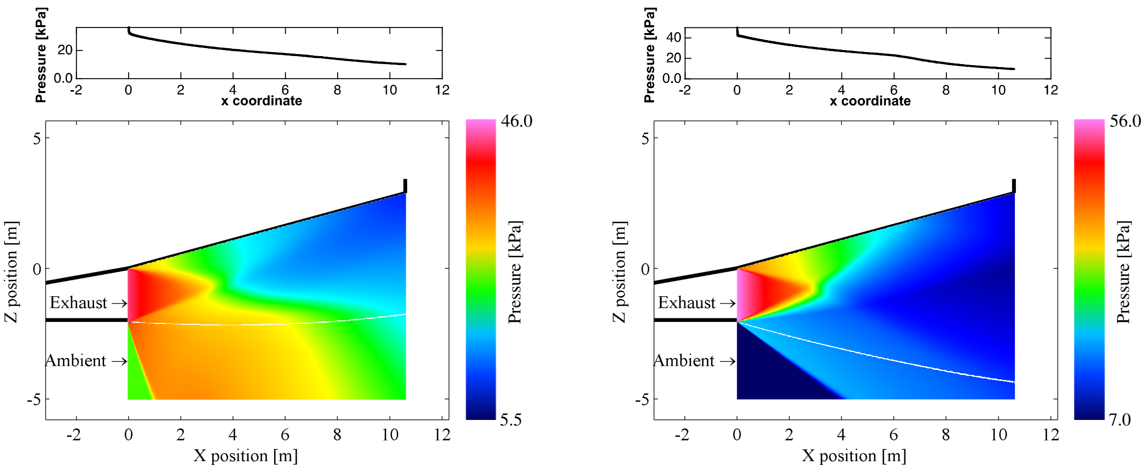

(a) Case 3. (b) Case 4.

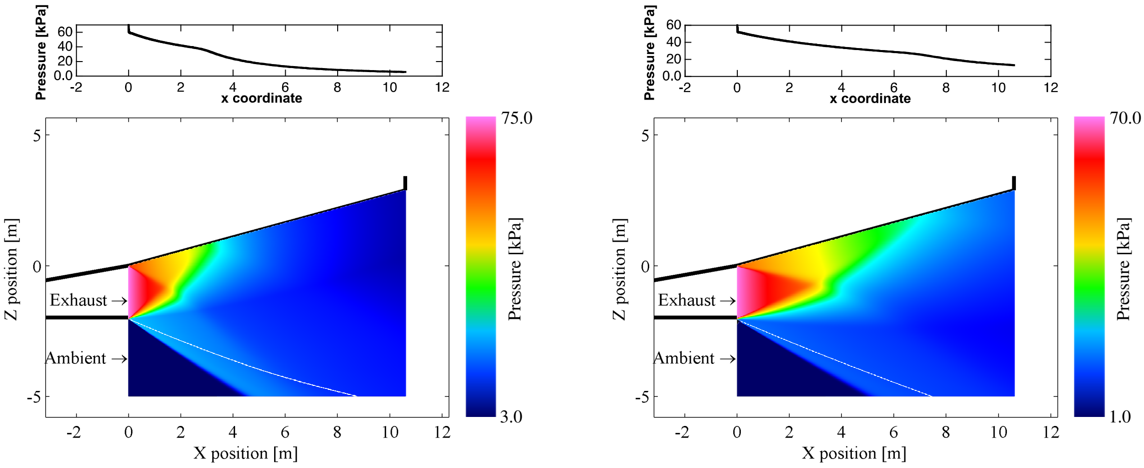

(c) Case 5. (d) Case 6.

Fig. B.6 Outputs of the two-dimensional Navier-Stokes CFD simulations for the external nozzle flow. Provided by Mr. Mikoshiba and Prof. Matsuo at Department of Mechanical Engineering, Keio University.

model are composed of

$$Ma_{\mathrm{e}},\ p_{\mathrm{e}},\ \gamma_{\mathrm{e}},\ Ma_{\mathrm{a}},\ p_{\mathrm{a}},\ \gamma_{\mathrm{a}},\ b_{\mathrm{ext}},\ l_{\mathrm{ext}}/e_{\mathrm{h}}. \tag{B.13}$$

A straightforward approach in the design of experiments is to specify lower/upper bounds of these inputs and to generate sample points that cover the rectangular space defined by these bounds.

In the present case, however, some region of the rectangular input space represents unrealistic input conditions. It is because, Ma_{e}, p_{e}, and γ_{e} are the outputs of the RBCC engine simulation, and they are correlated with each other. For example, Fig. B.7 shows all the pairs of Ma_{e} and p_{e} in the tabular data of the engine performance. In order to construct surrogate models with such constrained inputs efficiently, an adaptive sampling algorithm is developed as shown in Fig. B.8.

Step 1: First, a targeted value of the coefficient of determination is specified by the user, and it is de-

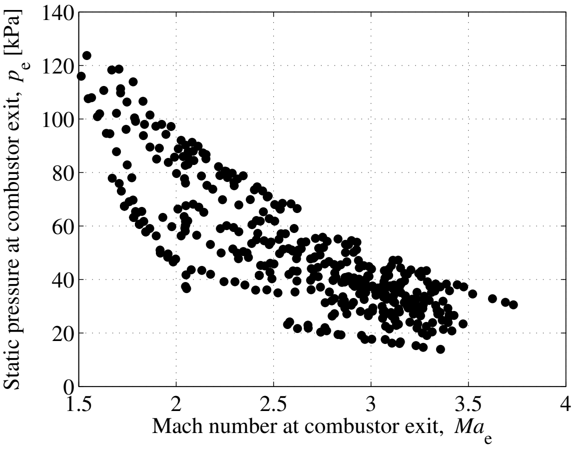

Fig. B.7 All the pairs of Ma_e and p_e in the RBCC engine performance dataset.

noted by R^2_{tgt}. The coefficient of determination is employed as an accuracy measure of surrogate models, and the surrogate models are constructed so that the specified targeted value is satisfied. In the present study, $R^2_{tgt} = 0.99$.

Step 2: Next, an operating mode of RBCC engines (ramjet mode or ejector-jet/scramjet mode) is specified. Additionally, an expansion condition of the external nozzle is chosen. In the present study, surrogate models for F_{ext} and M_{ext} are constructed in the following types of conditions:

Type 1: $Ma_\infty < 1.8$, ejector-jet/scramjet, over-expansion. (B.14)

Type 2: $Ma_\infty < 1.8$, ejector-jet/scramjet, under-expansion. (B.15)

Type 3: $Ma_\infty \geq 1.8$, ejector-jet/scramjet, under-expansion. (B.16)

Type 4: $Ma_\infty \geq 1.8$, ramjet, under-expansion. (B.17)

The other conditions (e.g., the combination of ramjet mode and over-expansion) do not exist in optimized flight trajectories.

Step 3: Value ranges of Ma_∞, $(\alpha + b_{wed})$, (T_R/S_{capt}), b_{ext}, (l_{ext}/e_h), and q_∞ are specified. These variables uniquely determine nozzle geometry, combustor exit flow conditions, and ambient flow conditions (see Chapter 5 for details). Ma_∞, $(\alpha + b_{wed})$ and q_∞ are selected as input variables for representing free-stream flow conditions, because flight trajectories are typically constrained based on these variables (e.g., $q_\infty \leq 50$ kPa). In the present study, the following value ranges are used:

$$(\alpha + b_{wed}) \in [0,\ 23]\ \text{deg}, \qquad T_R/S_{capt} \in [100,\ 400]\ \text{kN/m}^2,$$
$$b_{ext} \in [10,\ 20]\ \text{deg}, \qquad (l_{ext}/e_h) \in [2.3,\ 5.4]$$

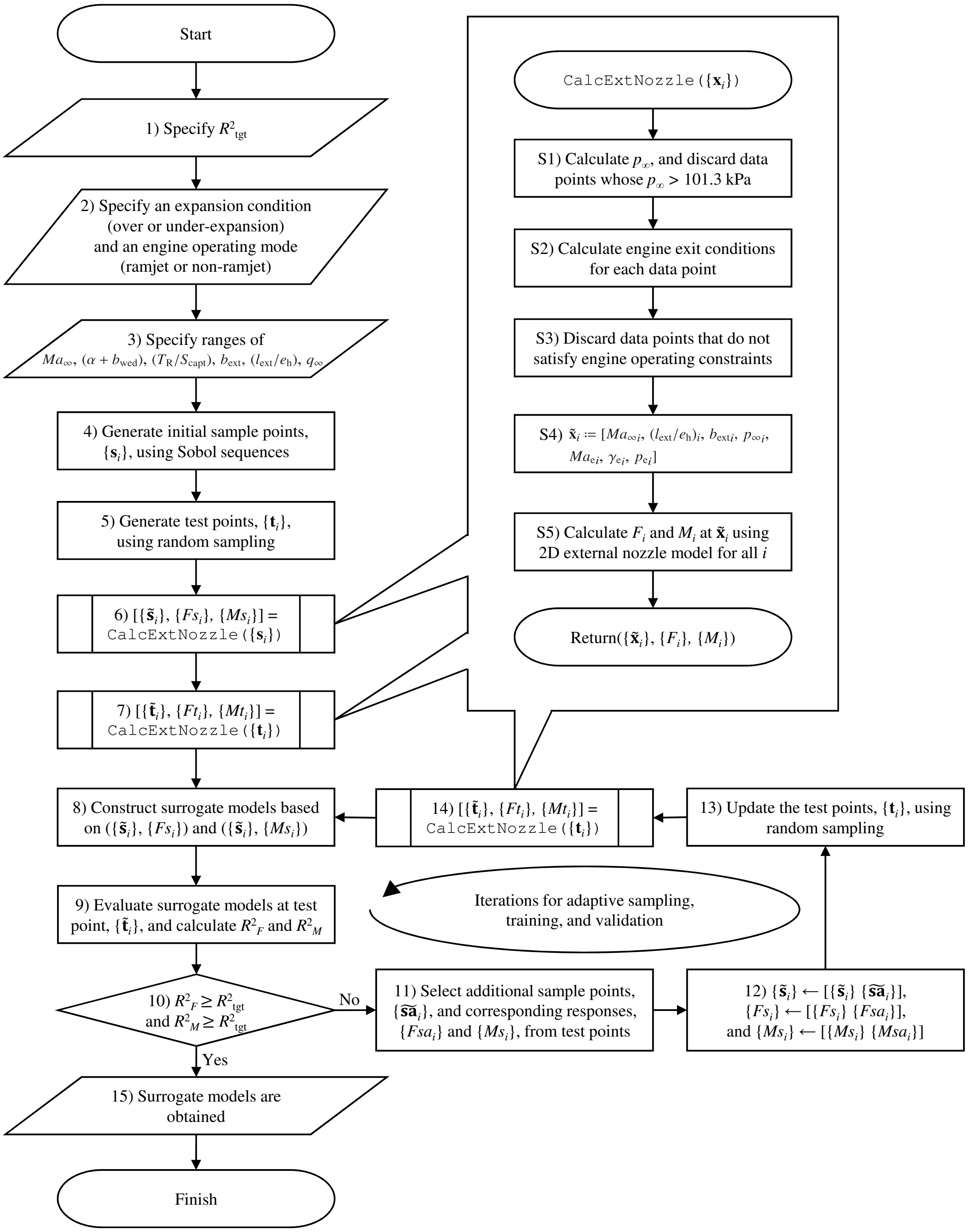

Fig. B.8 Flowchart for constructing surrogate models of external nozzle simulations.

and

$$\begin{cases} Ma_\infty \in [0.2,\ 1.2], & q_\infty \in [1,\ 50]\ \text{kPa}, \quad \text{for Type 1.} \\ Ma_\infty \in [0.2,\ 1.8], & q_\infty \in [1,\ 50]\ \text{kPa}, \quad \text{for Type 2.} \\ Ma_\infty \in [1.8,\ 15], & q_\infty \in [1,\ 50]\ \text{kPa}, \quad \text{for Type 3.} \\ Ma_\infty \in [3.0,\ 6.0], & q_\infty \in [10,\ 50]\ \text{kPa}, \quad \text{for Type 4.} \end{cases} \tag{B.18}$$

Step 4: Initial sample points are generated using a quasi-random sampling strategy based on Sobol sequences[116]. Uniformly distributed points in a unit cube whose dimension is 6 (the number of input variables described in Step 3) are produced by a Sobol sequence generator implemented by Fox[117]. Then, they are scaled so that the value range of each dimension coincides with the corresponding value bound specified in Step 3. The obtained sample points are denoted by

$$\mathbf{s}_i := [Ma_{\infty i},\ (\alpha + b_\text{wed})_i,\ (T_\text{R}/S_\text{capt})_i,\ b_{\text{ext}i},\ (l_\text{ext}/e_\text{h})_i,\ q_{\infty i}], \quad i = 1, \ldots, n_s, \tag{B.19}$$

where n_s is the number of initial sample points. By using low discrepancy sequences such as Sobol sequences, more uniformly distributed sample points can be obtained compared to conventional pseudo-random generators, especially when the number of sample points is small[116].

Step 5: Test points are created in a similar way to Step 4, but using a random sampling based on a pseudo-random number generator. The obtained test points are denoted by $\{\mathbf{t}_i\}_{i=1}^{n_t}$ where n_t indicates the number of test points. Data points that are used for training the parameters of a surrogate model are called sample points. On the other hand, test points are employed to validate the accuracy of the trained surrogate model.

Step 6: A set of input variables to the external nozzle model is prepared at each sample point, $\mathbf{s}_i$, for $i = 1, \ldots, n_s$, and it is denoted by $\tilde{\mathbf{s}}_i$. Then, the force, Fs_i, and the pitching moment, Ms_i, exerted on the external nozzle ramp per "unit ramp width times unit engine height" are calculated using the two-dimensional model in Section B.2. The calculation procedures are encapsulated in a subroutine `CalcExtNozzle()` as follows:

An input to `CalcExtNozzle()` is a set of data points, $\mathbf{x}_i := [Ma_{\infty i},\ (\alpha + b_\text{wed})_i,\ (T_\text{R}/S_\text{capt})_i,\ b_{\text{ext}i},\ (l_\text{ext}/e_\text{h})_i,\ q_{\infty i}], \quad i = 1, \ldots, n_d$. Then, it returns $\{\tilde{\mathbf{x}}_i\}$, $\{F_i\}$, and $\{M_i\}$.

Step S1: For the ith data point, static pressure of the ambient flow is computed from $Ma_{\infty i}$ and $q_{\infty i}$, and it is denoted by $p_{\infty i}$. Data points whose p_i values exceed 101.3 kPa are discarded, since they represent unrealistic flight conditions below sea level.

Step S2: Combustor exit flow conditions for each data point are calculated via procedures explained in Section 5.2.3, and $\{Ma_{\text{e}i},\ \gamma_{\text{e}i},\ p_{\text{e}i}\}$ is obtained for all i.

Step S3: Data points that do not satisfy the following constraints on the engine operating conditions are removed:

$$1\text{ kPa} \leq q_\text{in} \leq 100\text{ kPa} \qquad \text{if ejector-jet or scramjet} \tag{B.20}$$

$$30\text{ kPa} \leq q_\text{in} \leq 100\text{ kPa} \text{ and } 3.0 \leq Ma_\text{in} \leq 6.0 \qquad \text{if ramjet} \tag{B.21}$$

$$p_\text{e} \geq p_\text{a} \qquad \text{if proper/under expansion} \tag{B.22}$$

$$p_\text{e} < p_\text{a} \qquad \text{if over expansion} \tag{B.23}$$

Step S4: A set of input variables to the external nozzle flow model is obtained:

$$\tilde{\mathbf{x}}_i := [Ma_{\infty i},\ (l_\text{ext}/e_\text{h})_i,\ b_{\text{ext}i},\ p_{\infty i},\ Ma_{\text{e}i},\ \gamma_{\text{e}i},\ p_{\text{e}i}]. \tag{B.24}$$

Step S5: The values of F_ext and M_ext are evaluated for all $\tilde{\mathbf{x}}_i$ using the numerical model in Section B.2, and they are denoted by F_i and M_i.

Step 7: Inputs and responses of the external nozzle model are evaluated at test points, $\{\mathbf{t}_i\}$. As a result, $\{\tilde{\mathbf{t}}_i\}$, $\{Ft_i\}$, and $\{Mt_i\}$ are obtained.

Step 8: Surrogate models of F_ext and M_ext are constructed based on the input/output values of sample points ($\{\tilde{\mathbf{s}}_i,\ Fs_i\}$ and $\{\tilde{\mathbf{s}}_i,\ Ms_i\}$). Among a variety of surrogate modeling techniques[76], a radial basic function network (RBFN) is employed. For a set of sample input vectors, $\{\mathbf{X}_i\}_{i=1}^n$ ($\in \{\mathbb{R}^{n_x}\}$), and corresponding response scalar values, $\{Y_i\}_{i=1}^n$ ($\in \{\mathbb{R}\}$), the RBFN surrogate model, $f_\text{sur}\colon \mathbb{R}^{n_x} \to \mathbb{R}$, is written as follows:

$$f_\text{sur}(\mathbf{x}) = \sum_{j=1}^{n} \lambda_j\, \phi(\|\mathbf{x} - \mathbf{X}_j\|_2), \tag{B.25}$$

where $\mathbf{x}$ ($\in \mathbb{R}^{n_x}$) is the input vector, $\lambda_1, \ldots, \lambda_n$ are the weights, $\|\cdot\|_2$ denotes the Euclidean norm, and $\phi\colon \mathbb{R}_\geq \to \mathbb{R}$ is a radial basis function. Typical choices of the radial basis function include

$$\phi(r) = \begin{cases} \exp(-r^2/\beta^2) & \text{Gaussian.} \\ r^2 \log(r) & \text{thin plate spline.} \\ (r^2 + \beta^2)^{1/2} & \text{multiquadric.} \\ (r^2 + \beta^2)^{-1/2} & \text{inverse multiquadric.} \end{cases} \tag{B.26}$$

In the present study, the multiquadric basis with $\beta = 0.01$ is adopted. The weights are determined by solving linear equations arising from least-squares fit. The resultant surrogate functions for predicting F_ext and M_ext are denoted by F_sur and M_sur, respectively.

For evaluating longitudinal static stability of the vehicle in Section 5.2.5, partial derivative values of the external nozzle performance with respect to angle of attack are required. The simplest way for computing the derivative of a function is to adopt its finite difference approximation.

The numerical differentiation, however, yields numerical errors, and can results in slow convergence in gradient-based optimization. To overcome this difficulty, analytic differentiation of the RBFN surrogate model is implemented. When the multiquadric basis is considered, the following relation holds:

$$\frac{\partial f_{\mathrm{sur}}(\mathbf{x})}{\partial x_k} = \sum_{j=1}^{n} \lambda_j \frac{x_k - X_{j_k}}{\left(\|\mathbf{x} - \mathbf{X}_j\|_2{}^2 + \beta^2\right)^{\frac{1}{2}}}, \quad \text{for } k = 1, \dots, n_x, \tag{B.27}$$

where x_k is the kth element of $\mathbf{x}$, and X_{j_k} indicates the kth element of $\mathbf{X}_j$.

Step 9: The obtained surrogate models are evaluated at test points, and subsequently, the coefficients of determination are calculated as follows:

$$R_F^2 = 1 - \left\{\sum_i \left[Ft_i - F_{\mathrm{sur}}(\tilde{\mathbf{t}}_i)\right]^2\right\} \Bigg/ \left\{\sum_i \left[Ft_i - \frac{1}{n_t}\sum_j^{n_t} Ft_j\right]^2\right\}, \tag{B.28}$$

$$R_M^2 = 1 - \left\{\sum_i \left[Mt_i - M_{\mathrm{sur}}(\tilde{\mathbf{t}}_i)\right]^2\right\} \Bigg/ \left\{\sum_i \left[Mt_i - \frac{1}{n_t}\sum_j^{n_t} Mt_j\right]^2\right\}. \tag{B.29}$$

Step 10: Whether adaptive sampling iterations are terminated or not is determined. The stopping criterion is that both $R_F^2 \geq R_{\mathrm{tgt}}^2$ and $R_M^2 \geq R_{\mathrm{tgt}}^2$ are satisfied. Even though this condition is successfully met, the iterations are stopped when the number of iterations reaches the predefined maximum number, which is 10 in the present study.

Step 11: When the stopping criterion is not satisfied, new sample points are added to existing ones so as to achieve better accuracy. The additional sample points are selected from the test points at which the larger errors between surrogate predictions and actual responses are observed. the input vectors of these additional sample points are denoted by $\{\tilde{\mathbf{sa}}_i\}$, and the resulting response scalars are written as $\{Fsa_i\}$ and $\{Msa_i\}$. The number of additional sample points is 30. This adaptive sampling strategy is based on a simple idea that more sample points are required at the locations where the prediction accuracy was found to be poor.

Step 12: The additional sample points are combined with the existing ones in the following way:

$$\{\tilde{\mathbf{s}}\} \leftarrow [\{\tilde{\mathbf{s}}\}\,\{\tilde{\mathbf{sa}}\}], \tag{B.30}$$

$$\{Fs_i\} \leftarrow [\{Fs_i\}\,\{Fsa_i\}], \tag{B.31}$$

$$\{Ms_i\} \leftarrow [\{Ms_i\}\,\{Msa_i\}]. \tag{B.32}$$

Step 13: Since test points used in the previous iteration overlap with the updated sample points, the old test points are no longer valid. Therefore, test points are regenerated using random sampling, and they are denoted by $\{t_i\}$.

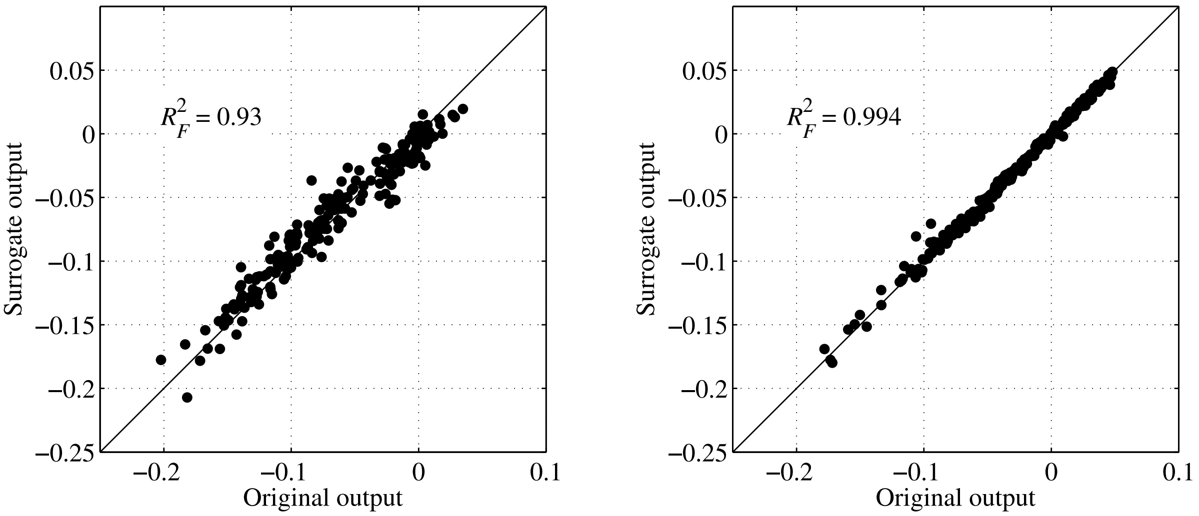

(a) Type 1: $Ma_\infty \le 1.8$, non-ramjet, over-exp.

(b) Type 2: $Ma_\infty \le 1.8$, non-ramjet, under-exp.

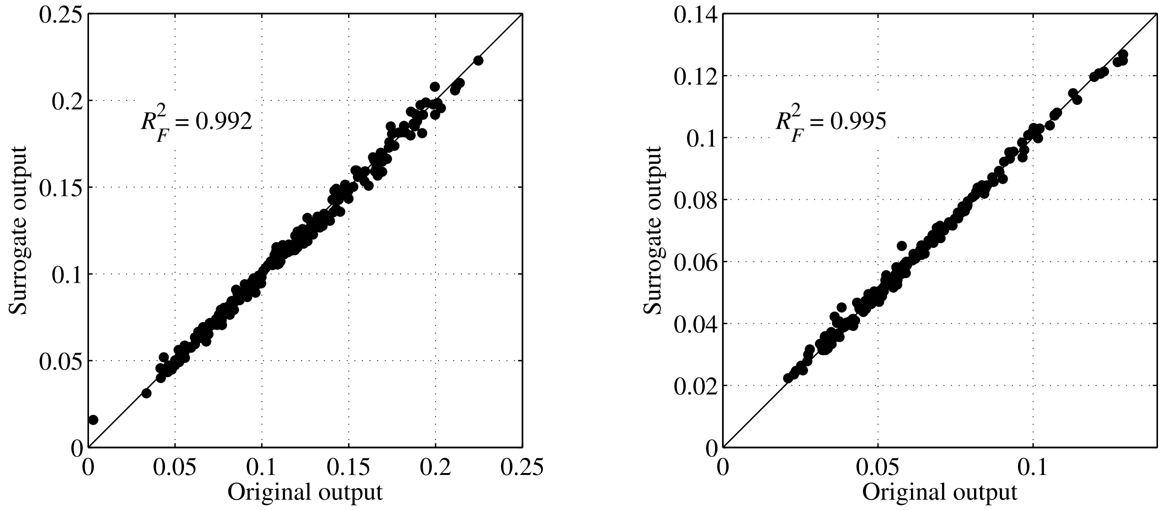

(c) Type 3: $Ma_\infty \ge 1.8$, non-ramjet, under-exp.

(d) Type 4: $Ma_\infty \ge 1.8$, ramjet, under-exp.

Fig. B.9 Accuracies of surrogate models for the output F_{ext} of the two-dim. external nozzle model.

Step 14: The updated test points are evaluated via `CalcExtNozzle()`, and it gives $\{\tilde{t}_i\}$, $\{Ft_i\}$, and $\{Mt_i\}$.

Step 15: Procedures from Step 8 to Step 14 are repeated until the termination criterion is satisfied in Step 10. When the criterion is successfully met, surrogate models of F_{ext} and M_{ext} whose R^2 values are larger than R^2_{tgt} are obtained.

Accuracies of the constructed surrogate models for the outputs, F_{ext} and M_{ext}, are presented in Fig. B.9 and Fig. B.10, respectively. Scatter plots between the original-model outputs and the surrogate-model outputs are depicted, and their R^2 values are shown as well. While the R^2 values of the surrogate models in Type 1 are less than the targeted value, $R^2_{\mathrm{tgt}} = 0.99$, the approximation accuracies are satisfactory overall.

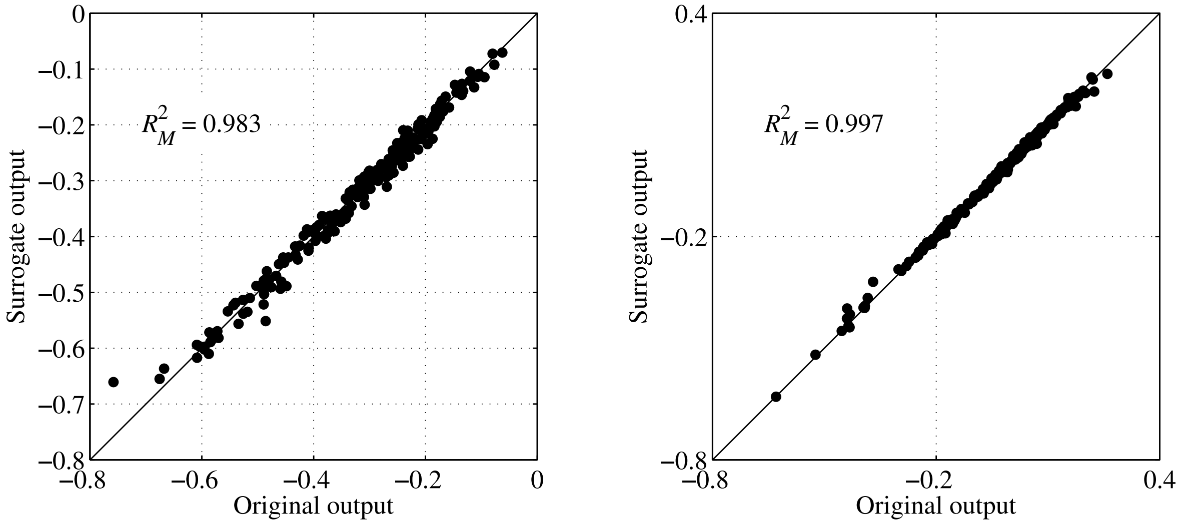

(a) Type 1: $Ma_\infty \leq 1.8$, non-ramjet, over-exp.

(b) Type 2: $Ma_\infty \leq 1.8$, non-ramjet, under-exp.

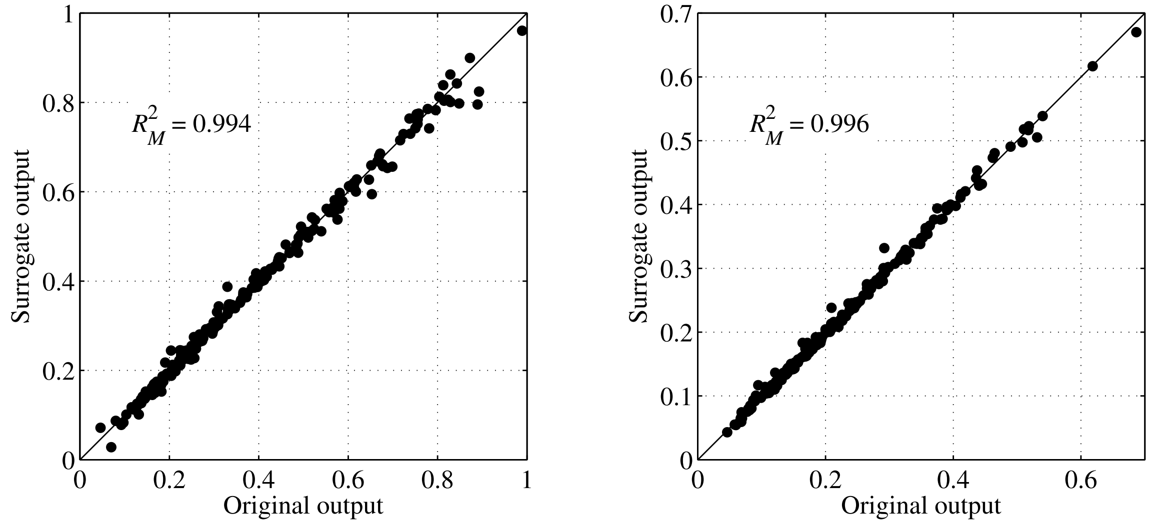

(c) Type 3: $Ma_\infty \geq 1.8$, non-ramjet, under-exp.

(d) Type 4: $Ma_\infty \geq 1.8$, ramjet, under-exp.

Fig. B.10 Accuracies of surrogate models for the output M_{ext} of the two-dim. external nozzle model.

Appendix C

Aerodynamic Analysis Model

In this chapter, the employed CFD methods for the aerodynamic analysis are briefly described first. Then, the procedures for predicting the aerodynamic characteristics of the mated configuration (the booster and the orbiter) are developed.

C.1 Overview of Employed CFD Methods

Computing the trajectory of a launch vehicle requires the aerodynamic properties of the vehicle for a wide range of flight conditions. This is different from the case of aircraft design problems, where a cruise condition may be defined as an aerodynamic design point. Therefore, the extensive use of state-of-the-art computational fluid dynamics (CFD) simulations, where governing equations of fluid are solved numerically, in large-scale MDO problems of RLVs is challenging [*], even though the available computational capabilities are increasing in recent years. It is also noted that, detailed investigations of the flow field around the vehicle (e.g., boundary layer) are not targeted in the present conceptual design study in contrast to scientific researches. Considering these, the following two types of engineering-level CFD methods are utilized depending on the flow speed: A502 PAN AIR code[118] and local surface inclination methods. These CFD calculation can be executed by preparing a set of vehicle surface panels without generating a mesh surrounding them. A computer program for automatically producing such panels based on the vehicle design variables developed mainly in Ref. 14 is employed in the present study with modifications.

In subsonic or transonic conditions, the A502 PAN AIR code[118] is employed. This is a linear potential flow solver using panel methods with a first-order compressibility correction. The PAN AIR code is applied when free-stream Mach number is less than 2.0, because the accuracy of the compressibility correction is deteriorated in higher Mach number.

In supersonic conditions (when free-stream Mach number is not less than 2.0), local surface inclination methods are used. A collection of methods for calculating vehicle surface pressure distribution

---

[*] In Ref. 25, where Euler CFD analysis was applied to the MDO of an RLV, the number of geometry parameters varied in the optimization was only four. In addition, control-surface deflection was not considered.

based only on the inclination angle between the local surface and the free-stream velocity vector is called local surface inclination methods. While the Newtonian method for hypersonic flow would be the most well-known local surface inclination method, its appropriate application condition is high hypersonic whose Mach number is typically more than 20[18]. Instead, a tangent cone method[119] and the Prandtl-Meyer expansion flow theory are applied to the windward and the leeward regions, respectively. In the tangent cone method, it is assumed that the local three-dimensional geometry of the vehicle is replaced with the equivalent cone. The pressure on the local surface is then given by static pressure behind an oblique shock wave caused by the cone. Another and probably more common approach for estimating windward pressure is the combination of the tangent wedge method and the tangent cone method. In this case, vehicle surface is divided several parts with two-dimensional or three dimensional surrounding flow, and the tangent wedge method or the tangent cone method are applied, respectively[18,103]. However, the tangent cone method alone has superior accuracy to the tangent wedge/cone method when they are applied to vehicle configurations such as those considered in the present study[14,119].

The above methods are not valid for estimating the pressure on the vehicle surface where flow separation occurs. Since such situations are observed in the fuselage base, the base pressure is estimated with empirical equations[120, p. 58] instead. In addition, the skin friction coefficient on each panel is calculated using the van Driest's II formula[121] assuming that the boundary layer is turbulent over the entire vehicle surface. This conservative turbulent assumption is adopted due to the difficulty in predicting the boundary layer transition in hypersonic flow[13]. Flow conditions at the outer edge of the boundary layer necessary in the van Driest's formula are obtained from the PAN AIR code or from the local surface inclination methods.

Lift coefficient, drag coefficient, and pitching moment coefficient around the predetermined reference point are obtained by integrating the pressure coefficient and the friction coefficient over the vehicle surface panels. When the airframe-propulsion integrated analysis for the RBCC propulsion system is conducted in Chapter 5, the external nozzle ramp is excluded from this pressure integration, because the force acting on the ramp is computed using the external nozzle model instead.

C.2 Aerodynamic Characterization of the Mated Vehicle Configuration

The above CFD methods are applicable to separated vehicles (i.e., the booster alone or the orbiter alone). In the mated vehicle configuration, where the orbiter is loaded onto the uppersurface of the booster fuselage, it is assumed that the airflow hits the orbiter along its body axis after the flow passes by the booster's nose as shown in Fig. C.1. In this figure, Ma, q, α, L, D, M, and $(x_{\mathrm{ref}}, z_{\mathrm{ref}})$ denote Mach number, dynamic pressure, angle of attack, lift force, drag force, pitching moment, and the position of a reference point around which the aerodynamic moment is calculated, respectively. In addition, S_{f} and c_{f} are the reference area and the reference length, respectively. Subscripts $(\cdot)_\infty$, $(\cdot)_{\mathrm{o}}$, and $(\cdot)_{\mathrm{b}}$ mean that the attached variables indicate the corresponding quantities of free-stream, orbiter, and booster, respectively.

Under this assumption, aerodynamic forces and moment of the mated vehicle are calculated by

$$\begin{aligned} L_\mathrm{m} &= L_\mathrm{b} + L_\mathrm{o}\cos\alpha - D_\mathrm{o}\sin\alpha \\ &= q_\infty\, S_{\mathrm{ref\,b}}\, C_{L\mathrm{b}} + q_\mathrm{o}\, S_{\mathrm{ref\,o}}\left(C_{L\mathrm{o}}\cos\alpha - C_{D\mathrm{o}}\sin\alpha\right), \qquad &(\mathrm{C.1}) \\ D_\mathrm{m} &= D_\mathrm{b} + L_\mathrm{o}\sin\alpha + D_\mathrm{o}\cos\alpha \\ &= q_\infty\, S_{\mathrm{ref\,b}}\, C_{D\mathrm{b}} + q_\mathrm{o}\, S_{\mathrm{ref\,o}}\left(C_{L\mathrm{o}}\sin\alpha + C_{D\mathrm{o}}\cos\alpha\right), \qquad &(\mathrm{C.2}) \\ M_\mathrm{m} &= M_\mathrm{b} + M_\mathrm{m} - L_\mathrm{o}\left(x_{\mathrm{ref\,o}} - x_{\mathrm{ref\,b}}\right) + D_\mathrm{o}\left(z_{\mathrm{ref\,o}} - z_{\mathrm{ref\,b}}\right) \\ &= q_\infty\, S_{\mathrm{ref\,b}}\, c_{\mathrm{ref\,b}}\, C_{M\mathrm{b}} + q_\mathrm{o}\, S_{\mathrm{ref\,o}}\left[C_{M\mathrm{o}} c_{\mathrm{ref\,o}} - C_{L\mathrm{o}}\left(x_{\mathrm{ref\,o}} - x_{\mathrm{ref\,b}}\right) + C_{D\mathrm{o}}\left(z_{\mathrm{ref\,o}} - z_{\mathrm{ref\,b}}\right)\right], \qquad &(\mathrm{C.3}) \end{aligned}$$

where variables with the subscript $(\cdot)_\mathrm{m}$ denote the corresponding quantities of the mated vehicle. Here, the reference point of the mated vehicle is defined as identical to that of the booster.

Flow conditions against the orbiter are computed based on two-dimensional flow approximations. In Model 1 (when flight speed is subsonic or low-supersonic), the flow conditions are assumed to be same as the free-stream conditions. Procedures for computing Ma_o and q_o in Model 2 (high-supersonic or hypersonic case) consist of two steps: 1) shock or expansion-wave calculation at the booster nose and 2) expansion-wave computation along the booster forebody uppersurface. In each optimal-control phase in MDO problems, the employed model (whether Model 1 or Model 2) is specified as shown in Table 4.4 and 5.2. In the following subsections, the detail of each step is explained.

C.2.1 Shock or Expansion-Wave Calculation at the Booster Nose

The inclination angle of the booster forebody uppersurface at the nose tip, which is denoted by θ_n, is calculated from the forebody length, b_lf, and the forebody upper height, b_h, as follows:

$$\theta_\mathrm{n} = \arctan\frac{2b_\mathrm{h}}{b_\mathrm{lf}}. \tag{C.4}$$

It is noted that the shape of the forebody uppersurface is defined as a quadratic function. The flow angle deflected by the pressure wave generated at the nose tip, θ_δ, is written as

$$\theta_\delta = \theta_\mathrm{n} - \alpha. \tag{C.5}$$

Therefore, an oblique shock wave is generated when θ_δ is positive, and expansion waves are generated when it is negative.

An explicit relation for a two-dimensional oblique shock wave[122, 120, pp. 119–122] gives a shock-wave angle, θ_s, as follows:

$$\theta_\mathrm{s} = \arcsin\sqrt{y_2 - b/3}, \tag{C.6}$$

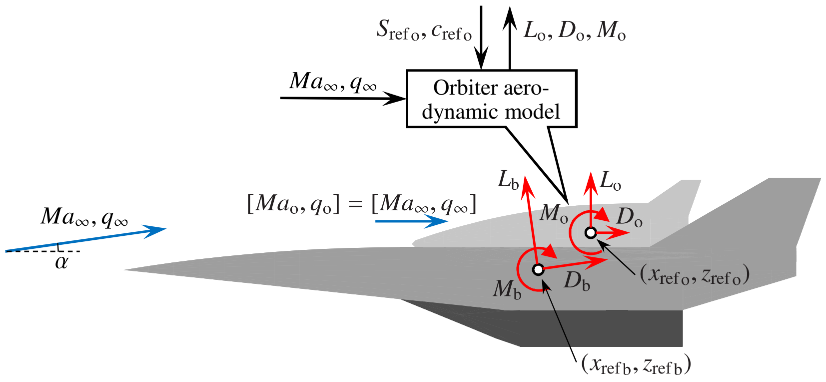

(a) Model 1: Subsonic or low-supersonic case.

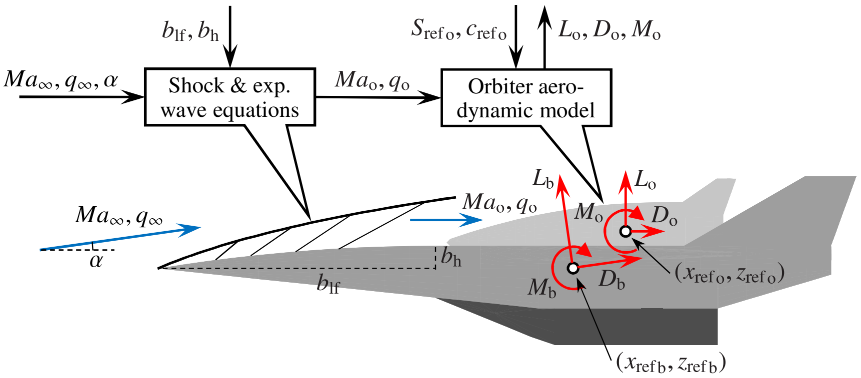

(b) Model 2: High-supersonic or hypersonic case.

Fig. C.1 Model overview for calculating aerodynamic characteristics of the mated vehicle configuration.

where

$$y_2 = -2\sqrt{\frac{-p}{3}}\cos\left(\frac{w}{3}+\frac{\pi}{3}\right), \tag{C.7}$$

$$w = \arccos\left[\frac{-q}{2}\left(\frac{3}{-p}\right)^{\frac{3}{2}}\right], \tag{C.8}$$

$$p = -\frac{b^2}{3} + c, \tag{C.9}$$

$$q = 2\left(\frac{b}{3}\right)^3 - \frac{bc}{3} + d, \tag{C.10}$$

$$b = -\frac{{Ma_1}^2 + 2}{{Ma_1}^2} - \gamma \sin^2\theta_\delta, \tag{C.11}$$

$$c = \frac{2{Ma_1}^2 + 1}{{Ma_1}^4} + \left[\frac{(\gamma+1)^2}{4} + \frac{\gamma-1}{{Ma_1}^2}\right]\sin^2\theta_\delta, \tag{C.12}$$

$$d = -\frac{\cos^2\theta_\delta}{{Ma_1}^4}. \tag{C.13}$$

Here, γ is the specific heat ratio of the airflow, which equals to 1.4. Subscripts $(\cdot)_1$ and $(\cdot)_2$ mean that the attached variables indicate the corresponding quantities before and after the shock wave, respectively. Then, the change ratios of flow conditions across the shock wave are calculated as follows:

$$Ma_2 = \sqrt{\frac{(\gamma-1){Ma_1}^2 \sin^2\theta_{\mathrm{s}} + 2}{\left[2\gamma {Ma_1}^2 \sin^2\theta_{\mathrm{s}} - (\gamma-1)\right] \sin^2(\theta_{\mathrm{s}} - \theta_\delta)}}, \tag{C.14}$$

$$\frac{q_2}{q_1} = \frac{2\gamma {M_1}^2 \sin^2\theta_{\mathrm{s}} - (\gamma-1)}{\gamma+1} \left(\frac{Ma_2}{Ma_1}\right)^2, \tag{C.15}$$

$$\frac{p_2}{p_1} = \frac{2\gamma {M_1}^2 \sin^2\theta_{\mathrm{s}} - (\gamma-1)}{\gamma+1}, \tag{C.16}$$

$$\frac{\rho_2}{\rho_1} = \frac{(\gamma+1){Ma_1}^2 \sin^2\theta_{\mathrm{s}}}{(\gamma-1){Ma_1}^2 \sin^2\theta_{\mathrm{s}} + 2}, \tag{C.17}$$

$$\frac{T_2}{T_1} = \left[2\gamma {Ma_1}^2 \sin^2\theta_{\mathrm{s}} - (\gamma-1)\right] \frac{(\gamma-1){Ma_1}^2 \sin^2\theta_{\mathrm{s}} + 2}{(\gamma+1)2{Ma_1}^2 \sin^2\theta_{\mathrm{s}}}, \tag{C.18}$$

where ρ and T denote density and temperature, respectively.

Isentropic Prandtl-Meyer flow relations, on the other hand, can be written using an approximate inverse Prandtl-Meyer function[123] in the following manner:

$$Ma_2 = \frac{1 + d_1 y + d_2 y^2 + d_3 y^3}{1 + e_1 y + e_2 y^2}, \tag{C.19}$$

$$\frac{q_2}{q_1} = \left(\frac{1 + \frac{\gamma-1}{2} Ma_1^2}{1 + \frac{\gamma-1}{2} Ma_2^2}\right)^{\frac{\gamma}{\gamma-1}} \left(\frac{Ma_2}{Ma_1}\right)^2, \tag{C.20}$$

$$\frac{p_2}{p_1} = \left(\frac{1 + \frac{\gamma-1}{2} Ma_1^2}{1 + \frac{\gamma-1}{2} Ma_2^2}\right)^{\frac{\gamma}{\gamma-1}}, \tag{C.21}$$

$$\frac{\rho_2}{\rho_1} = \left(\frac{1 + \frac{\gamma-1}{2} Ma_1^2}{1 + \frac{\gamma-1}{2} Ma_2^2}\right)^{\frac{1}{\gamma-1}}, \tag{C.22}$$

$$\frac{T_2}{T_1} = \frac{1 + \frac{\gamma-1}{2} Ma_1^2}{1 + \frac{\gamma-1}{2} Ma_2^2}, \tag{C.23}$$

where

$$y = \left(\frac{\nu_2}{\nu_\infty}\right)^{\frac{2}{3}}, \tag{C.24}$$

$$\nu_\infty = \frac{\pi}{2}\left(\frac{1}{\lambda} - 1\right), \tag{C.25}$$

$$\nu_1 = \nu(Ma_1, \gamma), \tag{C.26}$$

$$\nu(Ma, \gamma) = \sqrt{\frac{\gamma+1}{\gamma-1}} \arctan\sqrt{\frac{\gamma-1}{\gamma+1}(Ma^2 - 1)} - \arctan\sqrt{Ma^2 - 1}, \tag{C.27}$$

$$\nu_2 = -\theta_\delta + \nu_1, \tag{C.28}$$

and

$$
\begin{aligned}
a_1 &= \frac{1}{2}\eta_\infty, & a_2 &= \frac{3+8\lambda^2}{40}{\eta_\infty}^2, & a_3 &= \frac{-1+328\lambda^2+104\lambda^4}{2800}\eta_\infty^3,\\
d_1 &= a_1 - 1 - \frac{a_3-K}{a_2-K}, & d_2 &= a_2 - a_1 - \frac{(a_1-1)(a_3-K)}{a_2-K}, & d_3 &= \frac{(a_3-K)(a_1-K)}{a_2-K} - a_2 + K,\\
e_1 &= -1 - \frac{a_3-K}{a_2-K}, & e_2 &= -e_1 - 1, & &\\
\lambda &= \sqrt{\frac{\gamma-1}{\gamma+1}}, & K &= \frac{4}{3\pi}\left(1+\frac{1}{\lambda}\right), & \eta_\infty &= \left[\frac{3\pi}{2\lambda(1+\lambda)}\right]^{\frac{2}{3}}.
\end{aligned}
\tag{C.29}
$$

While an exact inverse of the Prandtl-Meyer function is not known, Eqs. (C.19–C.29) give its approximation whose error is less than 0.05 % over all the possible flow conditions[123].

During the flight, the value of θ_δ can become either positive or negative depending on the angle of attack and the booster nose geometry. This means that a single set of equations cannot describe the relations of the pressure wave(s) generated at the nose. In order to solve this problem, the following fifth-order polynomial models that approximate both the shock and expansion-wave equations are constructed:

$$
\frac{M_2}{M_1} = \exp\left(\sum_{\substack{i\geq 0,\ j\geq 0,\\ i+j\leq 5}} a^{(i,j)}\,{M_1}^i\,{\theta_\delta}^j\right),
\tag{C.30}
$$

$$
\frac{q_2}{q_1} = \exp\left(\sum_{\substack{i\geq 0,\ j\geq 0,\\ i+j\leq 5}} b^{(i,j)}\,{M_1}^i\,{\theta_\delta}^j\right),
\tag{C.31}
$$

$$
\frac{p_2}{p_1} = \exp\left(\sum_{\substack{i\geq 0,\ j\geq 0,\\ i+j\leq 5}} c^{(i,j)}\,{M_1}^i\,{\theta_\delta}^j\right),
\tag{C.32}
$$

$$
\frac{\rho_2}{\rho_1} = \exp\left(\sum_{\substack{i\geq 0,\ j\geq 0,\\ i+j\leq 5}} d^{(i,j)}\,{M_1}^i\,{\theta_\delta}^j\right),
\tag{C.33}
$$

$$
\frac{T_2}{T_1} = \exp\left(\sum_{\substack{i\geq 0,\ j\geq 0,\\ i+j\leq 5}} e^{(i,j)}\,{M_1}^i\,{\theta_\delta}^j\right).
\tag{C.34}
$$

The polynomial coefficients $[\{a^{(i,j)}\},\ldots,\{e^{(i,j)}\}]$ are determined by least square fits with the following input variable ranges: $M_1 \in [2, 15]$ and $\theta_\delta \in [-10, 20]$ deg. The accuracies of the constructed approximating models are shown in Fig. C.2.

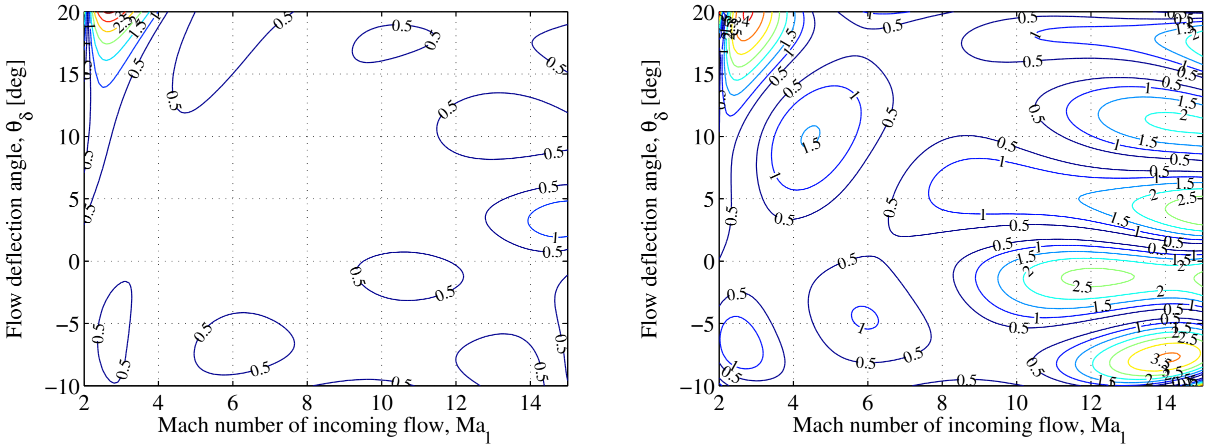

(a) Ma_2/Ma_1 (maximum error is 3.6 %).

(b) q_2/q_1 (maximum error is 4.6 %).

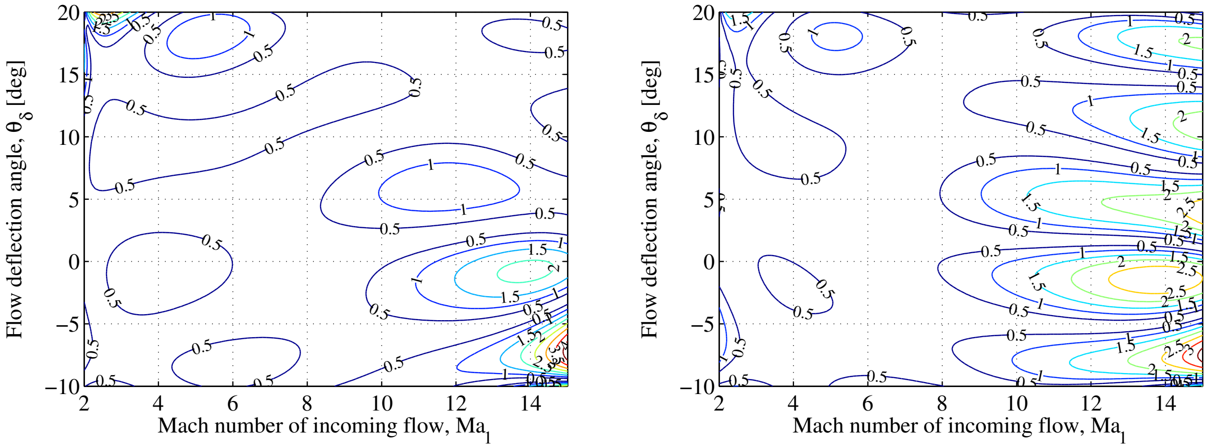

(c) p_2/p_1 (maximum error is 4.3 %).

(d) ρ_2/ρ_1 (maximum error is 3.7 %).

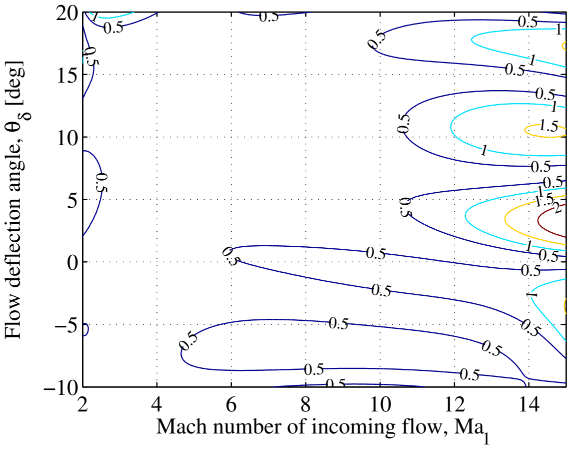

(e) T_2/T_1 (maximum error is 2.5 %).

Fig. C.2 Errors of approximating models for the shock and expansion-wave relations, in percentage.

C.2.2 Expansion-Wave Computation along the Booster Forebody Uppersurface

Behind the oblique shock or expansion waves at the booster nose tip, the airflow expands isentropically along the forebody uppersurface of the booster. The flow turn angle is given by θ_{n}, and it does not depend on angle of attack. The flow conditions after this turn are computed using Eqs. (C.19–C.29), and they define the conditions of airflow that hits the orbiter.

Appendix D

Aerodynamic Heating and Active Cooling Model

In this chapter, numerical models for aerodynamic heating and active cooling analysis are described. In the heating analysis model, heat fluxes on the vehicle surface and RBCC engines are computed when the vehicle shape, engine design, flight conditions, and surface temperature are specified. The obtained heat flux value and coolant mass rates are used in a TPS thermal analysis conducted in Chapter 3.

D.1 Heating and Cooling Model for RBCC Engines

When the performance of RBCC engines are calculated from $T_\mathrm{R}/S_\mathrm{capt}$ value and inlet inflow conditions in Eqs. (5.8–5.13), the following amounts of heat transferred per unit time are also evaluated:

$$\begin{aligned} Q_\mathrm{rckt}/T_\mathrm{R} = {} & a^{(0,0)}(Ma_\mathrm{in}) + a^{(1,0)}(Ma_\mathrm{in})\, q_\mathrm{in} + a^{(0,1)}(Ma_\mathrm{in})\, T_\mathrm{R}/S_\mathrm{capt} \\ & + a^{(2,0)}(Ma_\mathrm{in})\, {q_\mathrm{in}}^2 + a^{(0,2)}(Ma_\mathrm{in}) \left(T_\mathrm{R}/S_\mathrm{capt}\right)^2 + a^{(1,1)}(Ma_\mathrm{in})\, q_\mathrm{in}\, T_\mathrm{R}/S_\mathrm{capt}, \end{aligned} \tag{D.1}$$

$$\begin{aligned} Q_\mathrm{in}/S_\mathrm{capt} = {} & b^{(0,0)}(Ma_\mathrm{in}) + b^{(1,0)}(Ma_\mathrm{in})\, q_\mathrm{in} + b^{(0,1)}(Ma_\mathrm{in})\, T_\mathrm{R}/S_\mathrm{capt} \\ & + b^{(2,0)}(Ma_\mathrm{in})\, {q_\mathrm{in}}^2 + b^{(0,2)}(Ma_\mathrm{in}) \left(T_\mathrm{R}/S_\mathrm{capt}\right)^2 + b^{(1,1)}(Ma_\mathrm{in})\, q_\mathrm{in}\, T_\mathrm{R}/S_\mathrm{capt}, \end{aligned} \tag{D.2}$$

$$\begin{aligned} Q_\mathrm{cmb}/S_\mathrm{capt} = {} & c^{(0,0)}(Ma_\mathrm{in}) + c^{(1,0)}(Ma_\mathrm{in})\, q_\mathrm{in} + c^{(0,1)}(Ma_\mathrm{in})\, T_\mathrm{R}/S_\mathrm{capt} \\ & + c^{(2,0)}(Ma_\mathrm{in})\, {q_\mathrm{in}}^2 + c^{(0,2)}(Ma_\mathrm{in}) \left(T_\mathrm{R}/S_\mathrm{capt}\right)^2 + c^{(1,1)}(Ma_\mathrm{in})\, q_\mathrm{in}\, T_\mathrm{R}/S_\mathrm{capt}, \end{aligned} \tag{D.3}$$

where Q_rckt [kW], Q_in [kW], and Q_cmb [kW] denote heating rates of the embedded rockets, inlet, and combustor, respectively. $a^{(\cdot,\cdot)}\colon \mathbb{R} \to \mathbb{R}$, $b^{(\cdot,\cdot)}\colon \mathbb{R} \to \mathbb{R}$, and $c^{(\cdot,\cdot)}\colon \mathbb{R} \to \mathbb{R}$ are fitted based on the tabular data provided by JAXA[97]. It is noted that Q_rckt, Q_in, and Q_cmb are proportional to the rocket thrust, the squared size of the flow-passes, and the squared size of the flow-passes, respectively.

The thermal state of the RBCC engines during the flight is approximated to be steady, and it gives the required mass rate of the ethanol coolant, $\dot{m}_{\mathrm{cool,eng}}$ [kg/s], as follows:

$$\dot{m}_{\mathrm{cool,eng}} = \frac{Q_{\mathrm{rckt}} + Q_{\mathrm{in}} + Q_{\mathrm{cmb}}}{794}, \tag{D.4}$$

where 794 kJ/kg is the cooling capacity achieved by raising the temperature of the ethanol from 280 K to 500 K.

D.2 Heating and Cooling Model for Leading Edges of the Booster

The aerodynamic heat flux on the leading edge of nose, main wing, or RBCC engine cowls is given as

$$Q = Q_{\mathrm{heat}} - Q_{\mathrm{rad}}, \tag{D.5}$$

where Q_{heat} and Q_{rad} denote the heat transfer rate and the thermal radiation rate, respectively. The heat transfer rate on the leading edge is computed using the following Detra-Kemp-Riddell's formula for stagnation points[124]:

$$Q_{\mathrm{heat}} = 110 \times 10^3 \left(\frac{\rho}{\rho_{\mathrm{s}} R_{\mathrm{n}}}\right)^{0.5} \left(\frac{v}{v_{\mathrm{c}}}\right)^{3.15} \frac{h_0 - h_{300}}{h_{\mathrm{w}} - h_{300}} \ [\mathrm{kW/m^2}], \tag{D.6}$$

where ρ is the air density at flight altitude [kg/m^3], ρ_{s} is the air density at sea level (= 1.225 kg/m^3), R_{n} is the radius of curvature at the leading edge [m], v is the flight velocity [m/s], v_{c} is the reference velocity (=7925 m/s), h_0 is the enthalpy of the air at the stagnation point, h_{300} is the enthalpy of the air at 300 K, and h_{w} is the enthalpy of the air at the wall temperature. The enthalpy values are calculated by

$$h_0 = C_p T_{\mathrm{stag}} + \frac{v^2}{2} \sin^2(\pi/2 - \Lambda), \tag{D.7}$$

$$h_{300} = C_p \cdot 300.0, \tag{D.8}$$

$$h_{\mathrm{w}} = C_p T_{\mathrm{w}}, \tag{D.9}$$

where Λ denotes the sweepback angle of the leading edge against the free-stream, and C_p is the isobaric specific heat of the air, which is approximated to be 1010.4 J/(kg K) constant. T_{stag} and T_{w} indicate the temperature at the stagnation point and on the wall, respectively. The thermal radiation rate is evaluated, on the other hand, by the Stefan-Boltzmann law as follows:

$$Q_{\mathrm{rad}} = \frac{\sigma \epsilon}{1000} \left({T_{\mathrm{stag}}}^4 - {T_\infty}^4\right) \ [\mathrm{kW/m^2}], \tag{D.10}$$

where σ is the Stefan-Boltzmann constant [= 5.67×10^{-8}W/(m^{2}K^4)], and ϵ is the surface emissivity, whose value is assumed to be 0.8[59].

Cooling pipes are installed behind the leading edges, and their surfaces are actively cooled by increasing the temperature of ethanol in the pipes from 280 K to 500 K. It is assumed that the steady

Table D.1 Geometries of leading edges of the booster.

Component	Radius of curvature, R_n [m]	Sweepback angle, Λ [deg]	Total length, l_le [m]
Fuselage nose	0.1	0.0	b_wn
Main wing	$1.1019\, w_\mathrm{tc} (t/c)^2$ *	w_Λ	$2\, w_\mathrm{sp} / \cos \frac{w_\Lambda \pi}{180}$
Sidewalls of RBCC engine cowls	0.1	$73.0 - b_\mathrm{wed}$	$\frac{(N_\mathrm{rbcc}+1)\, e_\mathrm{h}}{\cos \frac{(73.0 - b_\mathrm{wed})\pi}{180}}$
Bottom wall of RBCC engine cowls	0.1	0.0	$N_\mathrm{rbcc} / 1.81\, e_\mathrm{h}$

* Based on the relation for symmetrical 4-digit NACA airfoils[125].

b_wn: Nose tip width.
w_tc: Chord length at 50 % exposed semi-span.
(t/c): Maximum thickness-to-chord-length ratio.
w_Λ: Sweepback angle at the leading edge.
w_sp: Exposed semi-span length.
b_wed: Inclination angle of forebody undersurface.
N_rbcc: Number of engine units.
e_h: Engine height at inlet.

thermal state of the surface with 600 K (the summation of 500 K and the temperature increment inside insulation material located outside the cooling pipes) is achieved as a consequence of the active cooling. Therefore, the stagnation point temperature, T_stag, and the wall temperature, T_w, are 600 K. The area of a leading edge that receives the heat flux of Q is defined as

$$A = \pi R_\mathrm{n}\, l_\mathrm{le}, \tag{D.11}$$

where l_le is the total length of the corresponding leading edge. The values of R_n, Λ, and l_le for each leading edge are presented in Table D.1.

Finally, the total required mass rate of the ethanol coolant, $\dot{m}_\mathrm{cool,le}$, is obtained by equating the incoming and outgoing amounts of heat:

$$\dot{m}_\mathrm{cool,le} = \frac{Q_\mathrm{n} A_\mathrm{n} + Q_\mathrm{w} A_\mathrm{w} + Q_\mathrm{cs} A_\mathrm{cs} + Q_\mathrm{cb} A_\mathrm{cb}}{794} \text{ [kg/s]}, \tag{D.12}$$

where the subscript $(\cdot)_\mathrm{n}$, $(\cdot)_\mathrm{w}$, $(\cdot)_\mathrm{cs}$, and $(\cdot)_\mathrm{cb}$ denote the quantities of the fuselage nose, main wing, sidewalls of engine cowls, bottom wall of engine cowls, respectively. The cooling capacity of the ethanol coolant is assumed to be 794 kJ/kg as in the case of regenerative cooling of RBCC engines.

D.3 Heating Model for the Booster Undersurface

The stationary thermal analysis introduced in Appendices D.1 and D.2 is not suitable to the undersurface of the booster, since passive thermal protection is installed there. Instead, an unsteady or transient thermal analysis is performed on the vehicle undersurface. Numerical methods for conducting the thermal analysis inside ceramic insulation tiles and for coupling it with the trajectory design are developed in Chapter 3. The surface heat flux required in the analysis is computed using 1) the shock or expansion-wave relations and 2) the reference temperature method[126,127]. Throughout this model, the air is considered as a mixture of ideal gases.

For the simplicity of the calculation, let the shape of the booster vehicle be approximated as a flat plate. Then, the relation for an oblique shock wave or that for expansion waves are applied to the booster undersurface when angle of attack is positive and when it is negative, respectively. The polynomial models that approximate both these shock and expansion-wave relations, shown in Eqs. (C.30–C.34), are employed. As a result, the following flow conditions at the outer edge of the boundary layer aroound the vehicle undersurface are obtained: Mach number, Ma_e, temperature, T_e, density, ρ_e, and static pressure, p_e. Flow speed, u_e, is given as

$$u_\mathrm{e} = Ma_\mathrm{e}\sqrt{\gamma R T_\mathrm{e}}, \tag{D.13}$$

where γ is the heat capacity ratio of the air (= 1.4), and R is the specific gas constant of the air [= 288.7 J/(kg K)]. T_aw denotes the recovery temperature that is written as

$$T_\mathrm{aw} = T_\mathrm{e}\left[1 + \frac{0.71^{\frac{1}{3}}}{2}(\gamma - 1){Ma_\mathrm{e}}^2\right]. \tag{D.14}$$

Let the reference temperature, T^*, be defined as

$$T^* = \frac{T_\mathrm{e} + T_\mathrm{w}}{2} + 0.22\frac{{u_\mathrm{e}}^2}{2C_p}, \tag{D.15}$$

where, T_w is the wall temperature, which depends on the thermal state experienced so far. C_p denotes the isobaric specific heat of the air [= 1010.4 J/(kg K)]. In the reference temperature method, the following relation holds for the compressive turbulent flow over a flat plate[126,127]:

$$C_H{}^* = \frac{0.037}{(Re_L{}^*)^{0.2}}(Pr^*)^{-2/3}. \tag{D.16}$$

Here, the averaged heat-transfer coefficient, $C_H{}^*$, Reynolds number, $Re_L{}^*$, and Prandtl number, Pr^*, are evaluated at the reference temperature, T^*. This means that

$$C_H{}^* = \frac{Q_\mathrm{conv}}{\rho^* u_\mathrm{e} C_p (T_\mathrm{aw} - T_\mathrm{w})}, \tag{D.17}$$

$$Re_L{}^* = \frac{\rho^* u_\mathrm{e} L}{\mu^*}, \tag{D.18}$$

$$Pr^* = \frac{\mu^* C_p}{\lambda^*}, \tag{D.19}$$

where ρ^*, μ^*, and λ^* are the values at a temperature of T^*. The characteristic length for calculating the Reynolds number, denoted by L, is the length of the booster fuselage, namely, b_l. The viscosity of air at the reference temperature, μ^*, is computed based on the Sutherland's formula as follows:

$$\mu^* = 1.458 \times 10^{-6}\frac{(T^*)^{3/2}}{T^* + 110.4}\ [\mathrm{kg/(m\ s)}]. \tag{D.20}$$

λ^* refers to the thermal conductivity of the air at the reference temperature, and it is given as

$$\lambda^* = 2.648 \times 10^{-3} \frac{(T^*)^{3/2}}{T^* + 245.4 \times 10^{(-12/T^*)}} \ [\mathrm{kW/(m\ K)}]. \tag{D.21}$$

Q_{conv} in Eq. (D.17) denotes the convective heat flux on the vehicle undersurface, and it is used in the TPS analysis. Thermal radiation from the surface, Q_{rad}, is estimated as follows:

$$Q_{\mathrm{rad}} = \sigma\epsilon\left({T_{\mathrm{w}}}^4 - {T_{\mathrm{e}}}^4\right), \tag{D.22}$$

where the surface emissivity, ϵ, is 0.8[59].

In reality, the value of heat-transfer coefficient varies locally depending on the local Reynolds number in the following manner:

$$C_H{}^*(x) = \frac{0.0296}{[Re^*(x)]^{0.2}}(Pr^*)^{-2/3}, \tag{D.23}$$

$$Re^*(x) = \frac{\rho^* u_{\mathrm{e}} x}{\mu^*}, \tag{D.24}$$

where x is the distance downstream from the leading edge of the plate. The value of Q_{conv} derived from Eq. (D.17) is the average of a locally varying heat flux value.

Appendix E

Mass-Property Estimation Model

In this appendix chapter, a numerical model for predicting the mass of reusable launch vehicles and its central position is described.

E.1 Statistical Vehicle Mass Model

Among several mass models applicable to reusable launch vehicles[54,128,129], HASA (Hypersonic Aerospace Sizing Analysis) developed by Harloff and Berkowitz[129] is employed with some modifications in the present study. HASA is based on historical data of U. S. Space Shuttle and hypersonic vehicles, where cold main structures with metal materials (mainly, aluminum alloys) are assumed. Modifying factor, mf, that is used to take into account technological progress is 1.0 in this dissertation. Using HASA, each component mass of a vehicle (i.e., booster or orbiter) is computed from the parameters gathered in Table E.1. These variables are present in or calculated from design variables of MDO problems.

- Fuselage of the booster or the orbiter: m_b [kg]

$$m_\mathrm{b} = 1.455 \left(\frac{b_\mathrm{l}\, lf_\mathrm{utl}}{D_\mathrm{be}} \right)^{0.15} \left(\frac{q_\mathrm{max}}{9.807} \right)^{0.16} {b_\mathrm{wa}}^{1.05}, \tag{E.1}$$

where D_be is the body equivalent diameter, which is given as

$$D_\mathrm{be} = \sqrt{\frac{4\, b_\mathrm{vol}}{b_\mathrm{l}\, \pi\, \eta_\mathrm{vol}}} \tag{E.2}$$

assuming that the vehicle volumetric efficiency, η_vol, is 0.7. In the case of the booster, the mass of integral tanks is included in m_b. Therefore, the ultimate load factor, lf_utl, which is defined as $1.5\, aa_\mathrm{max}$ in the original HASA, is replaced with $1.5\sqrt{lf_\mathrm{max}^2 + aa_\mathrm{max}^2}$, based on the discussion in p. 163 of Ref. 14.

Table E.1 Input variables to the vehicle mass estimation using HASA[129].

Symbol	Description
m_{to}	Vehicle takeoff mass = Gross mass of the mated vehicle (booster and orbiter) [kg]
m_{gross}	Gross mass of the separated vehicle (booster or orbiter) [kg]
m_{dry}	Dry mass of the separated vehicle (booster or orbiter) [kg]
b_{l}	Length of the fuselage [m]
b_{wa}	Wetted area of the fuselage [m^2]
b_{vol}	Volume of the fuselage [m^3]
w_{λ}	Taper ratio of the main wing
w_{tr}	Maximum thickness-to-chord-length ratio
w_{Λ}	Sweepback angle of the main wing at the mid chord [rad]
$w_{\text{Æ}}$	Aspect ratio of the main wing
w_{spn}	Span width of the main wing [m]
S_{ref}	Reference area of the main wing [m^2]
S_{tail}	Platform area of the tail wing [m^2]
$S_{\text{tps,b}}$	Area covered by the ceramic tile TPS (HTP-12[98]) of the booster [m^2]
$h_{\text{tps,b}}$	Thickness of the ceramic tile TPS (HTP-12[98]) of the booster [m]
$S_{\text{tps1,o}}$	Area covered by the C/C composite TPS of the orbiter (leading edges) [m^2]
$S_{\text{tps2,o}}$	Area covered by the ceramic tile TPS of the orbiter (the other surface) [m^2]
V_{cabin}	Cabin volume of the orbiter [m^3]
q_{max}	Maximum dynamic pressure [Pa]
lf_{max}	Maximum load factor [G]
aa_{max}	Maximum axial acceleration [G]
$T_{\text{a,max}}$	Maximum exerted airbreathing thrust [N]
$T_{\text{r,max}}$	Maximum exerted rocket thrust [N]
N_{eng}	Number of airbreathing engine units
S_{capt}	Frontal projected area of the inlet per engine unit [m^2]
T_{embr}	Thrust of RBCC embedded rocket engines per RBCC engine unit [N]
$T_{\text{rcea,v}}$	Vacuum thrust of an ethanol/LOX rocket engine [N]
$T_{\text{rclh,v}}$	Vacuum thrust of an LH2/LOX rocket engine [N]
N_{rclh}	Number of LH2/LOX rocket engines installed on the booster

- Main wing of the booster: m_{w} [kg]

$$m_{\text{w}} = 1.106\left[\left(m_{\text{dry}}\, lf_{\text{utl}}/1000\right)^{0.52} {S_{\text{ref}}}^{0.7} {w_{\text{Æ}}}^{0.47}\left(\frac{1+w_{\lambda}}{w_{\text{tr}}}\right)^{0.4}\left(0.3+\frac{0.7}{\cos w_{\Lambda}}\right)\right]^{1.017}. \tag{E.3}$$

- Tail wings of the booster (two total): m_{t} [kg]

$$m_{\text{t}} = 2 \times 30.23\, {S_{\text{tail}}}^{1.09}. \tag{E.4}$$

- Propellant tank of the booster and the orbiter: m_{tnk} [kg]

  Cylindrical tanks are employed to load LOX in the booster fuselage of the TSTO RLV with RBCC engines. Cylindrical tanks are also applied to the ethanol tank and the LOX tank in the orbiter. The total mass of tanks is calculated based on the analytical stress analysis for a thin cylinder with hemispherical shells as follows:

$$m_{\mathrm{tnk}} = \sum_{\text{all tanks}} 2.0 \times \rho\, \pi\, d_{\mathrm{tnk}} \left(t_{\mathrm{cyl}}\, l_{\mathrm{tnk}} + t_{\mathrm{hem}}\, d_{\mathrm{tnk}} \right), \tag{E.5}$$

  where t_{cyl} and t_{hem} denote the required thickness [m] of the cylinder and the hemisphere, respectively, which are calculated by

$$t_{\mathrm{cyl}} = sf \, \frac{p\, d_{\mathrm{tnk}}}{2\, \sigma_{\mathrm{uts}}}, \tag{E.6}$$

$$t_{\mathrm{hem}} = sf \, \frac{p\, d_{\mathrm{tnk}}}{4\, \sigma_{\mathrm{uts}}}. \tag{E.7}$$

  Length of the tank, l_{tnk}, is computed from the locations of tank ends. Diameter of the tank, d_{tnk}, and the number of tanks placed side by side are calculated so that the tanks are accommodated inside the fuselage with the margin of 2.5% fuselage width. As for the constants, p (= 245.2 kPa) is the internal pressure of the tank, sf (= 2.0) is the safety factor. In addition, ρ (= 2.83×10^3 kg/m^3) and σ_{uts} (= 588.4 MPa) denote the density and the ultimate tensile strength of the tank material (an aluminum alloy), respectively. Cabin mass of the orbiter is estimated in the similar manner as well.

- Landing gear of the booster and the orbiter: m_{gear} [kg]

$$m_{\mathrm{gear}} = \begin{cases} 0.0101\, {m_{\mathrm{to}}}^{1.124} & \text{for the booster.} \\ 0.0101\, {m_{\mathrm{dry}}}^{1.124} & \text{for the orbiter.} \end{cases} \tag{E.8}$$

  It is noted that the gear mass of the orbiter is calculated based on the dry mass of the orbiter alone, while that of the booster depends on the takeoff mass of the mated vehicle.

- Airbreathing thrust structure of the booster: m_{thrua} [kg]

$$m_{\mathrm{thrua}} = 0.00625\, \frac{T_{\mathrm{a,max}}}{9.807} + 31.3. \tag{E.9}$$

- Rocket engine thrust structure of the orbiter: m_{thrur} [kg]

$$m_{\mathrm{thrur}} = 0.0025\, \frac{T_{\mathrm{r,max}}}{9.807}. \tag{E.10}$$

- Thermal protection system (TPS) of the booster and the orbiter: m_{tps} [kg]

$$m_{\text{tps}} = \begin{cases} \rho_{\text{tps,b}}\, h_{\text{tps,b}}\, S_{\text{tps,b}} & \text{for the booster,} \\ \rho_{A,\text{tps1,o}}\, S_{\text{tps1,o}} + \rho_{A,\text{tps2,o}}\, S_{\text{tps2,o}} & \text{for the orbiter,} \end{cases} \tag{E.11}$$

where $\rho_{\text{tps,b}}$ is the density of the HTP-12 ceramic tile, 192.2 kg/m^3[98]. In the PCTJ-powered TSTO, it is assumed that $h_{\text{tps,b}} = 20.8$ mm. $\rho_{A,\text{tps1,o}}(= 40.0\ \text{kg/m}^2)$ and $\rho_{A,\text{tps2,o}}(= 4.0\ \text{kg/m}^2)$ denote the areal density of the orbiter TPS for leading edges and that for the other surface, respectively.

- Hydraulics system of the booster and the orbiter: m_{hyd} [kg]

$$m_{\text{hyd}} = 2.825 \left(\frac{S_{\text{ref}} + S_{\text{tail}}}{1000} \frac{q_{\max}}{9.807} \right)^{0.334} \left(b_l + w_{\text{spn}} \right)^{0.5} \tag{E.12}$$

- Electronics of the booster and the orbiter: m_{elect} [kg]

$$m_{\text{elect}} = 1.058\, {m_{\text{gross}}}^{0.5}\, {b_l}^{0.25}. \tag{E.13}$$

- Avionics of the booster and the orbiter: m_{tavcs} [kg]

$$m_{\text{tavcs}} = 40.04\, {m_{\text{gross}}}^{0.361}. \tag{E.14}$$

- Onboard equipment of the booster and the orbiter: m_{equip} [kg]

$$m_{\text{equip}} = 0.01\, m_{\text{gross}}. \tag{E.15}$$

- Payload of the orbiter: m_{pay} [kg]

$$m_{\text{pay}} = \frac{100}{4.3} V_{\text{cabin}}. \tag{E.16}$$

- RBCC engine of the booster: m_{rbcc} [kg]

$$m_{\text{rbcc}} = N_{\text{eng}} \left(\underbrace{\frac{1}{50} \frac{T_{\text{embr}}}{9.8}}_{\text{Embedded rockets}} + \underbrace{351.7\, S_{\text{capt}} + 109.4\, {S_{\text{capt}}}^{\frac{3}{2}}}_{\text{Dual-mode ramjet/scramjet flow-pass}} \right). \tag{E.17}$$

The mass of an RBCC engine unit is calculated by adding the embedded rocket mass (thrust-to-mass ratio is 50 including fuel feeding system) and dual-mode flow-pass structure mass. The flow-pass mass is computed with a polynomial model fitted by finite-element structural analyses[97].

- PCTJ engine of the booster: m_{pctj} [kg]

$$m_{\mathrm{pctj}} = N_{\mathrm{eng}} \left(\underbrace{1044\, S_{\mathrm{capt}}{}^{0.5834}}_{\text{Inlet duct}} + \underbrace{171.8\, S_{\mathrm{capt}}{}^{0.294}}_{\text{Variable-geometry inlet ramp}} + \underbrace{136.3\, S_{\mathrm{capt}}{}^{0.985}}_{\text{Variable-geometry nozzle}} \right.$$
$$\left. + \underbrace{765.6\, S_{\mathrm{capt}}}_{\text{Pre-cooler}} + \underbrace{928.6\, S_{\mathrm{capt}}}_{\text{Core engine}} \right). \tag{E.18}$$

The mass of inlet duct, variable-geometry inlet ramp, and variable-geometry nozzle are estimated on the basis of WATTS[128], another vehicle mass model than HASA, assuming the following design parameters: number of inlet flow-passes per an engine unit is 2, maximum total pressure at the inlet is 937.0 kPa, shape parameter of inlet flow-pass is 1.33, design Mach number is 5.0, nominal thrust per unit flow-capture area is 87.7 kN/m^2, and maximum nozzle inflow pressure is 772.2 kPa. The mass of pre-cooling system is calculated from the geometry of cooling pipes. The mass of a core engine is estimated using a statistical relation based on data of existing turbojet engines.

- Rocket engines of the booster or that of the orbiter: m_{rckt} [kg]

$$m_{\mathrm{rckt}} = \begin{cases} \dfrac{1}{61.2} \dfrac{T_{\mathrm{rclh,v}} N_{\mathrm{rclh}}}{9.8} & \text{for LH2/LOX rockets of the PCTJ-booster.} \\ \dfrac{1}{75} \dfrac{T_{\mathrm{rcea,v}}}{9.8} & \text{for an ethanol/LOX rocket of the orbiter.} \end{cases} \tag{E.19}$$

The thrust-to-mass ratio of the ethanol/LOX rocket engine is 75 based on Ref. 3. That of the LH2/LOX rocket engine is assumed to be 75 in reference to the value of LE-7A, a Japanese LH2/LOX rocket engine.

- Propellant of the booster and the orbiter: m_{ea} [kg] (ethanol), m_{lo} [kg] (LOX), and m_{lh} [kg] (LH2)
  Propellant mass during the flight are computed by multiplying remaining volumes in tanks and their density (789 kg/m^3 for ethanol, 1140 kg/m^3 for LOX, and 70.85 kg/m^3 for LH2). The propellant volume before the takeoff run is limited up to the total volume of the corresponding tanks. The volume of an integral tank is calculated by integrating the fuselage cross section between the forward end and the rear end, and multiplying it by a volume efficiency constant of 80 %.

E.2 Estimation of the Center of Mass

Centers of mass for vehicle components are located as shown in Table E.2, from which the position of the center of overall vehicle mass is derived. Table E.2 is largely based on p. 168 of Ref. 14. The orbiter is loaded onto the uppersurface of the booster at such a position that the center of mass does not move in the axial direction just before and just after the separation of the orbiter. This is equivalent to that the center of mass of the booster at the moment of staging is identical to that of the orbiter whose propellant

Table E.2 Position of center of mass for each vehicle component.

Component	Position of corresponding center of mass	
	X coordinate (axial)	Z coordinate (height)
Fuselage	Center of fuselage surface panels	
Main wing	Center of main wing surface panels	
Tail wings	Center of tail wings surface panels	
Propellant tank	Center of tank volume	Center of cross sec. at 50 % tank length
Cabin	Center of cabin volume	Center of cross sec. at 50 % cabin length
Landing gear	Center of vehicle dry mass	0.5 m above fuselage undersurface
Airbreathing thrust structure	50 % engine length	50 % engine height
Rocket engine thrust structure	Backward end of fuselage	Center of fuselage base
Thermal protection system	Center of thermal protection system panels	
Hydraulics system	Center of main wing and tail wings mass	
Electronic	10 % fuselage length	Center of mass of fuselage
Avionics	10 % fuselage length	Center of mass of fuselage
Onboard equipment	50 % fuselage length	Center of mass of fuselage
Payload	Center of cabin volume	Center of cross sec. at 50 % cabin length
RBCC engine	50 % engine length	50 % engine height
PCTJ engine	50 % engine length	50 % engine height
Rocket engine	Backward end of fuselage	Center of fuselage base
Propellant	Center of corresponding tank volume	

tanks are full.

Appendix F

Data Mining Techniques

A Pareto optimal solution of a complex multi-objective optimization problem contains high-dimensional information. As a result, the set of Pareto optimal solutions can be regarded as a large-scale and high-dimensional dataset, which is difficult to interpret directly. It is troublesome or infeasible to discover generic findings via inspecting each solution one by one. Therefore, the applications of data mining techniques and multivariate analysis to Pareto optimal solutions have been studied recently in order to extract comprehensive and useful knowledge.

The most widely used technique would be a scatter plot matrix[35–37]. Other than that, Jilla et al.[34] conducted analysis of variance (ANOVA) of the obtained Pareto optimal satellite designs. Jeong et al.[29] applied surrogate-assisted ANOVA and self-organizing maps to some aerodynamic design problems. Oyama et al.[31] proposed the application of proper orthogonal decomposition (POD) to Pareto optimal airfoil shapes. The overview of related previous researches can be found in Ref. 30.

F.1 Scatter Plot Matrix

In the present study, scatter plot matrices are employed for visualizing the relations between pairs of static variables (i.e., vehicle design parameters). Figure F.1 presents an example of a scatter plot matrix where three variables are involved. In the scatter plot matrix, diagonal elements indicate names of the parameters investigated, upper triangular elements illustrate scatter plots of corresponding pairs of parameters, and lower triangular elements show the Pearson product-moment correlation coefficients between them. The correlation coefficient is shown with a font size depending on its absolute value in order to improve visibility. The Pearson correlation coefficient, P, between pairs of parameters $\{s_i,\ t_i\}_{i=1}^{N_{\mathrm{sol}}}$[*] is

---

[*] It should be noted that the number of pairs is defined as the number of Pareto optimal solutions examined.

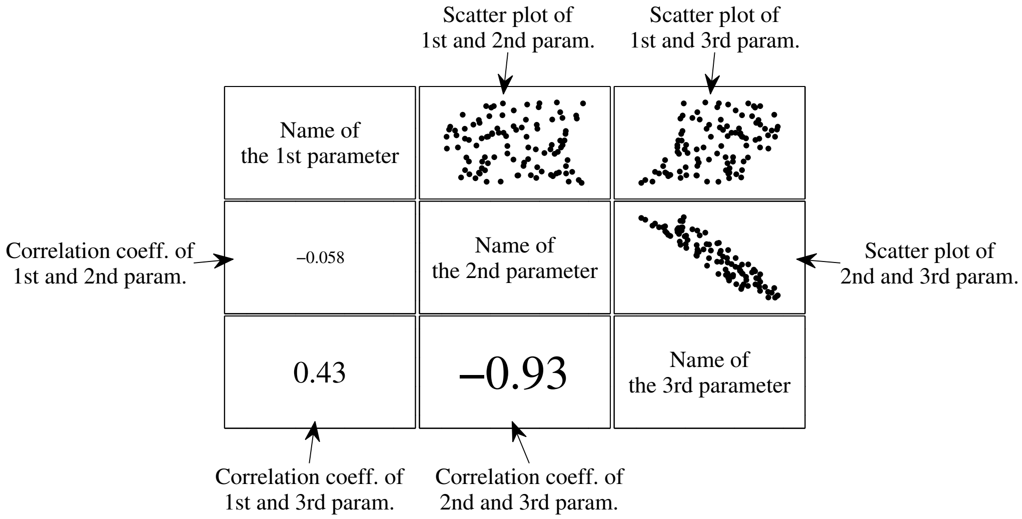

Fig. F.1 An example of a scatter plot matrix.

defined as

$$P := \frac{\sum_{i=1}^{N_{\mathrm{sol}}} (s_i - \bar{s})(t_i - \bar{t})}{\sqrt{\sum_{i=1}^{N_{\mathrm{sol}}} (s_i - \bar{s})^2} \sqrt{\sum_{i=1}^{N_{\mathrm{sol}}} (t_i - \bar{t})^2}}, \tag{F.1}$$

where $\bar{s}$ is the mean of $\{s_i\}_{i=1}^{N_{\mathrm{sol}}}$, $\bar{t}$ is the mean of $\{t_i\}_{i=1}^{N_{\mathrm{sol}}}$, and N_{sol} denotes the number of Pareto optimal solutions. The Pearson product-moment correlation coefficient is a measure of linear correlation that gives a value in $[-1,\ 1]$, where a larger positive value indicates stronger positive correlation, and a larger negative value suggests stronger negative correlation. Since the Pearson correlation coefficient cannot detect nonlinear associations, it is important to inspect the relevant scatter plot together. It is also noted that a significant correlation coefficient does not always means that there is the relation of cause and effect between the involved pair of parameters.

F.2 Proper Orthogonal Decomposition

In this dissertation, the snapshot POD is used for extracting knowledge from flight trajectories of Pareto optimal solutions. POD is also known as principal component analysis in statistics, and Karhunen-Loève expansion in signal processing. Suppose that we want to analyze a set of discrete “snapshot” vectors

$$\{x_i(\tau_k)\}_{k=1}^{N_{\mathrm{snap}}}, \quad i = 1, \ldots, N_{\mathrm{sol}}, \tag{F.2}$$

where $x_i(\tau_k)$ is the snapshot value of a dependent variable x of the ith Pareto optimal solution that is taken when an independent variable τ equals to τ_k. In the present study, the independent variable may be time, flight Mach number, or others. N_{sol} and N_{snap} are the number of Pareto optimal solutions and the number of discrete snapshots with respect to τ, respectively.

First, let us define the following snapshot matrix:

$$\mathbf{S} = \begin{bmatrix} x_1(\tau_1) & x_2(\tau_1) & \cdots & x_{N_{\mathrm{sol}}-1}(\tau_1) & x_{N_{\mathrm{sol}}}(\tau_1) \\ x_1(\tau_2) & x_2(\tau_2) & \cdots & x_{N_{\mathrm{sol}}-1}(\tau_2) & x_{N_{\mathrm{sol}}}(\tau_2) \\ \vdots & \vdots & \ddots & \vdots & \vdots \\ x_1(\tau_{N_{\mathrm{snap}}-1}) & x_2(\tau_{N_{\mathrm{snap}}-1}) & \cdots & x_{N_{\mathrm{sol}}-1}(\tau_{N_{\mathrm{snap}}-1}) & x_{N_{\mathrm{sol}}}(\tau_{N_{\mathrm{snap}}-1}) \\ x_1(\tau_{N_{\mathrm{snap}}}) & x_2(\tau_{N_{\mathrm{snap}}}) & \cdots & x_{N_{\mathrm{sol}}-1}(\tau_{N_{\mathrm{snap}}}) & x_{N_{\mathrm{sol}}}(\tau_{N_{\mathrm{snap}}}) \end{bmatrix}. \tag{F.3}$$

Since we are interested in the differences among solutions, the deviations from the nominal data,

$$\{x_0(\tau_k)\}_{k=1}^{N_{\mathrm{snap}}}, \tag{F.4}$$

are computed as follows:

$$\tilde{\mathbf{S}} = \mathbf{S} - \begin{bmatrix} x_0(\tau_1) & x_0(\tau_1) & \cdots & x_0(\tau_1) & x_0(\tau_1) \\ x_0(\tau_2) & x_0(\tau_2) & \cdots & x_0(\tau_2) & x_0(\tau_2) \\ \vdots & \vdots & \ddots & \vdots & \vdots \\ x_0(\tau_{N_{\mathrm{snap}}-1}) & x_0(\tau_{N_{\mathrm{snap}}-1}) & \cdots & x_0(\tau_{N_{\mathrm{snap}}-1}) & x_0(\tau_{N_{\mathrm{snap}}-1}) \\ x_0(\tau_{N_{\mathrm{snap}}}) & x_0(\tau_{N_{\mathrm{snap}}}) & \cdots & x_0(\tau_{N_{\mathrm{snap}}}) & x_0(\tau_{N_{\mathrm{snap}}}) \end{bmatrix}. \tag{F.5}$$

The nominal data is specified by the user. When POD is used for the model reduction in fluid mechanics, a mean flow field is usually employed as the nominal data[130]. However, when POD is applied to Pareto optimal solutions of a multi-objective optimization problem, the mean value of x in the solutions does not have a physical meaning[31]. Therefore, the value of x in a representative solution is used as the nominal data in the present study.

The snapshot POD is obtained by solving the following eigenvalue problem:

$$\mathbf{R}\psi_i = \lambda_i \psi_i, \quad i = 1, \ldots, N_{\mathrm{sol}}, \tag{F.6}$$

where $\mathbf{R} = \tilde{\mathbf{S}}^{\mathrm{T}}\tilde{\mathbf{S}}$, λ_i ($\in \mathbb{R}$) is the ith eigenvalue, and ψ_i ($:= [\psi_{i,1} \cdots \psi_{i,N_{\mathrm{sol}}}]^{\mathrm{T}} \in \mathrm{R}^{N_{\mathrm{sol}}}$) denotes the corresponding eigenvector. Here, it is assumed that eigenvalues are sorted in descending order, that is,

$$\lambda_1 \geq \lambda_2 \geq \cdots \geq \lambda_{N_{\mathrm{sol}}-1} \geq \lambda_{N_{\mathrm{sol}}}. \tag{F.7}$$

As a consequence, x of each solution is decomposed into that of the representative solution and the deviation from it as follows:

$$x_i(\tau_k) = x_0(\tau_k) + \sum_{j=1}^{N_{\mathrm{sol}}} a_i^{(j)} \cdot \tilde{x}^{(j)}(\tau_k), \quad i = 1, \ldots, N_{\mathrm{sol}}. \tag{F.8}$$

where the deviation is expressed by the linear combination of orthogonal base vectors, $\{\tilde{x}_i(\tau_k)\}_{k=1}^{N_{\mathrm{sol}}}$, $i = 1, \ldots, N_{\mathrm{sol}}$. $a_i^{(j)}$ is given as

$$a_i^{(j)} = \psi_{j,i}, \tag{F.9}$$

and $\{\tilde{x}^{(j)}(\tau_k)\}_{k=1}^{N_{\mathrm{sol}}}$ is computed by

$$\begin{bmatrix} \tilde{x}^{(j)}(\tau_1) \\ \tilde{x}^{(j)}(\tau_2) \\ \vdots \\ \tilde{x}^{(j)}(\tau_{N_{\mathrm{sol}}-1}) \\ \tilde{x}^{(j)}(\tau_{N_{\mathrm{sol}}}) \end{bmatrix} = \tilde{\mathbf{S}}\,(\psi_j{}^{\mathrm{T}})^{-1}, \quad \text{for } j = 1, \ldots, N_{\mathrm{sol}}. \tag{F.10}$$

Or, Eq. (F.10) can be collectively written as follows:

$$\begin{bmatrix} \tilde{x}^{(1)}(\tau_1) & \tilde{x}^{(2)}(\tau_1) & \cdots & \tilde{x}^{(N_{\mathrm{sol}}-1)}(\tau_1) & \tilde{x}^{(N_{\mathrm{sol}})}(\tau_1) \\ \tilde{x}^{(1)}(\tau_2) & \tilde{x}^{(2)}(\tau_2) & \cdots & \tilde{x}^{(N_{\mathrm{sol}}-1)}(\tau_2) & \tilde{x}^{(N_{\mathrm{sol}})}(\tau_2) \\ \vdots & \vdots & \ddots & \vdots & \vdots \\ \tilde{x}^{(1)}(\tau_{N_{\mathrm{sol}}-1}) & \tilde{x}^{(2)}(\tau_{N_{\mathrm{sol}}-1}) & \cdots & \tilde{x}^{(N_{\mathrm{sol}}-1)}(\tau_{N_{\mathrm{sol}}-1}) & \tilde{x}^{(N_{\mathrm{sol}})}(\tau_{N_{\mathrm{sol}}-1}) \\ \tilde{x}^{(1)}(\tau_{N_{\mathrm{sol}}}) & \tilde{x}^{(2)}(\tau_{N_{\mathrm{sol}}}) & \cdots & \tilde{x}^{(N_{\mathrm{sol}}-1)}(\tau_{N_{\mathrm{sol}}}) & \tilde{x}^{(N_{\mathrm{sol}})}(\tau_{N_{\mathrm{sol}}}) \end{bmatrix} = \tilde{\mathbf{S}} \begin{bmatrix} \psi_1{}^{\mathrm{T}} \\ \psi_2{}^{\mathrm{T}} \\ \vdots \\ \psi_{N_{\mathrm{sol}}-1}{}^{\mathrm{T}} \\ \psi_{N_{\mathrm{sol}}}{}^{\mathrm{T}} \end{bmatrix}^{-1}. \tag{F.11}$$

Due to the optimality of POD, a couple of principal modes typically dominate almost all the energy content. Here, the energy content of the jth mode, E_j, is defined as

$$E_j := \sum_{k=1}^{N_{\mathrm{snap}}} \left[\tilde{x}^{(j)}(\tau_k)\right]^2, \quad j = 1, \ldots, N_{\mathrm{sol}}. \tag{F.12}$$

As the energy contribution of a mode relates to the magnitude of its base vector, the variety of Pareto optimal trajectories can be found through inspecting dominant modes only. It is noted that the eigenvectors are normalized, that is,

$$\left\| [a_1^{(j)} \cdots a_{N_{\mathrm{sol}}}^{(j)}]^{\mathrm{T}} \right\|_2 = 1, \quad j = 1, \ldots, N_{\mathrm{sol}}. \tag{F.13}$$

Acknowledgement

While conducting the present research, I have received technical and mental supports from exceedingly many people. I think that one of the most precious assets obtained during my Ph.D. course is such personal connections. Although I want to mention all of them, it is impossible due to limitations of space. Therefore, I would like to express my appreciations to especially notable ones below.

Prof. Takeshi Tsuchiya, who has been my thesis supervisor since I was a student in a bachelor course, has helped me in every aspect raging from the guidance of general research direction to the instruction of detailed technical knowledge. I decided to study aeronautics and astronautics in the University of Tokyo, because I have been interested in reusable launch vehicles from my childhood. I am so fortunate that I could conduct my research on this exact topic under the supervision of Prof. Tsuchiya, a distinguished pioneer of this research field.

I want to appreciate the review of this dissertation by the following thesis committee members (see p. ii for their affiliations). Prof. Shinji Suzuki gave me profound comments on the practical usefulness of my research. Prof. Kojiro Suzuki offered me precious suggestions on this dissertation from both broad and detailed perspectives. From Assoc. Prof. Taro Imamura, I received comments that are beyond my imagination and make significant senses. Assoc. Prof. Nobuhiro Yokohama supplied me insightful and specific opinions on optimization techniques developed in this dissertation. Beside, I have to acknowledge that my research is highly influenced by his great previous work.

I have engaged in the present research while belonging to a collaborative research group consisting of members from Japan Aerospace Exploration Agency (JAXA) and some universities. Prof. Sadatake Tomioka at JAXA powerfully headed the research group, and supplied the performance data of the RBCC engine. Prof. Kojiro Suzuki and Assoc. Prof. Taro Imamura are members of this research group as well, and they gave me valuable comments on my study before I started to write this dissertation. Prof. Tetsuya Sato at Waseda University not only provided me the knowledge on the air-inlet of hypersonic airbreathing engines, but also gave encouraging comments on my research frequently. From Prof. Akiko Matsuo and her student, Mr. Ryo Mikoshiba, at Keio University, the results of CFD simulations were provided for the validation of the external-nozzle model built in this dissertation. Dr. Hideyuki Taguchi at JAXA has supplied extraordinary helps that are not limited to the present research. I do to hesitate to say that he is, so to speak, my secondary supervisor next to Prof. Tsuchiya. Concerning this dissertation, I have received a wide range of tuition on reusable launch vehicles, and the performance data of the PCTJ engine, from him.

The Suzuki-Tsuchiya laboratory at the University of Tokyo, where I have conducted my study, was

very comfortable to stay, and it made my research life better. I want to thank all the members of the laboratory. In addition, I have obtained a lot of technical advice from them. Especially, Dr. Yoshinori Matsuno and Dr. Palar Pramudita Satria are senior to me, and they gave me helpful information on optimization, surrogate modeling, data mining, and so forth. Dr. Chris Raabe, an assistant professor of the laboratory, kindly corrected my manuscripts in English several times.

Last but not least, my work could not be completed without unconditional supports from my family, particularly my parents. I also deeply thank them for their generous and tolerant understandings of my decision to study in the graduate school.

Takahiro Fujikawa

References

[1] Andrews, J., "RLV Design Issues for Future Commercial Space Applications," AIAA Paper 2000-5104, 2000.

[2] Boeing, General Dynamics, Lockheed, Martin Marietta, McDonnell Douglas, Rockwell, "Commercial Space Transport Study Final Report," 1994, http://www.hq.nasa.gov/office/hqlibrary/documents/CSTS_1994.pdf.

[3] Fujii, K., Ishimoto, S., Mugitani, T. and Minami, Y., "Present Status and Prospects of JAXA's Research on Future Space Transportation System," AIAA Paper 2012-5849, 2012.

[4] Strategic Headquarters for Space Policy, *Basic Plan on Space Policy*, Government of Japan, January, 2013, http://www8.cao.go.jp/space/plan/plan-eng.pdf.

[5] Strategic Headquarters for Space Policy, *Basic Plan on Space Policy*, Government of Japan, January, 2015, http://www8.cao.go.jp/space/plan/plan2/plan2.pdf (in Japanese).

[6] Ishimoto, S., Okita, K., "Design Study and Technology Development for Future Reusable Space Vehicles," *Proceedings of the 30th International Symposium on Space Technology and Science*, July 2015.

[7] Tani, K., Tomioka, S., Kato, K., Ueda, S., and Takegoshi, M., "Recent Activities in Research of the Combined Cycle Engine at JAXA," *Transactions of The Japan Society for Aeronautical and Space Sciences, Aerospace Technology Japan*, Vol. 8, No. ists27, 2010, pp. Ta_1–Ta_6.

[8] Ueda, S., Tomioka, S., Saito, T., Tani, K., and Yoshida, M., "R&D on Hydrocarbon-Fueled RBCC Engines for a TSTO Launch Vehicle," AIAA Paper 2015-3611, 2015.

[9] Taguchi, H., Futamura, H., Yanagi, R., and Maita, M., "Analytical Study of Pre-Cooled Turbojet Engine for TSTO Spaceplane," *Proceedings of the 10th AIAA/NAL-NASDA-ISAS International Space Planes and Hypersonic Systems and Technologies Conference*, Kyoto, Japan, Apr. 24–27, 2001.

[10] Taguchi, H., Kobayashi, H., Kojima, T., Ueno, A., Imamura, S., Hongoh, M., and Harada, K., "Research on Hypersonic Aircraft Using Pre-Cooled Turbojet Engines," *Acta Astronautica*, Vol. 73, 2012, pp. 164–172.

[11] Kodera, M., Ogawa, H., Tomioka, S. and Ueda, S., "Multi-Objective Design and Trajectory Optimization of Space Transportation Systems with RBCC Propulsion via Evolutionary Algorithms and Pseudospectral Methods," AIAA Paper 2014-629, 2014.

[12] Ogawa, H., Kodera, M., Tomioka, S. and Ueda, S., "Multi-Phase Trajectory Optimization for Access-to-Space with RBCC-Powered TSTO via Surrogate-Assisted Hybrid Evolutionary Algo-

rithms Incorporating Pseudo-Spectral Methods," AIAA Paper 2014-2360, 2014.

[13] Hirschel, E. H., Weiland, C., "Design of Hypersonic Flight Vehicles: Some Lessons from the Past and Future Challenges," *CEAS Space Journal*, Vol. 1, No. 1, 2011, pp. 3–22.

[14] Yokoyama, N., *A Study on Multidisciplinary Design Optimization and its Application to Conceptual Design of Space Planes (Fukugou-Ryouiki Saiteki-Sekkei oyobi sono Ucyuu-Oukannki Gainenn-Sekkei heno Ouyou ni Kansuru Kennkyuu)*, Ph. D. Dissertation of the Department of Aeronautics and Astronautics, The University of Tokyo, 2004 (in Japanese).

[15] Yokoyama, N., Suzuki, S., Tsuchiya, T., Taguchi, H. and Kanda, T., "Multidisciplinary Design Optimization of Space Plane Considering Rigid Body Characteristics," *Journal of Spacecraft and Rockets*, Vol. 44, No. 1, 2007, pp. 121–131.

[16] Tsuchiya, T. and Mori, T., "Optimal Design of Two-Stage-to-Orbit Space Planes with Airbreathing Engines," *Journal of Spacecraft and Rockets*, Vol. 42, No, 1, 2005, pp. 90–97.

[17] Kobayashi, H. and Tanatsugu, N., "Optimization Method on TSTO Spaceplane System Powered by Airbreather," AIAA Paper 2001-3965, 2001.

[18] Suzuki, H., Kanda, T., Kai, T., Kobayashi, H., Takasaki, K., Hirotani, T., and Kuratani, N., "Development of Optimal Design and Evaluation Program for Future Space Transportation System Concept," JAXA-RR-07-006, 2008 (in Japanese).

[19] Brown, N. F. and Olds, J. R., "Evaluation of Multidisciplinary Optimization Techniques Applied to a Reusable Launch Vehicle," *Journal of Spacecraft and Rockets*, Vol. 43, No. 6, 2006, pp. 1289–1300.

[20] Tormo, V. G. and Serghides, V. C., "Initial Sizing and Reentry-Trajectory Design Methodologies for Dual-Mode-Propulsion Reusable Aerospace Vehicles," *Journal of Spacecraft and Rockets*, Vol. 44, No. 5, 2007, pp. 1038–1050.

[21] Tsuchiya, T. and Mori, T., "Multidisciplinary Design Optimization for Hypersonic Experimental Vehicle," *AIAA Journal*, Vol. 45, No. 7, 2007, pp. 1655–1662.

[22] Matsuno, Y., Tsuchiya, T., Imamura, S., and Taguchi, H., "Multidisciplinary Design Optimization of Long or Short Range Hypersonic Aircraft," *Transactions of The Japan Society for Aeronautical and Space Sciences*, Vol. 57, No. 3, 2014, pp. 143–152.

[23] Gong, C., Chen, B. and Gu, L., "Design and Optimization of RBCC Powered Suborbital Reusable Launch Vehicle," AIAA Paper 2014-2361, 2014.

[24] Zhang, D., Tang, S. and Che, J. "Concurrent Subspace Design Optimization and Analysis of Hypersonic Vehicles Based on Response Surface Models," *Aerospace Science and Technology*, Vol. 42, 2015, pp. 39–49.

[25] Dufour, R., de Muelenaere, J., and Elham, A., "Trajectory Driven Multidisciplinary Design Optimization of a Sub-Orbital Spaceplane Using Non-Stationary Gaussian Process," *Structural and Multidisciplinary Optimization*, Vol. 52, No. 4, 2015, pp. 755–771.

[26] Martins, J. R. R. A. and Lambe, A. B., "Multidisciplinary Design Optimization: A Survey of Architectures," *AIAA Journal*, Vol. 51, No. 9, 2013, pp. 2049–2075.

[27] Balling, R. J. and Wilkinson, C. A., "Execution of Multidisciplinary Design Optimization Ap-

proaches on Common Test Problems," *AIAA Journal*, Vol. 35, No. 1, 1997, pp. 178–186.

[28] Frank, C. P., Pinon-Fischer, O. J., and Mavris, D. N., "A Design Space Exploration Methodology to Support Decisions under Evolving Requirements' Uncertainties and its Application to Suborbital Vehicles," *Proceedings of 53rd AIAA Aerospace Sciences Meeting*, AIAA Paper 2015-1010, 2015.

[29] Jeong, S., Chiba, K., and Obayashi, S., "Data Mining for Aerodynamic Design Space," *Journal of Aerospace Computing, Information, and Communication*, Vol. 2, No. 11, 2005, pp. 452–469.

[30] Obayashi, S., Jeong, S., Shimoyama, K., Chiba, K., and Morino, H., "Multi-Objective Design Exploration and its Applications," *International Journal of Aeronautical and Space Science*, Vol. 11, No. 4, 2010, pp. 247–265.

[31] Oyama, A., Nonomura, T., and Fujii, K., "Data Mining of Pareto-Optimal Transonic Airfoil Shapes Using Proper Orthogonal Decomposition," *Journal of Aircraft*, Vol. 47, No. 5, 2010, pp. 1756–1762.

[32] Ogawa, H. and Boyce, R. R., "Physical Insight into Scramjet Inlet Behavior via Multi-Objective Design Optimization," *AIAA Journal*, Vol. 50, No. 8, 2012, pp. 1773–1783.

[33] Ogawa, H., "Physical Insight into Fuel-Air Mixing for Upstream-Fuel-Injected Scramjets via Multi-Objective Design Optimization," *Journal of Propulsion and Power*, Vol. 31, No. 6, 2015, pp. 1505–1523.

[34] Jilla, C. D. and Miller, D. W., "Multiobjective, Multidisciplinary Design Optimization Methodology for Distributed Satellite Systems," *Journal of Spacecraft and Rockets*, Vol. 41, No. 1, 2004, pp. 39–50.

[35] Yuhara, T., "Conceptual Design Study on Low Boom LH2 Supersonic Transport – Considering Climate Change Impact –," *Proceedings of the 28th International Congress of the Aeronautical Sciences*, Sep. 2012.

[36] Tatsukawa, T., Watanabe, T., Oyama, A., and Kawakatsu, Y., "Multiobjective Design Exploration of a Many-Objective Space Trajectory Problem for Low-Thrust Spacecraft Using MOEA with Large Populations," AIAA Paper 2015-364, 2015.

[37] Oyama, A., Kawakatsu, Y., and Hagiwara, K., "Data Mining of Pareto-Optimal Solutions of a Solar Observatory Trajectory Design Problem," AIAA Paper 2012-2442, 2012.

[38] Dudas, C., Frantzen, M., and Ng, A. H. C., "A Synergy of Multi-Objective Optimization and Data Mining for the Analysis of a Flexible Flow Shop," *Robotics and Computer-Integrated Manufacturing*, Vol. 27, 2011, pp. 687–695.

[39] Deb, K., *Multi-Objective Optimization Using Evolutionary Algorithms*, John Wiley & Sons, Ltd., Chichester, UK, 2001.

[40] Zhou, A., Qu, B.-Y., Li, H., Zhao, S.-Z., Suganthan, P. N., and Zhang, Q., "Multiobjective Evolutionary Algorithms: A Survey of the State of the Art," *Swarm and Evolutionary Computation*, Vol. 1, No. 1, 2011, pp. 32–49.

[41] Betts, J. T., "Survey of Numerical Methods for Trajectory Optimization," *Journal of Guidance, Control, and Dynamics*, Vol. 21, No. 2, 1998, pp. 193–207.

[42] Betts, J. T., *Practical Methods for Optimal Control and Estimation Using Nonlinear Programming*, SIAM, Philadelphia, USA, 2001.

[43] Gill, P. E., Murray, W., and Saunders, M. A., "SNOPT: An SQP Algorithm for Large-Scale Constrained Optimization," *SIAM Review*, Vol. 47, No. 1, 2005, pp. 99–131.

[44] Wachter, A. and Biegler, L. T., "On the Implementation of a Primal-Dual Interior Point Filter Line Search Algorithm for Large-Scale Nonlinear Programming," *Mathematical Programming*, Vol. 106, No. 1, 2006, pp. 25–57.

[45] Brauer, G. L., Cornick, D. E., and Stevenson, R., "Capabilities and Applications of the Program to Optimize Simulated Trajectories (POST)," NASA CR-2770, 1977.

[46] Hargraves, C. R., and Paris, S. W., "Direct Trajectory Optimization Using Nonlinear Programming and Collocation," *Journal of Guidance, Control, and Dynamics*, Vol. 10, No. 4, 1987, pp. 338–342.

[47] Deb, K., Pratap, A., Agarwal, S., and Meyarivan, T., "A Fast and Elitist Multiobjective Genetic Algorithm: NSGA-II," *IEEE Transactions on Evolutionary Computation*, Vol. 6, No. 2, 2002, pp. 182–197.

[48] Prats, X., Puig, V., Quevedo, J., and Nejjari, F., "Multi-Objective Optimisation for Aircraft Departure Trajectories Minimising Noise Annoyance," *Transportation Research Part C*, Vol. 18, No. 6, 2010, pp. 975–989.

[49] Jiao, X., Jiang, J., "Multi-Objective Optimization of Reentry Trajectory Planning for Hypersonic Aircraft Based on Ant Colony Algorithm," *Proceedings of 2014 IEEE Chinese Guidance, Navigation and Control Conference*, Yantai, China, 8–10 Aug. 2014.

[50] Deb, K., "Multi-Objective Genetic Algorithms: Problem Difficulties and Construction of Test Problems," *Evolutionary Computation*, Vol. 7, No. 3, 1999, pp. 205–230.

[51] Iorio, A. and Li, X., "Rotated Problems and Rotationally Invariant Crossover in Evolutionary Multi-Objective Optimization," *International Journal of Computational Intelligence and Applications*, Vol. 7, No. 2, 2008, pp. 149–186.

[52] Yokoyama, N. and Suzuki, S., "Modified Genetic Algorithm for Constrained Trajectory Optimization," *Journal of Guidance, Control, and Dynamics*, Vol. 28, No. 1, 2005, pp. 139–144.

[53] Cowart, K. and Olds, J., "TCAT — A Tool For Automated Thermal Protection System Design," AIAA Paper 2000-5265, 2000.

[54] Rohrschneider, R. R., "Development of a Mass Estimating Relationship Database for Launch Vehicle Conceptual Design," AE8900 Special Project, School of Aerospace Engineering, Georgia Institute of Technology, 2002.

[55] Zhao, J. and Zhou, R., "Reentry Trajectory Optimization for Hypersonic Vehicle Satisfying Complex Constraints," *Chinese Journal of Aeronautics*, Vol. 26, No. 6, 2013, pp. 1544–1553.

[56] Jorris, T. R. and Cobb, R. G., "Three-Dimensional Trajectory Optimization Satisfying Waypoint and No-Fly Zone Constraints," *Journal of Guidance, Control, and Dynamics*, Vol. 32, No. 2, 2009, pp. 551–572.

[57] Zimmerman, C., Dukeman, G., and Hanson, J., "Automated Method to Compute Orbital Reentry

Trajectories with Heating Constraints," *Journal of Guidance, Control, and Dynamics*, Vol. 26, No. 4, 2003, pp. 523–529.

[58] ul Islam Rizvi, S. T., Linshu H., and Dajun, X., "Optimal Trajectory Analysis of Hypersonic Boost-Glide Waverider with Heat Load Constraint," *Aircraft Engineering and Aerospace Technology*, Vol. 87, No. 1, 2015, pp. 67–78.

[59] Bradford, J. E. and Olds, J. R., "Thermal Protection System Sizing and Selection for RLVs Using Sentry Code," AIAA Paper 2006-4605, 2006.

[60] Pesch, H. J., Rund, A., von Wahl, W., and Wendl, S., "On Some New Phenomena in State-Constrained Optimal Control if ODEs as well as PDEs are Involved," *Control and Cybernetics*, Vol. 39, No. 3, 2010, pp. 647–660

[61] Wachter, M. and Sachs, G., "Constraining Heat Input by Trajectory Optimization for Minimum-Fuel Hypersonic Cruise," *Asian Journal of Control*, Vol. 8, No. 4, 2006, pp. 307–313.

[62] Chudej, K., Pesch, H.J., Wachter, M., Sachs, G., Bras, F. L., "Instationary Heat Constrained Trajectory Optimization of a Hypersonic Space Vehicle by ODE-PDE-Constrained Optimal Control," *Variational Analysis and Aerospace Engineering*, Springer, 2009, pp. 127–143

[63] Miettinen, K. M., *Nonlinear Multiobjective Optimization*, Kluwer Academic Pub., Norwell, USA, 1999.

[64] Benson, D. A., Huntington, G. T., Thorvaldsen, T. P. and Rao, A. V., "Direct Trajectory Optimization and Costate Estimation via an Orthogonal Collocation Method," *Journal of Guidance, Control, and Dynamics*, Vol. 29, No. 6, 2006, pp. 1435–1440.

[65] Garg, D., Patterson, M., Hager, W. W., Rao, A. V., Benson, D. A., and Huntington, G. T., "A Unified Framework for the Numerical Solution of Optimal Control Problems Using Pseudospectral Methods," *Automatica*, Vol. 46, No. 11, 2010, pp. 1843–1851.

[66] Fujikawa, T., *Trajectory Design of a Hypersonic Flight Experimental Vehicle Using Pseudospectral Optimal Control with a Novel Adaptive Mesh Refinement Method (Gi-Supekutoru Saiteki-Seigyo no tameno Messyu Saibunnka-Hou to sore wo Mochiita Gokucyouonnsoku Jikkennki no Kidou Kentou)*, Master Thesis of the Department of Aeronautics and Astronautics, The University of Tokyo, 2013 (in Japanese).

[67] Fujikawa, T. and Tsuchiya, T., "Enhanced Mesh Refinement in Numerical Optimal Control Using Pseudospectral Methods," *SICE Journal of Control, Measurement, and System Integration*, Vol. 7, No. 3, 2014, pp. 159–167.

[68] Chankong, V. and Haimes, Y. Y., *Multiobjective Decision Making: Theory and Methodology*, Elsevier Science Publishing Co., Inc., New York, USA, 1983.

[69] Mueller-Gritschneder, D., Graeb, H., and Schlichtmann, U., "A Successive Approach to Compute the Bounded Pareto Front of Practical Multiobjective Optimization Problems," *SIAM Journal of Optimization*, Vol. 20, No. 2, 2009, pp. 915–934.

[70] Cayton, L., "Algorithms for Manifold Learning," *University of California, San Diego, Tech. Rep. CS2008-0923*, 2005.

[71] Tenenbaum, J. B., Silva, V., and Langford, J. C., "A Global Geometric Framework for Nonlinear

Dimensionality Reduction," *Science*, Vol. 290, 2000, pp. 2319–2323.

[72] Zhang, T., Yang, J., Zhao, D., and Ge, X., "Linear Local Tangent Space Alignment and Application to Face Recognition," *Neurocomputing*, Vol. 70, 2007, pp. 1547–1553.

[73] Daskilewicz, M. J., German, B. J., "Representing Sampled Pareto Frontiers as Parameterized Continuous Manifolds Using Self-Organizing Maps," *AIAA Journal*, Vol. 52, No. 11, 2014.

[74] Sacks, J., Welch, W. J., Mitchell, T. J., and Wynn, H. P., "Design and Analysis of Computer Experiments," *Statistical Science*, Vol. 4, No. 4, 1989, pp. 409–423.

[75] Simpson, T. W., Mauery, T. M., Korte, J. J., and Mistree, F., "Kriging Models for Global Approximation in Simulation-Based Multidisciplinary Design Optimization," *AIAA Journal*, Vol. 39, No. 12, 2001, pp. 2233–2241.

[76] Forrester, A. I. J., Sóbester, A. and Keane, A. J., *Engineering Design via Surrogate Modelling: A Practical Guide*, John Wiley & Sons, Chichester, 2008.

[77] Bryson, A. E. and Ho, Y.-C., *Applied Optimal Control: Optimization, Estimation, and Control*, Taylor & Francis, New York, 1975.

[78] Gill, P. E., Murray, W. and Saunders, M. A., "User's Guide for SNOPT Version 7: Software for Large-Scale Nonlinear Programming," http://web.stanford.edu/group/SOL/guides/sndoc7.pdf.

[79] Quinn, R. D. and Gong L., "A Method for Calculating Transient Surface Temperature and Surface Heating Rates for High-Speed Aircraft," NASA TP–2000–209034, 2000.

[80] Ng, W. H, Friedmann, P. P. and Waas, A. M., "Thermomechanical Analysis of a Thermal Protection System with Defects and Heat Shorts," AIAA Paper 2006–2212, 2006.

[81] Crank, J. and Nicolson, P., "A Practical Method for Numerical Evaluation of Solutions of Partial Differential Equations of the Heat-Conduction Type," *Mathematical Proceedings of the Cambridge Philosophical Society*, Vol. 43, No. 1, 1947, pp. 50–67.

[82] Elnagar, G., Kazemi, M. A., and Razzaghi, M., "The Pseudospectral Legendre Method for Discretizing Optimal Control Problems," *IEEE Transactions on Automatic Control*, Vol. 40, No. 10, 1995, pp. 1793–1796.

[83] Garg, D., Hager, W. W., and Rao, A. V., "Pseudospectral Methods for Solving Infinite-Horizon Optimal Control Problems," *Automatica*, Vol. 47, No. 4, 2011, pp. 829–837.

[84] Fornberg, B., *A Practical Guide to Pseudospectral Method*, Cambridge University Press, Cambridge, UK, 1998.

[85] Canuto, C., Hussaini, M. Y., Quarteroni, A., and Tang, T. A., *Spectral Methods in Fluid Dynamics*, Springer-Verlag, 1987, Section 2.3.

[86] Golub, G. H., "Some Modified Matrix Eigenvalue Problems," *SIAM Review*, Vol. 15, 1973, pp. 318–334.

[87] Trefethen, L. N., *Spectral Methods in Matlab*, SIAM, Philadelphia, USA, 2000

[88] Funaro, D. and Gottlieb, D., "A New Method of Imposing Boundary Conditions in Pseudospectral Approximations of Hyperbolic Equations," *Mathematics of Computation*, Vol. 51, No. 184, 1988, pp. 599–613.

[89] Fornberg, B., "A Pseudospectral Fictitious Point Method for High Order Initial-Boundary Value

Problems," *SIAM Journal on Scientific Computing*, Vol. 28, No. 5, 2006, pp. 1716–1729

[90] Fornberg, B., "Generation of Finite Difference Formulas on Arbitrarily Spaced Grids," *Mathematics of Computation*, Vol. 51, No. 184, 1988, pp. 699–706

[91] NOAA, NASA and US Air Force, "U. S. Standard Atmosphere, 1976," NASA TM–X–74335, 1976.

[92] Raymer, D. P., *Aircraft Design: A Conceptual Approach*, Fifth Edition, AIAA, Washington, DC, USA, 2012, pp. 688–690.

[93] Vallado, D. A. and McClain, W. D., *Fundamentals of Astrodynamics and Applications*, Third Edition, Springer, New York, USA, 2007, pp. 51–56.

[94] Taylor, J. W. R. (edit), *Jane's All the World's Aircraft 1989–90*, Jane's Information Group, London, 1989, pp. 242–243.

[95] Taylor, J. W. R. (edit), *Jane's All the World's Aircraft 1975–76*, Jane's Information Group, London, 1975, pp. 108–111.

[96] Jackson, P. (edit), *Jane's All the World's Aircraft 2003–2004*, Jane's Information Group, London, 2003, p. 684.

[97] Tomioka, S., Hiraiwa, T., Saito, T., Kato, K., Kodera, M., and Tani, K., "System Analysis of a Hydrocarbon-Fueled RBCC Engine Applied to a TSTO Launch Vehicle," *Proceedings of the 29th International Symposium on Space Technology and Science*, June 2013.

[98] Williams, S. D. and Curry, D. M., "Thermal Protection Materials: Thermophysical Property Data," NASA RP–1289, 1992.

[99] National Space Development Agency of Japan, "HOPE-X BBM Development Test on Structure and TPS Subsystems, Part 1," NASDA TMR–980006, 1999 (in Japanese).

[100] Patterson, M. A., Weinstein, M., Rao, A. V., "An Efficient Overloaded Method for Computing Derivatives of Mathematical Functions in MATLAB," *ACM Transactions on Mathematical Software*, Vol. 39, No. 3, 2013, pp. 17:1–17:36.

[101] Smith, T. R., Bowcutt, K. G., Selmon, J. R., Mirranda, L., Northrop, B., Maris, R., Unger, E. R., Lau, K. Y., Silvester, T., Alesi, H., Paull, A., Paull, R., and Dolvin, D. J., "HIFiRE4: A Low-Cost Aerodynamics, Stability, and Control Hypersonic Flight Experiment," AIAA Paper 2011-2275, 2011.

[102] Gülhan, A., Siebe, F., Thiele, T., Neeb, D., Turner, J. and Ettl, J., "Sharp Edge Flight Experiment-II Instrumentation Challenges and Selected Flight Data," *Journal of Spacecraft and Rockets*, Vol. 51, No. 1, 2014, pp. 175–186.

[103] Pezzella, G., Marini, M., Cicala, M., Vitale, A., Langener, T. and Steelant, J., "Aerodynamic Characterization of HEXAFLY Scramjet Propelled Hypersonic Vehicle," AIAA Paper 2014-2844, 2014.

[104] Sato, T., Taguchi, H., Tsuchiya, T., Tsue, M., Tomioka, S., Kobayashi, H., Kojima, T., Fujikawa, T., and Amano, Y., "Summary of the High Mach Integrated Control Experiment (HIMICO) for Air-breathers using the S-520 Sounding Rocket," *Proceedings of the 59th Space Sciences and Technology Conference*, Oct. 2015 (in Japanese).

[105] Enright, P. J., and Conway, B. A., “Optimal Finite-Thrust Spacecraft Trajectories Using Collocation and Nonlinear Programming,” *Journal of Guidance, Control, and Dynamics*, Vol. 14, No. 5, 1991, pp. 981–985.

[106] Elnagar, G., and Kazemi, M. A., “Pseudospectral Chebyshev Optimal Control of Constrained Nonlinear Dynamical Systems,” *Computational Optimization and Applications*, Vol. 11, 1998, pp. 195–217.

[107] Fahroo, F. and Ross, I. M., “Direct Trajectory Optimization by a Chebyshev Pseudospectral Method,” *Journal of Guidance, Control, and Dynamics*, Vol. 25, No. 1, 2002, pp. 160–166.

[108] Davis, P. J., and Polonsky, I., “Numerical Interpolation, Differentiation, and Integration,” *Handbook of Mathematical Functions with Formulas, Graphs, and Mathematical Tables*, edited by Abramowitz, M., and Stegun, I. A., U. S. Department of Commerce, National Bureau of Standards, Washington, D. C., 1964.

[109] Gong, Q., Kang, W., and Ross, I. M., “A Pseudospectral Method for the Optimal Control of Constrained Feedback Linearizable Systems,” *IEEE Transactions on Automatic Control*, Vol. 51, No. 7, 2006, pp. 1115–1129.

[110] Ross, I. M., and Fahroo, F., “Pseudospectral Knotting Methods for Solving Optimal Control Problems,” *Journal of Guidance, Control, and Dynamics*, Vol. 27, No. 3, 2004, pp. 397–405.

[111] Golub, G. H. and Welsch, J. H., “Calculation of Gauss Quadrature Rules,” *Mathematics of Computation*, Vol. 23, No. 106, 1969, pp. 221–230.

[112] Patterson, M. A. and Rao, A. V., “Exploiting Sparsity in Direct Collocation Pseudospectral Methods for Solving Optimal Control Problems,” *Journal of Spacecraft and Rockets*, Vol. 49 , No. 2, 2012, pp. 364–377.

[113] Isono, T., Tomioka, S., Takahashi, H., Sakuranaka, N., Ono, M. and Mikoshiba, R., “Evaluation of Influence of Flight Environment upon External Nozzle Flow in Wave-Rider Type Spaceplane,” *Proceedings of the 58th Space Sciences and Technology Conference*, Nov. 2014 (in Japanese).

[114] Liepmann, H. W. and Roshko, A., *Elements of Gasdynamics*, Wiley, Hoboken, 1957, pp. 284–304.

[115] Isono, T., Tomioka, S., Sakuranaka, N., “Construction of the Performance Prediction Model of Cowl Truccated Single Expansion Ramp Nozzle,” *Proceedings of Symposium on Shock Waves in Japan*, Mar. 2015 (in Japanese).

[116] Sobol, I. M., “Uniformly Distributed Sequences with an Additional Property,” *USSR Computational Mathematics and Mathematical Physics,* Vol. 16, No. 5, 1976, pp. 236–242.

[117] Fox, B., “Algorithm 647: Implementation and Relative Efficiency of Quasirandom Sequence Generators,” *ACM Transactions on Mathematical Software*, Vol. 12, No. 4, 1986, pp. 362–376.

[118] Magnus, A. E. and Epton, M. A., “PAN AIR—A Computer Program for Predicting Subsonic or Supersonic Linear Potential Flows About Arbitrary Configurations Using a Higher Order Panel Method, Vol. 1. Theory Document,” NASA CR–3251, 1980.

[119] Pittman, J. L., “Application of Supersonic Linear Theory and Hypersonic Impact Methods to Three Nonslender Hypersonic Airplane Concepts at Mach Numbers from 1.10 to 2.86,” NASA TP–1539, 1979.

[120] Bonner, E., Clever, W., and Dunn, K., "Aerodynamic Preliminary Analysis System II Part I – Theory," NASA CR–182076, 1991.

[121] White, F. M., *Viscous Fluid Flow*, McGraw-Hill, Inc., New York, 1974, p. 639.

[122] Thompson, M. J., "A Note on the Calculation of Oblique Shock-Wave Characteristics," *Journal of Aeronautical Sciences*, Vol. 17, No. 11, 1950, p. 744.

[123] Hall, I. M., "Inversion of the Prandtl-Meyer Relation," *The Aeronautical Journal*, Vol. 79, 1975, pp. 417–418.

[124] Detra, R. W., Kemp, N. H., and Riddell, F. R., "Addendum to 'Heat Transfer to Satellite Vehicles Re-entering the Atmosphere'," *Jet Propulsion*, Vol. 27, No. 12, 1957, pp. 1256–1257.

[125] Jacobs, E. N., Ward, K. E., and Pinkerton, R. M.. "The Characteristics of 78 Related Airfoil Sections from Tests in the Variable-Density Wind Tunnel," NACA R-460, 1935.

[126] The Japan Society of Mechanical Engineers (edit), *JSME Data Book: Heat Transfer, 4th Edition*, Maruzen Co., Ltd., Tokyo, 1986, p. 84 (in Japanese).

[127] Anderson, J. D. Jr., *Hypersonic and High-Temperature Gas Dynamics, Second Edition*, American Institute of Aeronautics and Astronautics, Reston, 2006, pp. 341–343.

[128] Glatt, C. R., "WAATS: A Computer Program for Weights Analysis of Advanced Transportation Systems," NASA CR–2420, 1974.

[129] Harloff, G. J. and Berkowitz, B. M., "HASA—Hypersonic Aerospace Sizing Analysis for the Preliminary Design of Aerospace Vehicles," NASA CR–182226, 1988.

[130] Hilberg, D., Lazik, W., and Fiedler, H. E., "The Application of Classical POD and Snapshot POD in a Turbulent Shear Layer with Periodic Structures," *Applied Scientific Research*, Vol. 53, 1994, pp. 283–290.